

# **Surface and interface study of kesterite-based and related thin-film solar cell structures**

Von der Fakultät für MINT - Mathematik, Informatik, Physik, Elektro- und  
Informationstechnik

der Brandenburgischen Technischen Universität Cottbus-Senftenberg

zur Erlangung des akademischen Grades

**Doktor der Naturwissenschaften**

(Dr. rer. nat.)

genehmigte Dissertation

vorgelegt von

M. Sc.

**Leonard Köhler**

geboren am 04.02.1988 in Meppen

Gutachter: Prof. Dr. Marcus Bär

Gutachter: Prof. Dr. Susan Schorr

Gutachter: Prof. Dr. Jürgen Reif

Tag der mündlichen Prüfung: 10. Mai 2017

"Über Halbleiter sollte man nicht arbeiten,  
das ist eine Schweinerei,  
wer weiß ob es überhaupt Halbleiter gibt."

<sup>1</sup>Wolfgang Pauli [1]

I think scientists, in particular Ph.D. students, always face a difficult choice. They can either trust the wisdom and the opinions of all the smart people around them, which is usually the more convenient and fruitful path to take, or they can try to find something meaningful where few people expect it. The immense success of modern semiconductor physics and the remaining significance of Pauli's findings, despite his distrust in semiconductors, prove the legitimacy of both approaches.

I hope that I could find a good balance between learning, on the one hand, from the brilliant people who guided me through my research field with their advice and, on the other hand, by following my own ideas and, of course, by try and error.

---

<sup>1</sup>One should not work on semiconductors. They are a mess.  
Who knows whether semiconductors exist at all.

# Declaration of Authorship

I, Leonard KÖHLER, declare that this thesis titled

'Surface and interface study of kesterite-based  
and related thin-film solar cell structures'

and the work presented in it are my own. I confirm that:

- This work was done wholly or mainly while in candidature for a research degree at this University.
- No part of this thesis has previously been submitted for a degree or any other qualification at this University or any other institution.
- This thesis is my first submission for a Ph.D. degree at any institution.
- Where I have consulted the published work of others, this is always clearly attributed.
- Where I have quoted from the work of others, the source is always given. With the exception of such quotations, this thesis is entirely my own work.
- I have acknowledged all main sources of help.

Signed:

---

Date:

---

"Now there are two ways in which you can increase your understanding of these issues.

One way is to remember the general ideas and then go home and try to figure out what commands you need and make sure you don't leave one out. Make the set shorter or longer for confidence and try to understand the tradeoffs by trying to do problems with your choice. This is the way I would do it because I have that kind of personality! It's the way I study -- to understand something by trying to work it out or, in other words, to understand something by creating it. Not creating it one hundred percent, of course; but taking a hint as to which direction to go but not remembering the details. These you work out for yourself.

The other way, which is also valuable, is to read carefully how someone else did it.

I find the first method best for me, once I have understood the basic idea. If I get stuck I look at a book that tells me how someone else did it. I turn the pages and then I say "Oh, I forgot that bit", then close the book and carry on.

Finally, after you've figured out how to do it you read how they did it and find out how dumb your solution is and how much more clever and efficient theirs is! But this way you can understand the cleverness of their ideas and have a framework in which to think about the problem. When I start straight off to read someone else's solution I find it boring and uninteresting, with no way of putting the whole picture together. At least, that's the way it works for me!"

Richard P. Feynman [2]

## *Abstract*

The chemical and electronic structure of the interfaces of kesterite-based and related absorber materials in thin-film solar cell device-relevant layer stacks have been investigated with x-ray based spectroscopic techniques (XPS, HAXPES, XAES, XES, and XAS).

The analyzed materials are CZTS absorbers grown at Uppsala University with their interfaces to the Mo back contact and to different  $\text{ZnO}_x\text{S}_{1-x}$ -buffer layers ( $x=[0; \sim\frac{6}{7}; 1]$ ), SnS absorbers with partly N-doped ZnO buffer layers produced in a collaboration at MIT and Harvard University, and  $\text{CuSbS}_2$  absorbers with (Cd,Zn)S buffer layers grown at NREL in collaboration with MIT.

We find an unchanged CZTS surface in this series which has a profound effect on the  $\text{ZnO}_x\text{S}_{1-x}$  growth. Instead of a constant composition throughout the buffer thickness, we find S-rich material growing directly on the CZTS in the ALD process. The composition changes towards the O-rich  $\text{ZnO}_x\text{S}_{1-x}$  that forms the main part of the buffer layer. The conduction band offset is therefore found to be around  $-0.21(\pm 0.15)$  eV. The measured cliff is reduced by chemical interface modification towards a flat band alignment.

The interface effect during annealing at the CZTS back contact where  $\text{MoS}_2$  forms occurs even at low annealing temperatures below  $500^\circ\text{C}$ . Sn spectra of liftoff CZTS back sides, annealed on the Mo contact, resemble the precursor at all temperatures while Sn spectra of CZTS front sides are almost single phase after standard annealing. We observe the stabilization of SnS at the back contact and different Sn-oxides. A TiN interlayer was effectively introduced to prevent reactions at the CZTS/Mo interface.

We find a strong impact of ALD deposited ZnO on oxidized SnS absorber surfaces, resulting in metallic Sn formation. In contrast, doped ZnO:N reduces the SnS much less aggressively, affecting mainly the SnO<sub>2</sub> species. The contact layers show the formation of Zn(OH)<sub>2</sub> that is mainly at the layer surface. The strong downwards bending for both ZnO and SnS at the ZnO/SnS junction that we find for undoped ZnO contact layers is drastically reduced if ZnO:N contact layers are used. The band alignment of both junctions shows a cliff in the conduction band. The smaller cliff of 0.2 eV for ZnO:N/SnS makes this junction much more interesting for solar cell applications than the ZnO/SnS with a large cliff of 0.55 eV.

The chemical analysis of the (Cd,Zn)S:Ga/CuSbS<sub>2</sub> reveals chemical interaction at the junction. We find an additional species on the high energy side of the Cu peak for all samples. Since we can also exclude a Cu-oxide, the second chemical environment of Cu is most likely a more Cu-rich Cu<sub>3</sub>SbS<sub>3</sub> or Cu<sub>12</sub>Sb<sub>4</sub>S<sub>13</sub> at the surface or interface. The second finding that is contrary to expectation for Cu is the weak but clear Cu signal on the thickest buffer layer where we don't find any Sb and don't expect any absorber signal. The Cu must be more mobile than Sb and diffuse into the buffer material forming a Cu species with E<sub>B</sub> similar to the Cu-rich species. The effect has to be observed on another sample to exclude contamination.

The interface species can be explained with the changed buffer composition at the interface, particularly low S and Cd content and increased Ga concentration, and could also be affected by the presence of O and hydroxides. We find an upwards surface band bending of -0.15 eV for the bare absorber. At the junction, we see downwards band bending of up to 0.2(±0.09) eV in the absorber and strong upwards band bending of -0.75(±0.28) eV in the buffer.

The junction is not an abrupt transition from one homogenous material to another. The buffer growth is strongly affected by the absorber. Also the electronic structure on both sides is significantly affected. We find a conduction band alignment with a large cliff of -1.3(±0.3) eV.

## Zusammenfassung

Die chemische und elektronische Struktur von Grenzflächen in Schichtstapeln mit unmittelbarer Bedeutung für Kesterit-basierte und verwandte Dünnschichtsolarzellen wurden mit Röntgen-basierten Spektroskopietechniken (XPS, HAXPES, XAES, XES, and XAS) untersucht.

Die untersuchten Materialien sind CZTS-Absorber, die an der Universität Uppsala hergestellt wurden, mit ihren Grenzflächen zu Mo Rückkontakten und zu verschiedenen  $\text{ZnO}_x\text{S}_{1-x}$ -Pufferschichten ( $x=[0; \sim\frac{6}{7}; 1]$ ), Sn-Absorber mit teilweise N-dotierten ZnO Pufferschichten, die in einer Zusammenarbeit am MIT und der Universität Harvard hergestellt wurden, und  $\text{CuSbS}_2$  Absorber mit (Cd,Zn)S-Pufferschichten, produziert am NREL in Zusammenarbeit mit dem MIT.

Unsere Untersuchungen zeigen eine chemisch unveränderte CZTS-Oberfläche die einen starken Einfluss auf das  $\text{ZnO}_x\text{S}_{1-x}$ -Wachstum hat. Statt eines konstanten Mischungsverhältnisses in der Puffeschicht zeigt sich ein S-angereichertes Material, dass im ALD-Prozess direkt auf dem CZTS wächst. Die Zusammensetzung ändert sich zu einem O-reicheren  $\text{ZnO}_x\text{S}_{1-x}$ , dass den größten Teil der Pufferschicht bildet. Der Leitungsbandversatz ergibt sich dadurch zu  $-0.21(\pm 0.15)$  eV. Dieses gemessene "cliff" wird durch die chemische Modifikation an der Grenzfläche zu einem flachen Bandübergang geändert.

Der Grenzflächeneffekt beim Ausheizen am CZTS Rückkontakt, wo sich  $\text{MoS}_2$  bildet, tritt auch bei niedrigen Ausheiztemperaturen unter  $500^\circ\text{C}$  auf. Sn-Spektren von "liftoff" CZTS-Rückseiten, die auf dem Mo-Kontakt ausgeheizt wurden, ähneln dem unkristallisierten Roh-CZTS bei allen Ausheiztemperaturen, während Sn-Spektren von CZTS-Frontseiten nach vollständigem Ausheizen nahezu reinphasiges Kesterit zeigen. Wir beobachten die Stabilisation von SnS am Rückkontakt sowie verschiedene Sn-Oxide. Eine TiN Zwischenschicht wurde erfolgreich eingeführt, um Reaktionen an der CZTS/Mo Grenzfläche zu verhindern.

Wir finden einen signifikanten Effekt von ALD-deponiertem ZnO auf oxidierte SnS-Absorberoberflächen, der zur Bildung von metallischem Sn führt. Dotiertes ZnO:N reduziert das SnS deutlich weniger aggressiv, hier werden hauptsächlich Dioxidspezies reduziert. Beide Kontaktschichten weisen  $\text{Zn(OH)}_2$  auf, das sich im Wesentlichen auf der Oberfläche findet. Die starke Abwärtsbiegung der Bänder an der Grenzfläche von ZnO und SnS, die sich für undotiertes ZnO-Kontaktmaterial findet, schwächt sich extrem ab, wenn ZnO:N Kontaktmaterial verwendet wird. Die Bandanordnung beider Kontakte zeigt ein "cliff" im Leitungsband. Das deutlich kleinere "cliff" von 0.2 eV in ZnO:N/SnS macht die deutlich bessere Eignung dieser Kombination für Solarzellenanwendungen klar, gerade im Vergleich zu ZnO/SnS mit einem großen "cliff"-Versatz von 0.55 eV.

Die chemische Analyse von  $(\text{Cd,Zn})\text{S}:\text{Ga}/\text{CuSbS}_2$  enthüllt chemische Veränderungen an der Grenzfläche. Wir finden in allen Proben eine zusätzliche Spezies mit erhöhter Bindungsenergie im Cu-Peak. Da wir ein Cu-Oxid ausschließen können, ist diese zweite chemische Umgebung von Cu aller Wahrscheinlichkeit nach eine Cu-reichere Verbindung wie  $\text{Cu}_3\text{SbS}_3$  oder  $\text{Cu}_{12}\text{Sb}_4\text{S}_{13}$  an der Oberfläche oder Grenzfläche. Ein weiteres unvorhergesehenes Ergebnis beim Cu ist das schwache aber klar erkennbare Cu-Signal das in der dicksten Pufferschicht auftritt. Hier ist kein Sb erkennbar und daher keinerlei Signal vom Absorber zu erwarten. Das Cu scheint daher mobiler als Sb zu sein und durch die Pufferschicht zu diffundieren, wo eine zusätzliche Cu-Verbindung gebildet wird. Dieser Effekt muss aber noch auf Vergleichsproben verifiziert werden, um Kontamination der Probe auszuschließen.

Die Grenzflächenverbindungen können durch die veränderte Puffer-Komposition an der Grenzfläche erklärt werden. Insbesondere niedriger S- und Cd-Gehalt und ein erhöhter Ga-Anteil spielen hier eine Rolle, ferner die Präsenz von O und Hydroxiden. Wir messen eine Oberflächen-Aufwärtsbiegung der Bänder von -0.15 eV für den reinen Absorber. Am p-n-Übergang zeigen die Bänder eine Abwärtsbiegung von  $0.2(\pm 0.09)$  eV im Absorber und eine starke Aufwärtsbiegung von  $-0.75(\pm 0.28)$  eV im Puffer.

Diese Grenzfläche ist keine scharfe Grenze zwischen zwei homogenen Materialien. Das Wachstum der Pufferschicht ist stark vom Absorber beeinflusst und auch die elektronische Struktur auf beiden Seiten wird verändert. Der Leitungsbandversatz zeigt ein großes "cliff" von  $-1.3(\pm 0.3)$  eV.



# Acknowledgements

This thesis would not have been finished if I hadn't had the support of many wonderful people throughout these years. I can only mention some of those who have played a vital role for my Ph.D. time.

I first want to thank my family and soon-to-be family and all those friends who all had an open ear for my problems and kept me optimistic through all the smaller and bigger failures that come with the work as a Ph.D. student. Most importantly, Alena, thank you for always being there for me and for believing in me more than I sometimes did.

I thank all the people who have created a great research environment around me at HZB. For me this is primarily Marcus Bär's group with Regan G. Wilks who could always explain why my findings were more difficult but also more interesting than I had thought; Jan-Hendrik Alsmeier who introduced me to the field of kesterite research; my CIGSSe counterpart Evelyn Handick who turned out to be the best colleague I could wish for; David E. Starr who from the start pointed out any flaws in my work; Thomas Kunze who took plenty of responsibility off my shoulders in Wannsee; and many others. I thank my external collaborators who gave me the opportunity to be a part of their research by providing me with solar cell fragments from the frontline of their production.

I am deeply thankful for the steady support from Uppsala University, namely the group around Charlotte Platzer-Björkman, Jonathan J. Scragg, Tove Ericson, and Tobias Törndahl. It was also a great pleasure to collaborate with Riley E. Brandt and Tonio Buonassisi from MIT as well as Chuanxi Yang and Roy Gordon from Harvard University and Lauryn Baranowski and Andriy Zakutayev from the National Renewable Energy Laboratory (NREL). Many thanks go to the *extended Heske group*, in particular to Monika Blum, Andreas Benkert and Dagmar Kreikemeyer-Lorenzo who introduced me to the SALSA and SXF endstation.

I am thankful for the inspiring and informative exchange with students and advisors in the MatSEC research school and the KESTCELLS project.

Financially, I am thankful for the generous support of the Graduate School *Materials for Solar Energy Conversion* as part of *Dahlem Research School* as well as the Impuls- und Vernetzungsfonds (VH-NG-423) for support of the Helmholtz-University Young Investigator Group I started my work in.

Lastly, I want to thank all of my thesis committee members, Prof. Susan Schorr and Regan G. Wilks — I have benefited greatly from all of our scientific conversations and interactions. In particular, I wish to thank my advisor, Prof. Marcus Bär. I've been fortunate to learn from his example in passion for research and his enthusiasm for our work. Most importantly, he gave me the motivation, freedom and flexibility to explore all aspects of research and academic activities.



# Contents

	<b>Page</b>
<b>Declaration of Authorship</b>	<b>iii</b>
<b>Abstract</b>	<b>v</b>
<b>Zusammenfassung</b>	<b>vii</b>
<b>Acknowledgements</b>	<b>ix</b>
<b>List of Figures</b>	<b>xv</b>
<b>List of Tables</b>	<b>xix</b>
<b>Abbreviations &amp; Symbols</b>	<b>xxi</b>
<b>1 Introduction</b>	<b>1</b>
1.1 Outline . . . . .	2
<b>2 Theoretical considerations</b>	<b>5</b>
2.1 p-n-junctions and diodes . . . . .	5
2.1.1 Solar cells . . . . .	7
2.1.2 Free electrons in matter . . . . .	8
<b>3 Experimental section</b>	<b>11</b>
3.1 Notation and electronic transitions . . . . .	11
3.1.1 XPS notation . . . . .	12
3.1.2 X-ray notation and Siegbahn notation . . . . .	12
Transition rules . . . . .	13
3.2 Synchrotron radiation . . . . .	14
3.3 PES . . . . .	16
3.3.1 Energy calibration . . . . .	18
3.3.2 XPS . . . . .	18
3.3.3 HAXPES . . . . .	18
3.3.4 XAES . . . . .	19
Modified Auger parameters $\alpha'$ . . . . .	19
3.4 X-ray absorption and emission . . . . .	20
3.4.1 XES . . . . .	21
3.4.2 XAS . . . . .	22
3.5 Peak fitting and analysis details . . . . .	23

<b>4</b>	<b>Cu<sub>2</sub>ZnSnS<sub>4</sub> with ZnO<sub>x</sub>S<sub>1-x</sub> buffer</b>	<b>25</b>
4.1	Kesterite-based thin film solar cells	25
4.2	The ZnO <sub>x</sub> S <sub>1-x</sub> system as buffer material	27
4.2.1	Sample preparation	28
	Cell parameters	30
4.3	Chemical structure of the Cu <sub>2</sub> ZnSnS <sub>4</sub> - ZnO <sub>x</sub> S <sub>1-x</sub> - interface	31
4.3.1	ZnS	31
4.3.1.1	PES measurements	31
	Core levels	33
	Wagner plot	39
4.3.1.2	X-ray absorption and emission	41
	XES comparison with HAXPES	41
	XES spectra	43
4.3.1.3	ZnS thickness	45
	Conclusion	46
4.3.2	ZnO	47
4.3.2.1	PES measurements	47
	Core levels	48
	Wagner plot	53
4.3.2.2	X-ray absorption and emission	56
	XES spectra	56
4.3.2.3	ZnO thickness	57
	Conclusion	58
4.3.3	ZnO <sub>x</sub> S <sub>1-x</sub>	60
4.3.3.1	PES measurements	60
	Core levels	61
	Wagner plot	66
4.3.3.2	X-ray absorption and emission	69
	XES spectra	69
	XAS spectra	71
4.3.3.3	ZnOS thickness	74
4.3.4	Reaction enthalpies and conclusion	76
	Conclusion	77
4.3.5	Buffer thickness comparison	78
4.4	Electronic structure of the Cu <sub>2</sub> ZnSnS <sub>4</sub> - ZnO <sub>x</sub> S <sub>1-x</sub> - interface	79
4.4.0.1	VBM composition and comparison to theory	80
4.4.1	Spectral shifts and band bending	82
4.4.2	Valence band maxima	84
	Conclusion	89
4.5	Summary	89
<b>5</b>	<b>Cu<sub>2</sub>ZnSnS<sub>4</sub> - back side reactions with molybdenum</b>	<b>91</b>
5.1	Molybdenum as back contact	91
5.1.1	Sample preparation	92
5.2	CZTS/Mo interface interaction	94
	Core levels	96
5.2.1	Lift-off samples	96

---

Conclusion	101
5.2.2 Model system samples	103
5.2.3 In situ annealing	107
Conclusion	109
<b>6 SnS solar cell absorber with ZnO contact layers</b>	<b>111</b>
6.1 SnS solar cells	111
ZnO contact layers	111
6.1.1 Sample preparation	112
6.2 Chemical structure of the SnS-ZnO interface	112
6.2.1 SnS-side of the interface	114
6.2.2 ZnO-side of the interface	119
Conclusion	121
6.3 Electronic structure of the SnS-ZnO interface	122
Conclusion	127
<b>7 The (Cd,Zn)S:Ga / CuSbS<sub>2</sub> interface</b>	<b>129</b>
7.1 CuSbS <sub>2</sub> as thin film solar cell absorber	129
7.1.1 Sample preparation	129
7.2 Chemical structure of the (Cd,Zn)S:Ga/CuSbS <sub>2</sub> interface	130
Conclusion	147
<b>A Additional graphs and tables</b>	<b>149</b>
A.1 Inelastic mean free paths for ZnOS/CZTS	150
A.2 ZnOS/CZTS	151
A.2.1 Auger lines	151
A.2.2 Additional elements	153
A.2.3 Additional information	154
A.2.4 Additional XAS spectra	158
ZnS series XAS spectra	158
ZnO series XAS spectra	160
ZnOS series XAS spectra	162
A.2.5 ZnS correction	163
A.3 ZnO/SnS	164
A.4 (Cd,Zn)S/CuSbS <sub>2</sub>	167
<b>Bibliography</b>	<b>171</b>



# List of Figures

1.1	NREL efficiency chart	3
2.1	p-n-junction properties	6
2.2	j-V-curve of a solar cell	7
2.3	Universal curve for pure elements	8
2.4	PES intensity depth-distribution	9
3.1	synchrotron radiation	14
3.2	Undulator	15
3.3	PES and XAES schematic	17
3.4	XES and XAS schematic	20
4.1	Full device structure	26
4.2	ZnOS series	28
4.3	ZnS survey Mg $K_{\alpha}$	32
4.4	ZnS shallow core level region	33
4.5	ZnS Cu fits	34
4.6	ZnS Sn $3d_{3/2}$ and 4d fits	34
4.7	ZnS $\alpha'_{Cu}$ and $\alpha'_{Sn}$	35
4.8	ZnS S 2p fits	36
4.9	ZnS S 2p fits 8 keV	36
4.10	ZnS/CZTS Zn $2p_{3/2}$ and LMM fits	37
4.11	ZnS/Mo Zn $2p_{3/2}$ and LMM fits	38
4.12	ZnS Zn 3p fits 8 keV	39
4.13	Wagner plot ZnS	40
4.14	HAXPES as XES simulation	41
4.15	HAXPES simulation and XES	42
4.16	ZnS S XES	43
4.17	ZnS-buffer thickness from PES core levels	45
4.18	ZnO survey Mg $K_{\alpha}$	47
4.19	ZnO shallow core level region	48
4.20	ZnO Cu fits	49
4.21	ZnO Sn $3d_{3/2}$ and 4d fits	49
4.22	ZnO S 2p fits	50
4.23	ZnO/CZTS Zn $2p_{3/2}$ and LMM fits	51
4.24	ZnO/Mo Zn $2p_{3/2}$ and LMM fits	52
4.25	Wagner plot ZnO	53
4.26	ZnO Zn 3p fits 8 keV	54

4.27 ZnO O 1s fits	55
4.28 ZnO $\alpha'_O$	55
4.29 ZnO S XES	56
4.30 ZnO O K XES	57
4.31 ZnO-buffer thickness from PES core levels	58
4.32 ZnOS survey Mg $K_\alpha$	60
4.33 ZnOS shallow core level region	61
4.34 ZnOS Cu fits	62
4.35 ZnOS Sn $3d_{3/2}$ and 4d fits	63
4.36 ZnOS $\alpha'_{Cu}$ and $\alpha'_{Sn}$	63
4.37 ZnOS S 2p fits	64
4.38 ZnOS S 2p fits 8 keV	64
4.39 ZnOS/CZTS Zn $2p_{3/2}$ and LMM fits	65
4.40 ZnOS/Mo Zn $2p_{3/2}$ and LMM fits	65
4.41 Wagner plot ZnOS	66
4.42 ZnOS Zn 3p fits 8 keV	67
4.43 ZnOS O 1s fits	68
4.44 ZnOS $\alpha'_O$	68
4.45 ZnOS S XES	69
4.46 Sulfate ZnOS <i>interm.</i> XPS	70
4.47 ZnOS O K XES	71
4.48 ZnOS Zn $L_3$ XAS	72
4.49 ZnOS O K XAS	73
4.50 ZnOS S $L_{2,3}$ XAS	73
4.51 ZnOS-buffer thickness from PES core levels	74
4.52 All series buffer thickness average	78
4.53 Shallow core level region 8 keV	79
4.54 Upper VB 8 keV	80
4.55 Theory, HAXPES and XES comparison	81
4.56 ZnS buffer and absorber shifts	82
4.57 ZnO buffer and absorber shifts	83
4.58 ZnOS buffer and absorber shifts	83
4.59 Valence band maxima linear fit	84
4.60 ZnS/CZTS and ZnO/CZTS band alignment	86
4.61 ZnOS/CZTS band alignment	88
5.1 CZTS/MoS <sub>2</sub> /Mo	91
5.2 CZTS/MoS <sub>2</sub> liftoff	92
5.3 Mo/MoS <sub>2</sub> /CZTS/MoS <sub>2</sub> /Mo/glass and TiN	93
5.4 HAXPES survey back contact series	94
5.5 HAXPES valence bands back contact series	95
5.6 Mo 3d spectra	96
5.7 Cu $2p_{3/2}$ fits and Cu LMM spectra 2 keV	98
5.8 Zn $2p_{3/2}$ fits and Zn LMM spectra 2 keV	100
5.9 Sn $3d_{5/2}$ fits and MNN spectra 2 keV	102
5.10 HAXPES survey model system	103
5.11 Sn $3d_{5/2}$ fits and Mo 3d spectra 8 keV	104



5.12	Valence states w/o annealing 8 keV	105
5.13	S XES on in situ annealed CZTS and Mo/TiN/CZTS	107
5.14	S XES in-situ heating of Mo/CZTS	108
6.1	ZnO/SnS sample structure	112
6.2	HAXPES survey SnS series	113
6.3	Sn 3d <sub>5/2</sub> fits measured with 2 and 6 keV.	114
6.4	Sn 3d 2 keV HAXPES fits normalized	114
6.5	Relative intensities of Sn species	115
6.6	S 2p fits measured with 2 and 6 keV.	116
6.7	Relative intensities of SnX and SX species in Sn and S fits	117
6.8	SnS chemistry at the interface	118
6.9	Zn 2p <sub>3/2</sub> fits measured with 2 and 6 keV.	119
6.10	Relative intensities of Zn species	119
6.11	O 1s and Cl 2s peaks measured with 2 keV.	120
6.12	SnS and ZnO chemistry in the stack	121
6.13	Position trends for all core levels	122
6.14	VB spectra of the SnS series	123
6.15	SnS band bending	124
6.16	ZnO/SnS band alignment	125
6.17	ZnO:N/SnS band alignment	126
7.1	2 keV HAXPES surveys CuSbS <sub>2</sub>	130
7.2	6 keV HAXPES surveys CuSbS <sub>2</sub>	131
7.3	Core levels from lightly oxidized CuSbS <sub>2</sub>	132
7.4	VB spectra measured with 2 and 6 keV HAXPES	134
7.5	VBM fits with 2 and 6 keV HAXPES.	135
7.6	Cu 2p <sub>3/2</sub> fits measured with 2 keV HAXPES.	136
7.7	Cu 3p 2 keV in	136
7.8	Sb 3d and O 1s fits measured with 2 keV HAXPES.	137
7.9	Ratio of Cu and Sb in the absorber	138
7.10	Buffer thickness calculated from Cu and Sb signals	139
7.11	S fits measured with 2 and 6 keV HAXPES.	140
7.12	Cd 3d and Zn 2p <sub>3/2</sub> fits 2 keV HAXPES.	141
7.13	G 2p <sub>3/2</sub> fits 2 keV HAXPES.	142
7.14	Core level shifts of (Cd,Zn)S:Ga/CuSbS <sub>2</sub>	143
7.15	CuSbS <sub>2</sub> /(Zn,Cd)S:Ga band alignment	144
7.16	(Cd,Zn)S:Ga composition	145
7.17	CuSbS <sub>2</sub> S XES	146
A.1	ZnO and ZnOS O Auger spectra	151
A.2	ZnS Cu and Sn Auger spectra	152
A.3	ZnOS Cu and Sn Auger spectra	152
A.4	ZnS/Mo O 1s fits	153
A.5	All Mo 3p <sub>3/2</sub> fits	154
A.6	All Na 1s spectra	154
A.7	C 1s shifts	155
A.8	C 1s fits	156

---

A.9 Zn(OH) <sub>2</sub> contribution to the buffer . . . . .	157
A.10 ZnS S L <sub>2,3</sub> XAS . . . . .	158
A.11 ZnS Cu L <sub>3</sub> XAS . . . . .	159
A.12 ZnS Zn L <sub>3</sub> XAS . . . . .	160
A.13 ZnO Cu L <sub>3</sub> and S L <sub>2,3</sub> XAS . . . . .	160
A.14 ZnO Zn L <sub>3</sub> XAS . . . . .	161
A.15 ZnO O K XAS . . . . .	162
A.16 ZnOS Cu L <sub>3</sub> XAS . . . . .	162
A.17 Subtraction of CZTS spectrum from <i>ZnS thick</i> . . . . .	163
A.18 C 1s fits measured with 2 keV. . . . .	164
A.19 SnS survey spectra 6 keV . . . . .	165
A.20 VB spectra 6 keV . . . . .	166
A.21 Cu 3p fits of HAXPES spectra . . . . .	167
A.22 Sb 4d fits of HAXPES spectra . . . . .	168
A.23 C 1s fits measured with 2 and 6 keV HAXPES. . . . .	169

# List of Tables

3.1	XAS XES probing depth . . . . .	21
4.1	Growth cycles and nominal thickness . . . . .	30
4.2	Solar cell parameters . . . . .	30
4.3	Reaction enthalpies . . . . .	76
A.1	IMFPs of core levels . . . . .	150
A.2	IMFPs for $\text{CuSbS}_2$ . . . . .	167
A.3	Photoionization cross sections $\sigma$ in $\text{CuSbS}_2$ . . . . .	168
A.4	Carbon shifts . . . . .	169



# Abbreviations & Symbols

$\alpha'$	modified Auger parameter
AES	Auger electron spectroscopy
ALD	atomic layer deposition
BS	back side
CB	conduction band
CBD	chemical bath deposition
CBM	conduction band minimum
CBO	conduction band offset
CIGSe	$\text{Cu}(\text{In,Ga})\text{Se}_2$
CIGSSe	$\text{Cu}(\text{In}_{1-x},\text{Ga}_x)(\text{S}_{1-y}\text{Se}_y)_2$
CZTS	$\text{Cu}_2\text{ZnSnS}_4$
CZTSe	$\text{Cu}_2\text{ZnSnSe}_4$
CZTSSe	$\text{Cu}_2\text{ZnSn}(\text{S,Se})_4$
$d_{\text{att}}$	attenuation length for measurement geometry
$d_{\text{em}}$	attenuation length of emitted photons
$d_{\text{exc}}$	attenuation length of photons with $E_{\text{exc}}$
$d_{\text{probe}}$	probing depth
DCM	double crystal monochromator
DEZ	diethyl zinc
$\Delta H_f$	standard formation enthalpy [ $\text{kJ}\cdot\text{mol}^{-1}$ ]
$\varepsilon$	electric field
$e$	Euler's number
$E_B$	binding energy
$E_{\text{exc}}$	excitation energy
$E_F$	Fermi energy
$E_G$	energetic band gap
$E_{\text{kin}}$	kinetic energy
$E_{\text{vac}}$	energetic vacuum level for electrons
$E_T$	tunnel barrier
FF	fill factor
FS	front side
$h$	Planck's constant
$h\nu$	photon energy
HAXPES	hard X-ray photoelectron spectroscopy
$I$	Intensity
$j_{\text{sc}}$	short circuit current
$V_{\text{OC}}$	open circuit voltage
KCN	potassium cyanide
$\nu$	photon frequency

---

PES	photoelectron spectroscopy
PFY	partial fluorescence yield
$\rho$	charge density
RBS	Rutherford backscattering
RF	radio frequency
$\sigma$	photoionization cross section
SLG	soda-lime glass
$T_{\text{ann.}}$	annealing temperature
TCO	transparent conductive oxide
TEY	total electron yield
TFY	total fluorescence yield
V	electric potential
VB	valence band
VBM	valence band maximum
VBO	valence band offset
XAS	X-ray absorption spectroscopy
XES	X-ray emission spectroscopy
XPS	X-ray photoelectron spectroscopy
XRD	X-ray diffraction
XRR	X-ray reflectivity
ZnOS	$\text{ZnO}_x\text{S}_{1-x}$ compound buffer

# Chapter 1

## Introduction

Solar cells on the earth must be adjusted to convert the energy from the available sun spectrum. Well established first generation solar cells (Si-wafer) with indirect bandgap and high material use are still dominating the photovoltaics market. Second generation, namely thin-film solar cells could completely replace them since they potentially combine all advantages of Si-cells with thinner absorber layers, resulting in more lightweight modules produced with less material- and energy consumption [3, 4].

Third generation cells including multijunction cells or concentrator cells can further push the limits of efficiency and widen the range of possible applications. These cells usually have certain limits that exclude them as fundamental technology for photovoltaic devices. Concentrator cells e.g. don't work in diffuse light and are of no use in cloudy regions. We are interested in harvesting light under various conditions to produce usable electricity, so our focus is on thin-film solar cell structures.

In figure 1.1 record efficiencies of different solar cell technologies are compared on a timeline. The depicted efficiencies are reached on lab-sized research cells and not on solar cell modules or in industrial level production. It is clear that efficiency alone does not determine the market share of a solar cell material. Availability, reliability and existing manufacturing structures play as important roles.

With over 20% efficiency the currently dominant technology in the photovoltaic market is multicrystalline Si as absorber material. One of its big disadvantages is the indirect band gap that results in a relatively bad light absorption compared to many absorber materials with direct band gap. This is why multicrystalline Si absorbers need to be of macroscopic thickness to absorb most of the incoming light.

Thin-film solar cells use better light absorbers and have typical absorber thicknesses around 1  $\mu\text{m}$ . This way, they require less material and can be built much lighter and more versatile. Dominant technologies here are CdTe and CuInS<sub>2</sub>-related cells, especially Cu(In<sub>1-x</sub>Ga<sub>x</sub>)(S<sub>1-y</sub>Se<sub>y</sub>)<sub>2</sub> (CIGSSe). On a lab scale, those can compete with silicon cells in efficiency. The production costs can potentially be lowered in mass production. A major problem of these materials is the scarcity of the used elements, namely In, and

Ga [6] that bring the risk of price explosions when large amounts are needed for solar cell mass production.

The search for more available alternative materials yielded, among others, the possibility to replace In and Ga in CIGSSe with much more abundant Zn and Sn, resulting in the complex kesterite-absorber materials  $\text{Cu}_2\text{ZnSn}(\text{S},\text{Se})_4$  (CZTSSe).

The positive slope seen for all materials in figure 1.1 even after decades of extensive research proves the constant progress in photovoltaics research. Especially upcoming thin-film solar cell materials are mostly still far away from their theoretical performance limitations according to their Shockley-Queisser limits [7]. The reduction of some of these performance gaps is the aim to which our research is meant to contribute.

This work will treat problems at the absorber front- and back side in the CZTS solar cell technology as well as the alternative earth-abundant absorber systems SnS and  $\text{CuSbS}_2$ .

## 1.1 Outline

In the following chapter 2, the basic theoretical background is presented to understand characteristics of thin-film solar cells and the role of their interfaces. In chapter 3 the experimental approaches are presented and in detail specified.

The four interface-projects are presented in chapters 4-7. Each of these chapters includes an introduction into the respective material system and the detailed sample production route, followed by the experimental results and a chapter-specific conclusion.



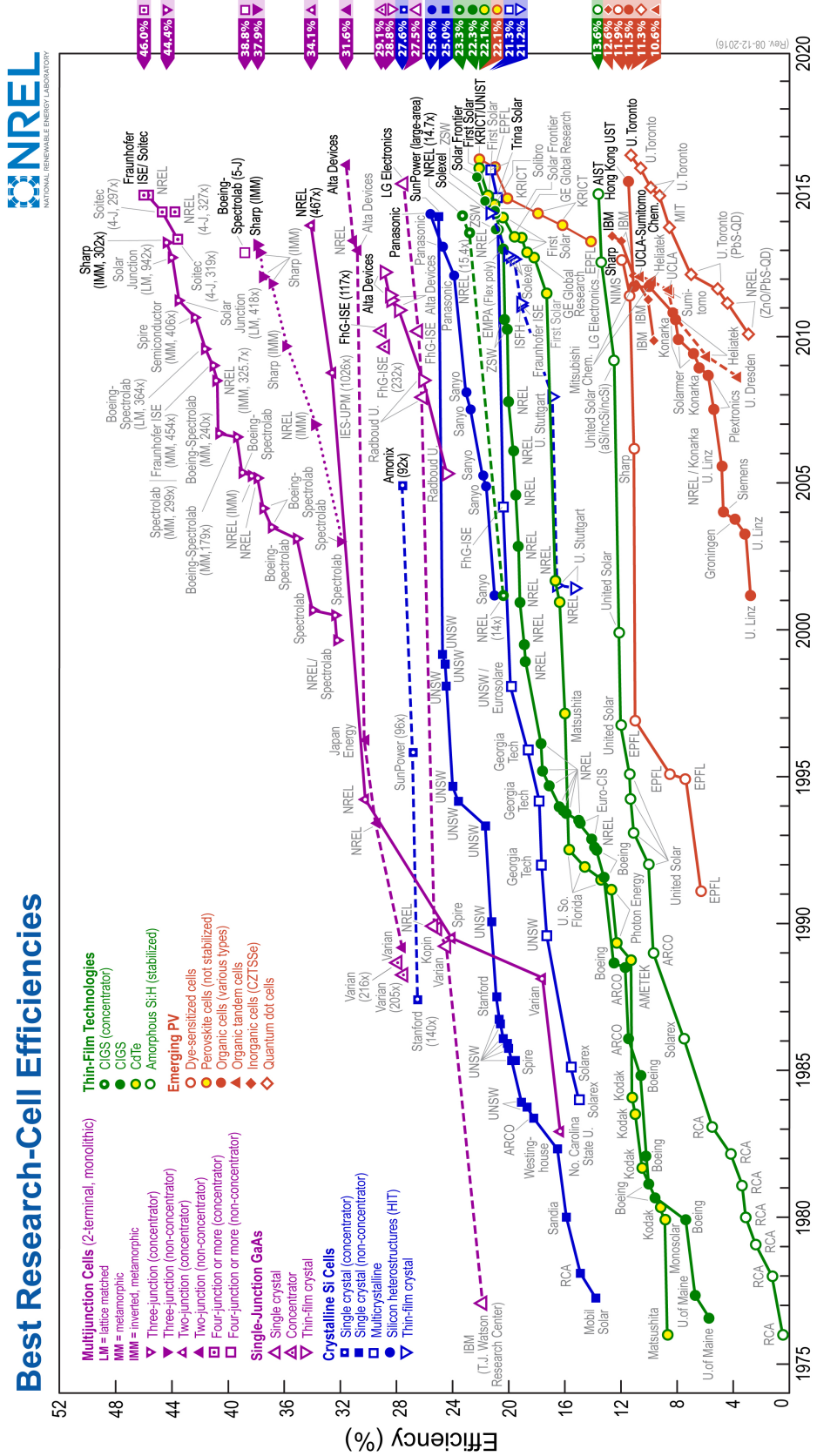


FIGURE 1.1: Record efficiencies of competing solar cell technologies according to [5] on a timeline. Kesterite based cells (red diamonds) are, aside from rapidly improving perovskite cells, the leading technology among the emerging materials (red).



## Chapter 2

# Theoretical considerations

This chapter sets the basic theoretical background needed to follow the implications of the details specified in the experimental and analysis parts.

### 2.1 p-n-junctions and diodes

Diodes made from semiconductors are versatile devices that have electrical conduction in one direction but not in the other. This behaviour is caused by the p-n-junction, an alignment of two semiconductor materials with different properties in the range of the band gap.

The energy diagram of a p-n-homojunction is dominated by the position of the Fermi energy ( $E_F$ ) in the respective band gap  $E_G$  (blue) with size  $E_G$  on either side of the junction. The p-semiconductor has  $E_F$  close to the valence band maximum (VBM) while in the n-semiconductor it is closer to the conduction band minimum (CBM). The resulting structure is shown in figure 2.1 following the depletion-approximation in equilibrium [8]. The p-material has free positive majority charge carriers (holes) while the n-material has (negative) electrons as majority charge carriers. Driven by the concentration difference at the p-n-contact, both majority carrier types diffuse over the junction forming a space charge region (SCR). The expansion of the SCR into the two semiconductor materials is defined by an equilibrium of forces. The first is the driving force of diffusion i.e. the concentration gradient of holes and electrons in between the p- and n-side. The second force results from diffusion of electrons and holes into opposite directions i.e. a net charge flux in one direction over the junction that results in a coulomb force against the diffusion direction. The SCR is not necessarily symmetric. A typical reason for asymmetries is a difference in doping density between the p- and n-side as illustrated in figure 2.1.

In equilibrium we expect curved bands like in 2.1 with a space charge region due to the

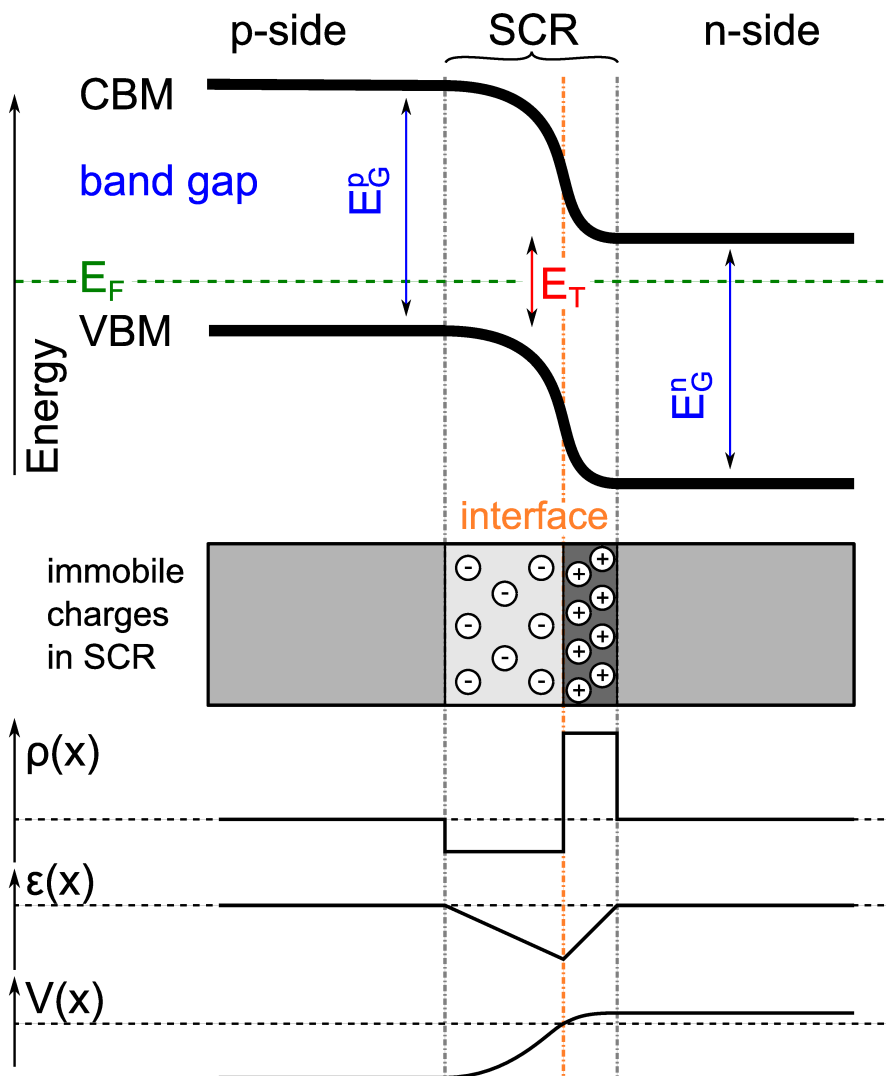


FIGURE 2.1: Properties of a p-n-homojunction in the classical description following the depletion-approximation with abrupt space charge region (SCR) in equilibrium [8]. The energy diagram allows to depict important energetic parameters (red). The picture of excess charge carriers and the charge density ( $\rho$ ) illustrate the asymmetric space charge region with electric field  $\epsilon$  and potential  $V$  across the junction.

depletion of majority carriers close to the junction.

Outside the SCR the semiconductor acts like the pure bulk material without a junction. All property changes are located in the SCR, as seen in the charge density ( $\rho$ ) graph, the electric field ( $\epsilon$ ) graph, and the potential ( $V$ ) graph.

The offsets of conduction and valence band (CBO and VBO) are critical parameters if we optimize a p-n-junction to separate photogenerated electron-hole-pairs. Another crucial parameter is the tunnel barrier  $E_T$ . If this is too small, recombination will take place right at the junction before separated charge carriers can be extracted.

### 2.1.1 Solar cells

Solar cells are diodes that have been optimized to extract electric energy from incoming light. To achieve this, several properties need to be assured. A fundamental necessity is that light needs to be absorbed in the cell generating energetically activated charge carriers which is called the inner photoelectric effect [9].

In this energy conversion, all photons with energy  $h\nu$  smaller than the bandgap ( $E_G$ ) of the light absorber are lost and if more energy than  $E_G$  is transferred to an electron, the excess is lost when the electron thermalizes to the conduction band minimum (CBM). Since the sun spectrum contains a continuous range of photon energies, both losses cannot be avoided. For each bandgap and the collected light spectrum, the Shockley-Queisser limit gives the maximal energy fraction that can be collected without internal losses.

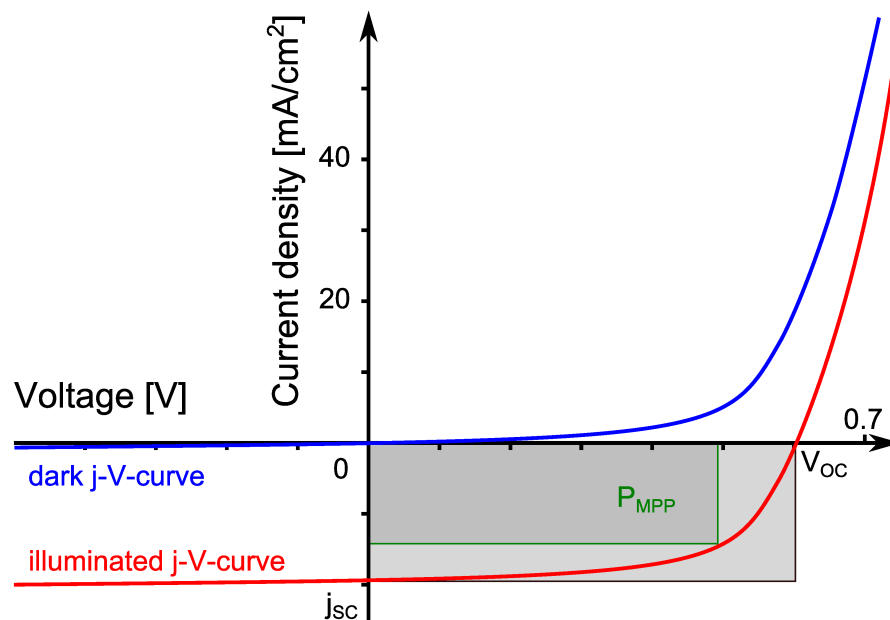


FIGURE 2.2: The diode characteristic or j-V-curve of a solar cell in the dark (blue) and under illumination (red). Under illumination, the whole curve is shifted down the current density axis so an open circuit voltage ( $V_{OC}$ ) and the short circuit current ( $j_{SC}$ ) can be read from the curve. The highest power that can be extracted from this cell is graphically represented by the green box ( $P_{MPP}$ ) i.e. the largest box that can be drawn below the curve in the positive range of  $V_{OC}$ .

The ideal bandgap ( $E_G$ ) for terrestrial light absorption has been found to be in the range of 1-1.5 eV with maxima at 1.15 eV and 1.35 eV [7, 10]. If the light energy has been absorbed, a suited (semiconductor) structure like the p-n-junction is needed to extract the electric energy before the charge carriers recombine. The j-V-curves in figure 2.2 is a standard measurement to characterize solar cells, giving short circuit current  $j_{SC}$ , open circuit voltage  $V_{OC}$ , and the fill factor ( $FF = \frac{P_{MPP}}{j_{SC} \cdot V_{OC}}$ ) that gives the percentage of maximal extractable power  $P_{MPP}$  from the maximum theoretical power  $j_{SC} \cdot V_{OC}$ , i.e. the

dark grey area of the green box over the whole grey area in figure 2.2.

The efficiency is defined as  $\eta = \frac{P_{MPP}}{P_{in}}$  where  $P_{in}$  is the power of the incoming light.

### 2.1.2 Free electrons in matter

The ability of electrons to travel in matter is crucial for most of our measurements. Electrons can only travel short distances in matter before they scatter inelastically and lose energy. For methods that depend on resolving the energy of electrons extracted from a solid like photoelectron spectroscopy (PES), the inelastic mean free path (IMFP) i.e. the average way an electron can travel before it scatters inelastically, is a crucial parameter. The IMFP depends heavily on the kinetic electron energy ( $E_{kin}$ ) as shown in figure 2.3.

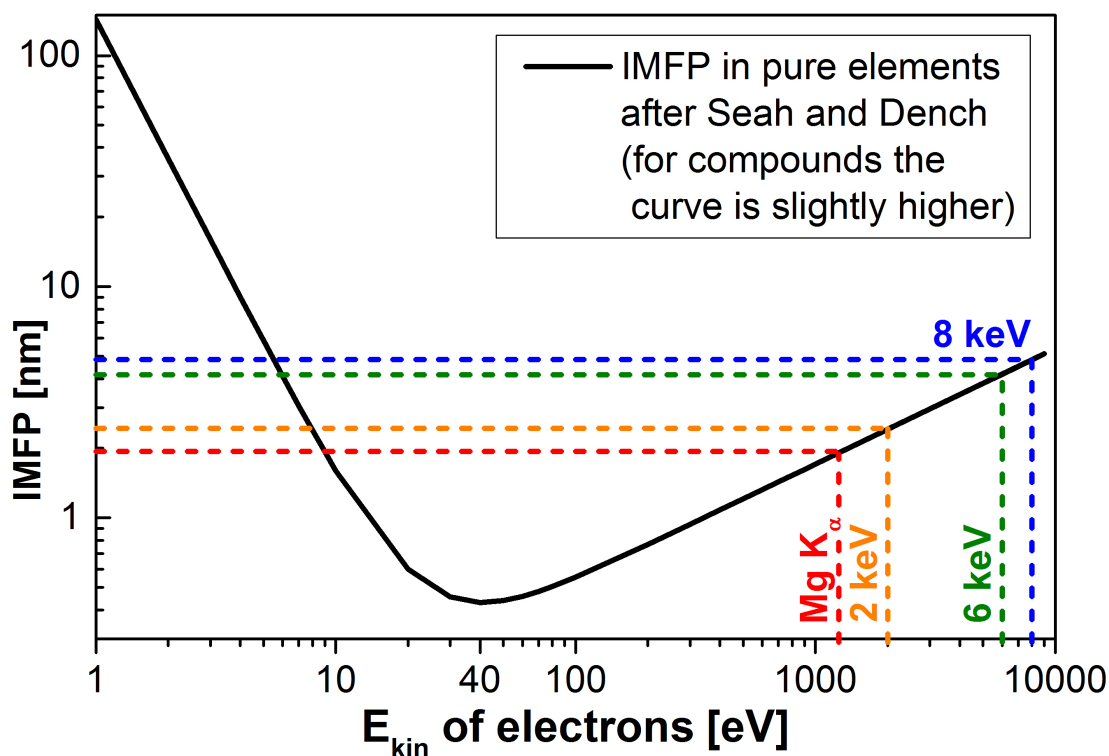


FIGURE 2.3: Universal curve of inelastic mean free path (IMFP) of electrons in pure elemental materials over their  $E_{kin}$  according to [11]. The IMFP of compounds is usually higher but trends are the same.

The most frequently used excitation energy ( $E_{exc}$ ) for PES in this work are indicated as colored lines with the respective reached IMFP. It has to be noted that the actual electron energy is reduced by the respective binding energy ( $E_B$ ) so the given lines show the maximal IMFP of very shallow core levels close to the Fermi level ( $E_F$ ).

For more accurate, material specific values we used the IMFP calculated with the TPP2M code [12]. The values are shown in table A.1 (see page 150).

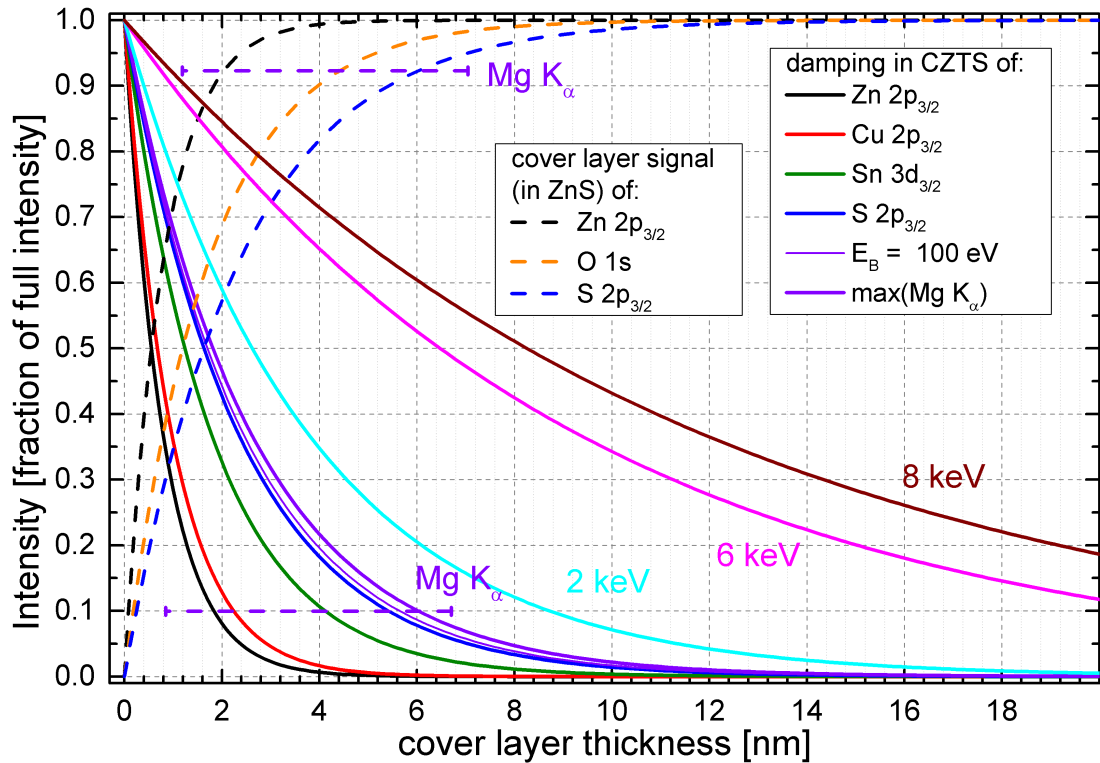


FIGURE 2.4: Depth distribution of intensity measured from prominent core levels with  $\text{Mg K}_\alpha$  and of maximal  $E_{\text{kin}}$  for several excitation energies  $E_{\text{exc}}$ . The intensities are normalized to the value a very thick pure sample would yield. Lines show the remaining intensity for a sample covered by another layer with similar IMFP dependent on the cover layer thickness. The dashed lines show the intensity from an uncovered thin layer dependant on its thickness.

The probability for an electron to escape the sample in normal direction from a depth  $d$  depends on the IMFP, resulting in a depth dependant intensity decay. Compared to an undamped signal  $I_0$  from an uncovered surface we can measure

$$I(d) = I_0 \cdot e^{-\frac{d}{\text{IMFP}}} \quad (2.1)$$

if the material is covered by a layer of thickness  $d$ . The IMFP in the covering material has to be used in formula 2.1.  $I(0)$  depends on  $\sigma$ , the element concentration, and the transmission function and geometry of the measurement system.

For the integrated intensity measured from a layer with thickness  $d$  and we find

$$I_{\text{int}}(d) = \int_0^d I(d) = I_0 \cdot \text{IMFP} \cdot \left(1 - e^{-\frac{d}{\text{IMFP}}}\right)$$

$$I_{\text{int}}(d \gg \text{IMFP}) \approx I_0 \cdot \text{IMFP} \propto \text{IMFP}$$

This means, we can define an effective probing volume  $V = A \cdot \text{IMFP}$  using the illuminated and measured area  $A$  that is identical for all measurements in one system and the IMFP. With

$$I_{\text{int}}(d) \propto A \propto \text{IMFP}$$

we can account for changes in the measured intensity that are caused by varying IMFP by simply dividing by the IMFP value in nm. We neglect the unit because the IMFP is only a scaling factor in this case. If we are interested in the signal  $I_{\text{int}}(d)$  from a thin coverlayer instead of a buried layer, the exponential term must be subtracted from 1 before this factor is used in equation 2.1 because we measure only the surface contribution up to  $d$  instead of the bulk signal from thickness  $d$ .

The depth dependent signal decay for several core levels and different  $E_{\text{exc}}$  is shown in figure 2.4 along with the signal intensities expected from thin cover layers. For the cover layers the plotted function is  $1-I(d)$  because the intensity from deeper than  $d$  is missing. The normalization removes any factors from derivations and integrations. The respective IMFP values can be found in table A.1. To calculate the intensity ratio from within a certain depth  $d$  we use

$$\int_0^{\text{IMFP}} I(d) = 0.63 \quad \text{and} \quad \int_0^{3 \cdot \text{IMFP}} I(d) = 0.95$$

This shows that about two thirds of the signal come from a depth of less than one IMFP from the surface. Since 95% of the exponentially attenuated signal originates from within  $3 \cdot \text{IMFP}$  from the surface, we consider this value as probing depth.

$$d_{\text{probe}} \approx 3 \cdot \text{IMFP}$$

With IMFP variations in the range from  $<1$  nm for Zn 2p measured with Mg  $K_{\alpha}$  to 12 nm for valence states measured with 8 keV, our probing depth varies between about 3 nm and 36 nm.

If we measure a species S1 that is located only right at the surface and compare to a bulk species S2 containing an identical element, we only have to consider the IMFP to account for the probed volume of the bulk species. Neglecting the bulk-signal decay caused by a very thin surface species, we have to divide the bulk signal by the IMFP to account for the probed volume while the entire volume of the surface species is measured in all cases of changed  $E_{\text{exc}}$  and for all binding energies. If we measure two different core levels C1 and C2 that come from the two species, the following expression for the intensity ratios should be valid:

$$\begin{aligned} \frac{I(\text{S1},\text{C1}) / \sigma(\text{C1}) / \text{TF}(\text{C1})}{I(\text{S2},\text{C1}) / \sigma(\text{C1}) / \text{TF}(\text{C1}) / \text{IMFP}(\text{C1})} &\approx \frac{I(\text{S1},\text{C2}) / \sigma(\text{C2}) / \text{TF}(\text{C2})}{I(\text{S2},\text{C2}) / \sigma(\text{C2}) / \text{TF}(\text{C2}) / \text{IMFP}(\text{C2})} \\ \Leftrightarrow \frac{I(\text{S1},\text{C1})}{I(\text{S2},\text{C1})} \cdot \text{IMFP}(\text{C1}) &\approx \frac{I(\text{S1},\text{C2})}{I(\text{S2},\text{C2})} \cdot \text{IMFP}(\text{C2}) \end{aligned} \quad (2.2)$$

The photoionization cross sections  $\sigma$  and analyzer transmission functions TF, that are identical for the different species of one core level, cancel out. If this equation is not true, either the assumption of a surface species on a bulk material is not given or the attribution to the investigated species is not valid. The formula also applies if we use different  $E_{\text{exc}}$  instead of looking at different core levels.



# Chapter 3

## Experimental section

This chapter contains information that helps to understand the following measurements and their interpretations as well as experimental specifications of the used facilities and machines. The measurement techniques are presented including information about settings and calibrations.

### 3.1 Notation and electronic transitions

In literature we find several ways to specify electronic states. Since we do not need any of the highly specialized vector-notations used e.g. in computational and theoretical analysis, we use the most common notations that describe the electronic state independent of its occupation.

Depending on the binding energy ( $E_B$ ) of the states below the Fermi energy ( $E_F$ ) we divide them into *core levels* with a binding energy of more than around 50-100 eV<sup>1</sup> and *shallow core levels* with roughly  $E_B < 100$  eV. All electronic states are described more precisely in two different notations. Used parameters are quantum numbers including:

- the principal quantum number ( $n$ )
- the orbital quantum number ( $l$ )
- the spin quantum number ( $s = \pm \frac{1}{2}$ )
- the total angular momentum quantum number ( $j = |l + s|$ )

The principal quantum number ( $n = 1, 2, 3, 4, \dots$ ) is partly specified using the capital letters K, L, M, N, ... when transitions are described. The orbital quantum number ( $l = 0, 1, 2, 3, \dots, n-1$ ) is similarly specified with the letters s, p, d, f, ... to describe energy states.

---

<sup>1</sup>The distinction is not sharp but more about the general range of  $E_B$ .

### 3.1.1 XPS notation

This notation is used to specify energy levels by writing

$$n l_j$$

where the orbital quantum number ( $l = 0, 1, 2, 3, \dots$ ) is specified as s, p, d, f, ... and  $n$  and  $j$  are shown as numbers.

An example is S  $2p_{1/2}$  giving the sulfur state with  $n = 2$ ,  $l = 1$  (written as p) and  $s = -\frac{1}{2}$  resulting in  $j = |1 - \frac{1}{2}| = \frac{1}{2}$ .

### 3.1.2 X-ray notation and Siegbahn notation

This notation is usually used to describe transitions between energy levels, so we use it in XES, XAS, and XAES. It describes transitions, giving the involved states in the type

$$n_i$$

where  $n = 1, 2, 3, 4, \dots$  is written as K, L, M, N, ... and  $i$  counts up the possible combinations of  $l$  and  $s$ , starting with lowest  $l$  and lowest  $s$ .

In XES the edges are specified by the final state (i.e. the depleted state) in x-ray notation; for XAS the initial state (excited state) is given.

For XAES, all three involved states are specified in this notation (see 3.3.4).

Transitions can be described in the shorter Siegbahn notation where both involved states are specified. The  $n$  value of the final state is defined as in the x-ray notation and the  $n$ -difference  $\Delta n = 1, 2, 3, \dots \hat{=} \alpha, \beta, \gamma, \dots$  to the initial state is added in the type

$$n_{\Delta n_i}$$

If multiple transitions are possible due to variable  $l$  and  $s$ , they are specified with an index  $i$ .

This notation is used to describe e.g. x-ray sources that use Mg  $K_\alpha$  or Al  $K_\alpha$  transition lines to produce x-ray beams with defined photon energy  $h\nu$ . The Mg  $K_\alpha$ -line is the result of transitions to the magnesium K-level ( $n = 1$ ) from the next higher L-levels ( $n = 2$ ) resulting in  $\Delta n = 2 - 1 = 1$  written as  $\alpha$ . Without a specification  $i$  this notation sums up the multiple Mg  $K_\alpha$ -lines of different intensity and energy that will later be used to explain satellite lines (see page 18).

**Transition rules** define whether an electron can directly change from one state to another (radiative transition). The most important exclusion are selection rules in dipole approximation for electronic transitions in this work are:

$$\Delta n \neq 0$$

$$\Delta l = \pm 1$$

$$\Delta j = \pm 1; 0$$

These rules can, however, sometimes be suspended by hybridizing states.

## 3.2 Synchrotron radiation

If X-ray radiation does not arise from electronic transitions, it is usually produced in synchrotrons using the principle of relativistic electromagnetism. This type of facility can be used as an energy-tunable light source. A brief description follows [13] to explain the used methods. Very fast electrons (at realistic energies close to the speed of light) are needed for this. After linear acceleration, a so called booster ring is used to reach the required kinetic energy until the electrons are injected into a storage ring. This is a large evacuated tube aligned in a curved and closed trajectory. The energy losses of the stored electrons are compensated using klystrons.

Bending magnets simply bend the trajectory of the electrons to produce radiation and other insertion devices placed in straight sections of the storage ring use the same basic principle.

$$\gamma \equiv \frac{1}{\sqrt{1 - \frac{v^2}{c^2}}} \quad (3.1)$$

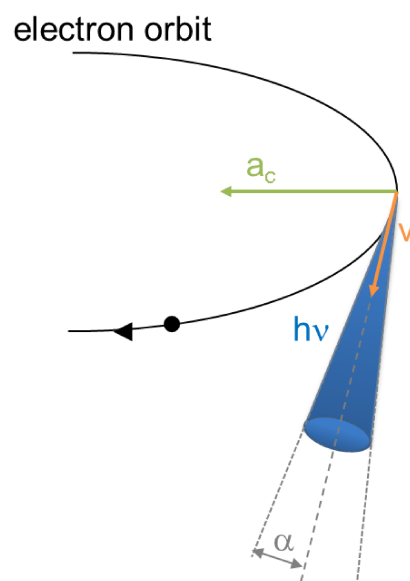


FIGURE 3.1: An electron traveling through a constant magnetic field with the relativistic velocity  $v$  is accelerated towards the center with acceleration  $a_c$ . The radiation is emitted in a cone with angle  $\alpha$ . [13]

In 3.1<sup>2</sup> the emission collimated along the tangential direction with an angle  $\alpha \cong \frac{1}{2\gamma}$  of a charged particle at relativistic speed traveling through a constant magnetic field is sketched.

The emitted radiation covers the entire electromagnetic spectrum. The critical energy  $E_C$  can be written as

$$E_C = \frac{3ehB\gamma^2}{4\pi m} \quad (3.2)$$

with the charge  $e$ , the mass  $m$ , Planck's constant  $h$ , and the magnetic flux  $B$  of the bending magnetic.  $E_C$  represents the energy that divides the radiation emission into two parts of equal intensity. This equation can be rewritten for synchrotron radiation, using electrons with energy  $E_r$  and  $\gamma = \frac{E_r}{mc^2}$  to

$$E_C [keV] = 0.655 \cdot E_r^2 [GeV] \cdot B [T] \quad (3.3)$$

The specific energy spectrum depends on the electron trajectory and the magnetic field of the emitting devices. The used devices are bending magnets, wigglers, and undula-

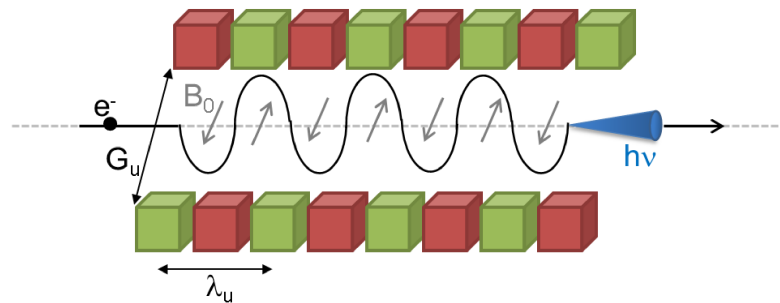


FIGURE 3.2: Undulator schematic with alternating polarity of permanent magnets with a magnetic field density of  $B_0$ . The electron trajectory (black) and the resulting synchrotron radiation (blue) are indicated.  $G_U$  represents the distance between the magnetic arrays called undulator gap and  $\lambda_U$ , the undulator frequency, is the distance between equally poled magnets.

tors. Bending magnets are dipole magnets that accelerate the electrons perpendicular to their trajectory and generate a uniform magnetic field perpendicular to the electron orbit. Wigglers are high field superconducting magnet arrays causing the electron to oscillate with large deviation angles around the ideal trajectory. Undulators use lower field arrays of magnets. Here the electrons slightly oscillate around the ideal trajectory, see figure 3.2.

They consist of stacked permanent magnet arrays with alternating polarity in a distance  $\lambda_U$ , called undulator frequency. The magnetic field  $B_0$  causes electrons to oscillate on

<sup>2</sup>With special thanks to E. Handick for providing the figure.

their path which emits radiation. The emission cones can be adjusted to overlap resulting in constructive interference and therefore an increase in intensity at chosen photon energies.[13] These conditions can be described with the non-dimensional magnetic strength  $K$  defined as

$$K \equiv \frac{eB_0\lambda_U}{2\pi mc} = 0.9337 \cdot B_0 [T] \lambda_U [cm] \quad (3.4)$$

A wiggler is defined by  $K \gg 1$  and the resulting emission is similar to the emission of bending magnets.  $K=1$  or smaller is characteristic for an undulator with constructive interference of the emission cones raising the photon intensity at a wavelength  $\lambda$ . Changes in  $B_0$  caused by a change of the undulator gap  $G_U$  result in changes of the photon energy. This allows a specific tuning to the experimental needs. The resulting synchrotron radiation is led through beamlines to the endstation to provide the needed radiation for experiments.

### 3.3 PES

Photoelectron spectroscopy (PES) uses the photoelectric effect, where photons eject bound electrons from a material, to gain information about electronic and chemical structures in a sample. Since electrons quickly lose kinetic energy when traveling through matter, the measurements are performed in vacuum.

The determined binding energy ( $E_B$ ) of photoelectrons is sensitive to electronic and chemical changes in the material. The process is illustrated in figure 3.3.

In the basic band structure (energy vs space coordinate) we see the conduction and valence band (CB and VB) and  $E_F$  in the band gap as well as core levels of very different energies. The energetic vacuum level  $E_{Vac}$  is also shown. Electrons above this level have left the sample and possess a positive kinetic energy  $E_{kin}$  that is measured in PES experiments. If an electron is hit by a photon with energy  $h\nu$  and the energy is transmitted, the electron makes an energetic jump indicated by the dashed vertical lines in figure 3.3. The right hand axis shows that  $E_B$  and the work function  $\phi$ , i.e. the energetic barrier to leave the sample, have to be overcome to eject the electron into vacuum. Otherwise, in the inner photoelectric effect, the electron cannot be measured. If the photon energy is sufficient to overcome  $E_B$  and to extract the electron from the material into vacuum, the remaining part of the transmitted photon energy  $h\nu$  can be found as kinetic energy  $E_{kin}$  of the photoelectron. The relation of the discussed energetic variables is

$$h\nu = E_{kin} + E_B + \phi \quad (3.5)$$

This means we can vary  $E_{kin}$  by varying  $h\nu$  as long as the photon energy is sufficient to eject electrons. PES spectra are usually shown on binding energy scale ( $E_B$ ) calculated

from equation 3.5.

The secondary Auger process will be discussed separately in section 3.3.4 (page 19).

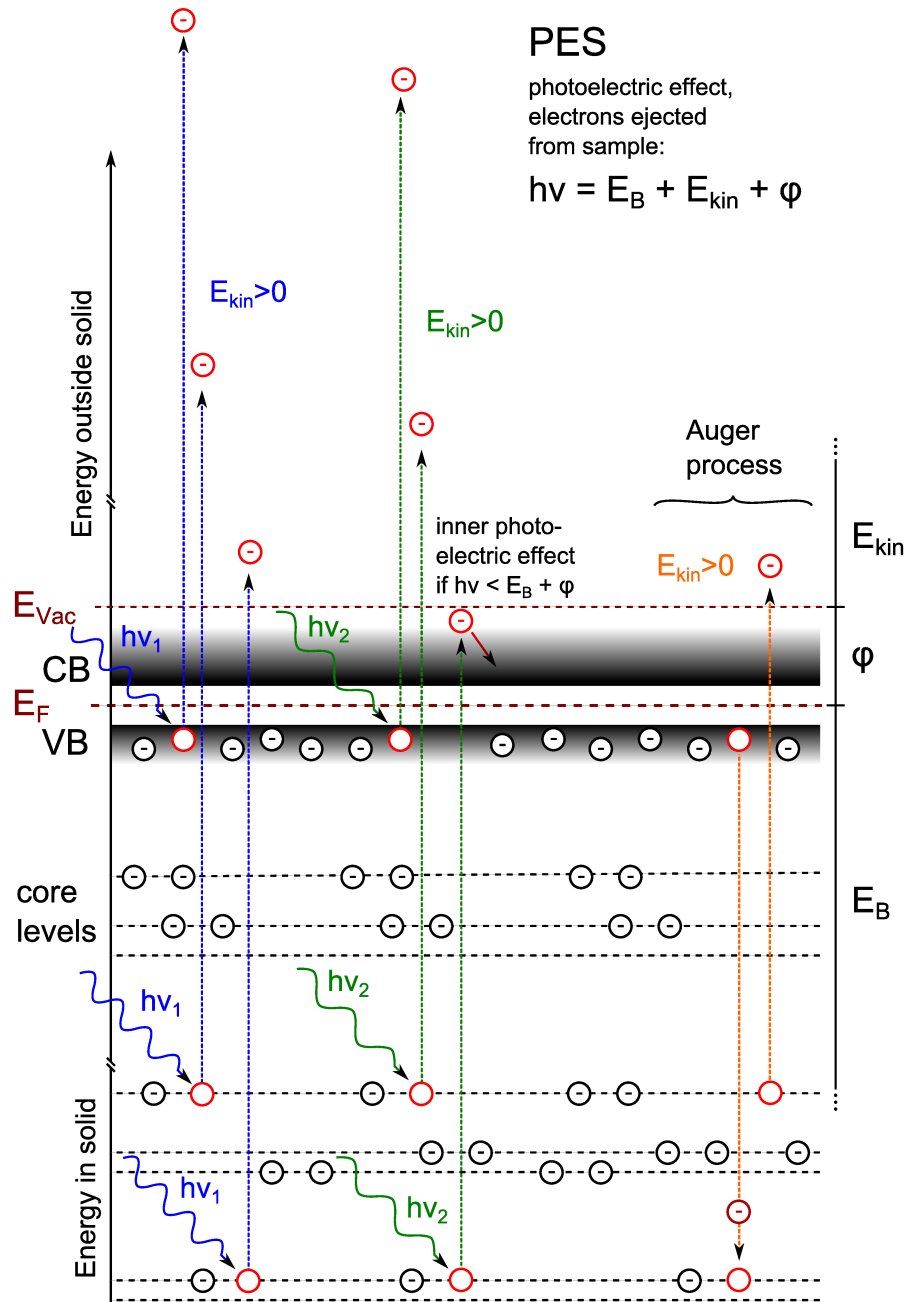


FIGURE 3.3: PES process for different photon energies  $h\nu$ . The kinetic energy  $E_{kin}$  of the escaping electron is defined by  $h\nu$ , the binding energy ( $E_B$ ) and the work function ( $\varphi$ ) that is needed for electrons at the surface to reach the vacuum level ( $E_{Vac}$ ) from  $E_F$ . In the secondary Auger process, electrons are emitted by energy that is released in the transition of bound electrons to lower, x-ray-depleted energy levels.

### 3.3.1 Energy calibration

The measured kinetic energy in PES ( $E_{\text{kin}}$ ) depends on  $h\nu$ ,  $E_{\text{B}}$ , and  $\phi$ .

With a defined excitation energy and by measuring sharp lines with known position  $E_{\text{B}}$ , the relation between  $E_{\text{B}}$  and  $E_{\text{kin}}$  can be calibrated without specific knowledge about the effect of  $\phi$ . Such a calibration also removes any constant shift that is caused by the work function of the electron analyzer.

Calibration checks and beamline energy calibrations are usually done with Au 4f peaks measured on a clean Au foil.

### 3.3.2 XPS

Lab-based X-ray photoelectron spectroscopy (XPS) measurements were conducted using non-monochromatized Mg  $K_{\alpha}$  (1253.56 eV) and Al  $K_{\alpha}$  (1486.58 eV) radiation. The SPECS PHOIBOS 150 MCD-9 electron energy analyzer was calibrated according to D. Briggs et al. [14] using clean Au, Ag, and Cu surfaces. The base pressure in the analysis chamber was  $< 4 \cdot 10^{-10}$  mbar. For the collection of the XPS core level and Auger line spectra the pass energy was set to 20 eV. For wide range spectra a pass energy of 50 eV was used.

The non-monochromatized Mg  $K_{\alpha}$  (and Al  $K_{\alpha}$ )-line contains multiple secondary lines of higher energy and intensity. These additional lines cause weaker and shifted copies of all measured XPS-features with defined shift and intensity ratio to the main line. If these satellites overlap with the analyzed region they have to be considered.

### 3.3.3 HAXPES

Synchrotron-based hard x-ray photoelectron spectroscopy (HAXPES) experiments with an excitation energy of 2, 6, and 8 keV were conducted at the HiKE end-station (2 and 6 keV) [15] on the KMC-1 beamline [16] of the BESSY II electron storage ring, and at the beamlines BL15XU [17, 18] (6 keV) and BL47XU [19] (8 keV) of the SPring-8 electron storage ring. The setup geometry allows to measure with horizontally polarized x-rays with the direction of polarization normal to the analyzer entrance slit and normal emission from the sample. The base pressure at HiKE and BL47XU HAXPES endstations was  $< 1 \cdot 10^{-8}$  mbar and  $< 1 \cdot 10^{-7}$  mbar at BL15XU; all are equipped with a Scienta R4000 hemispherical electron energy analyzer with similar setups for beamline and analyzer. The beamlines are equipped with double crystal monochromators (DCMs), allowing to tune the excitation energy between 2.0 and 10.0 keV at BESSY II, 4.0 and 36.0 keV at BL15XU, and between 5.2 and 37.7 keV at BL47XU at SPring-8. A pass energy of 200 eV was used for all measurements (except for survey spectra



measured at HiKE using 500 eV) and the excitation energy was calibrated by measuring multiple Au 4f spectra of a grounded clean Au foil and setting the Au 4f<sub>7/2</sub> binding energy equal to 84.00 eV. Alternative, E<sub>F</sub> determinations on clean Au foils were used. Spectra were recorded using photon energies of 2 and 6 keV at BESSY II where 6 keV photons are the 3<sup>rd</sup> reflection order of the Si(111) DCM crystal set in 1<sup>st</sup> order for 2 keV, thus both photon energies are transmitted for all HiKE measurements. Photon energies of 6 and 8 keV were used at SPring-8 using the 3<sup>rd</sup> and 4<sup>th</sup> reflection order of a Si(111) DCM crystal, respectively.

For all HAXPES measurements the samples were only briefly exposed to air (< 5 min). The top surface of the samples was short circuited to the Mo layer and grounded to avoid charging due to photoelectron loss.

### 3.3.4 XAES

The secondary Auger process is used for the x-ray excited Auger electron spectroscopy (XAES). It depends on the relaxation of electrons into deeper (x-ray-) depleted core levels. The released energy can eject another electron from the sample. The E<sub>kin</sub> of this Auger electron depends only on the E<sub>B</sub> of the depleted state, the state from which the second electron drops down, and the state from which the Auger electron is ejected. The common notation for such an Auger line is listing the three states in the given order in x-ray notation.

The Zn LMM line for example with multiple transitions into the two depleted L levels from M-levels ejects Auger electrons from M-levels.

Due to the independence of E<sub>exc</sub>, on the common E<sub>B</sub>-scales used for PES, the Auger lines appear at E<sub>B</sub> positions that have no relation to the involved process and shift for different E<sub>exc</sub> as expected from equation 3.5. Auger lines are therefore labeled in other spectra but for analysis they are always shown on a E<sub>kin</sub> scale.

**Modified Auger parameters**  $\alpha'$  are used to take advantage of the reversed dependence of external effects  $\Delta E$  (like sample charging,  $\phi$ , and especially linear miscalibration i. e. energy shifts) on Auger line positions on a kinetic energy scale (E<sub>kin</sub>(X<sup>Auger line</sup>)) and core level positions on a binding energy scale (E<sub>B</sub>(X<sup>core level</sup>)) of an element X. If the real kinetic energy positions E<sub>kin</sub><sup>real</sup>(X) are shifted by an unrecognized effect, we find

$$\begin{aligned} E_B(X^{\text{core level}}) &= h\nu - \left( E_{\text{kin}}^{\text{real}}(X^{\text{core level}}) + \Delta E \right) \\ E_{\text{kin}}(X^{\text{Auger line}}) &= E_{\text{kin}}^{\text{real}}(X^{\text{Auger line}}) + \Delta E \end{aligned}$$

Any (positive) shift  $\Delta E$  in the measured spectra will lower the energetic position of E<sub>B</sub>(X<sup>core level</sup>) and increase E<sub>kin</sub>(X<sup>Auger line</sup>). The sum of both is therefore independent of the mentioned influences and consequently unaffected by systematic shifts caused

by varying settings in different measurement systems. It is called the modified Auger parameter

$$\alpha'_X = E_B(X^{\text{core level}}) + E_{\text{kin}}(X^{\text{Auger line}}) \quad (3.6)$$

and allows for a much more reliable comparison between species measured in different measurement systems. Suitable sharp Auger features and core levels have to be selected and ideally they should be similar in kinetic energy so that the information depth is comparable.

### 3.4 X-ray absorption and emission

X-ray emission and absorption spectroscopy (XES and XAS) are other techniques to measure electronic states. The basic principles are shown in figure 3.4.

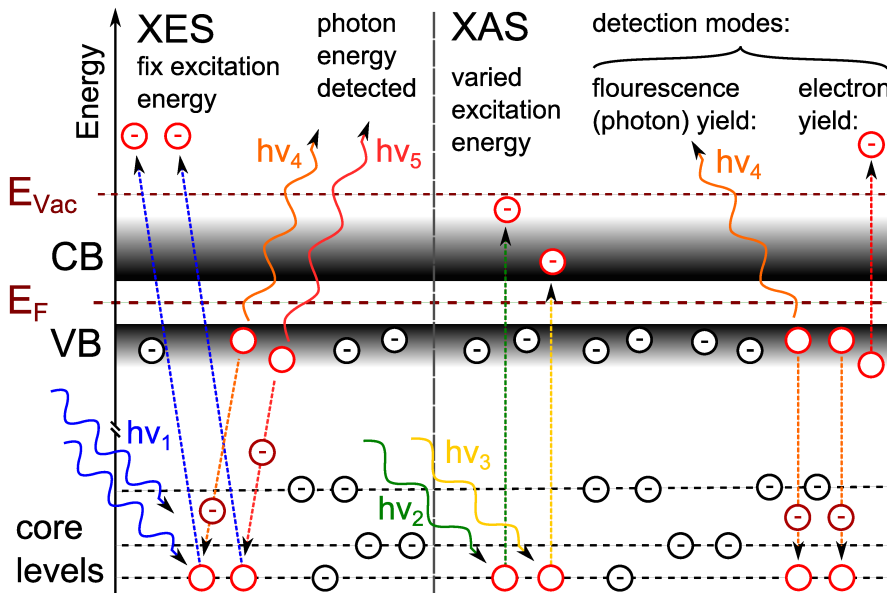


FIGURE 3.4: Basic processes of x-ray emission and absorption spectroscopy (XES and XAS). XES uses constant  $E_{\text{exc}}$  and energy-resolved photon detection to quantify the density of occupied states from which electrons relax. XAS uses varied  $E_{\text{exc}}$  to excite electrons into unoccupied valence band states. Their density of states is quantified by measuring the yield of secondary processes.

Without the IMFP limitations that arise from extracting electrons like in HAXPES, the transmission of photons through the sample becomes the limiting factor. The photon attenuation lengths that define the probing depth have been calculated following Henke et al. [20, 21]. Since exciting and emitted photons both have to be transmitted to/from the probing depth, both attenuation lengths  $d_{\text{exc}}$  and  $d_{\text{em}}$  are crucial. The measurement attenuation length is calculated as

$$d_{\text{att}} = \frac{1}{\left(\frac{1}{\sin(\alpha) \cdot d_{\text{exc}}} + \frac{1}{\sin(\beta) \cdot d_{\text{em}}}\right)} \stackrel{\alpha \approx \beta}{=} \frac{\sin(\alpha)}{\left(\frac{1}{d_{\text{exc}}} + \frac{1}{d_{\text{em}}}\right)} \quad (3.7)$$

which is always dominated by the smaller (depth-limiting) attenuation [22]. The angles  $\alpha$  of the exciting and  $\beta$  of the emitted photons to the sample surface increase the path through the material to escape if they differ from  $90^\circ$ . The effectively reached depth is therefore reduced.

For  $\sin(\alpha) \cdot d_{\text{exc}} \approx \sin(\beta) \cdot d_{\text{em}}$  we have  $d_{\text{att}} \approx \frac{\sin(\alpha) \cdot d_{\text{exc}}}{2}$ .

TABLE 3.1: Probing depth calculated with equation 3.7 from attenuation lengths calculated according to [20, 21] for different materials. In XES we have constant  $E_{\text{exc}}$  and a range of measured emission energies. The lowest and highest of these in the relevant measurement window was used to calculate  $d_{\text{att}}$ . For XAS the measured energy (the main peak for fluorescence yield) is constant and the range of  $E_{\text{exc}}$  causes a low and high value for  $d_{\text{att}}$ . We see that lower photon energy does not necessarily result in a larger attenuation length (and  $d_{\text{probe}}$ ).

		measurement $d_{\text{att}}$ [nm]					
		XES		XAS			
		S	O	S	O	Cu	Zn
ZnO	low	13	88	13	114	242	295
	high	14	89	13	91	248	110
ZnS	low	17	105	23	101	386	472
	high	15	108	18	111	396	181
CZTS	low	21	78	30	77	130	126
	high	17	76	22	76	103	119

As for electrons that limit the probing depth for PES, we have an exponential decay for photon transmission in matter (equation 2.1)

$$I(d) = I_0 \cdot e^{-\frac{d}{d_{\text{att}}}} \quad (3.8)$$

This can also be used for thickness determination of covering thin films. The probing depth is equivalently defined as  $d_{\text{probe}} \approx 3 \cdot d_{\text{att}}$ .

### 3.4.1 XES

XES is a pure photon-in-photon-out technique and thus not limited by the IMFP of photoelectrons. In figure 3.4 the involved processes are illustrated. A constant excitation energy  $h\nu_1$  is used to deplete core level. The decay of electrons from energetically higher occupied states provides energy for photon emission. The energy of the emitted photons  $h\nu_4$  and  $h\nu_5$  is measured. The intensity at every detected energy depends on the density of occupied states at the respective binding energy above the depleted core level.

Other influencing factors are transition rules and -probabilities.

Synchrotron-based soft x-ray emission spectroscopy at the O K edge was performed in the soft x-ray fluorescence SXF endstation [23] of ALS beamline 8.0.1. Using the same beamline S  $L_{2,3}$  XES was performed at the SALSA VLS [24] endstation. The

sample was aligned in an angle of about  $45^\circ$  to the incoming beam and the respective detector in SXF. The incoming beam is perpendicular to the sample surface in the VLS endstation.

All samples were transferred into the chamber after a short air-exposure.

A photon energy of 180 eV was used for S  $L_{2,3}$  XES in VLS. A photon energy of 560 eV was used for O K XES in SXF.

The energy axes of S  $L_{2,3}$  XES data have been calibrated using the sharpest lines of a CdS reference at 150.6 eV and 151.8 eV emission energy [25]. O XES has been calibrated with a ZnO:N<sub>2</sub> line at 525.5 eV. Good agreement is also found with the literature value of observed second order Zn  $L_2$  emission at ( $\frac{1034.7}{2} = 517.35$ ) eV [26]. For XAS calibration, well known edges of Cu metal at 932.6 eV [27] and TiO<sub>2</sub> at 140.1 eV have been used.

Elastic peaks of the x-ray source in the measurement window of XES have been measured to calibrate the S  $L_{2,3}$  absorption spectra. The Zn  $L_2$  energy scale was calibrated to match each other by using the ZnS absorption edge of a reference sample.

### 3.4.2 XAS

The basic processes for XAS measurements are shown in figure 3.4. A specific excitation energy  $h\nu_2$  is used to excite electrons from a selected core level into unoccupied states in the conduction band (CB). The transition probability depends on the density of unoccupied states at the right energy in the CB. By varying the excitation energy (e.g. to  $h\nu_3$ ) the density of unoccupied states at a different energy can be probed. With a scan over a range of excitation energies, the conduction band states can be measured. Several techniques to measure successful transitions into the CB are common. The direct measurement of absorbed (lost) photons by measuring the remaining ones in transmission mode requires very thin samples and is not applicable for our layer stacks. We rely on indirect methods that depend on electrons that relax into the depleted core levels. The energy is either released in the Auger process (see section 3.3.4) or by emission of (x-ray-) photons (as described for XES) that can be detected. The photon signal is called fluorescence yield. The other way is the Auger process that results in ejected electrons. Measuring the sample current that arises from this electron loss results in the electron yield.

XAS can, due to the different detection modes, be used as photon-in-photon-out technique with high probing depth or, limited by the IMFP of Auger electrons, give very surface sensitive information in electron yield.

All electronic transitions are also influenced by transition rules and -probabilities.

Synchrotron-based soft x-ray absorption (XAS) spectroscopy was performed in the soft x-ray fluorescence SXF endstation [23] of ALS beamline 8.0.1. The sample handling and geometry was identical to the handling described for XES.

XAS spectra of the O K, Zn L<sub>3</sub>, Cu L<sub>3</sub>, and S L<sub>2,3</sub> edge were measured with photon energies in a range of 518-560 eV, 1000-1040 eV, 920-940 eV, and 157-170 eV, respectively. XAS spectra were recorded in three different modes.

The total fluorescence yield (TFY) mode using a channeltron detector captures all emitted photons also unwanted transitions for the specific experiment. This increases the background signal compared to the signal from transitions right at the edge where the focus of interest is.

A better option with less signal intensity is the partial fluorescence yield (PFY) mode where the SXF detector is centered to the XES window of the respective edge. This mode is more strictly related to the investigated edge. For both fluorescence modes probing depths of above 20 nm are reached because only photons have to be transmitted through the material (see table 3.1).

A third mode, total electron yield (TEY), measures the electric current lost from the sample with escaping Auger electrons that is proportional to the absorbed photons. This mode is much more surface sensitive since it is limited by the ability of the Auger photoelectrons to escape the sample. The probing depth is in the range of the shallow core levels measured.

### **3.5 Peak fitting and analysis details**

The core level and Auger line positions were determined using fits with Voigt profiles and linear backgrounds. The Voigt is a convolution of two components: a Lorentzian function accounting for the lifetime broadening of the peak, caused by the existence of core holes under x-ray bombardment and a Gaussian that describes the experimental broadening caused by the measurement uncertainty. In narrow fit regions the linear background approximation can compete with more realistic background models that come closer to the step-function background that would be caused by a perfectly sharp peak without any broadness. The linearity makes any influences of this background in the fits much more obvious and also considering the independence of this background from the fitted peaks, this choice of background is the most practical and still very accurate.

To calculate surface compositions, the fitted areas of core levels were used taking into account the respective photoionization cross-sections, the inelastic mean free paths of the photoelectrons, and the transmission function of the electron analyzer, all of which have a direct linear impact on the measured signal. For shallow core levels only the photoionization cross-sections were used since the other values are nearly identical in this small energy range.

Fits are shown with subtracted linear background to prevent deceptive shifts of the peak maxima and to allow better comparison between fitted peaks and the spectrum. Residuals are usually magnified to prove the fit quality.

Valence band maxima are determined using a linear approximation of the leading edge, i.e. finding the interception point of a flat background around and beyond  $E_F$  and the best linear fit of the leading edge as measured with PES. This method gives the best value for the valence band maximum since the experimental broadening doesn't shift the VBM to smaller binding energies if the fit range is properly chosen.

Inelastic mean free paths (IMFPs) of electrons in solids were calculated with the TPP-2 formula [28] using the QUASES code written by S. Tougaard [12]. The error margin is assumed to be smaller than 20%.

## Chapter 4

# $\text{Cu}_2\text{ZnSnS}_4$ with $\text{ZnO}_x\text{S}_{1-x}$ buffer

### 4.1 Kesterite-based thin film solar cells

$\text{Cu}_2\text{ZnSnS}_4$  (CZTS) films that are close to today's  $\text{Cu}_2\text{ZnSn}(\text{S},\text{Se})_4$  (CZTSSe) kesterite materials have already been described and investigated in the 80's of the last century [29] but the application as solar cell absorber was considered much later. The first working kesterite-based solar cell with below 1% efficiency was presented in 1997 [30]. A good overview covering the developments in the field of kesterite photovoltaics including the absorber materials CZTS, CZTSSe, and CZTSe ( $\text{Cu}_2\text{ZnSnSe}_4$ ) can be found in several review articles like [31–36] and will be briefly presented here.

The narrow stable range in the CZTS phase diagram and the formation of binary phases ( $\text{Cu}_2\text{S}, \text{SnS}_2, \text{ZnS}, \text{Cu}_2\text{SnS}_3$ ) [37] whenever conditions change [38] (e.g. at surfaces and interfaces) make the production of phase pure CZTS very difficult.

The behaviour of the CZTS phase with detailed crystal structure, (dis-)order and defects was intensely investigated [39–42].

Theoretical approaches have helped to understand the behaviour of the kesterite phase with thermodynamic models [43] and predictions about the chemical potential, concentration, and formation enthalpies of defects e.g. [44–46].

The most common production routes include a two step process with a mostly off-stoichiometric precursor and an annealing step. The crystallization of kesterite on partial solar cells is performed in S-rich (or S- and Sn-rich) atmosphere to prevent loss of those at the needed crystallization temperatures above 500°C. Fast annealing helps to minimize element loss [47]. Order-disorder transitions have been found in the course of optimizing the bulk material [48].

However, the formation of secondary phases at surfaces and interfaces of device-relevant thin films is very common. A wide spread approach to remove detrimental surface phases is chemical etching. This alters the surfaces and opens up many options in optimizing interfaces as shown e.g. in [49–52].

Research about the role of Na in the Mo back contact [53], its relation to O [54] and later

the beneficial effect of Na on  $\text{Cu}(\text{In}_{1-x}\text{Ga}_x)(\text{S}_{1-y}\text{Se}_y)_2$  (CIGSSe) as well as CZTSSe solar cells [55–57] further improved the kesterite cell performance. Na diffusion can also play a role in the growth of  $\text{ZnO}_x\text{S}_{1-x}$ -based buffer layers because it is mobile in ZnO [58, 59] and can affect the structural growth and the electronic structure of small ZnO structures [60].

Among various techniques to produce kesterite-based thin film solar cells e.g. sputtering, coevaporation, electrodeposition, ink-based deposition, and direct wet-chemical processes, a hydrazine approach has significantly ramped up the efficiency [61] of  $\text{Cu}_2\text{ZnSn}(\text{S},\text{Se})_4$  cells and was used for the current efficiency record above 12% [62]. Recently the first kesterite even exceeding 13% was confirmed (unpublished).

Other approaches like Se kesterites [63], CZTS nanocrystals [64], Ge-kesterite nanocrystal solar cells with 6.8% efficiency [65] and others show the interest in kesterite-based solar cell technologies.

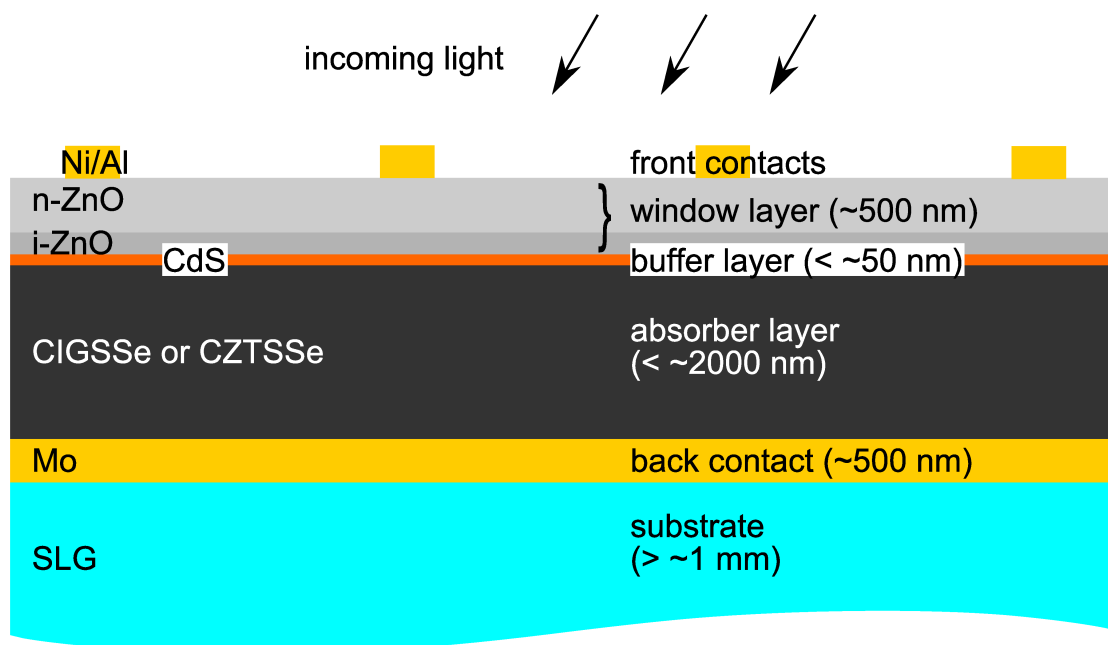


FIGURE 4.1: Typical structure of thin film solar cell devices specified for CIGSSe or CZTSSe absorber. Typical material choices and thicknesses are given for the individual layers. The thicknesses are not to scale since buffer- and window layer structures are very thin compared to the lower layers. SLG refers to soda-lime glass.

The typical complete thin-film solar cell structure as it has been adapted from CIGSSe to CZTSSe cells is sketched in figure 4.1. The most common substrate is soda lime glass (SLG) that is covered with a back contact material like Mo in sufficient thickness to assure good conduction. The absorber material, thinner than around  $2 \mu\text{m}$ , is covered by a buffer material, typically CdS. This n-type layer forms the p-n-junction of the device with the p-type absorber. It is also intended to optimize the band alignment and ideally also compensate crystal lattice mismatches and protect the absorber from any harmful effect of the window layer deposition.



The window layer is a transparent conductive oxide (TCO), usually n-ZnO/i-ZnO. On the window layer the front contact grid is attached.

In this work we focus on the structure up to the buffer layer so we have a 4-layer stack with 2 electronically relevant interfaces and the effects of the substrate. The SLG contains Na that diffuses into the CZTS and is discussed to accumulate at the surface during and after the annealing (i.e. crystallization) step [66]. The absorber/Mo interface at the backside of the kesterite is not chemically inert. The detailed chemistry at this interface will be discussed in chapter 5.

The buffer/absorber interface is a crucial junction in the cell and will be discussed in chapter 4 as well as for different related absorber materials in chapters 6 and 7.

We use x-ray based spectroscopic techniques that have been shown to be well suited to investigate semiconductor devices [67–70]

Having been developed as a cheap and abundant alternative to the well-established CIGSSe absorbers, the CZTSSe is still mostly used in the device structure that has been found to be optimal for CIGSSe. The main drawback of kesterite-based cells is the relatively low open circuit voltage ( $V_{OC}$ ) when compared to CIGSSe. An optimized band alignment between  $\text{Cu}_2\text{ZnSnS}_4$ -absorber and buffer layer will help to improve  $V_{OC}$  and efficiency of the devices.

Even though the world record kesterite solar cells have all been made using CdS buffer layers, we have no reason to believe that there is no better buffer material available. For Se-free CZTS solar cells, the efficiency record above 9% was achieved with an altered  $\text{Zn}_{1-x}\text{Cd}_x\text{S}$ -buffer [71]. CdS buffer have been applied and optimized for years to fit the needs of the similar CIGSSe solar cells. As a result, the CdS buffer for CZTS is an obvious choice that had a jump start compared to other buffers that are based on more abundant elements. On CZTS, a cliff-like conduction band offset (CBO) has been reported for CdS buffers in [72]. To reach the ideal small spike in the conduction band offset for this type of solar cell [73–75], a modified or entirely different buffer material has to be used.

Replacing the CdS would also remove the expensive and toxic elements cadmium from the cell stack.

## 4.2 The $\text{ZnO}_x\text{S}_{1-x}$ system as buffer material

In this study we focus on the  $\text{ZnO}_x\text{S}_{1-x}$ -system. ZnO and ZnS with (optical) band gaps of around 3.3 eV and 3.6 eV show a strong bowing when being alloyed, reducing the band gap to 2.6 eV for around 35-60% S/(S+O) according to transmission measurements [76]. Additionally, an increasing lattice parameter for higher S-content [76, 77]

will change the strain, nucleation, and therefore the chemical interface structure for different  $\text{ZnO}_x\text{S}_{1-x}$  compounds grown on the same CZTS. An additional option for band alignment is the use of Se in the  $\text{ZnO}_x\text{S}_{1-x}$  material, since  $\text{ZnO}_x\text{Se}_{1-x}$  has shown strong bowing as well [58, 78].

$\text{ZnO}_x\text{S}_{1-x}$  allows for adjustment of the band gap and in particular of the conduction band minimum (CBM) [79] by altering the sulfur to oxygen ratio.  $\text{ZnO}_x\text{S}_{1-x}$  deposited by atomic layer deposition (ALD) has been used as buffer for high efficiency CIGSSe-cells [80] and for CIS-cells [81]. Chemical bath deposition (CBD) to produce  $\text{ZnO}_x\text{S}_{1-x}$  buffer layers on CZTSe [82] yielded efficiencies above 5%. While CZTS-based devices with pure ZnO buffers have low  $V_{\text{OC}}$ , cells with pure ZnS are completely blocking [83]. To find a fitting  $\text{ZnO}_x\text{S}_{1-x}$  compound buffer material for CZTS absorbers, we consequently monitor the chemical and electronic structure of the resulting interface.

### 4.2.1 Sample preparation

The buffer material is usually in a layer stack of a thin film solar cell acting as buffer between absorber and window layer. Even though we look at a partial device here without the top layers (from the window upwards, compare figure 4.1, page 26) we call the  $\text{ZnO}_x\text{S}_{1-x}$ -layers buffer layers, referring to the intended use in the full device.

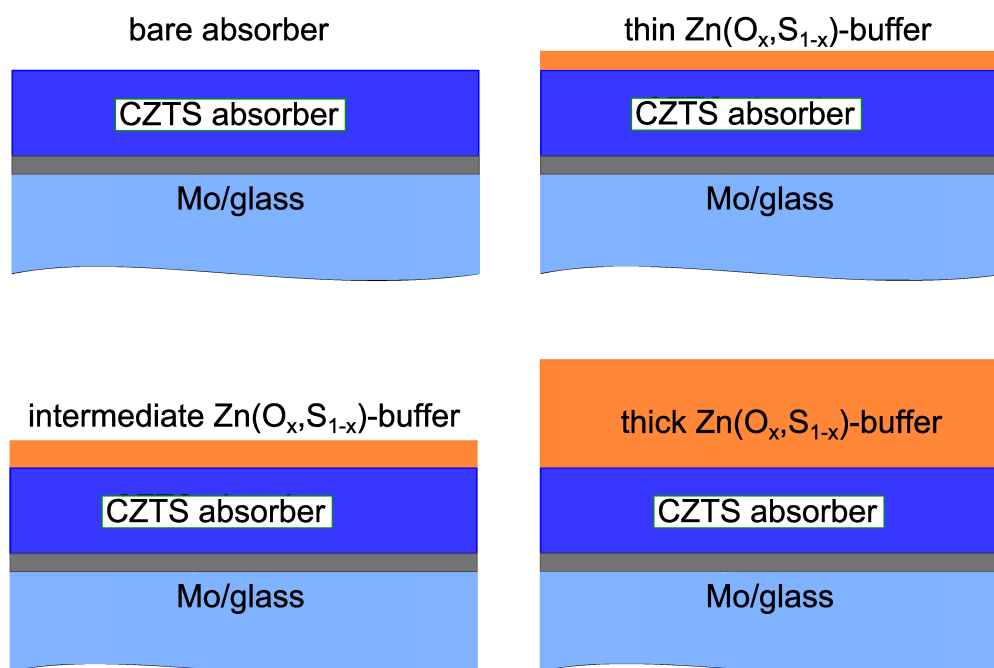


FIGURE 4.2: A thickness series of the three buffer compounds has been deposited on CZTS. The thin and intermediate layers are grown as thin as possible while still having a complete coverage of the CZTS surface. The thick layer is grown to the device-relevant thickness.

CZTS-precursors have been grown by reactive magnetron sputtering in a Von Ardenne CS600 sputtering system with two magnetrons and a front side heater, all facing the substrate with an angle of  $45^\circ$  at 160 mm distance (see [84] for more details). The used sputter targets had a diameter of 102 mm and a thickness of 6 mm. The target materials were a CuSn-alloy with 65 at.% Cu and 35 at.% Sn (purity 99.999%) and pure Zn (purity 99.994%).

A pulsing frequency of 20 kHz was chosen in the sputter process. The sulfur was supplied through  $\text{H}_2\text{S}$  atmosphere with purity of 99.5%. The material thickness of around  $2\ \mu\text{m}$  was reached after a deposition time of 50 min. The precursors have been grown on Mo-coated soda-lime glass [84] followed by annealing in a S-rich atmosphere.

The annealing was performed in a tube furnace under static argon atmosphere (35 kPa) at  $560\ ^\circ\text{C}$  for 10 min. The precursors were positioned in a small graphite box with about 20 mg sulfur in order to prevent sulfur loss. Annealing details are discussed in [85], the decomposition of CZTS is discussed in [86] and in this work on page 103 and following, section 5.2.2 and 5.2.3.

The crystallized CZTS was KCN-etched (120 s in 5 wt% KCN) to remove detrimental Cu-phases from the surface and transferred through air (few minutes) into the atomic layer deposition (ALD) system for buffer deposition. ZnS, ZnO, and Zn(O,S) buffers were deposited in a thickness series as shown in Fig. 1. The used deposition system (MP3 Uppsala University [87]) was set to a sample temperature of  $120^\circ\text{C}$ . The ALD precursors were diethyl zinc (DEZ) to provide zinc,  $\text{H}_2\text{O}$  for oxygen, and  $\text{H}_2\text{S}$  for sulfur with  $\text{N}_2$  steps in between. The cycles for the pure binary compound were consequently DEZ/ $\text{N}_2$ / $\text{H}_2\text{O}$ / $\text{N}_2$  for ZnO and DEZ/ $\text{N}_2$ / $\text{H}_2\text{S}$ / $\text{N}_2$  for ZnS. The  $\text{ZnO}_x\text{S}_{1-x}$  deposition was done with sequences of one cycle ZnS and six cycles ZnO. This composition had yielded the best solar cells of 4.6% in combination with CZTS [88]. With the CZTS layers used in this work, 3.1% efficiency could be reached. Every buffer deposition run also included parallel deposition on Mo-coated SLG without any CZTS to produce a reference buffer layer. These references will be referred to with the addition of (*Mo*) to the name or as  $\text{ZnO}_x\text{S}_{1-x}/\text{Mo}$ . The grown samples are listed in table 4.1.

The CZTS has been produced in identical but separate sputter- and annealing runs for the three series, so small differences in the material are possible. The CZTS is therefore labeled with the intended buffer of the series in the type  $\text{CZTS}^{\text{ZnO}_x\text{S}_{1-x}}$ .

Additionally, a piece of absorber from each CZTS growth run was covered with a CBD CdS buffer [88] to produce a full device for comparison.

All three  $\text{CZTS}^{\text{ZnO}_x\text{S}_{1-x}}$  materials with the respective full buffer thickness and the CdS buffer for comparison were completed to full thin film solar cell devices. The window layers consisting of a thin intrinsic ZnO and a thicker Al-doped ZnO layer were deposited with RF-sputtering.

To calculate nominal thicknesses<sup>1</sup> thick ZnOS layers identically grown directly on bare

<sup>1</sup>This is the intended thickness. It is based on the assumption of constant linear growth of the buffer materials and of identical growth speed for all three materials.

TABLE 4.1: Thickness series if the three buffer compositions with number of ALD growth cycles and nominal thickness<sup>1</sup> as extrapolated from thick ZnOS samples with 140 cycles and measured by XRR to be 33 nm thick.

sample name	ZnS [cycles]	thickness <sup>1</sup> [nm]	ZnOS [cycles]	thickness <sup>1</sup> [nm]	ZnO [cycles]	thickness <sup>1</sup> [nm]
bare CZTS	0	0	0	0	0	0
thin	15	3.5	21	5	30	7
intermediate	25	6	35	8	50	12
thick	70	16	140	33	140	33

glass substrates were measured with X-ray reflectivity (XRR) [88]. Differences in nucleation are likely to occur for growth on Mo or CZTS but the growth speed after nucleation is supposed to be alike.

**Cell parameters** as shown in 4.2 have been extracted from I-V-curves. We see blocking behavior for the ZnS buffer. For ZnO, the short circuit current ( $j_{\text{SC}}$ ) is very similar to the reference with CdS buffer on the identical CZTS, but we see a huge loss in open circuit voltage ( $V_{\text{OC}}$ ). The cell parameters of the ZnOS/CZTS device show that this material clearly outperforms the two binary Cd-free compounds. There is some  $j_{\text{SC}}$  loss and  $V_{\text{OC}}$  still doesn't reach the nearly 0.6 eV of the CdS/CZTS reference cell but from these results the  $\text{ZnO}_x\text{S}_{1-x}$  approach is very promising.

TABLE 4.2: Solar cell parameters measured on the investigated CZTS and buffers finished as devices.

absorber	buffer	efficiency [%]	FF [%]	$j_{\text{SC}}$ [ $\text{mA}\cdot\text{cm}^{-2}$ ]	$V_{\text{OC}}$ [V]
$\text{CZTS}^{\text{ZnS}}$	CdS	5.1	56.6	14.6	0.613
	ZnS	0.00	2.75	0.00	0.005
$\text{CZTS}^{\text{ZnOS}}$	CdS	5.8	63.4	15.5	0.591
	ZnOS	3.1	55.1	13.7	0.415
$\text{CZTS}^{\text{ZnO}}$	CdS	5.0	59.1	13.1	0.612
	ZnO	1.0	42.2	13.2	0.182

## 4.3 Chemical structure of the $\text{Cu}_2\text{ZnSnS}_4$ - $\text{ZnO}_x\text{S}_{1-x}$ - interface

The chemical structure of the CZTS-  $\text{ZnO}_x\text{S}_{1-x}$ - interface will be analyzed with XPS, XAES, HAXPES, XES, and XAS. We start with the binary compounds as a foundation for the discussion of the ZnOS buffer material.

### 4.3.1 ZnS

#### 4.3.1.1 PES measurements

Survey spectra of the ZnS series are shown in figure 4.3. In the bare CZTS spectrum (black line), we see Cu, Zn, Sn, and S lines.

The Zn and S lines gain intensity with thicker buffer, while Cu and Sn lines are attenuated and eventually vanish for the thick buffers. All spectra show O and C signals that are discussed in section A.2.3 on page 154. The Na signals (as mentioned on page 27) that are found on a few samples will be addressed there, too.

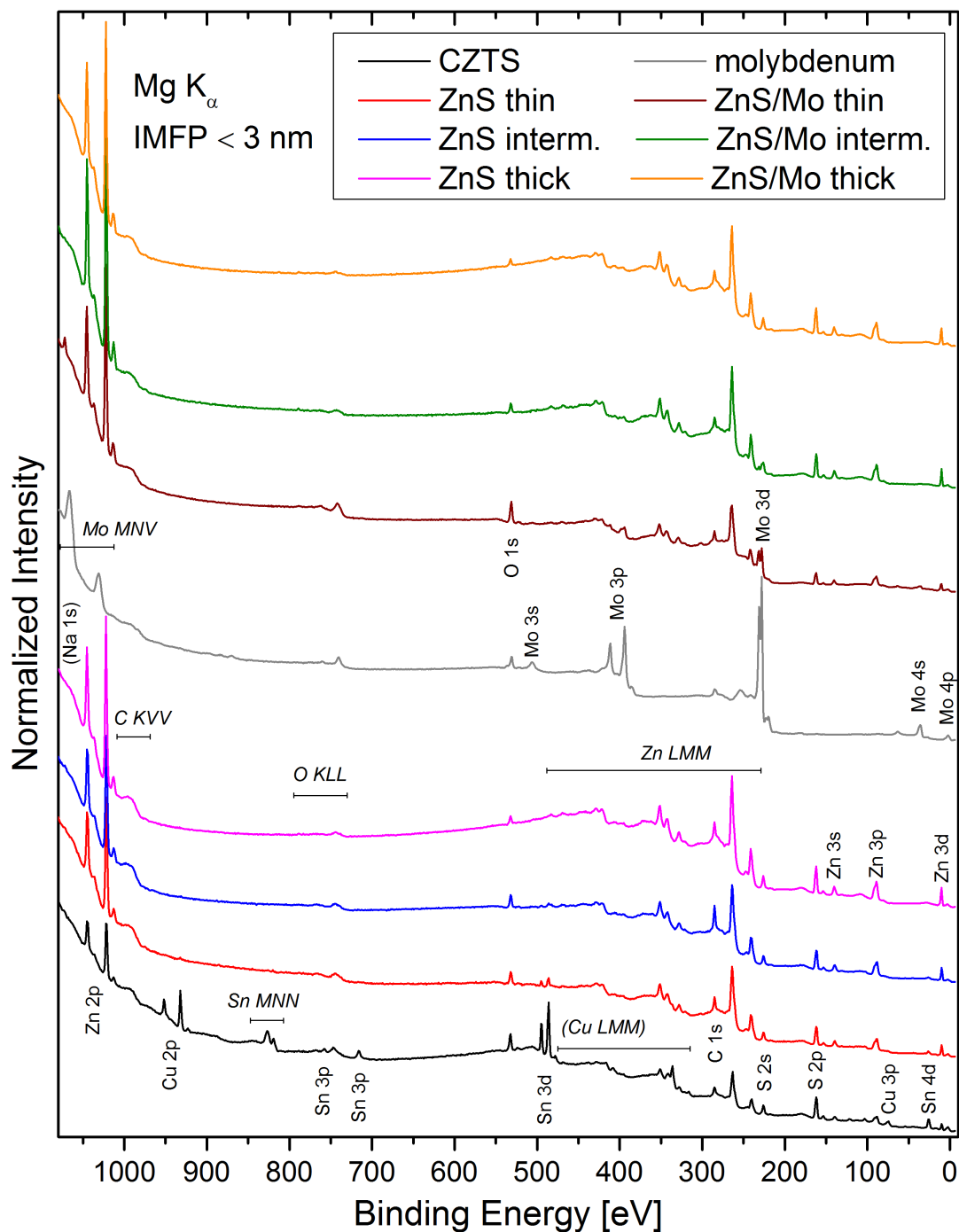


FIGURE 4.3: Survey spectra of all samples from the ZnS series normalized in the flat region at 600 eV. Vertical offsets have been added for clarity.

A more detailed picture can be seen in the shallow core level region (figure 4.4) with sharp shallow core levels of Cu, Zn, and Sn and a broader S line. These spectra, measured with 8 keV, exhibit a larger probing depth (see section 2.1.2) so we see CZTS-related Cu- and Sn-signals in all spectra including *ZnS thick*. Furthermore, all lines from buried material appear more pronounced compared to the cover layer signals that show stronger relative signals with Mg  $K_\alpha$ -excitation.

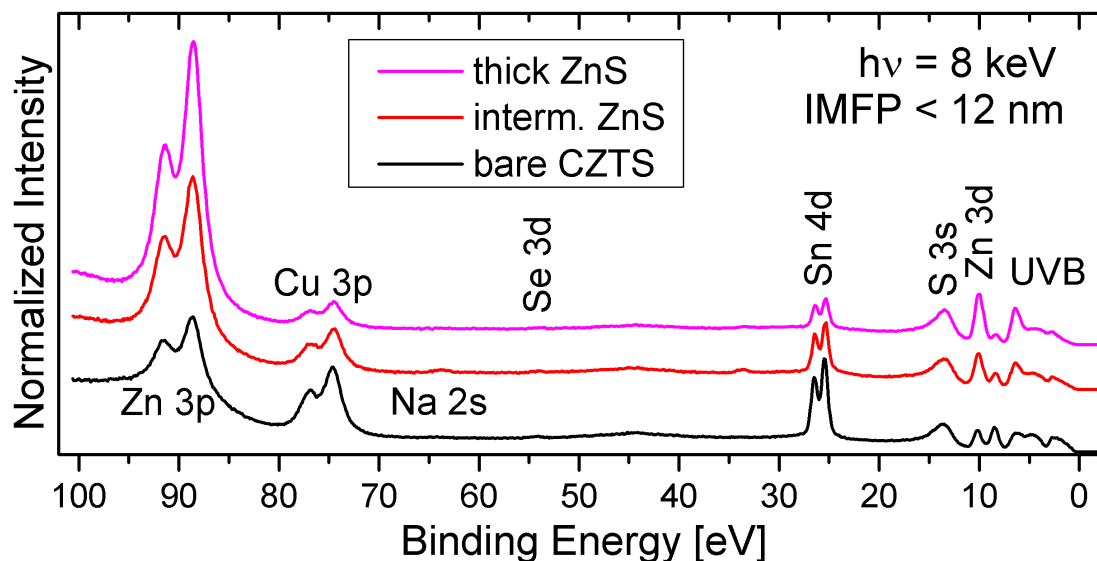


FIGURE 4.4: shallow core level region spectra of selected samples measured with 8 keV and normalized in the flat region at 50 eV. Vertical offsets have been added for clarity.

**Core levels** of Cu, Zn, Sn, and S from CZTS and of Zn and S for buffer layers have been measured with XPS and HAXPES. To complete the picture, regions for Mo, C, O, and Na core levels were measured, as well as sharp features of Zn, Cu, and Sn Auger lines.

By measuring the Cu signal from the CZTS through thin buffer layers with XPS we can observe position and intensity changes compared to bare CZTS as shown in figure 4.5. The change of the signal strength depends on the buffer thickness. Position shifts indicate either chemical changes, contact problems or interface induced band bending. The strong intensity decay illustrates how surface sensitive the XPS measurements are (see page 45 for layer thicknesses). Linear backgrounds have been subtracted (compare section 3.5). We observe only one main species that is the CZTS phase. Energy ranges of Cu-compounds are indicated for comparison [89]

Measurements of the Cu 3p line (figure 4.5b) at higher excitation energy of 8 keV (IMFP of 11.4 nm compared to 2.4 nm for Mg  $K_\alpha$  as shown on page 150) reach down to the buried interface covered with thicker buffer layers. The Cu 3p is spin-orbit split into two components with an energy difference of 2.42 eV that are summed up for clarity. The relative surface contribution to the overall signal is significantly smaller for this excitation

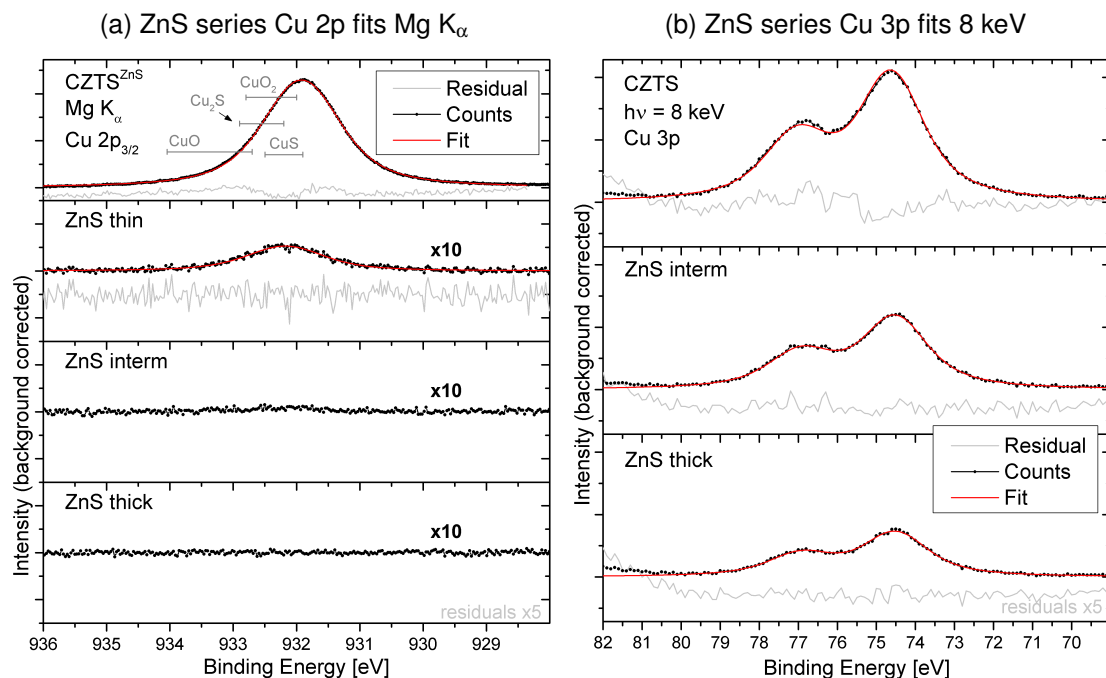


FIGURE 4.5: Cu  $2p_{3/2}$  and 3p spectra measured with  $\text{Mg K}_\alpha$  and 8 keV excitation and fits. The residuals have been magnified for better visibility.

energy (see page 150). We see a Cu signal through all ZnS-layers, even the thickest one. The potential Sn 4p background is neglected because of the flat shape and low intensity (compare page 79, figure 4.53).

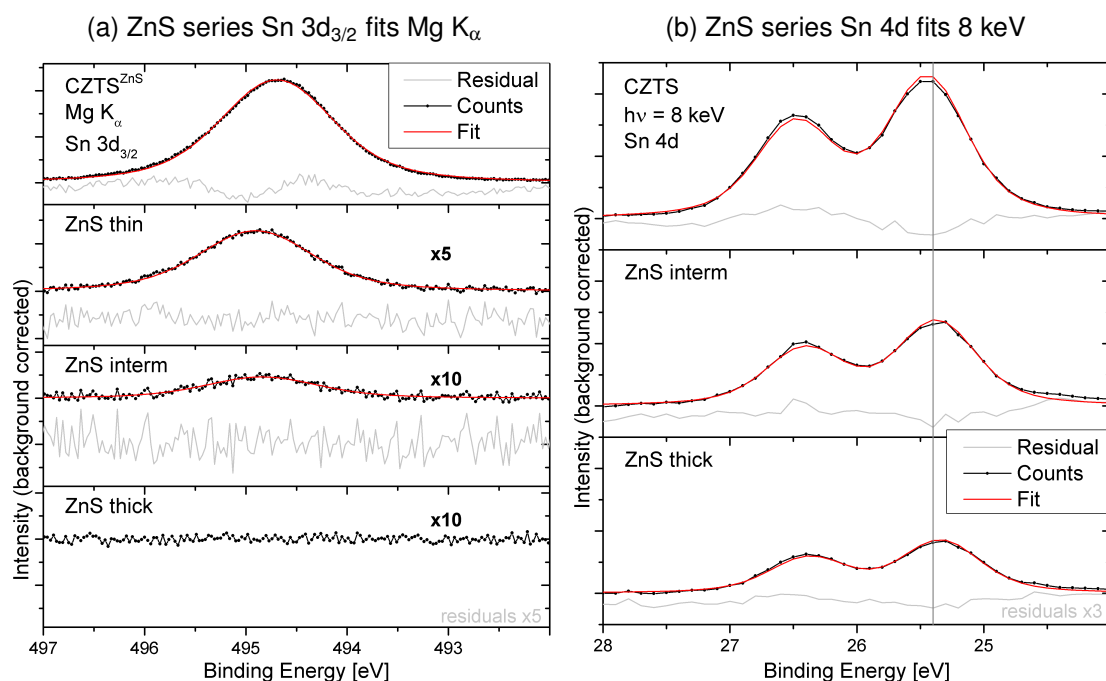


FIGURE 4.6: Sn  $3d_{3/2}$  and 4d spectra measured with  $\text{Mg K}_\alpha$  and 8 keV excitation and fits. The residuals have been magnified for better visibility.

Excited Sn 3d core electrons have a larger IMFP than Cu 2p electrons excited with



the same photon energy (see page 150). This agrees with our findings in figure 4.6. The Sn signal loses less intensity when measured through the buffer layers. The signal decay will be used to calculate the buffer layer thickness later (see page 45).

The Sn 4d signal measured at 8 keV confirms the trends from the Cu 3p measurements as shown in figure 4.6b. The measured spin orbit splitting of 1.05 eV was summed up to a double peak. This core level overlaps with the oxygen (O 2s) signal for the samples that purposely contain oxygen. In this ZnS/CZTS-series no O 2s signal is found in the spectra. The modified Auger parameters  $\alpha'$  of Cu and Sn are used to determine chemical changes independent of any charging effects. The Auger lines are shown on page 152 in figure A.2.

The  $\alpha'_{\text{Cu}}$ -value as shown in figure 4.7 is stable in or below the range of  $\text{Cu}_2\text{-O}$  or -S (compare [90–93]). To our knowledge, no  $\alpha'$ -values for Cu or Sn in CZTS have been published. Our results represent the pure CZTS species of Cu and Sn since additional species are not found in the detail spectra of the respective core levels and Auger lines. The  $\alpha'_{\text{Sn}}$ -values in this work have been calculated with the Sn  $3d_{3/2}$  peak instead of the stronger Sn  $3d_{5/2}$  to avoid the overlapping satellite peak of the non monochromatized Mg  $K_\alpha$  excitation. The doublet splitting of 8.45 eV is therefore added to the values taken from literature to account for this difference. From [91] we expect values around the SnS Auger parameter at 929.75 eV. Oxidized Sn ranges about 2 eV lower. The only change in Sn chemistry which these Auger parameters could suggest is a very light reduction by the incoming ZnS. Within the error margin, we can claim unchanged Sn in the CZTS surface.

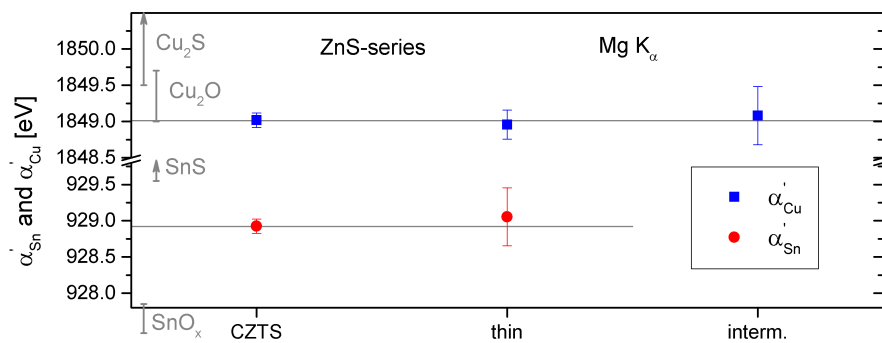


FIGURE 4.7: Modified Auger parameter  $\alpha'_{\text{Cu}}$  and  $\alpha'_{\text{Sn}}$  show that the chemistry of the absorber doesn't change after ZnS deposition.

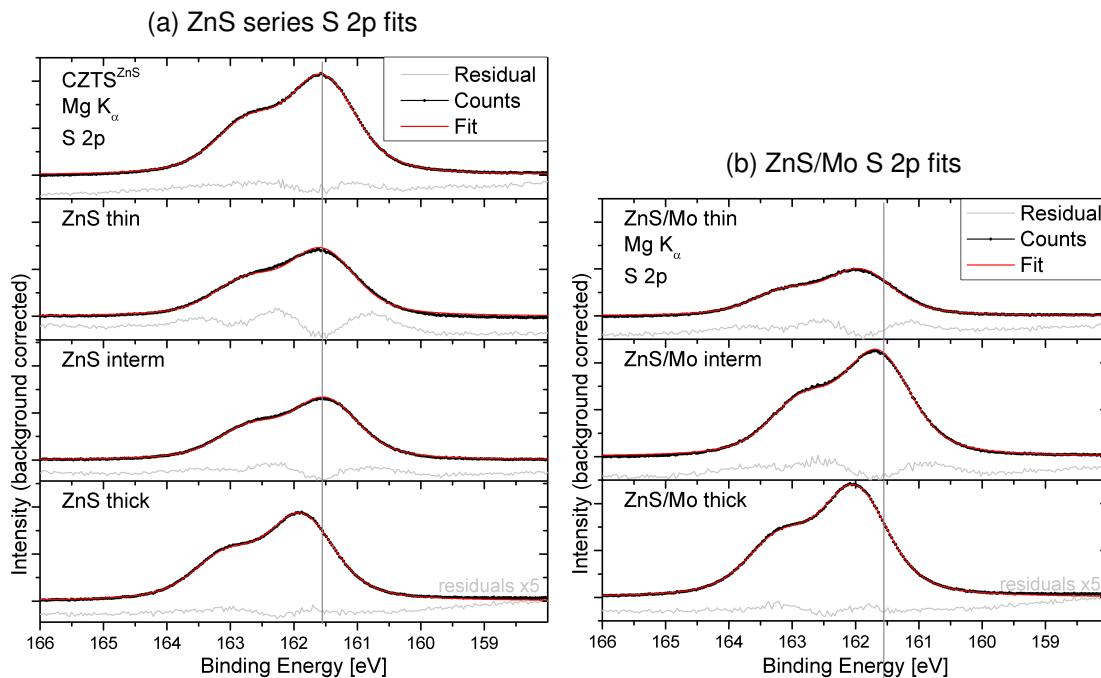


FIGURE 4.8: S 2p spectra of ZnS measured with  $\text{Mg K}_\alpha$  excitation and fits. The residuals have been magnified for better visibility.

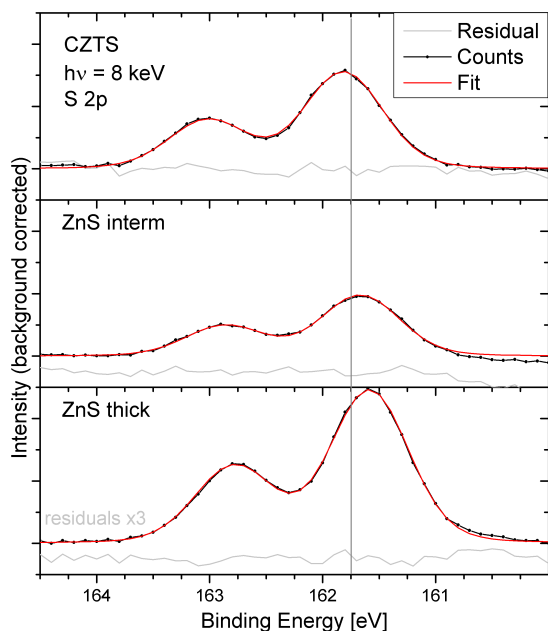


FIGURE 4.9: S 2p spectra measured with 8 keV excitation and fits. The residuals have been magnified for better visibility.

In the S 2p XPS spectra we find a spin orbit splitting of 1.20 eV in agreement with literature (e.g. [94]). For clarity, the two components have been summed up to a double peak in figure 4.8a.

The different S-compounds (CZTS and ZnS) don't show energy-separated peaks so the single contribution in the fits contains signal from both absorber and buffer.

The thick ZnS layer shows a clear shift to higher  $E_B$ . With HAXPES (figure 4.9) we observe decreased S 2p intensity for ZnS *intermediate* and a shift to lower binding energy. The doublet splitting is identical to XPS.

The Zn 2p lines in the ZnS series (see figure 4.10 and 4.11) also show only one species. Note that the Zn 2p electrons have a shorter IMFP than the Cu 2p electrons due to the higher binding energy (see page 150). So the main signal contribution for the buffer layer samples in these fits comes from the buffer material. If a weak signal from the absorber is collected for ZnS *thin* it cannot be distinguished in the fits. This is either caused by signal weakness or by nearly identical Zn 2p peak positions for CZTS and ZnS.

The Zn LMM is fitted to get more chemical information. This Auger line is composed of multiple Auger transition lines that are chemically very sensitive. The line shape of single-species samples (bare CZTS and thick ZnS samples) was used to get a fit model that was used multiple times for multiple-species samples (e.g. ZnOS). The fits were done for all 21 samples (including the ZnS, ZnOS, and ZnO series on CZTS and on Mo, respectively) simultaneously, causing the residual to show remaining features. The model shape was adjusted to account for a shape changes of  $\text{Zn}(\text{OH})_2$  signals. The sharpest feature ( $\text{Zn L}_3\text{M}_{45}\text{M}_{45}$ ) was used to determine the Zn LMM position. The Zn LMM line for the ZnS series shows a single species like the Zn 2p line. Closer inspection can be done using Wagner plots (figure 4.41) and comparing modified Auger parameters ( $\alpha'$ ). The references on Mo do not show changed  $\alpha'$  as we will discuss in figure 4.13.

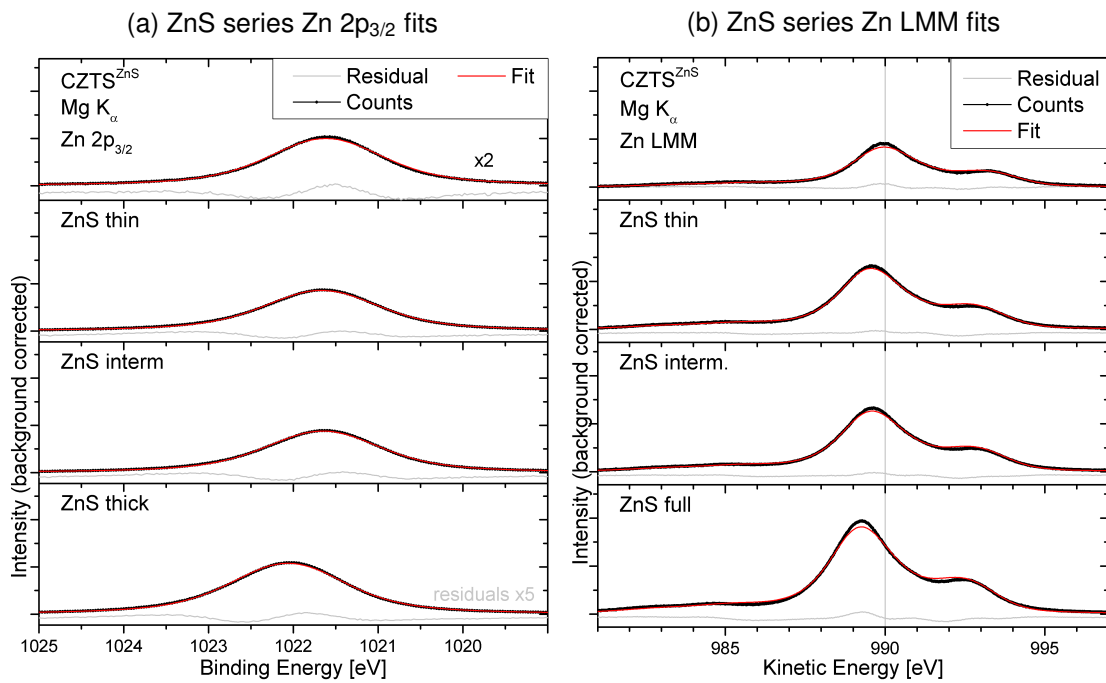


FIGURE 4.10: Zn 2p<sub>3/2</sub> and Zn LMM spectra of ZnS/CZTS measured with Mg K<sub>α</sub> excitation and fits. The Zn 2p residuals have been magnified for better visibility.

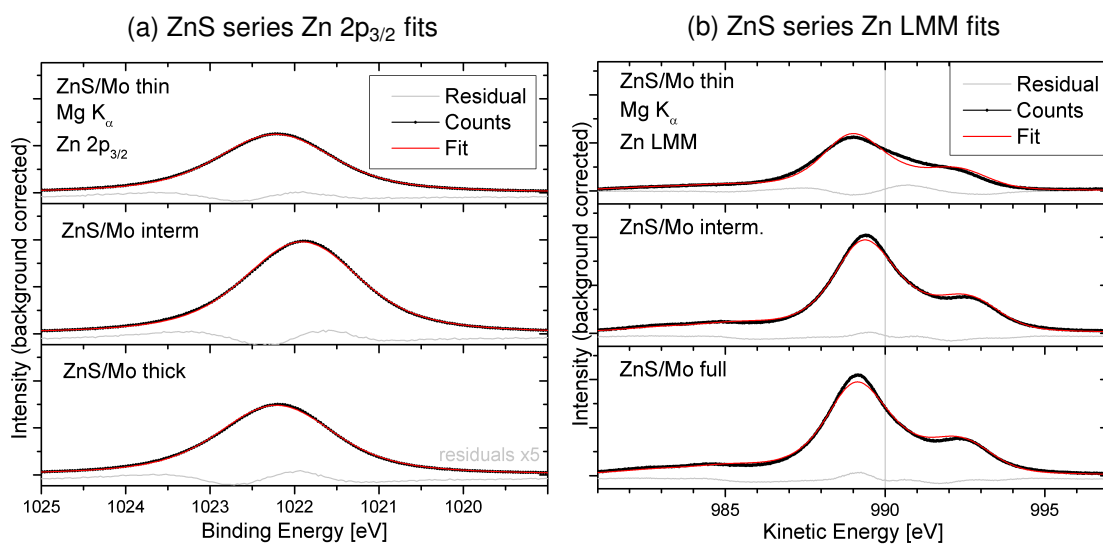


FIGURE 4.11: Zn  $2p_{3/2}$  and Zn LMM spectra of ZnS/Mo measured with  $\text{Mg K}_\alpha$  excitation and fits. The Zn  $2p$  residuals have been magnified for better visibility.

The Zn 3p fits of HAXPES spectra (figure 4.12) make a distinction of species possible when the results from Cu lines are considered. The doublet with fitted spin orbit splitting of 2.94 eV makes it easier to find shape changes.

The position of the buried CZTS species with respect to the position found for bare CZTS has been fixed in position according to the respective shift found in the Cu 3p spectra. With this fit restriction we find the expected evolution from pure CZTS to a ZnS-dominated spectrum. The CZTS is, however, still visible through the thick ZnS layer due to the increased IMFP at this  $E_{\text{exc}}$  (see page 150).

The following comparison of  $\text{Zn-}\alpha'$ -values of the series will exclusively use values measured with Mg  $K_{\alpha}$ -excitation.

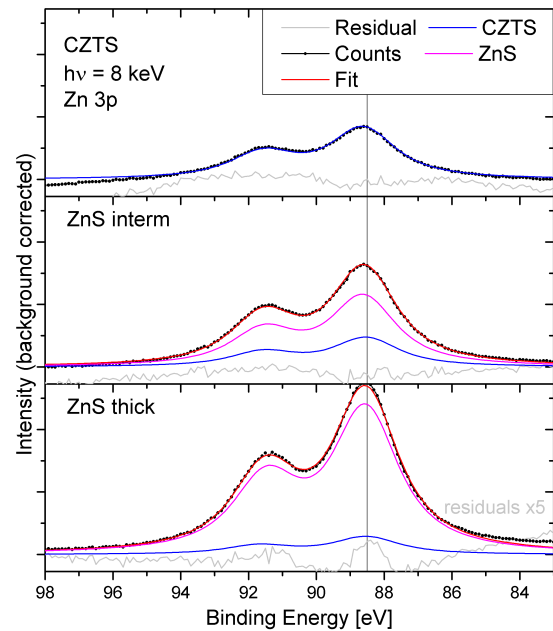


FIGURE 4.12: Zn 3p spectra measured with Mg  $K_{\alpha}$  excitation and fits. The residuals have been magnified for better visibility.

**The Wagner plot** in figure 4.13 reveals the small difference between the bare CZTS sample and the ZnS-covered samples. The shift in the Zn LMM is slightly more pronounced, so  $\alpha'$  changes from  $2011.5(\pm 0.2)$  eV to  $2011.0(\pm 0.3)$  eV. This proves the chemical change in the measured surface which is composed of ZnS as compared to literature [90, 93, 95–97]. A similar system with CIGSSe instead of CZTS was investigated in [98].  $\alpha'$ -error margins range from 0.17 eV to 0.34 eV depending on the clarity of the fits that determine the line positions. The residuals caused by the sharpness difference in the Auger line fits and the spectra do not affect the error margin too much, since the maxima positions are still sufficiently distinct.

Additionally, we see a shift of the ZnS signal along the iso- $\alpha'$  line of 2011.0 eV. This indicates an identical shift of the whole spectrum and consequently means band bending [99]. We can read out the difference between very thin samples on CZTS and *ZnS thick* to be around  $0.4(\pm 0.2)$  eV. The data points of the references on Mo scatter around the point of *ZnS thick*. *ZnS/Mo thin* shows a Na signal on the surface. The error margin is increased, especially for the Zn LMM value, because the Na LMM line has nearly the same position and shape as the Zn LMM. The respective Zn LMM fit does not reveal an additional species but we have to consider the additional signal that can slightly influence the position. Additional elements are discussed in the appendix, see 153.

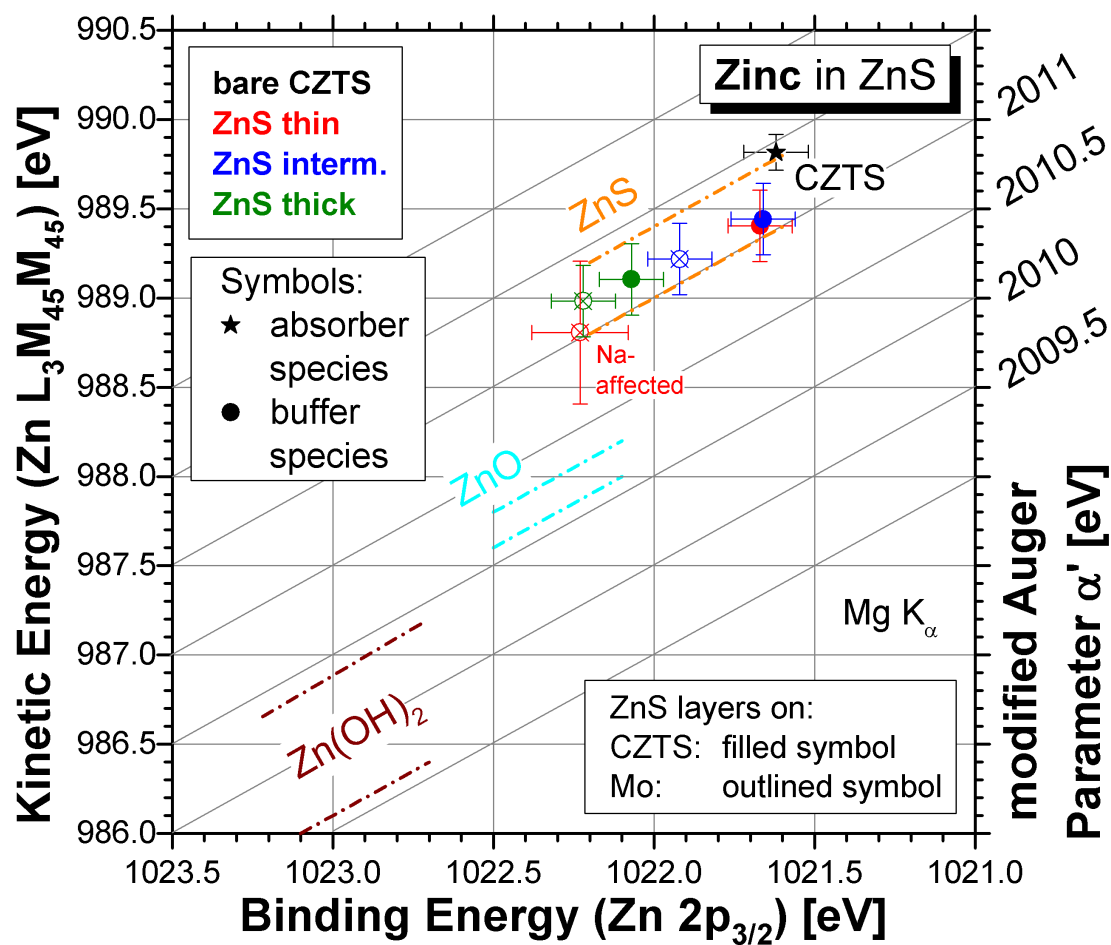


FIGURE 4.13: Wagner plot containing Zn  $2p_{3/2}$  and Zn  $L_3M_{45}M_{45}$  positions of all samples from the ZnS series. Diagonal lines indicate identical  $\alpha'$ . Literature references for ZnS, ZnO, and Zn(OH)<sub>2</sub> are in between the respectively labeled dashed lines.

### 4.3.1.2 X-ray absorption and emission

The chemical stability of CZTS and ZnS at their interface can also be investigated with S  $L_{2,3}$  XES. Compared to PES, this photon-in-photon-out technique has a much larger probing depth of 15- 21 nm (see table 3.1).

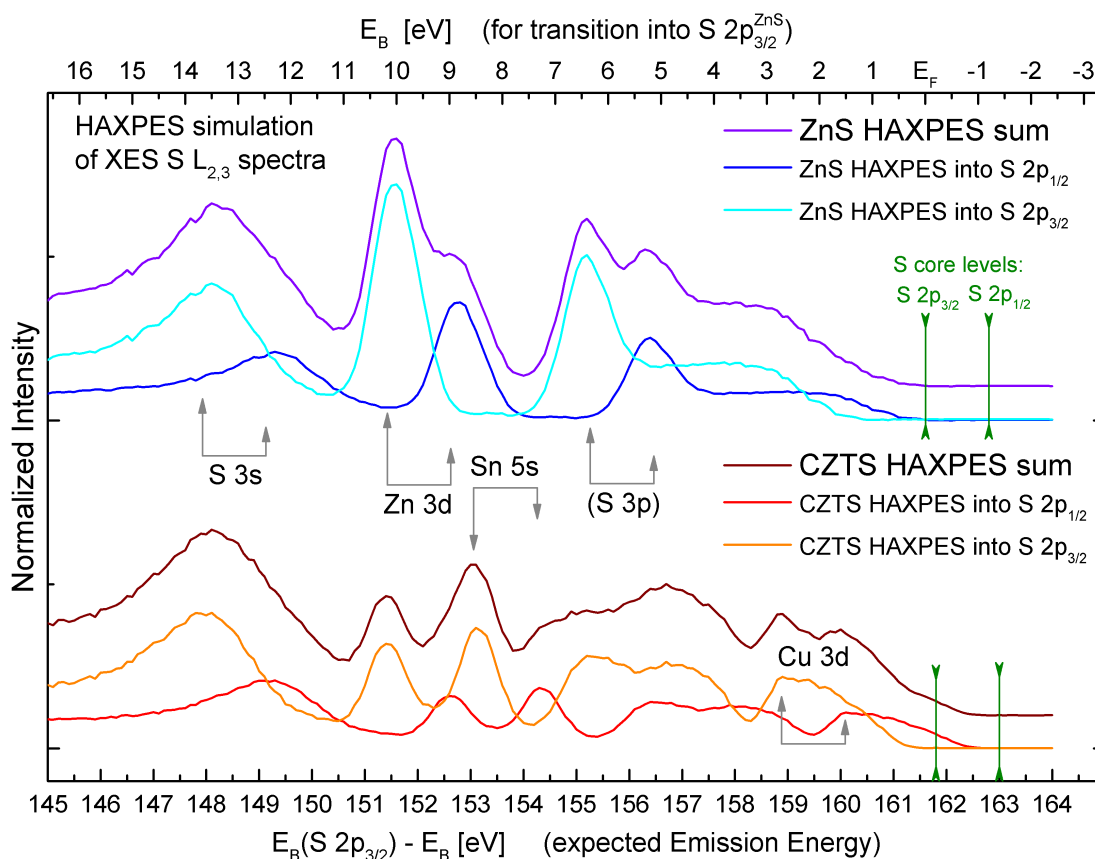


FIGURE 4.14: Added HAXPES spectra as simulation of XES spectra of CZTS and ZnS normalized to the highest spectral feature. Vertical offsets have been added for clarity.

**Comparing with HAXPES valence band spectra** of the same sample helps to identify the spectral features. We will discuss the spectra of bare CZTS and pure ZnS first and compare with the respective HAXPES measurements. The used HAXPES spectra are explained in figure 4.14.

If we excite a S 2p state to measure XES, the detected photons come from transitions from occupied states to S 2p core levels. The first emission features measured below the S 2p binding energy ( $\approx 162$  eV) therefore indicate the occupied states at the VBM. Differences in shape between the HAXPES VB spectra and the XES spectra below  $E_B$  of the excited edge are still expected due to differing transition probabilities and forbidden transitions in XES. We have to carefully compare to calculations and experimental techniques like HAXPES, that are not limited by transition rules, to make sure that the states at the VBM are accessible with the excited edge. The high degree of hybridization to S-states in CZTS makes the DOS in the VB recognizable in S  $L_{2,3}$  XES

spectra (see 4.15).

The S 2p core level is split by 1.2 eV, so we have to consider two 'VB-spectrum-like' contributions from transitions into the depleted  $2p_{1/2}$  and  $2p_{3/2}$  states.

We used the splitting of S 2p (1.2 eV as measured with HAXPES) and the ratio of the density of states (1:2) of the two components to simulate the expected signal for the S  $L_{2,3}$  XES spectra. The Fermi level from the HAXPES measurements has been shifted to the respective S 2p positions, indicated in green. To achieve this, the energy scale that simulates the emission energy scale is calculated by subtracting the binding energy from the measured binding energy of the respective S 2p core level. The two contributions ( $L_2$  and  $L_3$  emission), scaled by the DOS of the respective excited state (measured by HAXPES intensity) were added up. The resulting HAXPES sums (purple and brown line) can be compared to XES spectra.

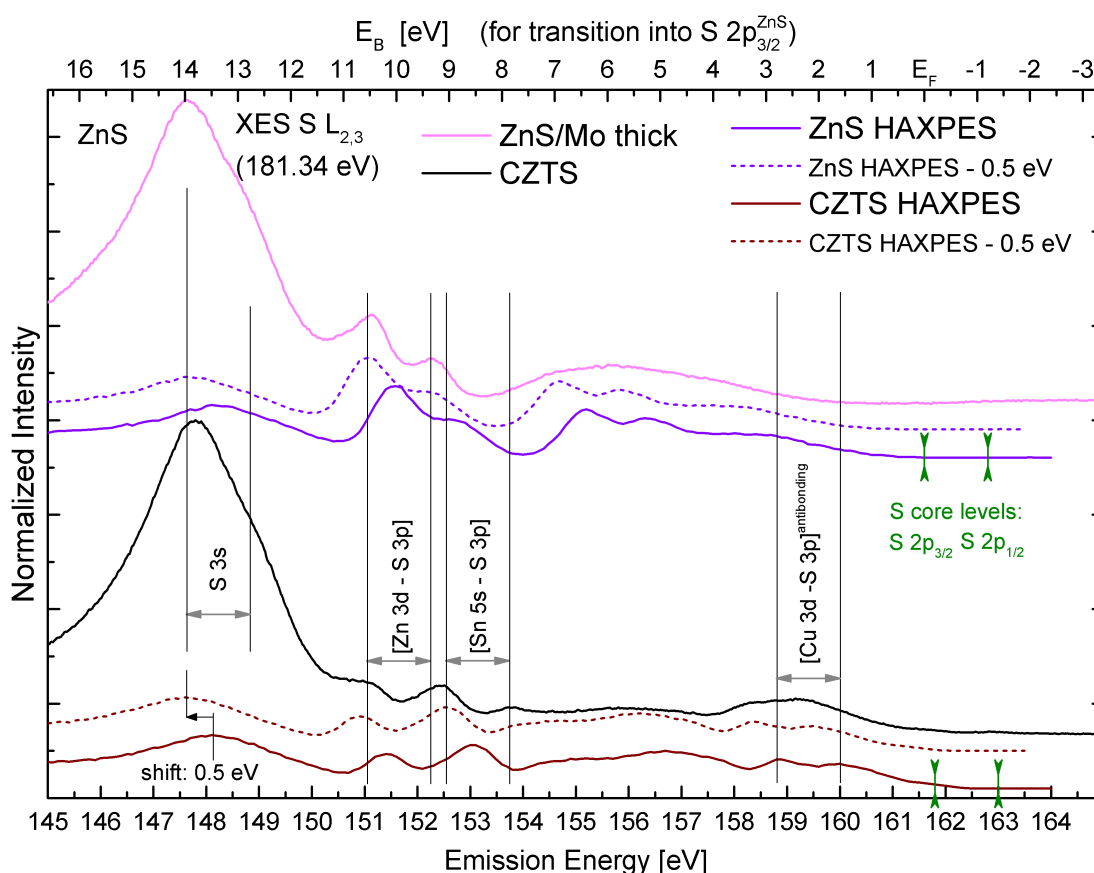


FIGURE 4.15: Added HAXPES spectra normalized to the match the intensity of the features with emission energy of 150 eV and above as simulation of XES spectra normalized to the main peak. The shift was additionally applied to align the features with the as measured XES spectra. Vertical offsets have been added for clarity.

We see a high similarity between the XES spectra and the HAXPES simulations (figure 4.15) but to align the features of both spectra, the simulated curves need a shift of 0.5 eV to lower energy on the emission energy scale. Since the energy calibration of HAXPES (with Au 4f) and XES (with CdS emission lines) was carefully carried out, the difference must come from differences in the initial and final states of the techniques.



If we look into the details of the XES spectra, we see a dominant S 3s peak with an emission energy of around 147.7 eV as well as signatures of valence states. Note that the excited S 2p has a doublet splitting of about 1.2 eV so all electrons from valence states can relax into either S  $L_2$  (S  $2p_{1/2}$ ) or S  $L_3$  (S  $2p_{3/2}$ ) that are indicated in green. For S 3s the two features are not clearly separated. The Zn 3d with XPS-derived binding energy of about 10.2 eV and a doublet splitting as small as 0.1 eV shows two separated features at around 151.1 eV and 152.3 eV. The one at higher emission energy that decays into S  $2p_{1/2}$  appears more pronounced for CZTS because it overlaps with the Sn 5s decay into S  $2p_{3/2}$ . The weaker signal of the transition from Sn 5s to S  $L_2$  can be seen at 153.8 eV. The remaining very broad valence states around 156 eV are primarily derived from hybridized Zn 4s – S 3p states. The CZTS shows another broad Cu-related feature around 159 eV as similarly seen for  $\text{CuInSe}_2$  compounds [100] and especially CIGSse [101].

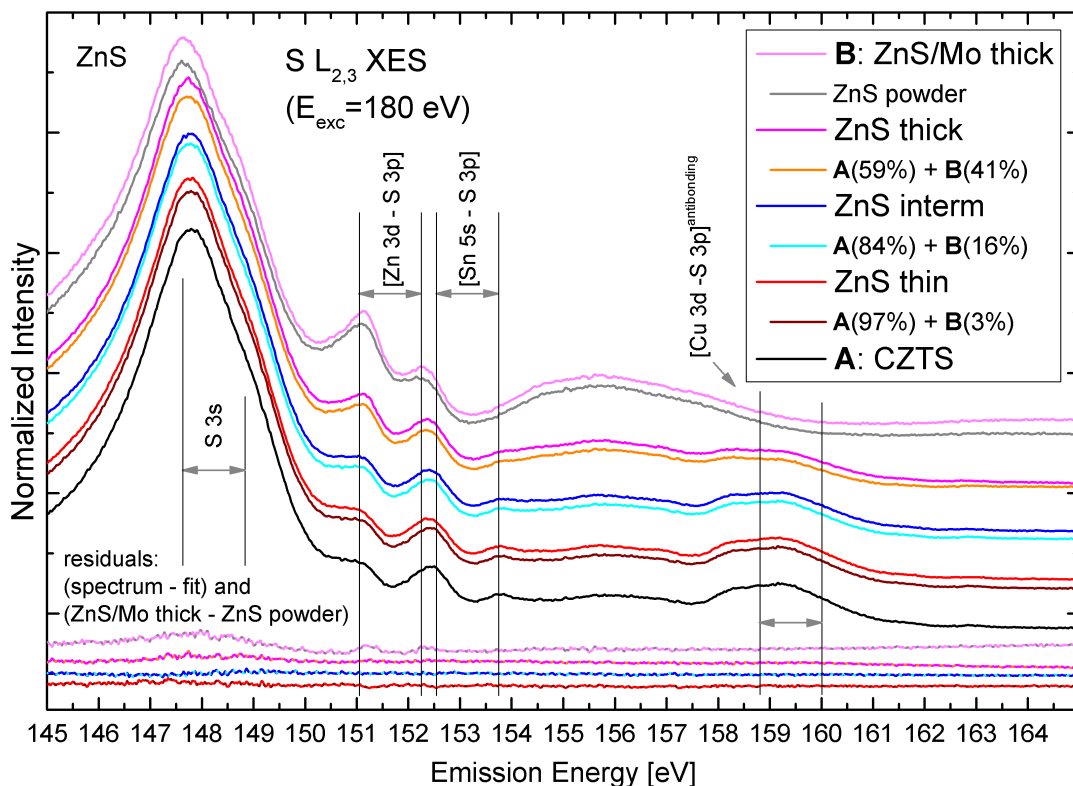


FIGURE 4.16: S  $L_{2,3}$  XES spectra of the ZnS series and superposition of CZTS and ZnS S  $L_{2,3}$  XES spectra to reproduce the signals measured on ZnS/CZTS-structures. No additional features of other S-compounds are visible. Vertical offsets have been added for clarity.

**Spectral differences** within the series are shown in the XES comparison of spectra in figure 4.16. The thick ZnS/Mo (B: light magenta line) has a spectrum that is very similar to a ZnS powder reference (gray line) and measurements from literature [102]. The broader Zn 3d features in the powder spectrum are presumably due to the increased surface contribution where surface effects like oxidation can take place. The kesterite

(A: black line) shows, among others, an additional broad Cu-related signal around 158-161 eV.

All spectra of ZnS layers on CZTS can be reproduced by adding up the spectra of CZTS (A) and *ZnS/Mo thick* (B) in the fitting ratio. *ZnS thin* (red line) is identical to 97% of CZTS and only 3% of ZnS (brown line). *ZnS intermediate* (blue line) can be reproduced by adding 84% CZTS and 16% ZnS (cyan line) and *ZnS thick* (magenta line) still requires 59% of CZTS signal and 41% ZnS (orange line).

This near perfect reproduction supports the assumption of an abrupt ZnS/CZTS contact and unchanged chemical environments for the S in both layers.

### 4.3.1.3 ZnS thickness

The calculated buffer thickness for all samples of the ZnS series is shown in figure 4.17. The signal intensities of thick buffer layers and bare CZTS were used as  $I_0$ , respectively, in equation 2.1. The values calculated from the decaying signal of the absorber give mostly consistent values whereas the values calculated from the buffer signal that builds up are mostly smaller, especially for measurements with Mg  $K_\alpha$  excitation. The error margin is larger here, because both Zn and S signals from the buffer overlap with the respective signals from the absorber.

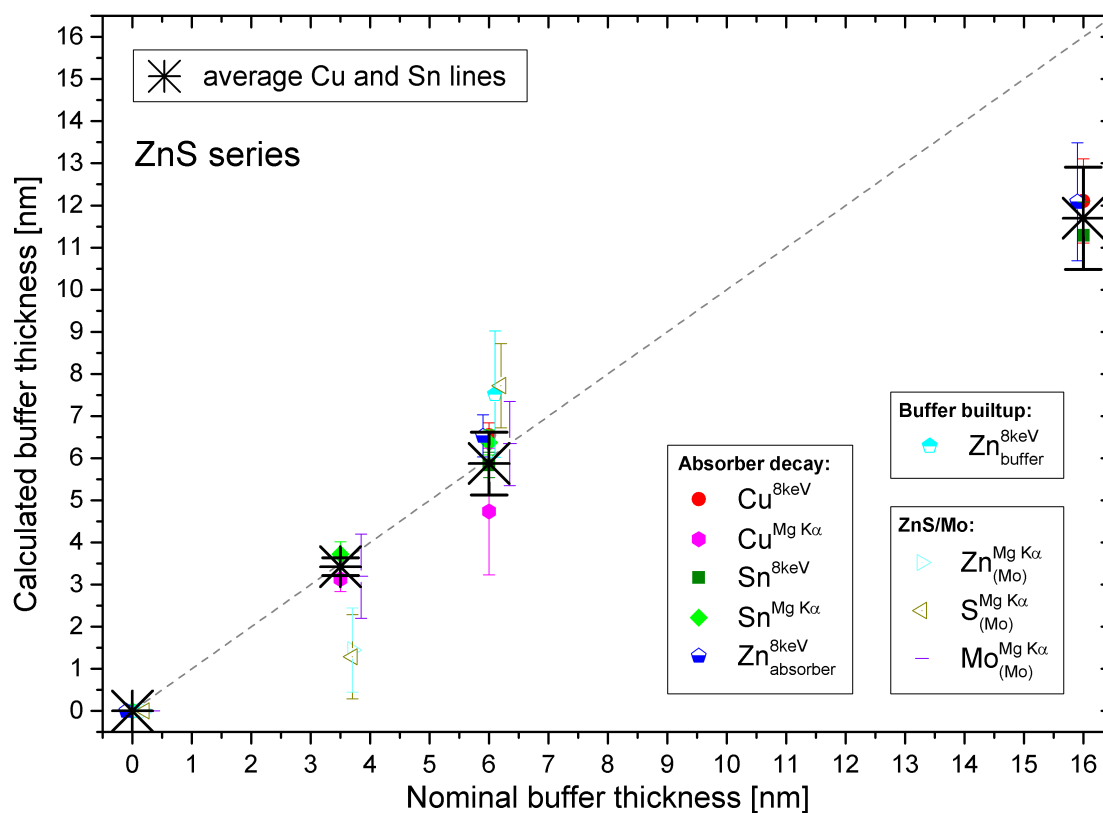


FIGURE 4.17: ZnS-buffer thickness calculated from all core levels. Included are the reference buffers grown on Mo. Thicknesses calculated from absorber lines are more reliable because they are less affected by adventitious surface species of e.g. C and O. Averages are therefore calculated from Cu and Sn signals that originate exclusively from the absorber. The dashed line is a guide to the eye and represents the nominal growth speed.

The dashed grey line represents the expected growth rate of  $0.24 \frac{\text{nm}}{\text{cycle}}$  as reported in [103]. The ZnS growth follows this line for thin layers and doesn't show any differences in growth on CZTS and Mo. The unexpected small value for *ZnS thick* is surprising since there is no reason for the growth to change speed while the layer is forming. These values are exclusively measured by HAXPES with the highest probing depth

and for the small remaining signals, the error in the calculation can easily be underestimated. The highest reached IMFP values are indicated on the nm-scale with a green line.

**Conclusion:** After examination of the chemical structure of the ZnS series, all evidence points towards a pure ZnS growing directly on the pure CZTS. There is no indication for secondary phase formation or diffusion. The results can be used to compare to the mixed buffer in section [4.3.3](#), see page [60](#).

## 4.3.2 ZnO

### 4.3.2.1 PES measurements

In the survey spectra of the ZnO/CZTS series in figure 4.18, being composed of Zn and O lines accompanied by C, we see closed ZnO layers and no CZTS signal.

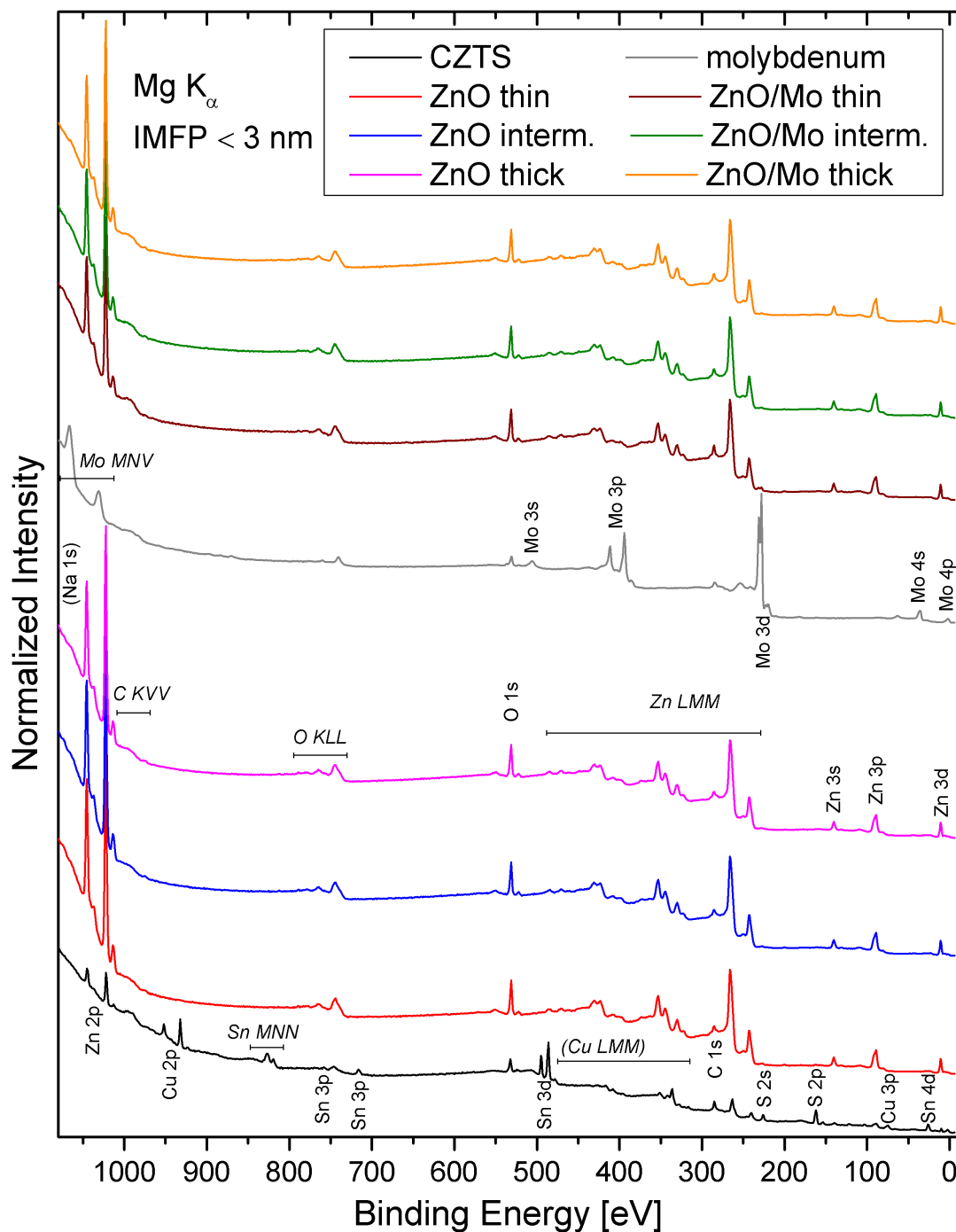


FIGURE 4.18: Survey spectra of all samples from the ZnO series normalized in the flat region at 600 eV. Vertical offsets have been added for clarity.

In the bare CZTS spectrum (black line), we see Cu, Zn, Sn, and S lines. All spectra show O and C signals that are discussed in section A.2.3 on page 154.

A more detailed picture can be seen in the shallow core level region (figure 4.19) with sharp shallow core levels of Cu, Zn, and Sn and broader S and O lines. These spectra, measured with 8 keV, exhibit a larger probing depth (see section 2.1.2) so all lines from buried material appear more pronounced compared to the cover layer signals that show stronger relative signals with Mg  $K_\alpha$ -excitation.

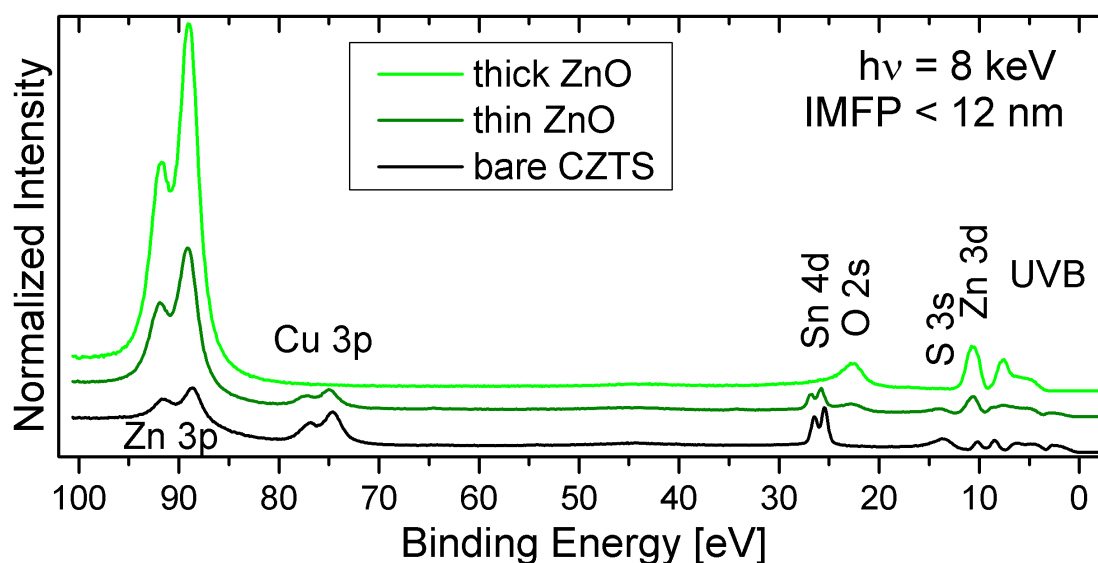


FIGURE 4.19: Shallow core level region spectra of selected samples measured with 8 keV and normalized in the flat region at 50 eV. Vertical offsets have been added for clarity.

**Core levels** have been measured as described in section 4.3.1.1.

The energy range of the XPS Cu 2p line of *ZnO thin* is flat (see figure 4.5a), meaning that the thinnest layer is already too thick to allow any penetration of Mg  $K_\alpha$ -excited Cu 2p electrons. The species in CZTS matches the observed peak in the previous ZnS series in position and peak shape. Measurements of the Cu 3p line at higher excitation energy of 8 keV (figure 4.5b) reach down to the buried interface (see table A.1). The Cu 3p is spin-orbit split into two components. The thick ZnO layer is thick enough to block the complete signal from the absorber but *ZnO thin* allows for a strong signal of the buried CZTS to be captured. All Cu 3p spectra have been corrected for a Sn 4p background (see page 79, figure 4.53).

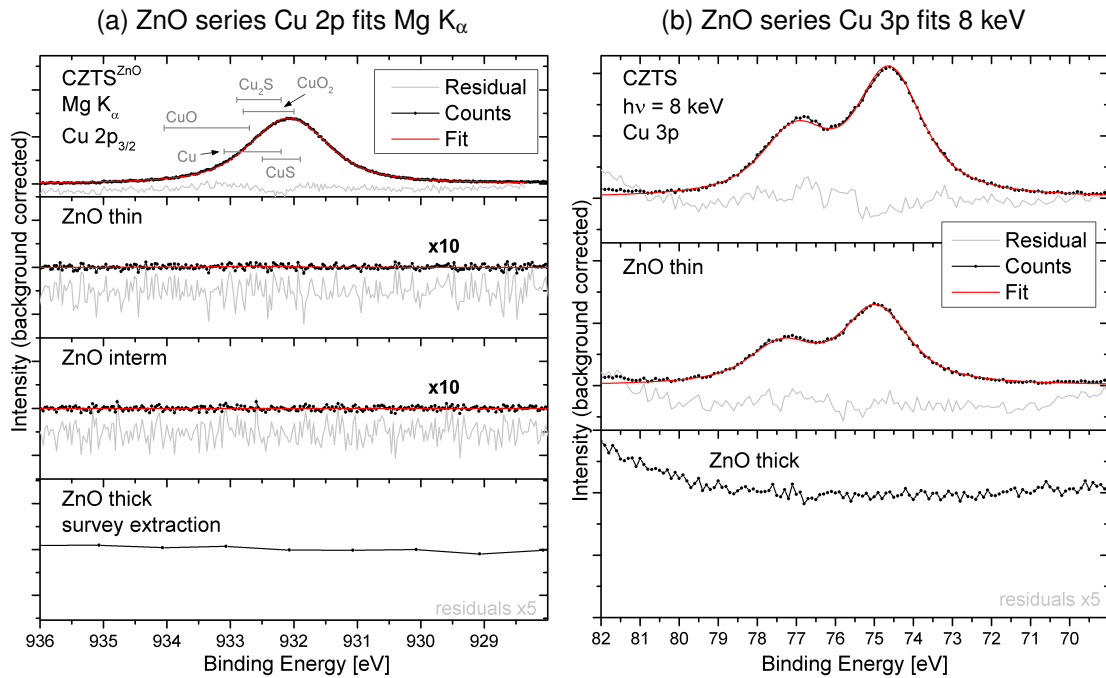


FIGURE 4.20: Cu  $2p_{3/2}$  and  $3p$  spectra measured with  $\text{Mg K}\alpha$  and 8 keV excitation and fits. The residuals have been magnified for better visibility.

Excited Sn  $3d$  core electrons have a larger IMFP (see page 150). This agrees with our findings shown in figure 4.6. The very weak peak seen in *ZnO thin* is most likely CZTS right at the interface. The shift to higher binding energy could therefore be caused by oxidation to SnO or interface induced band bending of the CZTS phase. Sn is the most reactive metal in the CZTS surface so we always expect traces of SnO.

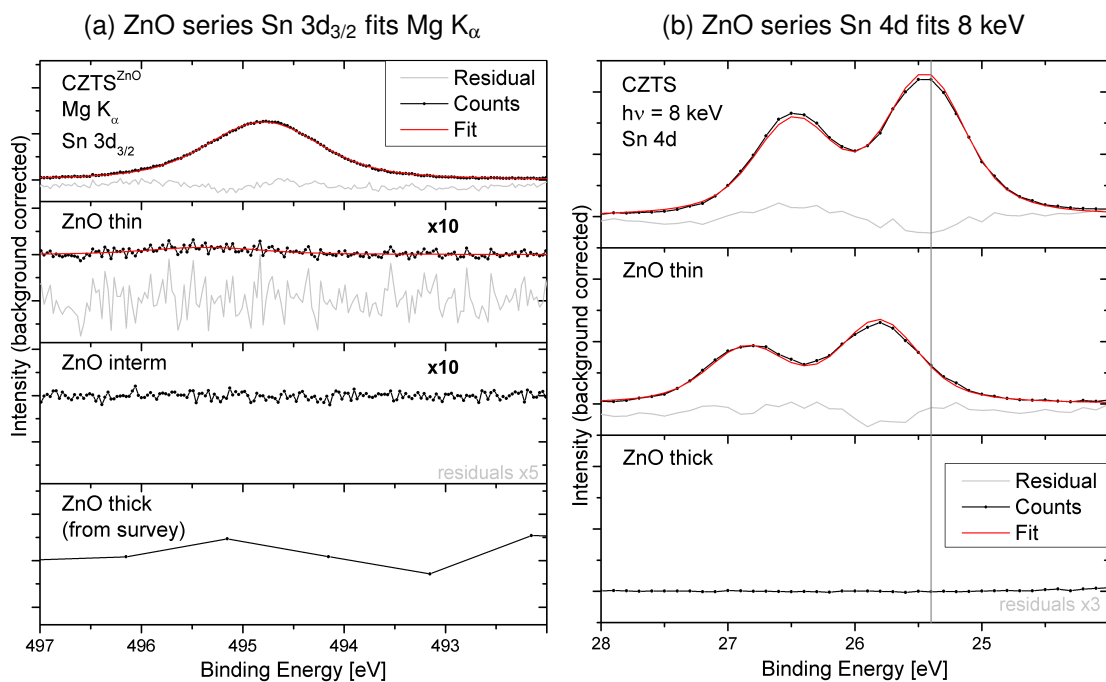


FIGURE 4.21: Sn  $3d_{3/2}$  and  $4d$  spectra measured with  $\text{Mg K}\alpha$  and 8 keV excitation and fits. The residuals have been magnified for better visibility.

The Sn 4d signal (spin orbit splitting summed up to a double peak) measured at 8 keV can resolve the unclear speciation from the Sn 3d measurements because the penetration depth is enlarged (figure 4.6b). We see only one species and the buried CZTS (*ZnO thin*) shows a significant shift to higher binding energy as seen in XPS. This Sn 4d core level overlaps with the O 2s peak at around 24 eV. This broad peak shows multiple species as the O 1s (see figure 4.27). The flat flank of this peak was not separately modeled in the fits but included in the linear background. The validity of this is shown in *ZnO thick* where the O 2s background in the relevant range is fitted with a linear function in the absence of a Sn signal.

The intensities of the Sn 3d fits have been used to scale the spectrum of a SnO-sample. The resulting Sn-background caused by broad Sn 4p emission around 90 eV was subtracted from the measured Zn and Cu 3p spectra to get reliable fits in the binding energy range from 50-100 eV (see page 79, figure 4.53).

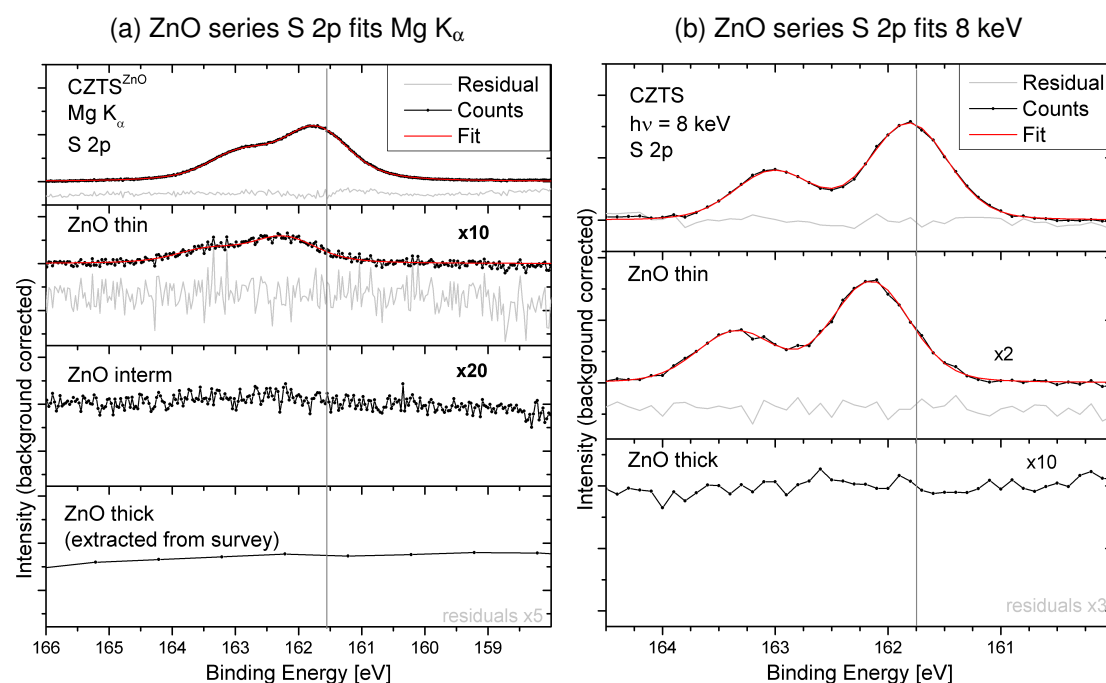


FIGURE 4.22: S 2p spectra of ZnO/CZTS measured with  $\text{Mg K}\alpha$  and 8 keV excitation and fits. The residuals have been magnified for better visibility.

The examination of S in figure 4.22 follows the trends of Cu and Sn for this S-free buffer. We see one S-species (CZTS) before and after ZnO deposition with an energy shift to higher binding energy for buried CZTS. The attenuation is slightly weaker than for Sn, which is in agreement with the larger IMFP (see page 150).

The HAXPES measurements give the same results already seen in XPS. A very weak signal can be fitted for the thick layer, but the intensity is zero within the error margin, so this signal will not be included in further analysis.

The Zn 2p fits in figure 4.23a and the Zn LMM fits in figure 4.23b of the ZnO series show single phase CZTS for the bare sample and a two-phase signal composed of



ZnO (green line) and another species (magenta line) for all  $\text{ZnO}^2$  layers. We attribute the second signal to the presence of  $\text{Zn(OH)}_2$  at the surface. The presence of  $\text{Zn(OH)}_2$  may be due to the use of water as oxygen-source during deposition. Sulfates can be ruled out for the S-free ZnO/Mo system that shows the same speciation. The line positions of both species for both Zn 2p and Zn LMM are extremely stable. The ratios of the two species in Zn 2p and Zn LMM, however, do not match each other, especially when we assume surface  $\text{Zn(OH)}_2$ . The  $\text{Zn(OH)}_2$  would be bigger compared to the ZnO signal if we look at the excited Zn 2p core electrons with the smaller IMFP. We can best explain this with the high shape uncertainty in the Zn LMM fits. The Zn LMM shape in oxidized Zn compounds (like ZnO and  $\text{Zn(OH)}_2$ ) is often reported to be broader compared to the LMM structure found in ZnS or pure Zn. This would lead to a higher Zn LMM energy and less relative intensity for the  $\text{Zn(OH)}_2$ -species compared to the dominant ZnO species. We do not have any indication on how to modify the shape and without a pure ZnO sample, we cannot define a different shape. We therefore disregard this intensity mismatch and consider an increased error margin for the Zn Auger line positions.

The reference layers on Mo give identical Zn signals as shown in figure 4.24. The  $\text{Zn(OH)}_2$  contributes with about 25% to the measured Zn signal (see figure A.9 on page 157).

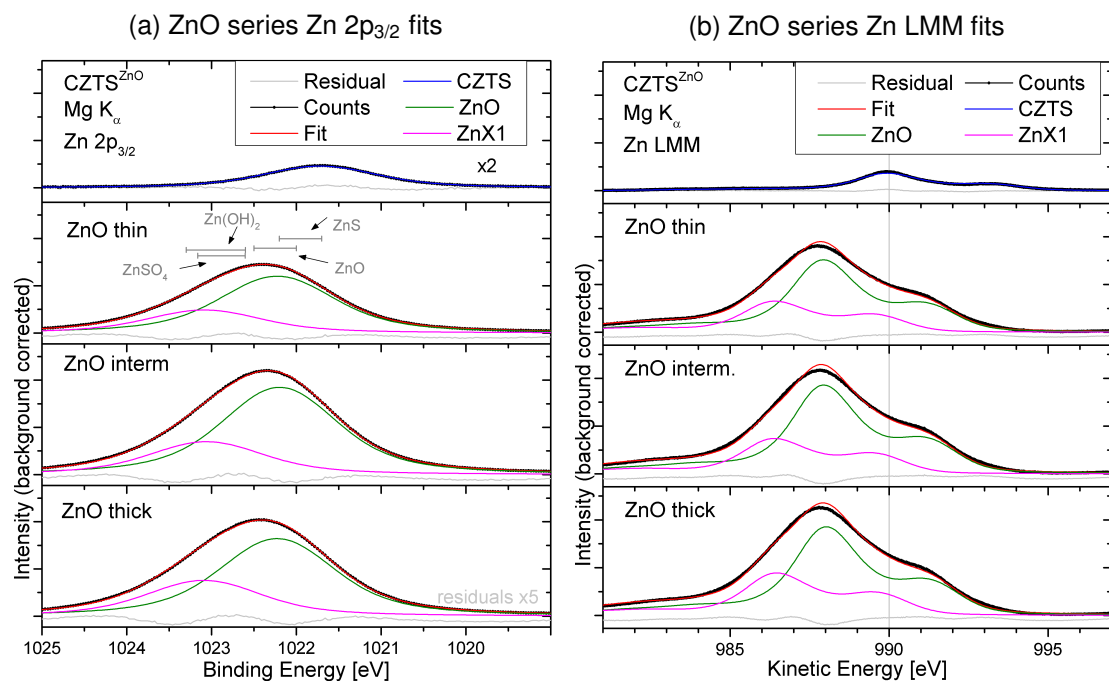


FIGURE 4.23: Zn  $2p_{3/2}$  and Zn LMM spectra of ZnO/CZTS measured with  $\text{Mg K}_\alpha$  excitation and fits. The Zn 2p residuals have been magnified for better visibility.

<sup>2</sup> We observe the same species in the ZnOS series.

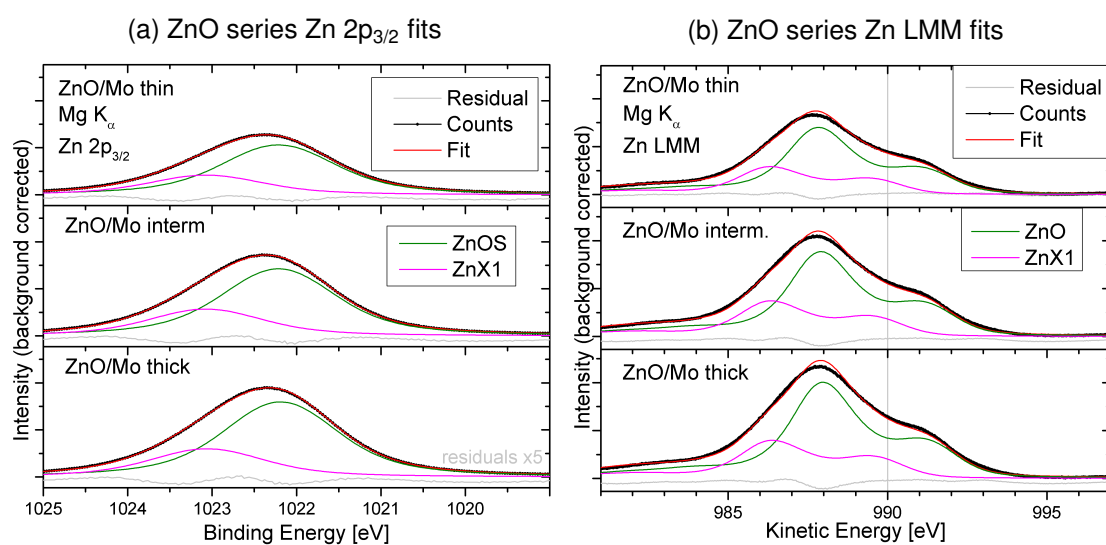


FIGURE 4.24: Zn  $2p_{3/2}$  and Zn LMM spectra of ZnO/Mo measured with Mg  $K_\alpha$  excitation and fits. The Zn  $2p$  residuals have been magnified for better visibility.

The Wagner plot in figure 4.25 shows that all ZnO-surfaces are identical. The ZnO-point shows  $\alpha' = 2010.3(\pm 0.2)$  eV in accordance with literature values while  $\text{Zn}(\text{OH})_2$  has  $\alpha' = 2009.6(\pm 0.3)$  eV [90, 95–97].

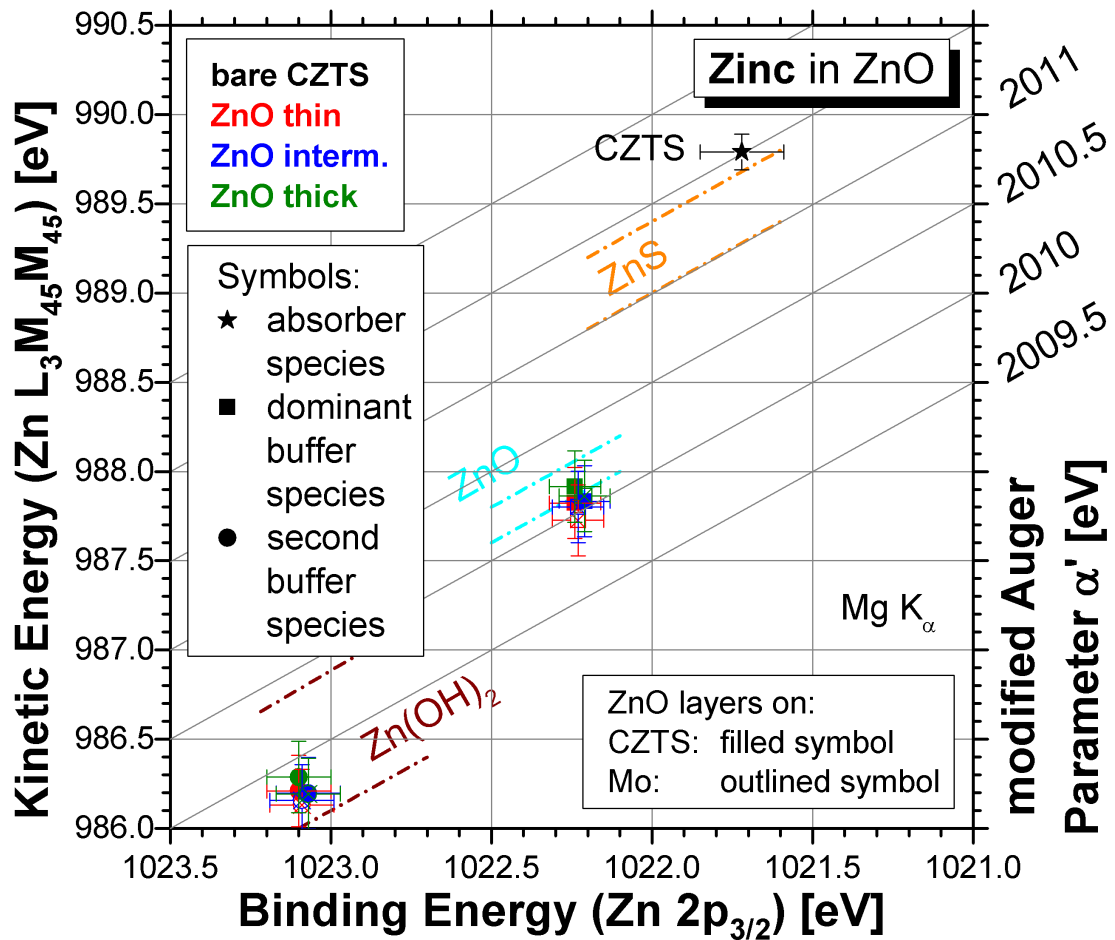


FIGURE 4.25: Wagner plot containing  $\text{Zn } 2p_{3/2}$  and  $\text{Zn L}_3\text{M}_{45}\text{M}_{45}$  positions of all samples from the ZnO series. Diagonal lines indicate identical  $\alpha'$ . Literature references for  $\text{ZnO}$ ,  $\text{ZnS}$ , and  $\text{Zn}(\text{OH})_2$  are in between the respectively labeled dashed lines.

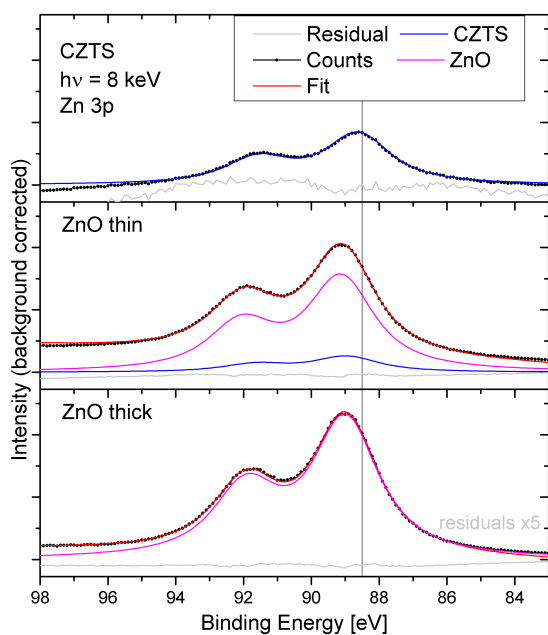


FIGURE 4.26: Zn 3p spectra measured with  $\text{Mg K}_\alpha$  excitation and fits. The residuals have been magnified for better visibility.

The Zn 3p fits of HAXPES spectra as shown in figure 4.22b have been performed as described for ZnS. Here the interface region is reached by the measurement due to the higher IMFP (see table A.1 and we find that the buffer peak positions stay as fix as seen in XPS. The CZTS in contrast shows a shift to higher binding energy at the interface. The  $\text{Zn(OH)}_2$  is heavily reduced compared to XPS measurements speaks in favor of  $\text{Zn(OH)}_2$  as surface species. The hydroxide is the best explanation but the stability and distribution stays unclear.

The O 1s peak in figure 4.27 reveals two species for all the ZnO layers. The bare CZTS and Mo are discussed for the ZnS series in figure on page 153. The thick O-rich buffers obscure the signal from the CZTS or Mo-surface. The sharp main peak is dominated by ZnO at around 531 eV. The other peak must belong to the  $\text{Zn}(\text{OH})_2$ -species and contains surface oxygen, too.

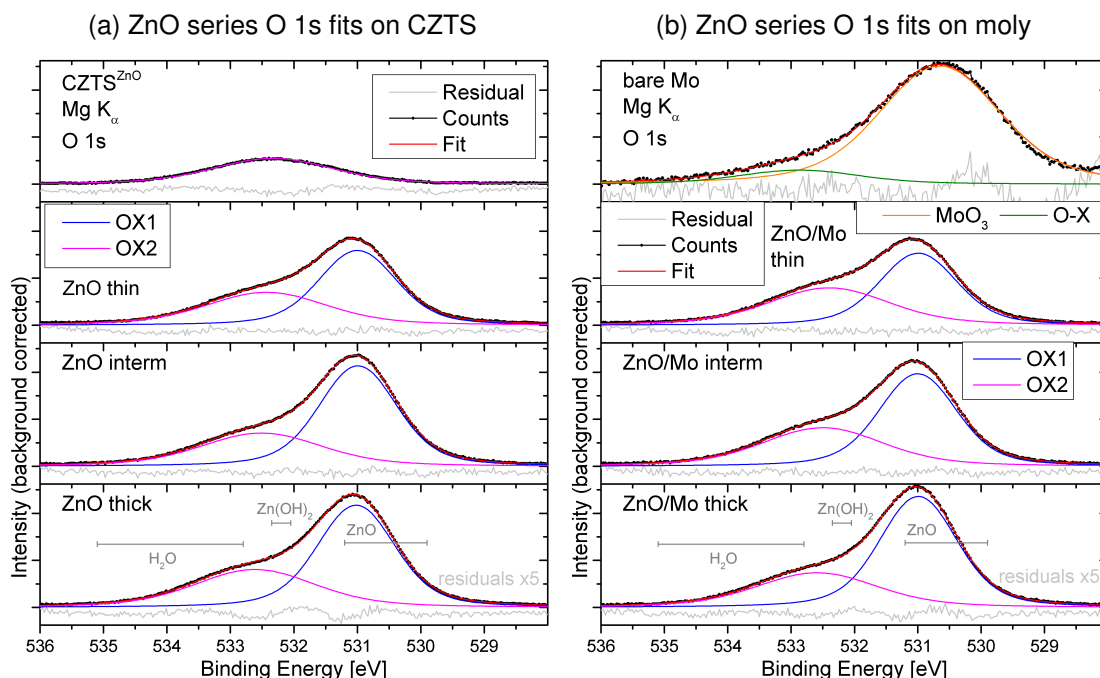


FIGURE 4.27: O 1s spectra measured with  $\text{Mg K}_\alpha$  excitation and fits. The residuals have been magnified for better visibility.

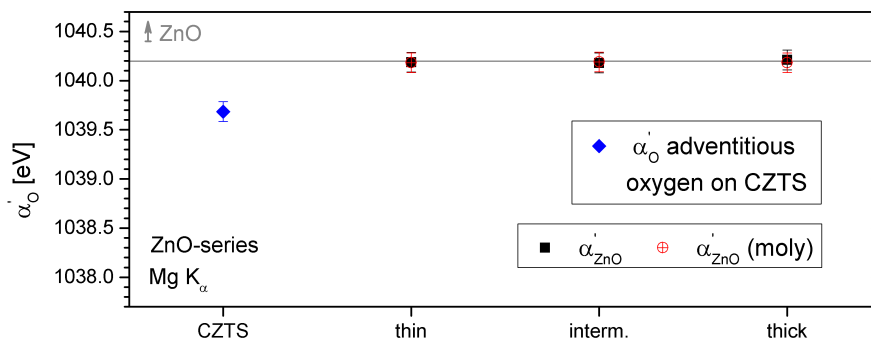


FIGURE 4.28: Modified Auger parameter  $\alpha'_0$  of ZnO shows a stable chemical environment for all ZnO samples on Mo and CZTS. The range for ZnO reported in literature extends out of the shown region.

Combined with Auger lines shown on page 151 in figure A.1a, we get the Auger parameters in figure 4.28. The value for CZTS represents adventitious oxygen. The other values represent ZnO, even though our values are lower than reports from literature [104, 105], indicated in gray. Ranges for Cu- and Sn-oxides are above the shown region (see [89]).

### 4.3.2.2 X-ray absorption and emission

**XES spectra** have been measured at the S  $L_{2,3}$  and O K edge.

The S-free ZnO buffer layers only damps the S  $L_{2,3}$  XES signal originating from the CZTS as shown in figure 4.29. The CZTS used for the ZnO series has not been measured so we first compare the two other CZTS samples. The differences between the two kesterites (gray and black line) are small. In the difference spectrum (green line) we see that  $\text{CZTS}^{\text{ZnOS}}$  has a slightly stronger antibonding Cu 3d signal and  $\text{CZTS}^{\text{ZnS}}$  has more intensity in the Zn 3d range.

We use  $\text{CZTS}^{\text{ZnOS}}$  to create difference spectra with the buried CZTS from the ZnO series and to check for remaining signatures. The noise level increases for thicker layers but no significant new features appear in the spectra. In particular we see no characteristic sulfate features. We can deduce that the ZnO deposition doesn't affect the CZTS surface more than oxygen traces that come in contact with a bare CZTS surface.

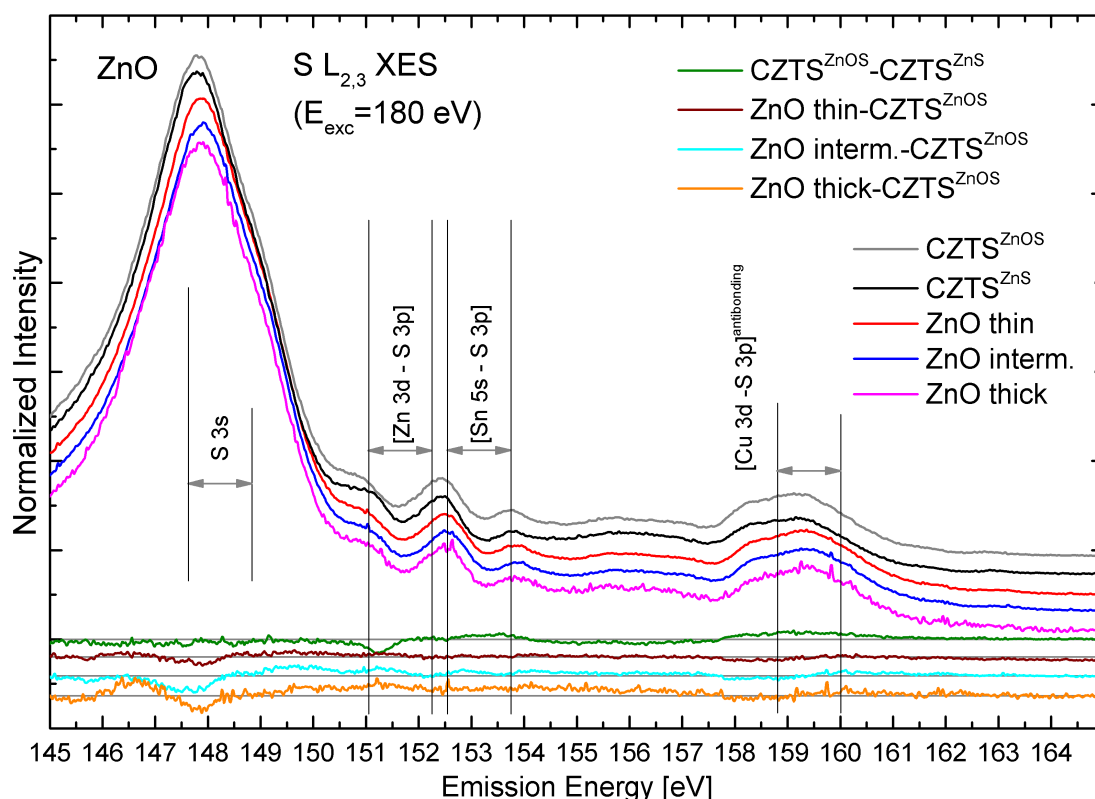


FIGURE 4.29: Spectral subtraction of the S  $L_{2,3}$  XES spectra of the ZnO series and two CZTS-samples normalized to the main peak. No additional features of other S-compounds are visible. Vertical offsets have been added for clarity.

The O K emission edge in figure 4.30 shows that the oxygen is in contact with the CZTS. The attribution of signals to electronic states is based on measured and identified valence states of the respective materials (see figure 4.54 and 4.55) combined with reference spectra of ZnO [106, 107]. The three main features that arise from hybridization of O 2p with Zn 3d, 4s, and 4p make up the spectrum for all measured samples. For *ZnO intermediate* and especially *ZnO thin* we see additional contributions in the regions of 521 eV (Sn 5s hybrid) and 517 eV. The latter is caused by Zn  $L_2$  emission detected in second order of the spectrometer and excited by higher harmonics of the beamline [108].

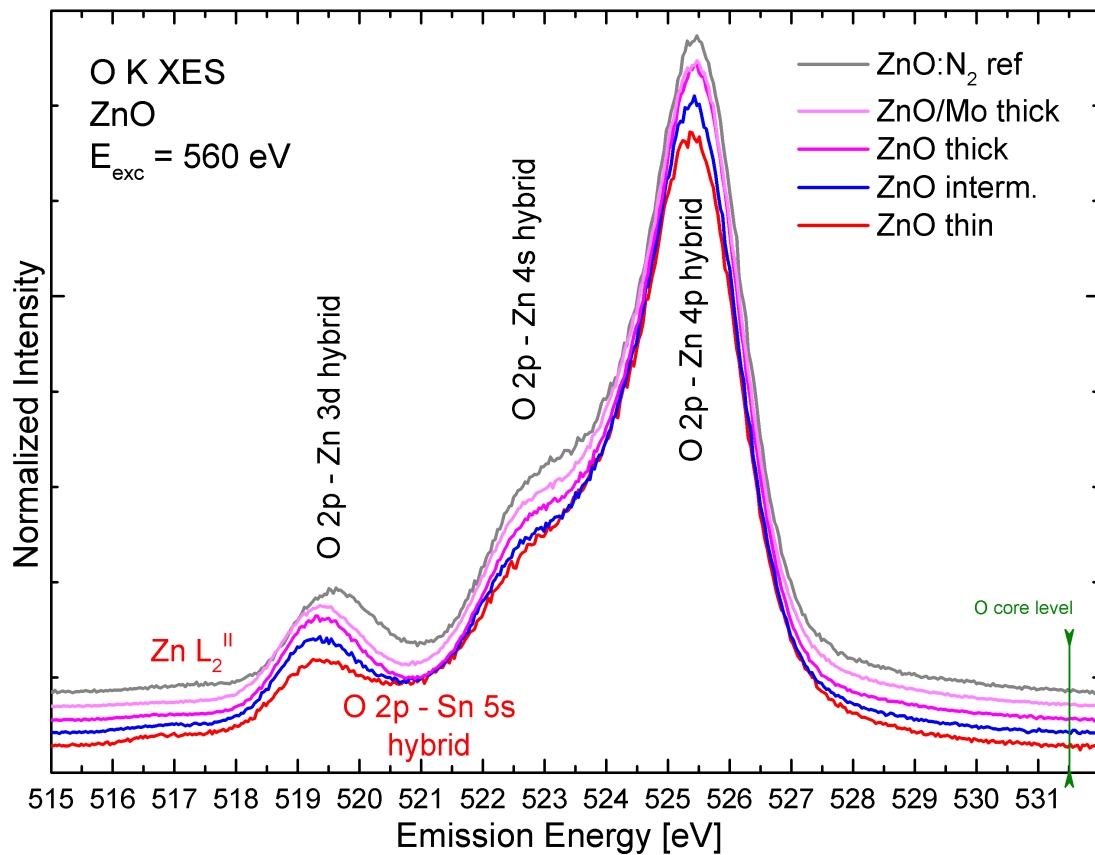


FIGURE 4.30: O K XES spectra of the ZnO series normalized to the main peak. The changes for thinner layers indicate that the CZTS has an effect on the ZnO buffer. Vertical offsets have been added for clarity.

#### 4.3.2.3 ZnO thickness

The calculated buffer thickness for all samples of the ZnO series is shown in figure 4.31. The signal intensities of thick buffer layers and bare CZTS were used as  $I_0$ , respectively, in equation 2.1. The values calculated from the decaying signal of the absorber give mostly consistent values whereas the values calculated from the buffer signal that builds up are mostly smaller, especially for measurements with Mg  $K_\alpha$  excitation. The error

margin is larger here, because Zn signals from the buffer overlap with the respective signals from the absorber and we find a  $\text{Zn}(\text{OH})_2$  surface layer that alters the signal from the ZnO buffer layer.

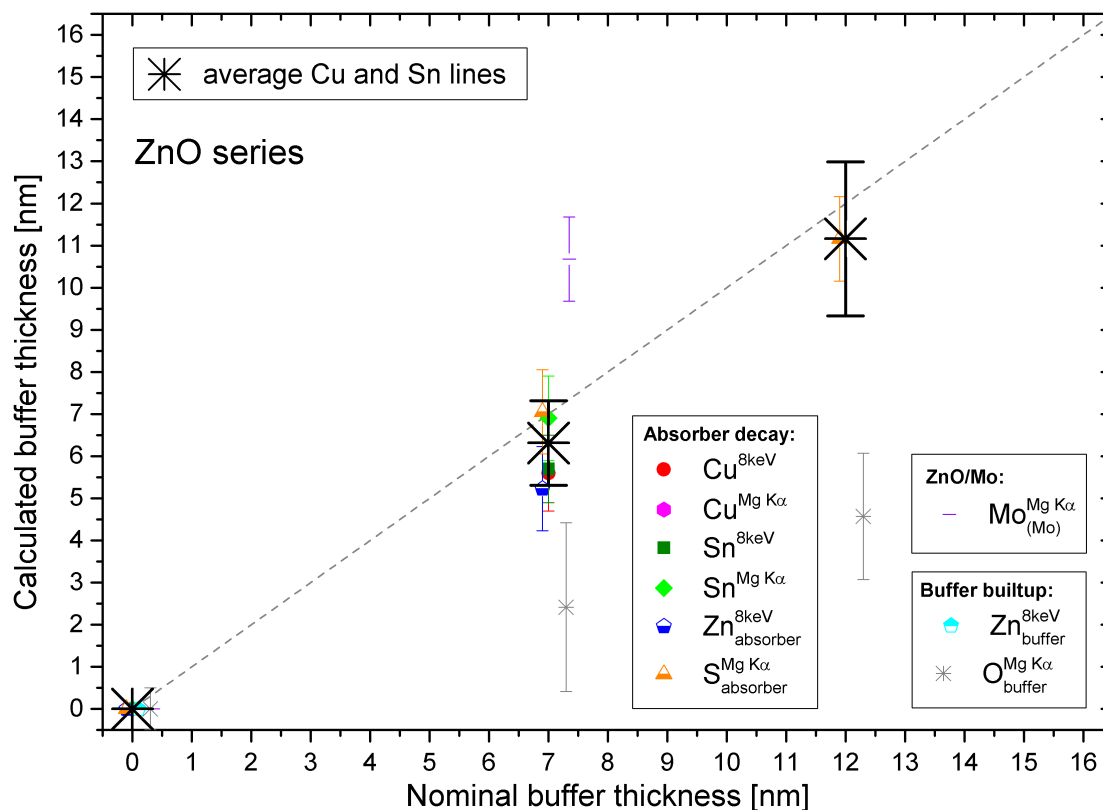


FIGURE 4.31: ZnO-buffer thickness calculated from all core levels. Included are the reference buffers grown on Mo. Thicknesses calculated from absorber lines are more reliable because they are less affected by surface  $\text{Zn}(\text{OH})_2$  and Further species of e.g. C and O. Averages are therefore calculated from Cu, Sn, and S signals that originate exclusively from the absorber. The dashed line is a guide to the eye.

The dashed line represents the expected growth rate of  $0.24 \frac{\text{nm}}{\text{cycle}}$  as reported in [103]. The ZnO growth follows this line for thin layers. The offset could indicate a delayed nucleation.

For *ZnO interm.* we have only one datapoint (Sn 2p) to calculate the thickness. This buried interface is at the border of the information depth, similar to *ZnS thick*. Within the increased error margin due to the  $\text{Zn}(\text{OH})_2$  surface species, we see the expected growth speed.

**Conclusion:** The examination of the chemical structure of the ZnO series suggests a buffer layer growing directly on the pure CZTS. We see effects on the O in XES but there is no indication for secondary phase formation or diffusion. The results will be used to compare to the mixed buffer in section 4.3.3, see page 60. We find an additional species that we attribute to  $\text{Zn}(\text{OH})_2$  that is formed from the  $\text{H}_2\text{O}$  in the ZnO precursor.



Due to high uncertainties in the Auger line fits compared to the Zn 2p fits and HAXPES measurements of Zn 3p core levels we assume a  $\text{Zn(OH)}_2$  that is mainly located at the sample surface.

### 4.3.3 $\text{ZnO}_x\text{S}_{1-x}$

#### 4.3.3.1 PES measurements

In the bare CZTS spectrum in figure 4.32 (black line) we see Cu, Zn, Sn, and S lines. The visibility of strong CZTS signals reveals that the thin and intermediate layers are very thin. In contrast, the signal of the thin ZnOS/Mo layer (brown line) shows significantly stronger Zn- and O-line intensities.

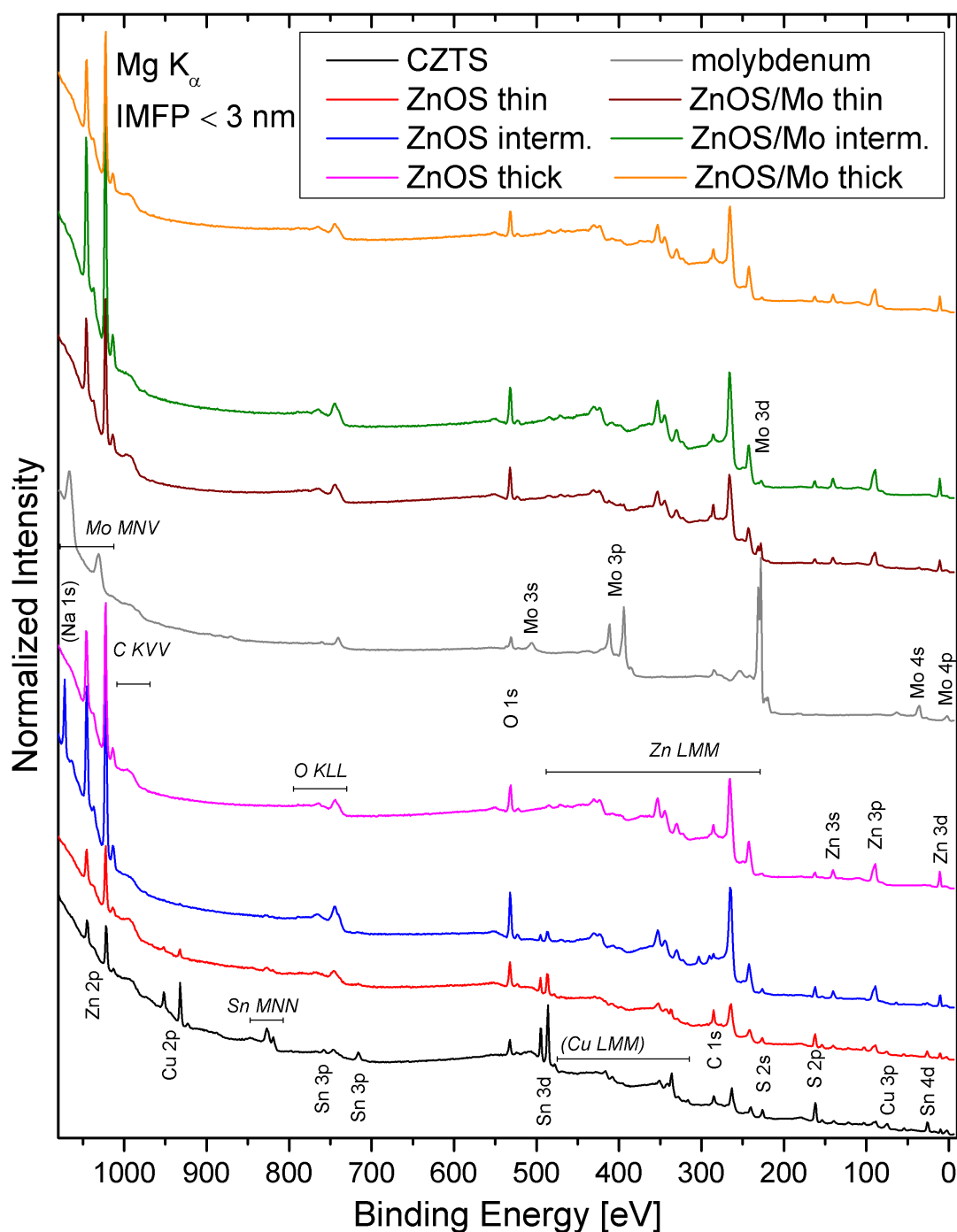


FIGURE 4.32: Survey spectra of all samples from the ZnOS series normalized in the flat region at 600 eV. Vertical offsets have been added for clarity.

From this observation we have to consider a slower nucleation and growth of ZnS on CZTS compared to Mo. All spectra show O and C signals that are discussed in section A.2.3 on page 154.

A more detailed picture can be seen in the shallow core level region (figure 4.33) with sharp shallow core levels of Cu, Zn, and Sn and broader S and O lines. These spectra, measured with 8 keV, exhibit a larger probing depth (see section 2.1.2) so all lines from buried material appear more pronounced compared to the cover layer signals that show stronger relative signals with Mg  $K_{\alpha}$ -excitation.

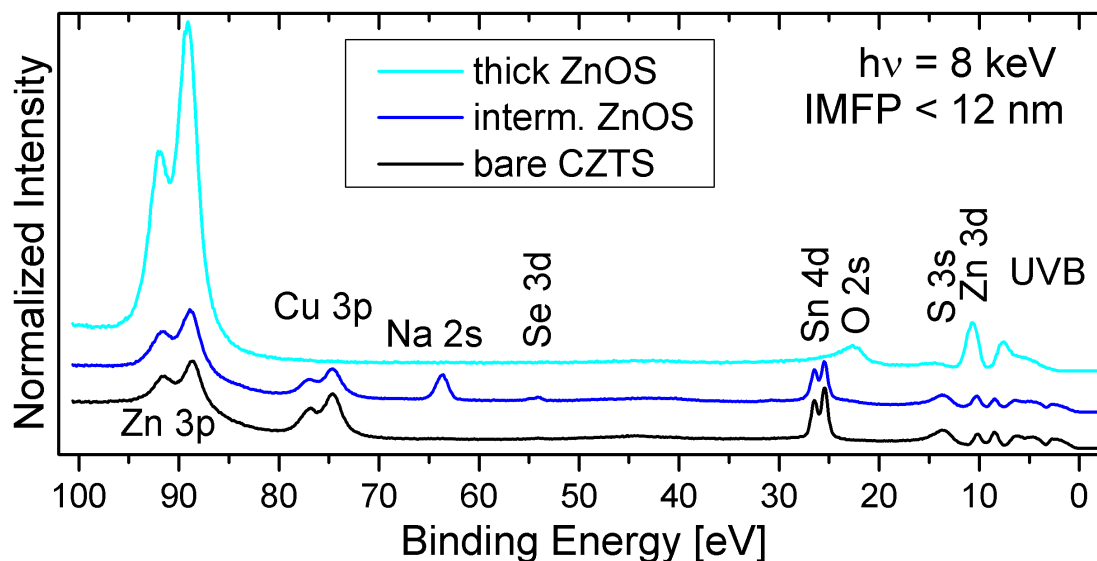


FIGURE 4.33: Shallow core level region spectra of selected samples measured with 8 keV and normalized in the flat region at 50 eV. Vertical offsets have been added for clarity.

**Core levels** are measured as detail scans. The IMFPs for photoelectrons are very similar in ZnO and ZnS (see page 150). We use the ZnO values for our calculations because we have a more O-rich and S-poor  $\text{ZnO}_x\text{S}_{1-x}$  compound ( $x \approx 0.9$  from precursor flux).

In the Cu 2p spectra in figure 4.34a we see that ZnOS grows slower than the binary buffers<sup>3</sup>. While *ZnS intermediate* (25 cycles) and *ZnO thin* (30 cycles) dim the signal from the underlying Cu in CZTS to a nearly flat line, we still see a Cu peak through *ZnOS intermediate* (35 cycles).

Measurements of the Cu 3p line at higher excitation energy of 8 keV reach down to the buried interface covered with thicker buffer layers as shown in figure 4.34b. The Cu 3p is spin-orbit split into two components. The thick ZnOS layer is thick enough to block the complete signal from the absorber but *ZnOS intermediate* allows for a strong signal of the buried CZTS to be captured.

<sup>3</sup>Figure 4.5a and 4.20a

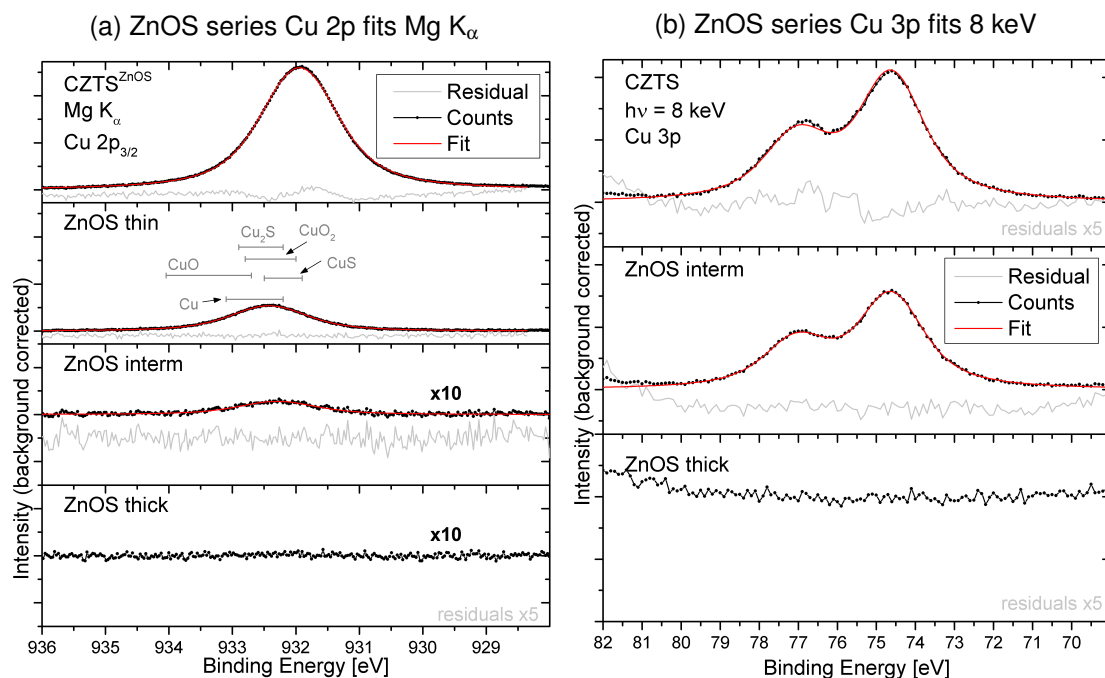


FIGURE 4.34: Cu  $2p_{3/2}$  and  $3p$  spectra measured with Mg  $K_{\alpha}$  and 8 keV excitation and fits. The residuals have been magnified for better visibility.

The Sn  $3d$  and  $4d$  signals<sup>4</sup> measured at Mg  $K_{\alpha}$  and 8 keV confirm the trends from the Cu measurements as shown in figure 4.35. The Sn  $4d$  overlaps with the oxygen ( $O 2s$ ) signal for the samples that contain significant amounts of oxygen as mentioned in the ZnO chapter<sup>5</sup>. The Sn fit does not perfectly match the measured signal. Small amounts of oxidized Sn can explain this, however, a multispecies fit does not yield a significantly better residual so we use this simplest model with only one fit contribution. We also have to consider the Na found particularly on the *ZnOS intermediate* sample and the sulfate species (see 4.46) that affects the  $O 2s$  background.

The Auger parameters in figure 4.36 repaint the picture seen in figure 4.7 on page 35. It will not be discussed again here. The Auger spectra are shown in figure A.2. We see stable CZTS for all samples.

In the ZnOS series we see a contribution from Se  $3d$  (green species, compare 64). The Se source is the furnace that has been used to anneal Se-kesterite samples before. The cleaning procedure was not sufficient to remove all the Se. However, this amount of Se is not playing a major role for the band alignment and will be neglected for further analysis. In the surface of the CZTS that was used for the ZnOS series which has been grown first after the furnace cleaning, we find less than 1.9% of the S to be replaced by Se. for *ZnOS thin* we find 0.46% Se. For the other CZTS surfaces we do not see any Se signal. These ratios were calculated from S  $2p$  and Se  $3p$  fit areas as shown in figure 4.37 using the photoionization cross sections of 17.46 and 28.39, respectively,

<sup>4</sup>The two spin orbit split components are summed up to a double peak

<sup>5</sup>see page 50

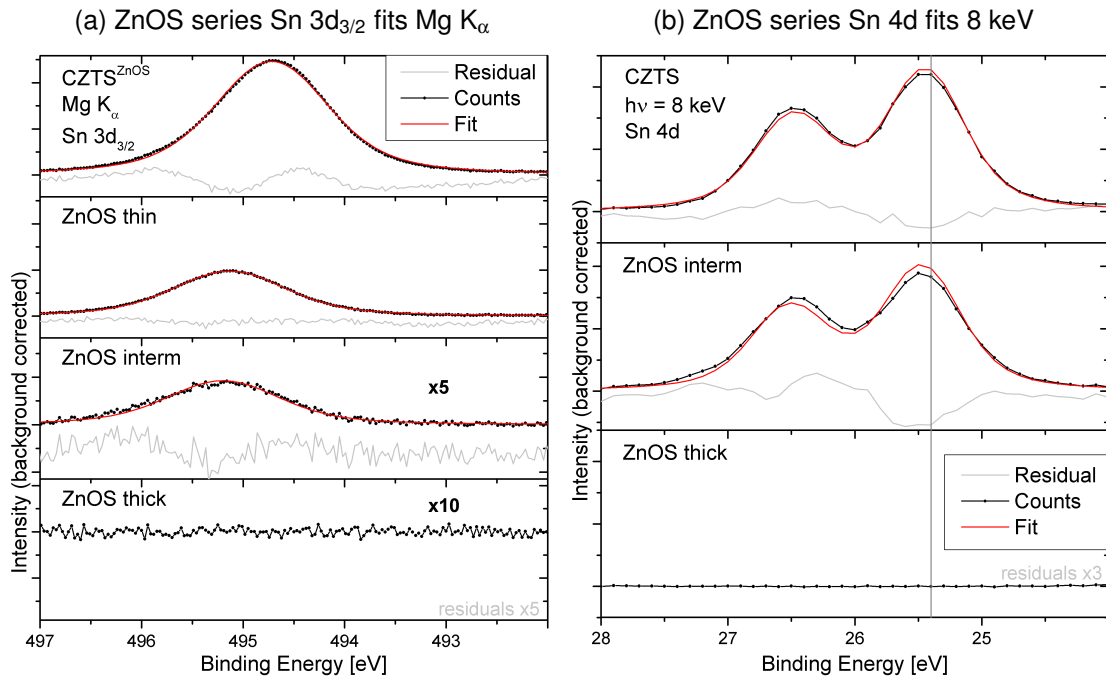


FIGURE 4.35: Sn  $3d_{3/2}$  and 4d spectra measured with  $\text{Mg K}\alpha$  and 8 keV excitation and fits. The residuals have been magnified for better visibility.

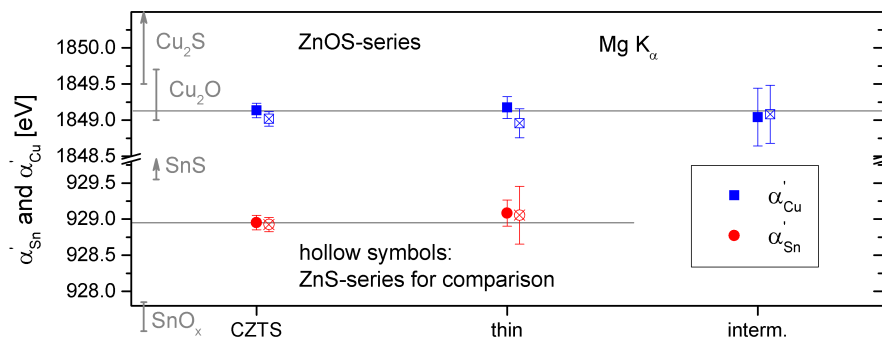


FIGURE 4.36: Modified Auger parameter  $\alpha'_{\text{Cu}}$  and  $\alpha'_{\text{Sn}}$  show that the chemistry of the absorber doesn't change after ZnOS deposition.

from an interpolation of values calculated following [109–111].

The S 2p lines of the reference layers on Mo in figure 4.37b show a clear S signal from the buffer material

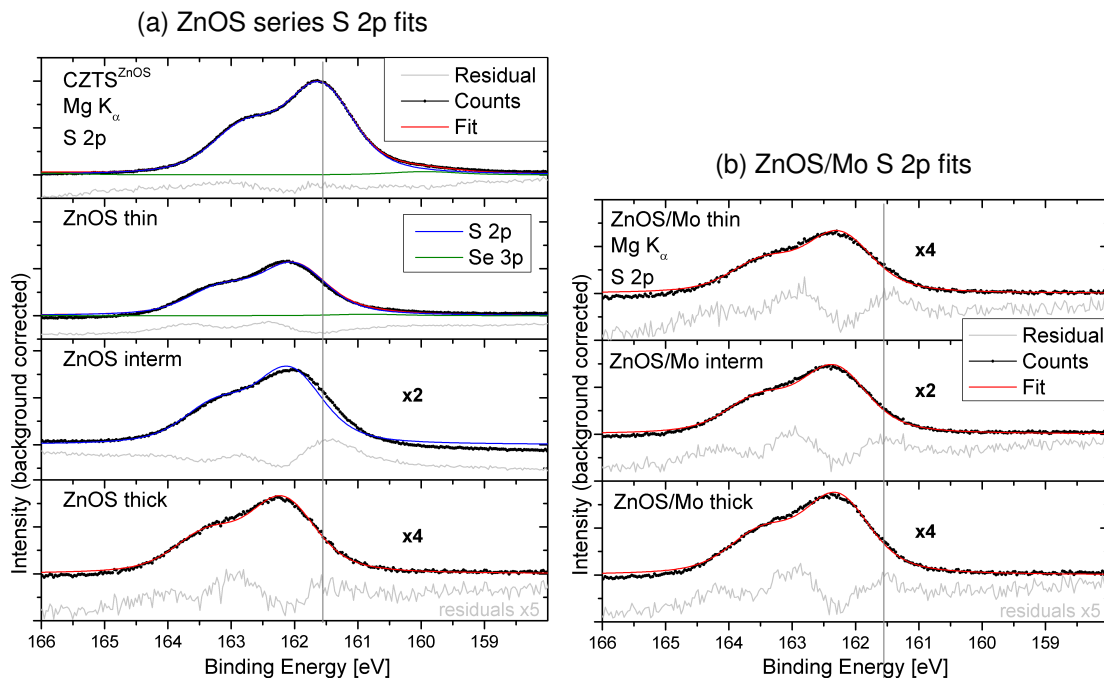


FIGURE 4.37: S 2p spectra of ZnOS measured with  $\text{Mg K}_\alpha$  excitation and fits. The residuals have been magnified for better visibility.

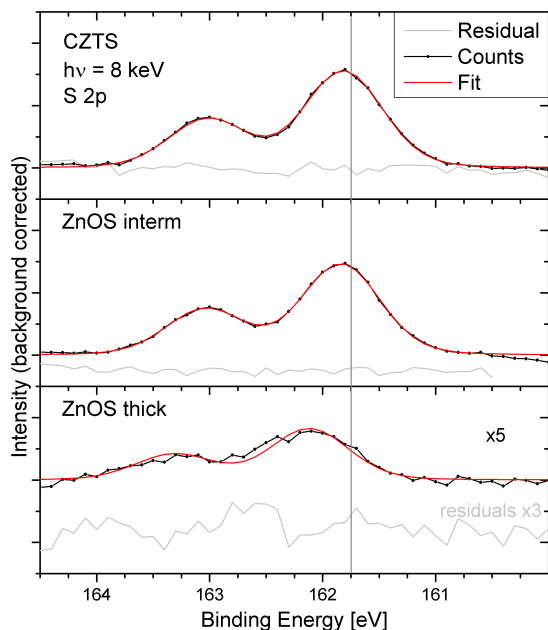


FIGURE 4.38: S 2p spectra measured with 8 keV excitation and fits. The residuals have been magnified for better visibility.

these spectra.

The S 2p spectra of ZnOS buffers (figure 4.37a) be fitted with one S species although we see deviations from the fit for the thin layers on CZTS. The relatively low S-content in ZnOS can already be seen from the lower S 2p line intensity if we compare the thick layers to bare CZTS. The thick ZnOS looks identical to the respective layer on Mo. The thin and intermediate ZnOS layer on CZTS show variations that cannot be clearly attributed to additional species. This indicates that S appears in a different chemical environment at the ZnOS/CZTS interface.

The previously mentioned sulfate signal appears outside the fitted window (compare figure 4.46). The HAXPES spectra of S 2p in figure 4.38 show a single signal. The spectral distortion is not observed for

The Zn 2p and Zn LMM fits of the ZnOS series (see figures 4.39a and 4.39b) show an evolution from the single-phase CZTS to a signal composed of two buffer-species. For thicker ZnOS layers these can be identified as a ZnOS compound that is close to the properties of pure ZnO and  $\text{Zn}(\text{OH})_2$ , a well known surface species of ZnO.

The identical buffer components are found in the ZnOS layers grown on Mo as shown in figure 4.40a and 4.40b. The  $\text{Zn}(\text{OH})_2$  contributes with about 27% to the measured Zn signal (see figure A.9 on page 157).

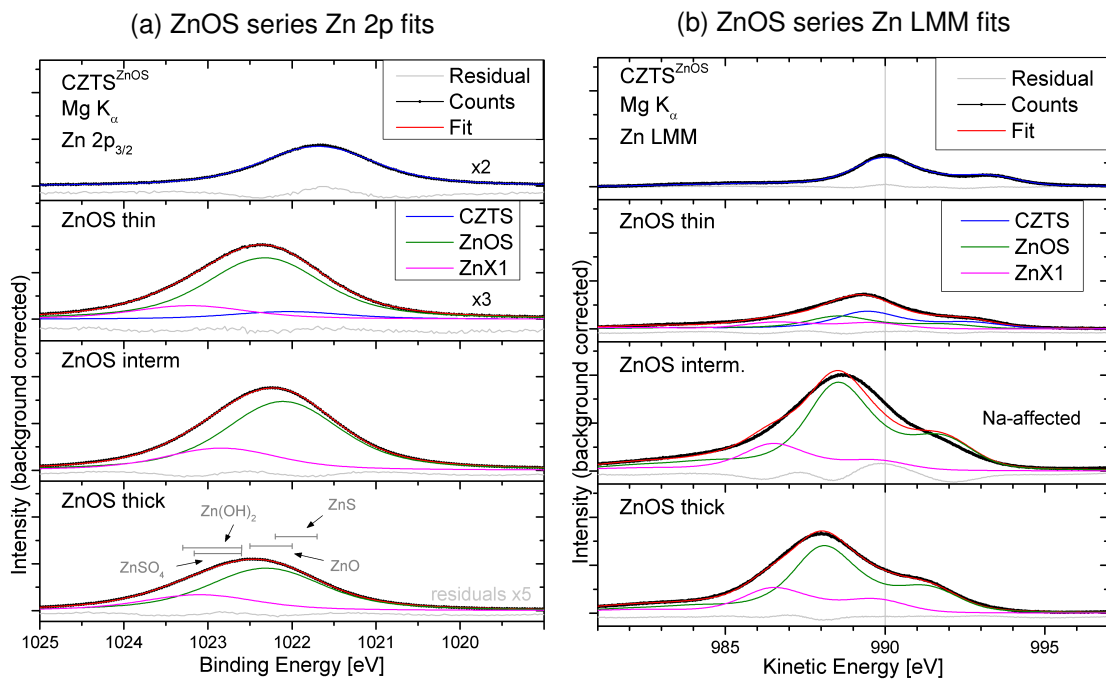


FIGURE 4.39: Zn  $2p_{3/2}$  and Zn LMM spectra of ZnOS/CZTS measured with Mg  $K_{\alpha}$  excitation and fits. The Zn 2p residuals have been magnified for better visibility.

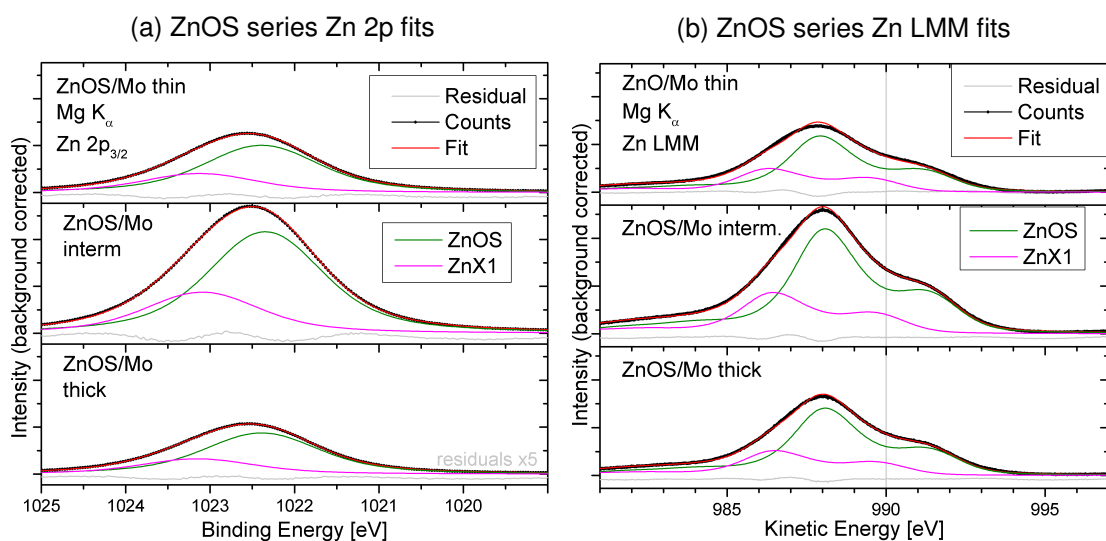


FIGURE 4.40: Zn  $2p_{3/2}$  and Zn LMM spectra of ZnOS/Mo measured with Mg  $K_{\alpha}$  excitation and fits. The Zn 2p residuals have been magnified for better visibility.

The **Wagner plot** in figure 4.41 shows the CZTS species and a dominant ZnOS species with  $\alpha'=2010.5(\pm 0.3)$  eV. This is slightly higher than the value seen for pure ZnO. As for pure ZnO, we see a  $\text{Zn}(\text{OH})_2$  species with  $\alpha'$  below 2010.0 eV.

*ZnOS intermediate* shows a Na signal. It cannot be resolved whether this is causing the shift along the iso- $\alpha'$  lines or whether this is an interface effect.

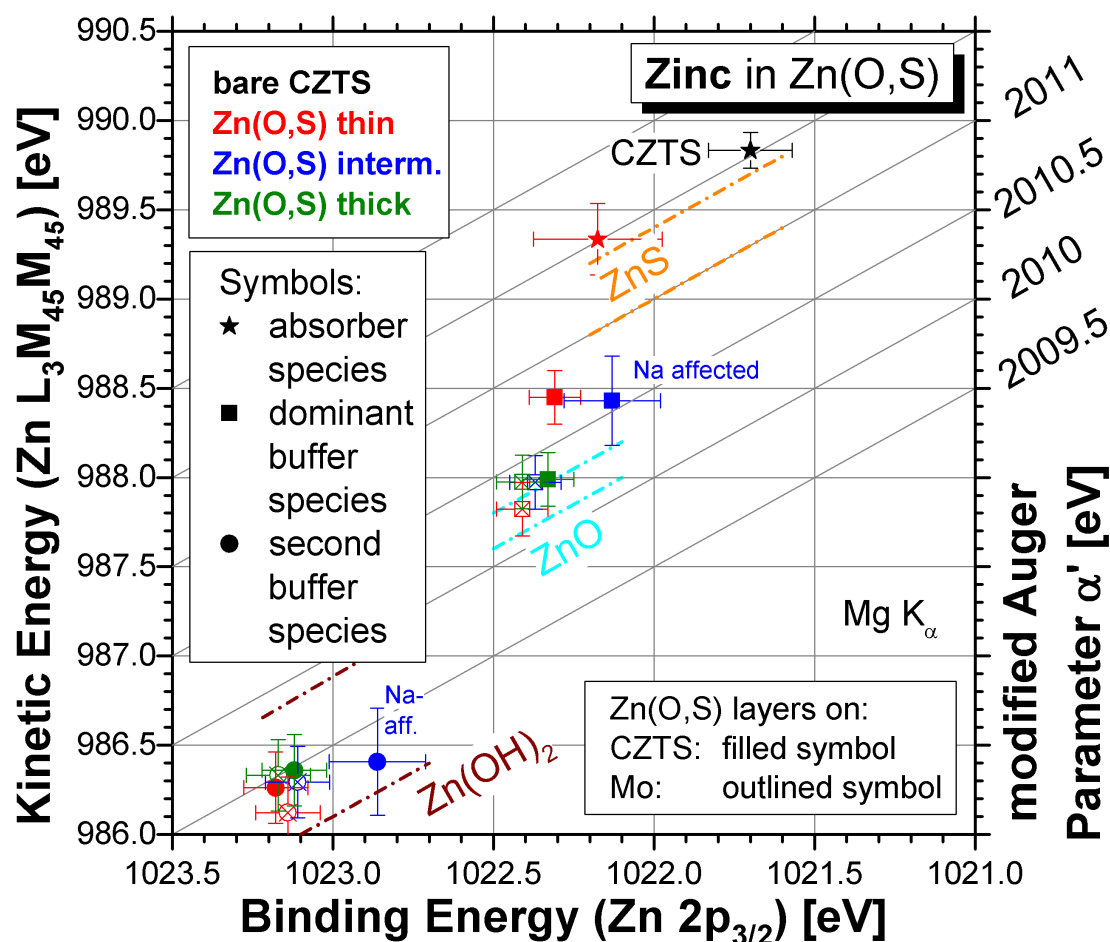


FIGURE 4.41: Wagner plot containing Zn  $2p_{3/2}$  and Zn  $L_3M_{45}M_{45}$  positions of all samples from the ZnOS series. Diagonal lines indicate identical  $\alpha'$ . Literature references for ZnOS, ZnO, and  $\text{Zn}(\text{OH})_2$  are in between the respectively labeled dashed lines.

The thin and intermediate layers grown on CZTS differ drastically from the respective layers on Mo and the thick layers, all being identical in speciation.

We see three species for *ZnOS thin*. The CZTS appears shifted around 0.5 eV ( $\pm 0.2$  eV) down on the iso- $\alpha'$  line. While the Zn 2p position did not show a significant change in line position, the Auger parameter reveals that we have a compound that is more like ZnS than like ZnO.

In *ZnOS intermediate* we do not find a CZTS species although a small signal might contribute to the Zn LMM spectrum with higher kinetic electron energy. A stronger effect is caused by Na in the sample surface since the Na KLL Auger line overlaps with the Zn LMM line. We could not fit an additional Na-line into the spectrum but the residual shows that the background has changed. The ZnOS and  $\text{Zn}(\text{OH})_2$  point of *ZnOS*



*intermediate* in the Wagner plot are shifted up the iso- $\alpha'$  line by 0.3 eV compared to all other samples. We consider this to be an effect of the Na in the surface.

The Auger parameter of the ZnOS species is located between the value from *ZnOS thin* and the other samples.

We can conclude a very S-rich and O-poor  $\text{ZnO}_x\text{S}_{1-x}$  to nucleate on CZTS (in contrast to growth on Mo) and incorporation of more and more O in the layer growth process.

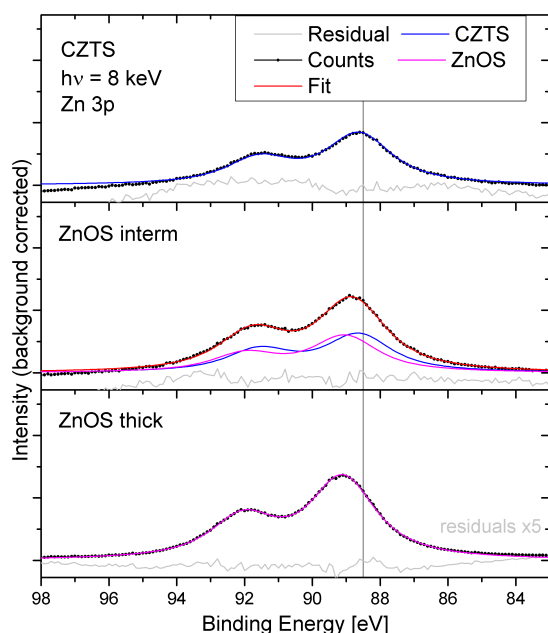


FIGURE 4.42: Zn 3p spectra measured with  $\text{Mg K}\alpha$  excitation and fits. The residuals have been magnified for better visibility.

found on all ZnOS buffer layers.

For *ZnOS thin* we see a very small increase in the actual buffer signal (blue line) while the increase in the region of  $\text{Zn(OH)}_2$  and adventitious oxygen (magenta line) is much stronger. This confirms the assumption of less oxygen in the buffer compound for the thinnest layer as seen from figure 4.41.

*ZnOS intermediate* shows clear signs of sulfate in the S 2p spectra<sup>6</sup>. The signature in the O 1s is displayed in green. The fit reveals a ZnOS signal and still a dominant  $\text{Zn(OH)}_2$  signal. Both are shifted to lower binding energy compared to the other samples in the series.

The two thick layers (on CZTS and Mo) are similar with a strong ZnOS and  $\text{Zn(OH)}_2$  signal. Towards thinner ZnOS/Mo layers the intensity of the ZnOS peak (blue line) decreases compared to the  $\text{Zn(OH)}_2$  species. This can also be seen for the samples on CZTS and supports the theory of a surface  $\text{Zn(OH)}_2$ . The bare Mo is discussed separately (page 154).

The oxidized Mo doesn't seem to appear in the spectrum of ZnOS/Mo thin. It must

Zn 3p lines measured with an excitation of 8 keV support the previous results. The fit was performed as described for the ZnS series. We can see the buried CZTS Zn-species (blue line) at the expected position at lower binding energy compared to the ZnOS species (magenta line).

The surface  $\text{Zn(OH)}_2$  is heavily reduced compared to XPS measurements which again speaks in favor of  $\text{Zn(OH)}_2$  as surface species.

The O 1s fits in figure 4.43a and b show two species, OX1 attributed to ZnOS (magenta line) and another being composed of  $\text{Zn(OH)}_2$  and adventitious oxygen species (blue line). We group these O species because adventitious oxygen that is found on the CZTS roughly matches the energetic position of the  $\text{Zn(OH)}_2$  peak that is

<sup>6</sup>see page 70, figure 4.46

contribute to the ZnOS signal since the Mo 3p spectra clearly show that the oxidized Mo is not reduced below the buffer layers.

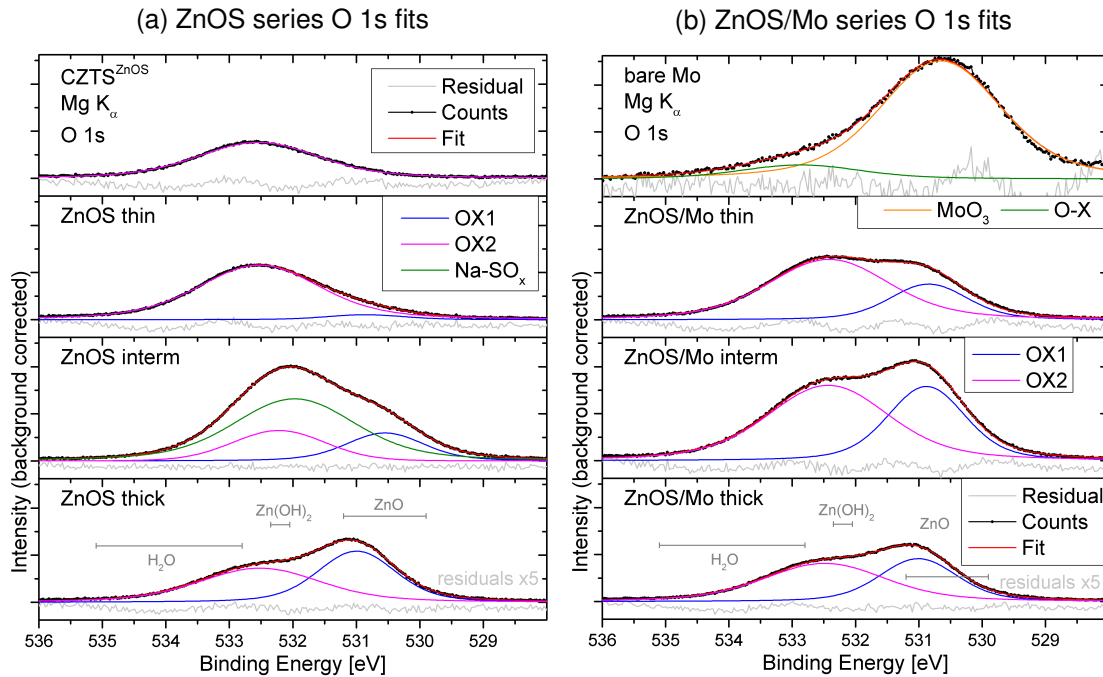


FIGURE 4.43: O 1s spectra of ZnOS/Mo measured with Mg  $K_{\alpha}$  excitation and fits. The residuals have been magnified for better visibility.

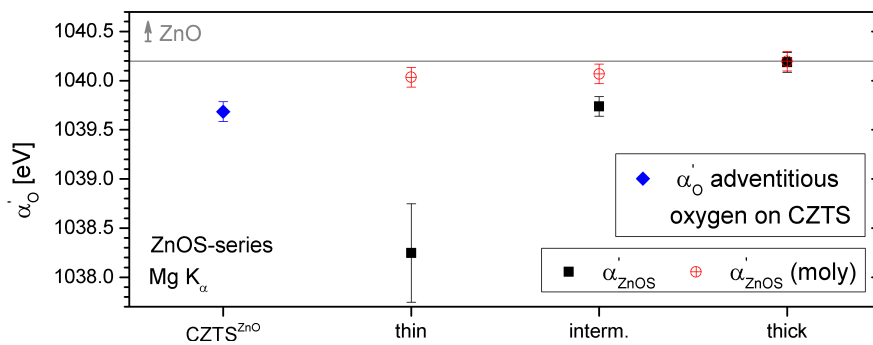


FIGURE 4.44: Modified Auger parameter ZnOS  $\alpha'_O$  shows clear chemical changes for thin ZnOS on CZTS

Combined with Auger lines shown on page 151 in figure A.1b we get the Auger parameters in figure 4.44. The value for CZTS represents adventitious oxygen. The layers on Mo show the same  $\alpha'_O$  we found for pure ZnO (figure 4.28) as well as the thick ZnOS on CZTS. For ZnOS thin [intermediate] we see a massively [slightly] reduced  $\alpha'_O$  supporting the previously mentioned change in buffer composition.

## 4.3.3.2 X-ray absorption and emission

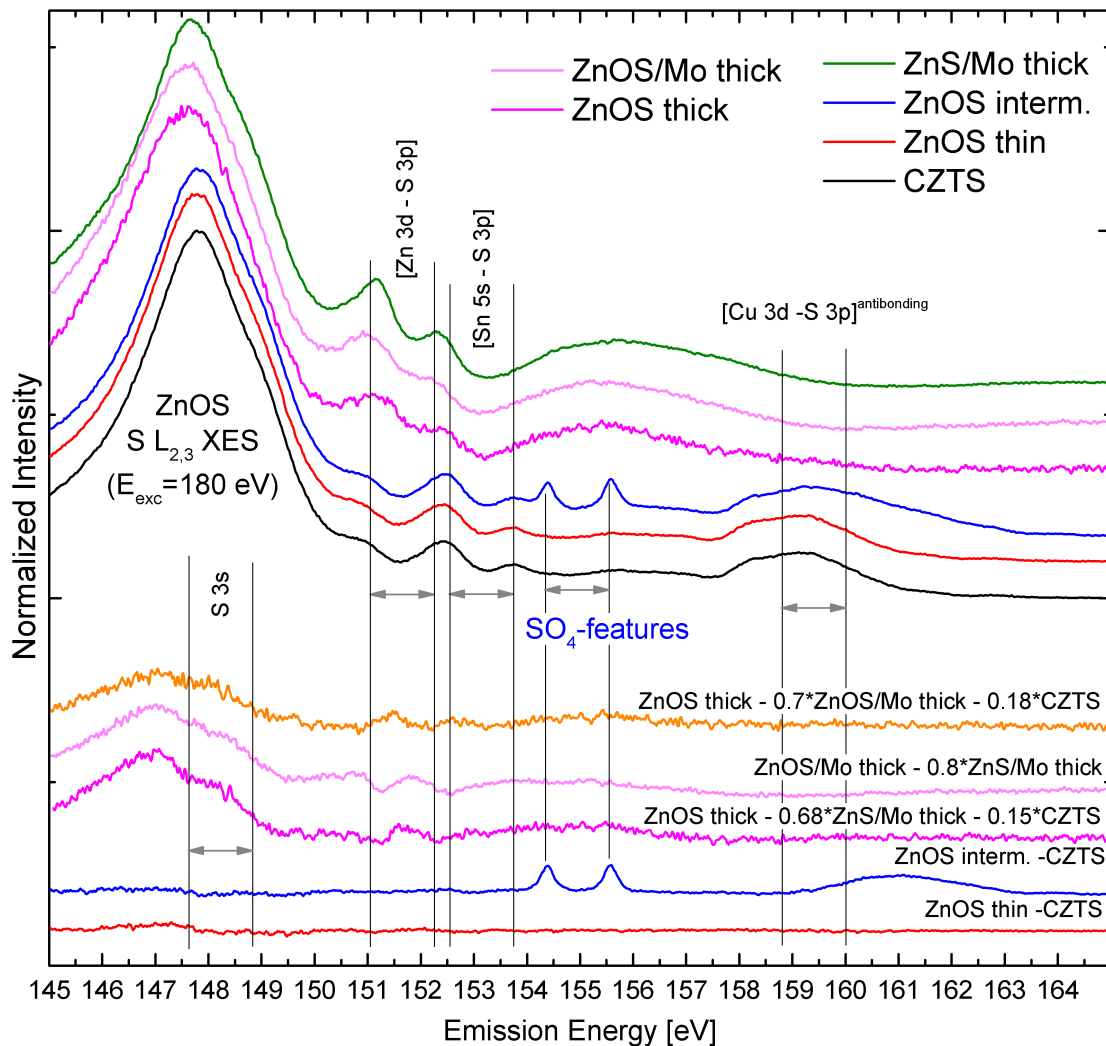


FIGURE 4.45: Spectral comparison of the  $\text{S L}_{2,3}$  XES spectra of the ZnOS series and  $\text{ZnS/Mo thick}$ , all normalized to the main peak. Vertical offsets have been added for clarity. The pure ZnOS spectrum ( $\text{ZnOS/Mo thick}$ ) resembles a noisy ZnS spectrum.

**XES spectra** measured at the S edge of ZnOS series (figure 4.45) reveal a high similarity between the CZTS spectrum and the thin layers, reproducing the findings for ZnS. The slow nucleation and slower growth speed causes the thin layers to have only minor effects on the spectra. Instead, the CZTS shape stays unchanged except for a little increase in noise. S-free ZnO (as shown) and hydroxide cover layers do not affect the XES measurements too much due to the high information depth ( $\approx 23$  nm). The difference spectrum of  $\text{ZnS thin}$  and the CZTS sample is completely flat. The same is true for  $\text{ZnOS intermediate}$  (blue line) except for a new feature that appears. Electronic states close to the Fermi level<sup>7</sup> also contribute to the spectrum. This is characteristic for sulfates. Closer inspection of the respective S 2p spectrum (red line) in figure 4.46 in comparison to  $\text{ZnOS thin}$  and  $\text{thick}$  shows a feature at 169 eV that proves the existence

<sup>7</sup>here visible close to the S 2p core levels around 161 eV

of sulfate in this sample.

We cannot explain the origin of this sulfate but it may be related to the high Na content we found on this sample. Na enhances the formation of sulfates [66], especially under x-ray illumination<sup>8</sup>.

If we focus on the analysis of the thick ZnOS layers we see similarities to the pure ZnS (green line) but less sharp Zn-related features. Difference spectra give a better idea about the contributions in the spectra. The Cu 3d-dominated region is a good indicator for the contribution of CZTS. The thick layer on CZTS can well be composed of the CZTS and ZnOS/Mo spectrum. Only very small remaining features close to the Zn 3d features remain along with a part of the broad S 3s feature.

The same sample can also be fitted using the CZTS and pure ZnS spectra with a near identical result.

If we also look at the difference spectrum of ZnOS/Mo and ZnS/Mo, we see that the only spectral difference is the ratio of the S 3s feature and the signal at higher emission energy. A ZnS layer can therefore not be identified if it is buried under a ZnOS layer. Even though we clearly see signal from the interface and the buried CZTS these XES investigation does not allow to detect a modified interface layer.

The O K emission edge in figure 4.47 shows that the oxygen is in contact with the CZTS as seen for the ZnO series (page 57). Differences to pure ZnO are not visible except for the high noise levels we see for thin ZnOS layers that indicate a very thin buffer. The shown range includes a Zn  $L_2^{\text{II}}$  feature of Zn  $L_2$  emission in second order that shows the presence of Zn independent of the bonding to O. For the bare CZTS this feature is visible but already small compared to the O-signal. After deposition of the O-rich precursor material, this feature disappears relative to the much stronger O K emission. So here, a clear statement about possible interlayers that contain Zn is impossible due to the very dominant O K emission.

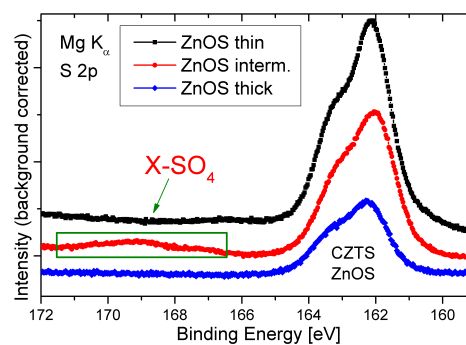


FIGURE 4.46: XPS sulfate signature. Vertical offsets have been added for clarity.

<sup>8</sup>Unpublished, private communication with M. Bär

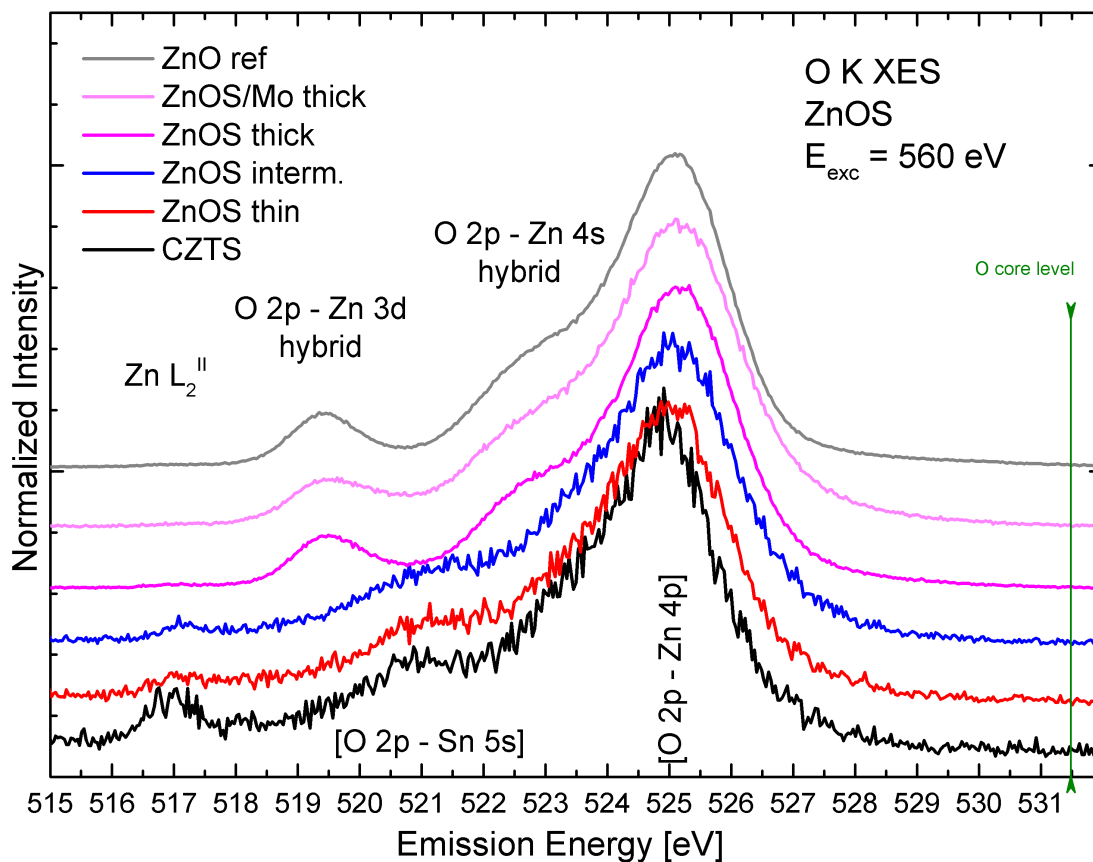


FIGURE 4.47: O K XES spectra of the ZnOS series normalized to the main peak. Vertical offsets have been added for clarity.

**XAS spectra** have been measured as described on page 158. All XAS spectra have been normalized to the edge jump, partly after linear backgrounds fitted to the plateau below the edge jump were subtracted. Vertical offsets between the spectra have been added for clarity.

The  $\text{Zn L}_3$  XAS spectra in figure 4.48 show clear differences between the thin ZnOS layers on CZTS and the thick layers far away from the junction. The spectra are dominated by the CZTS-shape for *ZnOS thin* and *intermediate* and do not indicate the presence of ZnO. Only the thick layers resemble the ZnO reference, especially in TEY (figure 4.48b) but the features are less pronounced.

A major difference to the ZnO reference is seen for thin ZnOS layers in both PFY and TEY. Feature (a), the strongest indicating feature for ZnS-type bonding, is increased for *ZnOS thin* compared to the CZTS. Also *ZnOS intermediate* shows feature a more pronounced than CZTS in PFY. In TEY, the more surface sensitive method, this feature is less pronounced, which indicates the formation of a less ZnS-like surface compared to *ZnOS thin*.

The less pronounced ZnS-features in the much more surface sensitive PFY spectra can be explained with the  $\text{Zn}(\text{OH})_2$  surface layer. The ZnS features are most pronounced for *ZnOS thin*, still visible for *ZnOS intermediate*, and cannot be seen in the spectra of the thick ZnOS layers.

The ZnO features (d) and (e) are less pronounced for the thick layers than in the ZnO reference and the respective ZnO layers.

In summary for these buffers with nominal thickness about 5 nm and 8 nm, which is easily enough layer thickness to dominate the measured spectra, we find no clear indication for ZnO-type Zn bonds but in contrast see spectra that resemble the respective ZnS layers (see figure A.12a) and the ZnS reference (light gray line). For thicker buffer layers the spectral shape changes towards the ZnO layers (see figure A.14a) and the ZnO reference (dark gray line).

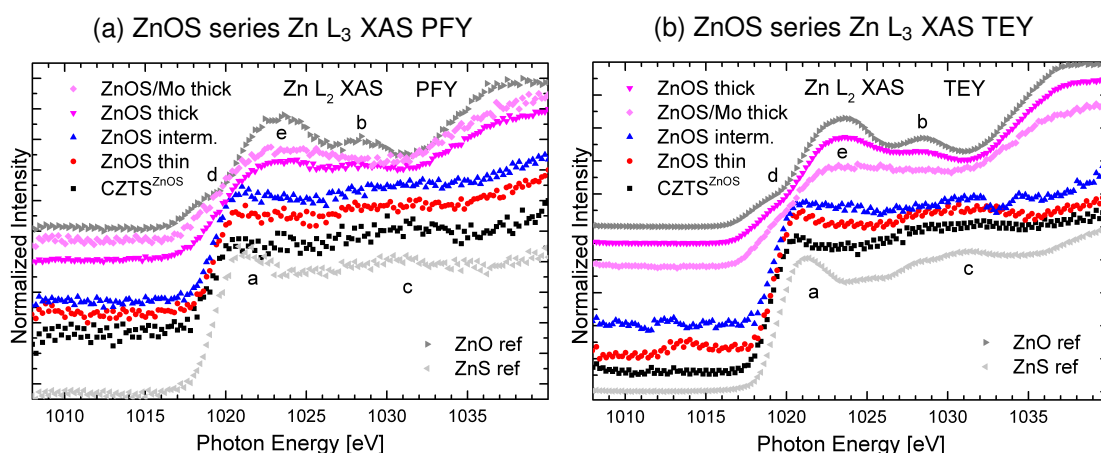


FIGURE 4.48:  $\text{Zn L}_3$  XAS spectra of the ZnOS series. A linear background has been subtracted.

The O K XAS in figure 4.49 shows no edge jump for thin ZnOS samples and CZTS but only a peak. This can only be explained if no significant ZnO layer has formed.

The comparison of PFY and TEY for thick layers shows that the signal from the surface near bulk region is identical to the surface. In TEY for *ZnOS intermediate* we see the starting formation of a ZnO-like compound, indicated by the formation of features a and b. This is in perfect agreement with the observation from Zn  $L_3$  XAS spectra.

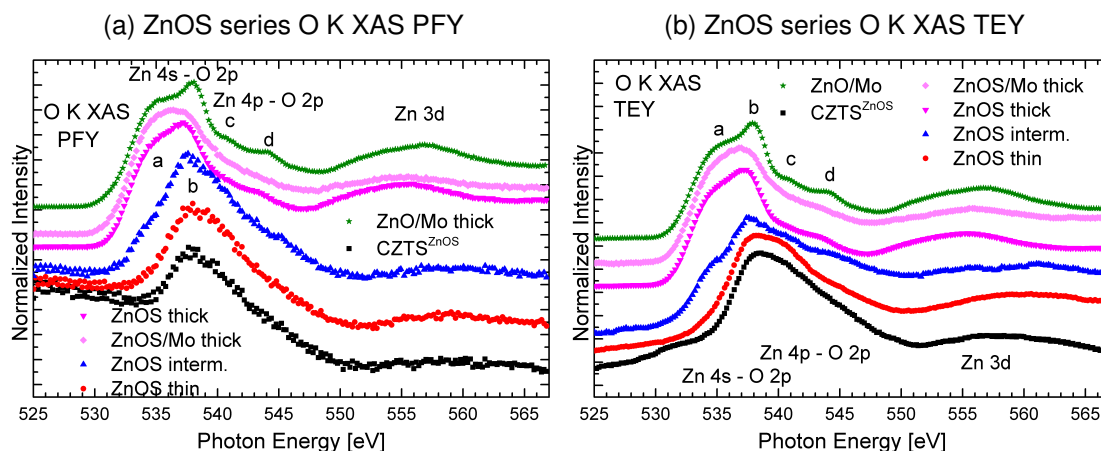


FIGURE 4.49: O K XAS spectra of the ZnOS series. A linear background has been subtracted.

The chemical environment of the S in the ZnOS buffers causes no structure or sharp features like in the ZnS reference in S  $L_{2,3}$  XAS as shown in figure 4.50. Compared to the better resolved ZnS spectra seen in figure A.10 (see page 158) we see no indication (i.e. feature (b)) for pure ZnS in this series. The ZnOS signal resembles the ZnO S  $L_{2,3}$  XAS from figure A.13b (page 160) that is exclusively caused by buried CZTS. This speaks in favour of a ZnO with partly substituted O by S. The feature b that would indicate the presence of ZnS could be hidden by the intensity from CZTS in the same energy region, especially if it is already weakened by the presence of small amount of oxides in the phase.

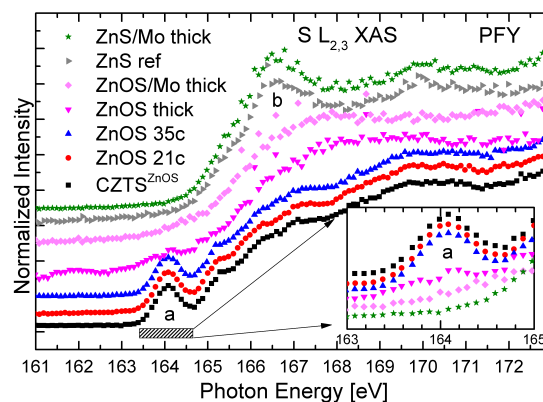


FIGURE 4.50: S  $L_{2,3}$  XAS spectra of the ZnOS series.

The Zn  $L_3$  and O K XAS spectra strongly indicate the presence of a ZnS-like interlayer and the absence of ZnO-like bonds in the initial stage of ALD-ZnOS growth on CZTS.

### 4.3.3.3 ZnOS thickness

The calculated buffer thickness for all samples of the ZnOS series is shown in figure 4.51. The signal intensities of thick buffer layers and bare CZTS were used as  $I_0$ , respectively, in equation 2.1. The values calculated from the decaying signal of the absorber give mostly consistent values whereas the values calculated from the buffer signal that builds up are mostly smaller, especially for measurements with  $\text{Mg K}\alpha$  excitation. The error margin is larger here, because Zn and S signals from the buffer overlap with the respective signals from the absorber and we find a  $\text{Zn(OH)}_2$  surface layer that alters the signal from the ZnOS buffer layer.

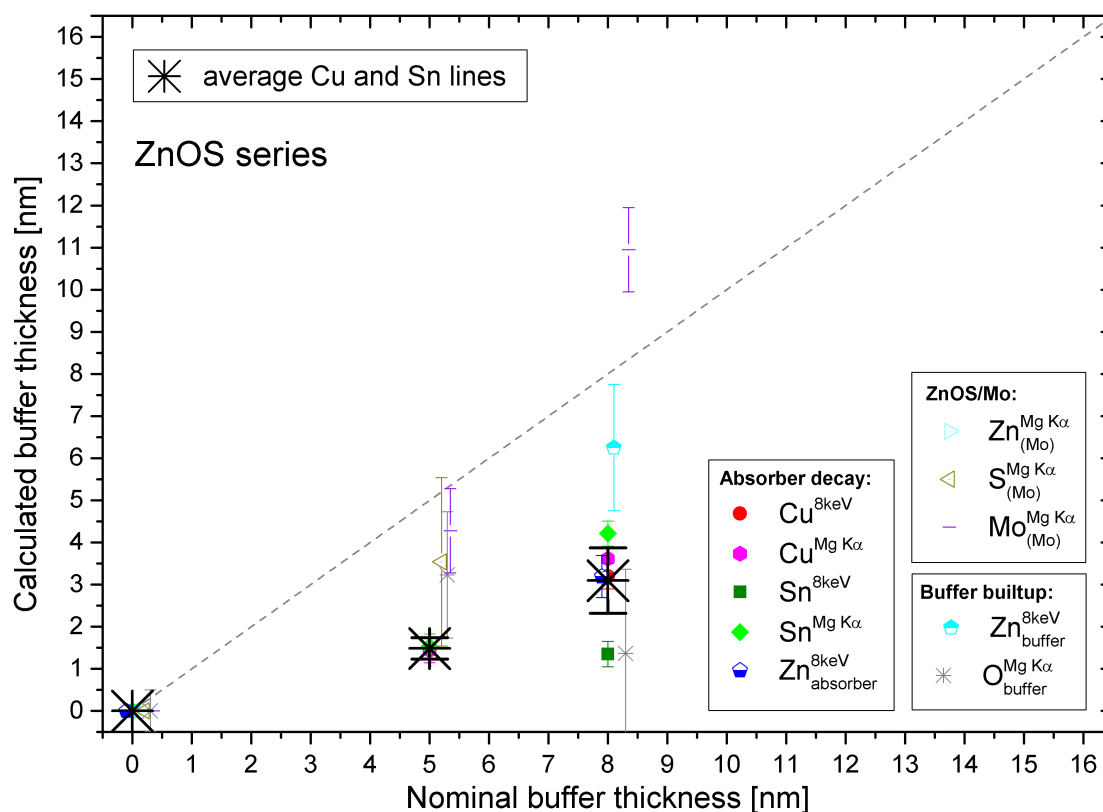


FIGURE 4.51: ZnOS-buffer thickness calculated from all core levels. Included are the reference buffers grown on Mo. Thicknesses calculated from absorber lines are more reliable because they are less affected by surface  $\text{Zn(OH)}_2$  and further species of e.g. C and O. Averages are therefore calculated from Cu and Sn signals that originate exclusively from the absorber. The dashed line is a guide to the eye.

The dashed line represents the expected growth rate of  $0.24 \frac{\text{nm}}{\text{cycle}}$  as reported in [103] for the exact same material growth. The ZnOS growth does not follow this line for thin layers. We know from [103] that the growth speed reaches in average the given expected growth rate when growing to the device relevant thickness of 16 to 33 nm. The growth speed is therefore expected to increase after the initial stage of the buffer deposition that we have observed here. We already see an increase in growth speed after our first measurement point at 5 nm nominal thickness.



The identical buffer grown directly on Mo shows a faster growth in the observed range. This significant nucleation effect of the ZnOS compound on the CZTS surface corresponds well with our assumption of S-rich ZnOS growth with decreasing S-content while the layer is getting thicker. The low S-supply (1 growth cycle out of 7 contains S) slows the growth speed down during the first growing nanometers of buffer material of the ZnO precursor material is not or only partly incorporated. Later, with full incorporation of the incoming oxygen and sulfur precursors, the growth speed will reach or even exceed the expected  $0.24 \frac{\text{nm}}{\text{cycle}}$ .

### 4.3.4 Reaction enthalpies and conclusion

If we compare reaction enthalpies of possible interface compounds<sup>9</sup> as shown in table 4.3, we see that first of all the values for CZTS differ a lot. The experimental value [112] is valid for the surface since it was determined by sputtering off a CZTS surface. The DOS calculations are done for bulk material in this order [113, 114]. Further standard values are obtained from [115] and theoretically approved by [116].

TABLE 4.3: Reaction enthalpies of CZTS and related compounds. For CZTS we see a very high experimental value obtained by sputter rate analysis [112] and two DOS calculation values [113, 114]. All values are also given per atom for easier comparison.

$\Delta H_f \left[ \frac{-\text{kJ}}{\text{mol}} \right]$	Cu	Zn	Sn	CZTS	from
$-\text{O}_{1/2}$	84			930	sputter rate analysis [112]
$-\text{S}_{1/2}$	41			337	DOS calculation [113]
$-\text{O}_1$	158	349	286	406	DOS calculation [114]
$-\text{S}_1$	54	207	110		
$-\text{O}_2$			570		
$-\text{S}_2$			153		

$\Delta H_f \left[ \frac{-\text{kJ}}{\text{mol}\cdot\text{atom}} \right]$	Cu	Zn	Sn	CZTS	from
$-\text{O}_{1/2}$	56			116	sputter rate analysis [112]
$-\text{S}_{1/2}$	27			42	DOS calculation [113]
$-\text{O}_1$	79	175	143	51	DOS calculation [114]
$-\text{S}_1$	27	104	55		
$-\text{O}_2$			190		
$-\text{S}_2$			51		

We assume a CZTS- $\Delta H_f$  in the range of the calculated value  $\left(406 \frac{-\text{kJ}}{\text{mol}}\right)$  to be most useful to compare to the enthalpies of other compounds. The stable CZTS phase that with the tendency to decompose requires an (absolute)  $\Delta H_f$ - value per atom for CZTS that is above the sum of the respective  $\Delta H_f$  for the binaries but still close enough to make decomposition possible with e.g. changed composition.

In an O-free case, the highest  $\Delta H_f$  per atom is found for ZnS and SnS while Cu-S-compounds have a lower  $\Delta H_f$ . In sum, ZnS, SnS, and two CuS will have a summed up formation enthalpy of  $406 \frac{-\text{kJ}}{\text{mol}}$  which is approximately the same as the  $406 \frac{-\text{kJ}}{\text{mol}}$  calculated in [114].

CZTS is supposed to be stable at 200°C [48] which is well above the the ALD temperature of 120°C. A secondary ZnS phase or ZnS buffer is therefore expected to show no chemical interaction with the CZTS.

The oxides of the involved metals show relatively high  $\Delta H_f$ , suggesting an O-sensitive surface. Cu-O bonds are not likely to form if we consider higher (absolute) enthalpy for Sn- and Zn-oxides. This is in agreement with our findings of chemically mostly inert Cu in CZTS.

<sup>9</sup>All standard enthalpy values are at 25°C, 1 molar concentration, and 1 atmosphere of pressure.

ZnO as buffer could have two effects:

Firstly oxygen bonds may form on the CZTS surface, especially to Zn and Sn atoms. Secondly the ZnO precursor could react with excess S from the CZTS surface. Considering the lower  $\Delta H_f$  of ZnS compared to ZnO, this is not a favourable reaction to occur. The growth of ZnOS on CZTS must be dominated by the nucleation. Nucleation of ZnO on a CZTS-surface is, according to our findings, not favourable in the presence of competing S, resulting in the formation of a ZnS interlayer. This explains, how the low concentration of sulfur in the  $\text{ZnO}_x\text{S}_{1-x}$ -ALD-precursor dominates the first phase of the buffer growth while the ZnO-precursor gets mostly lost in the system.

The formation enthalpy of  $\text{Zn}(\text{OH})_2$  is tabulated as  $642 \frac{\text{kJ}}{\text{mol}}$  (or 130 per atom) [117]. This supports the stability of a  $\text{Zn}(\text{OH})_2$ -layer at room temperature.

**Conclusion:** We find an unchanged CZTS surface in this series which has a profound effect on the  $\text{ZnO}_x\text{S}_{1-x}$  growth. Instead of a constant composition throughout the buffer thickness, we find S-rich material growing directly on the CZTS. The composition then gradually changes towards the O-rich  $\text{ZnO}_x\text{S}_{1-x}$  that forms the main part of the buffer layer. This effect makes it harder to adapt a  $\text{ZnO}_x\text{S}_{1-x}$  buffer to the needs of a kesterite-based solar cell. Even ideal  $\text{ZnO}_x\text{S}_{1-x}$  buffers cannot be grown directly on CZTS because this will massively alter the buffer composition.

### 4.3.5 Buffer thickness comparison

The averaged buffer thickness for all samples in the three series is shown on a growth-cycles scale in figure 4.52 to illustrate the deviation from the expected growth rate of  $0.24 \frac{\text{nm}}{\text{cycle}}$  as reported in [103].

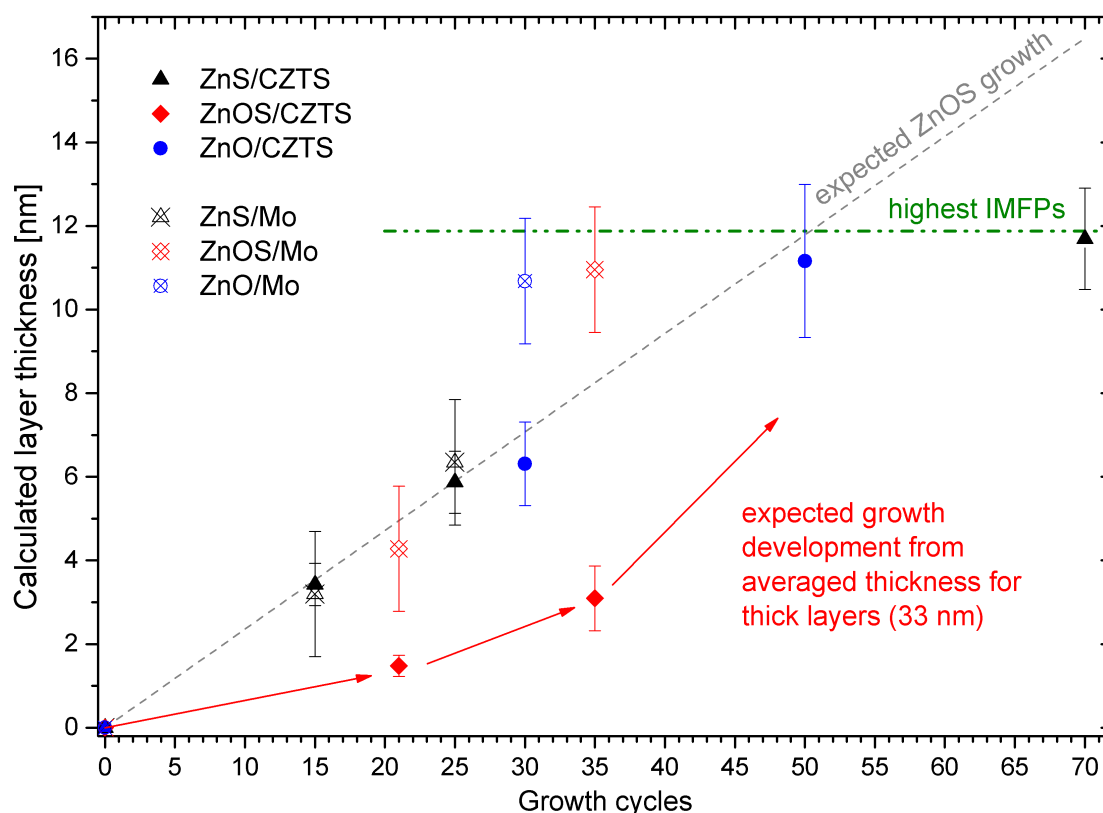


FIGURE 4.52:  $\text{ZnO}_x\text{S}_{1-x}$ -buffer thickness averaged from most reliable absorber core levels. Included are the reference buffers grown on Mo.

The ZnS growth doesn't show any differences between CZTS and Mo as substrate and follows the expected growth speed.

ZnO/CZTS also stays in the expected range within the errorbars. The growth on Mo (with only one data point) is faster.

ZnOS/Mo grows very similar to ZnO/Mo, exceeding the expected growth speed.

In contrast, the thin layers of ZnOS/CZTS show significantly smaller thickness. We explain this with preferred ZnS nucleation on CZTS, where the low S-supply (1 growth cycle out of 7 contains S) causes a significantly reduced growth speed while the incoming ZnO precursor is lost from the sample surface. After incorporation of an increasing amount of O into the growing ZnS layer, the growth speed recovers to expected  $0.24 \frac{\text{nm}}{\text{cycle}}$ .

#### 4.4 Electronic structure of the $\text{Cu}_2\text{ZnSnS}_4$ - $\text{ZnO}_x\text{S}_{1-x}$ - interface

The shallow core level region in figure 4.53 shows features of most elements that we have discussed previously. The spectra have been shown separately in 4.4,4.19 and 4.33. A  $\text{SnO}_2$  spectrum is used to quantify the Sn background in the region around 90 eV.

We see Zn and Cu 3p lines that are overlapping with this broad Sn 4p background. Due to the relatively low contribution and flat shape, combined with a multiphase Sn in the reference as obtained from peak fit analysis that brings additional differences between the measured background and the hidden background in CZTS, the best choice is to neglect this background signal in the Zn and Cu 3p fits in section 4.3.

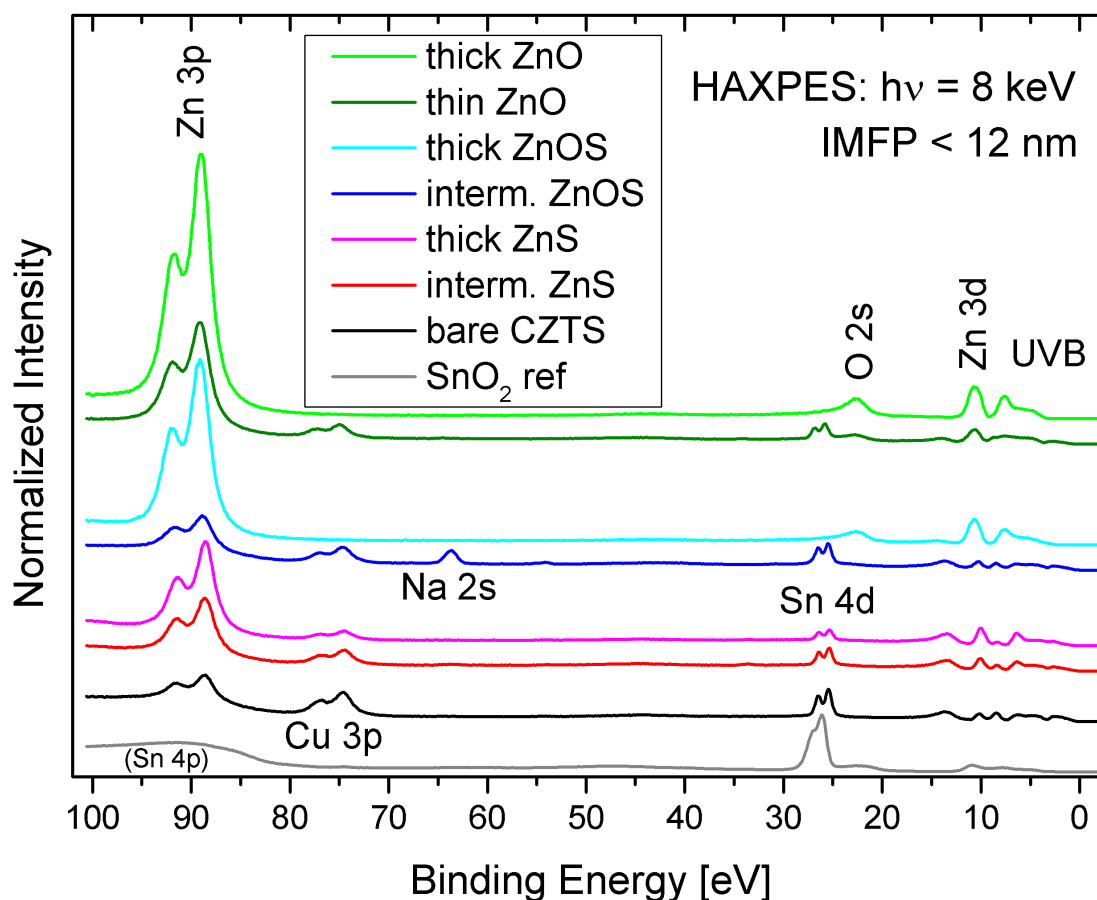


FIGURE 4.53: Shallow core level region of selected samples measured at 8 keV and normalized to the intensity at 100 eV. Vertical offsets have been added for clarity. The  $\text{SnO}_2$  is used to eliminate the Sn 4p background below the Zn 3p and Cu 3p peaks for line fits.

We see signature lines of CZTS in the thin and intermediate layers. The sodium on  $\text{ZnOS}$  *interm.* is visible, too.  $\text{ZnO}$  and  $\text{ZnOS}$  *thick* show a pure buffer signal but  $\text{ZnS}$  *thick* clearly shows Sn and Cu peaks. We therefore extract the ZnS signal from this

spectrum as shown in figure A.17, resulting in the spectrum "ZnS corrected" that is used as best representation of a pure ZnS.

#### 4.4.0.1 VBM composition and comparison to theory

The VB composition of the separate layers involved in our studies can be revealed with comparison of the VB spectra of bare CZTS and buffer materials to theoretical predictions.

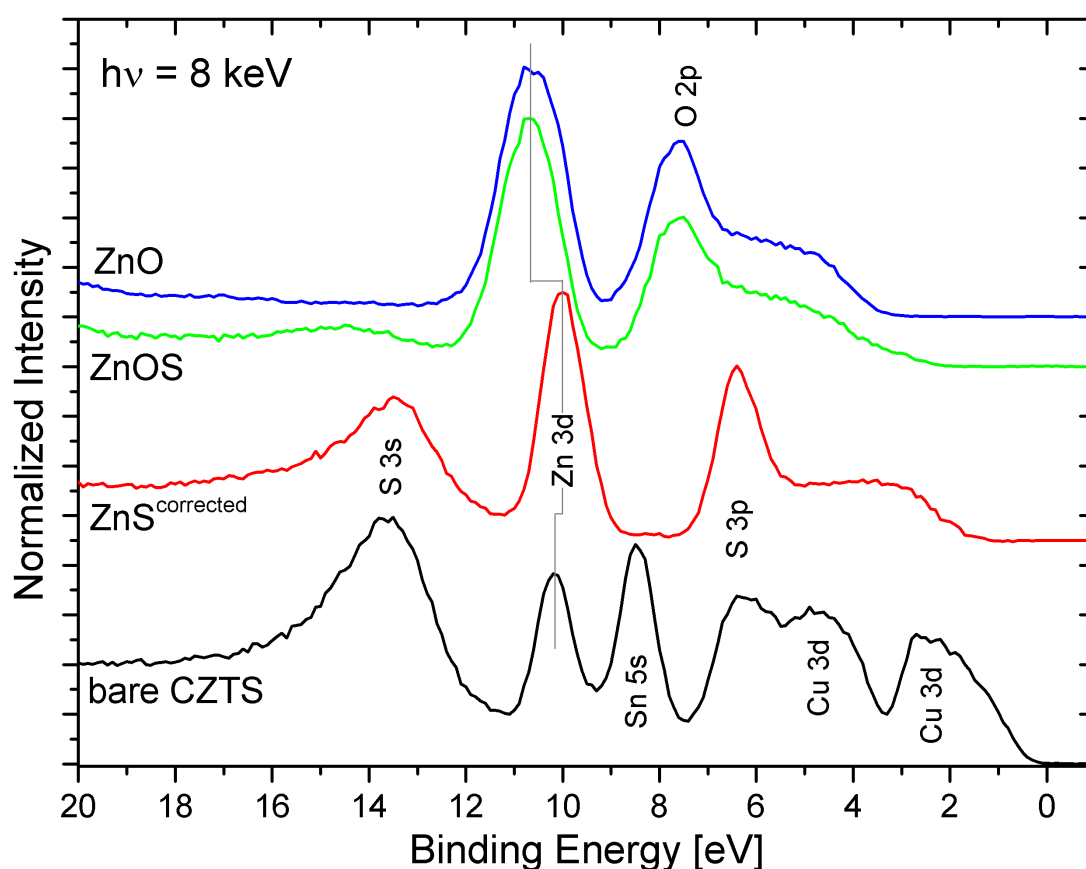


FIGURE 4.54: Upper VB of CZTS and pure buffer materials measured at 8 keV and normalized to the highest spectral feature. Vertical offsets have been added for clarity.

The valence band structures of the thick buffers (figure 4.54) all show a dominant Zn 3d feature. Electronic states have been identified using VB-states observed in XES and XAS including the respective references and others [118, 119]. In the valence band we find delocalized VB-states, however, the dominant contributions to the density of states can be identified. For ZnO, mainly the O 2p with a shoulder on the low binding energy side defines the VBM. For ZnOS an additional broad S 3s feature appears around 14 eV and S 3p is changing the shape of the shoulder up to the VBM, narrowing the band gap. This S 3p is the dominant line for the ZnS VBM, too. In ZnS the Zn 3d and a strong S 3s appear at lower binding energy compared to the other buffer layers.

CZTS combines the ZnS lines with Sn 5s and Cu 3d features. The VBM is composed of S 3p and Cu 3d lines as theoretically predicted [120–122].

In figure 4.55 our HAXPES VBM is combined with VBM spectra from the literature<sup>10</sup>. We see that HAXPES can resolve the CZTS valence band structure in agreement with more bulk sensitive resonant XES measurements at the S  $L_3$  edge from [123]. Mind that the HAXPES energy scale is shifted by 0.24 eV to define the VBM  $\hat{=}$  0 (instead of  $E_F=0$ ). Theoretical calculations using  $G_0W_0$  [120] come closer to predicting the experimental line positions than others (e.g. [121]) but are still only correct very close to the VBM (here about 6 eV). Different scattering cross sections and signal yields including forbidden transitions cause significant changes in shape of the shape between HAXPES and XES results. The direct attribution of calculated PDOS does, however, help to understand the valence band composition.

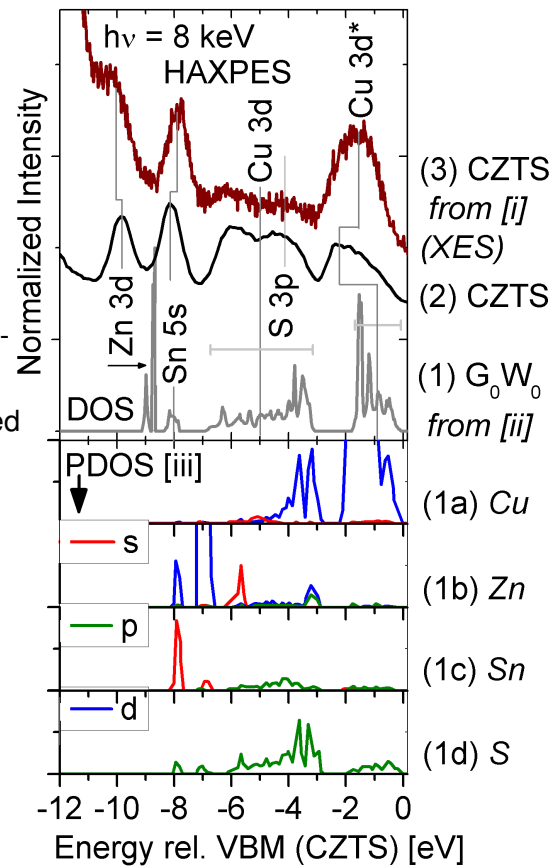


FIGURE 4.55: Valence band maximum of CZTS measured with HAXPES and XES and theoretically calculated<sup>10</sup>. All intensities have been normalized to comparable standard. Vertical offsets have been added for clarity.

<sup>10</sup> i $\hat{=}$ [123], ii $\hat{=}$ [120], iii $\hat{=}$ [121]

### 4.4.1 Spectral shifts and band bending

Core level shifts have been calculated by subtracting the respective peaks positions in binding energy. The position from the bare CZTS sample was subtracted for absorber shifts and the position of the respective thick buffer layer for buffer shifts. Positive shifts consequently represent a higher binding energy at the interface, which is a downwards band bending. The shifts are shown with negative Y-scale so upwards band bending goes up and vice versa. The calculated buffer thickness scale shows the bare CZTS on the left hand side and the thickest measured layers on the right. Average values have been calculated from Cu and Sn shifts for the buffer layers and from all reliable position shifts for the buffer layers.

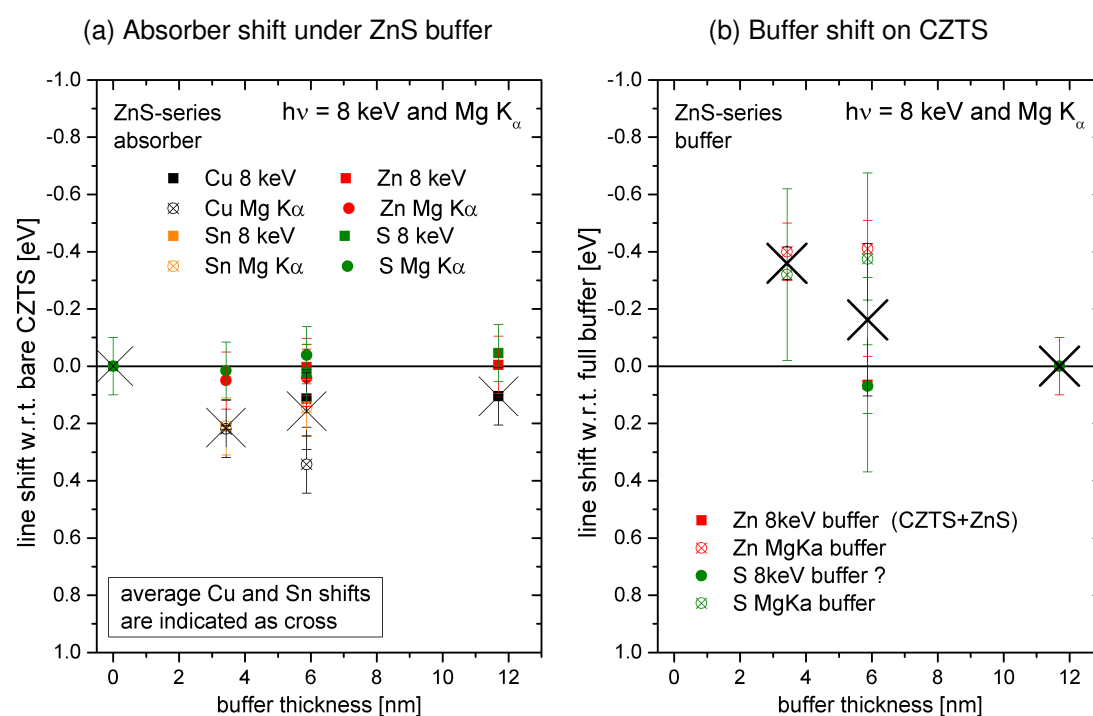


FIGURE 4.56: Shifts of absorber and buffer lines measured with XPS and HAXPES.

The CZTS buried under ZnS (figure 4.56a) shows a small downwards band bending towards the interface. The highest value for *ZnS thin* is  $0.21(\pm 0.1)$  eV.

In the buffers of the ZnS series (figure 4.56b) we see an upwards bend banding towards the interface, reaching  $-0.36(\pm 0.1)$  eV.

The absorber in the ZnO series (figure 4.57a) shows a larger downwards band bending than the ZnS series  $-0.43(\pm 0.15)$  eV. Due to the thick layers we only have data for this relatively thick layer.

The respective buffers (figure 4.57b) show no bending within the error range.

The ZnOS series does not show an abrupt junction as previously shown. Here we consider both values of the thin layers. We find an absorber shift of  $0.45(\pm 0.1)$  eV



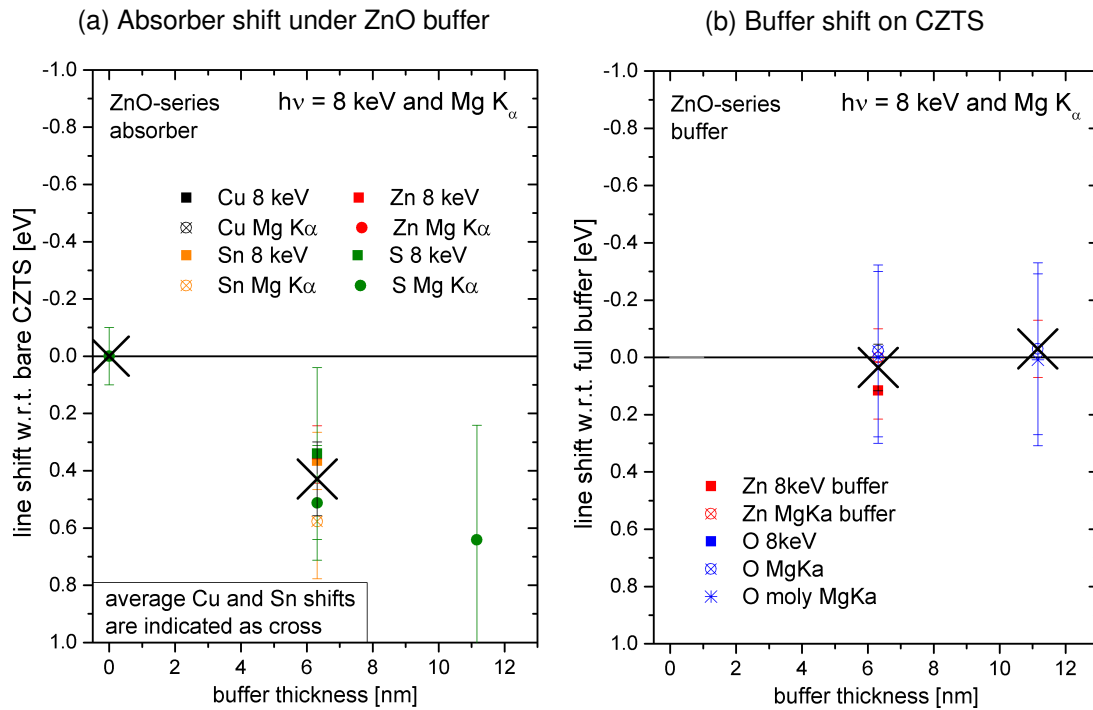


FIGURE 4.57: Shifts of absorber and buffer lines measured with XPS and HAXPES.

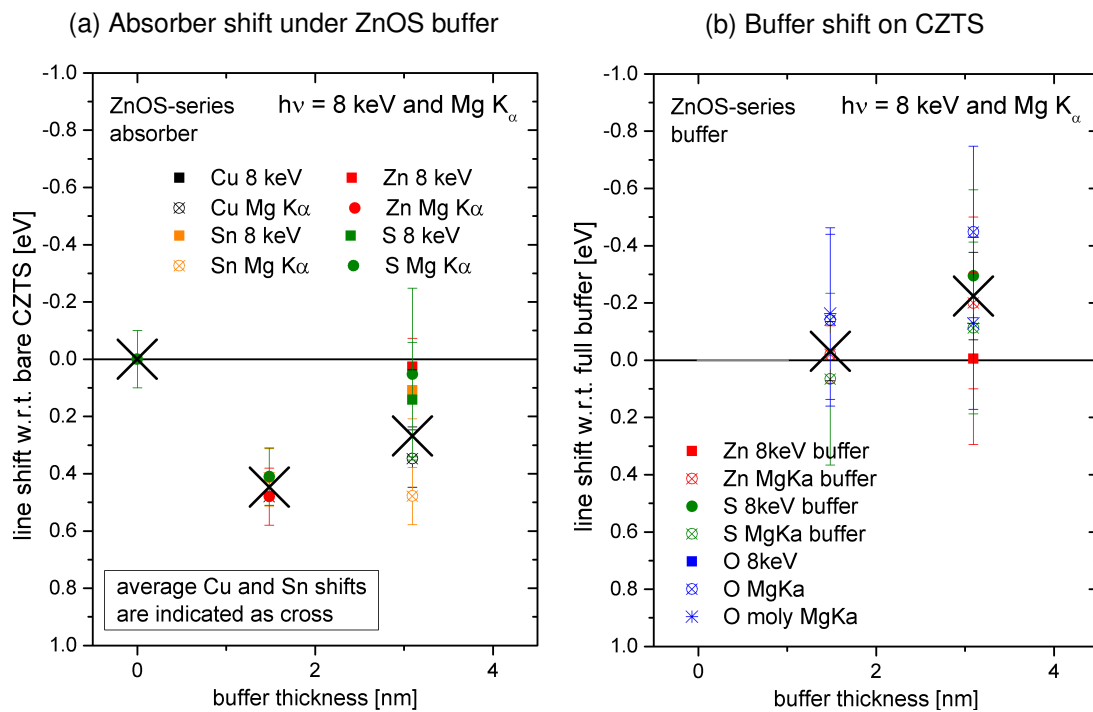


FIGURE 4.58: Shifts of absorber and buffer lines measured with XPS and HAXPES.

for *ZnOS thin* and  $0.27(\pm 0.15)$  eV for *ZnOS intermediate*. This is interpreted as a downwards bending towards the interface. The absorber bends up by  $-0.03(\pm 0.15)$  eV for *ZnOS thin* and  $0.12(\pm 0.15)$  eV for *ZnOS intermediate*. Since we consider modified ZnS-like interlayer, the main bending appears between the two investigated thin layers. This agrees with the unbent ZnS buffer seen in 4.56.

#### 4.4.2 Valence band maxima

The electronic properties are significantly influenced by the VBM and the occupied electronic states with the smallest binding energy. The VBM is composed of O states for ZnO, S states for ZnS, and in CZTS we see very shallow states that are caused by Cu and S. This has been discussed earlier (page 80, figure 4.55 and 4.54).

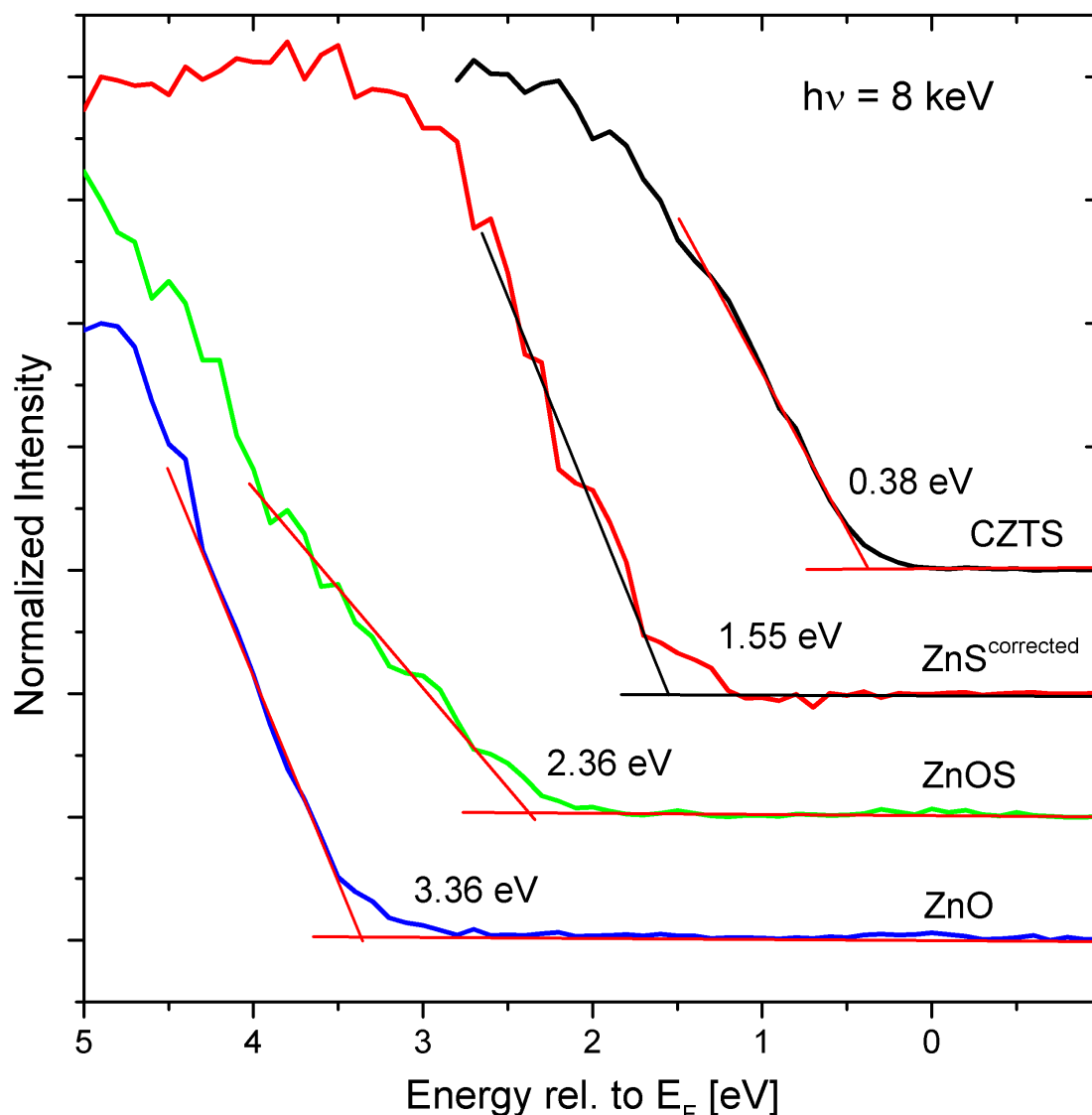


FIGURE 4.59: Linear extrapolation of the leading edges of the valence band maxima of CZTS and pure buffer materials measured at 8 keV. The spectra have been normalized to the intensity at  $\approx 5$  eV. Vertical offsets have been added for clarity.

With a linear approximation of the leading edge of the VBM spectra we can determine the valence band maxima. We see a monotonic trend for the VBM values where higher oxygen content means a higher VBM because the S 3p states that give rise to the ZnS VBM vanish more and more as S is replaced by O. For CZTS the additional Cu 3d states cause DOS even closer to the Fermi level so this VBM has the smallest value. We have to assume an uncertainty of 0.1 eV for these VBM values (0.2 for the corrected ZnS

spectrum) but they are only valid in the bulk far away from the absorber buffer interface. The band bending at the interface causes the whole spectra to shift in energy so we have to correct these values for interface induced band bending (IIBB) if we want to calculate conduction band offsets.

This is done by using the spectral shifts identified in the core level fits (see section 4.4.1 on page 82) to modify the VBM values. The conduction band position is defined by adding the optical band gap ( $E_G^{\text{optical}}$ ) of 3.55 eV for ZnS, 3.3 eV for ZnO and 2.6 eV for the used ZnOS buffer [79] to the corrected VBM position. We assume a combined error margin of ( $\pm 0.15$ ) eV.

For ZnS we find a positive CB offset (spike) of 1.45 eV. From the blocking behavior of the respective solar cell such a spike was expected. The ZnO buffer shows a cliff of -0.45 eV which increases the recombination at the junction since holes in the CZTS VBM can come close to the electrons in the ZnO CB. This cell will suffer from recombination at the interface where absorber VBM and buffer CBM come very close. The cell efficiency shown in table 4.2 therefore has an efficiency below 1% and in particular a low  $V_{\text{OC}}$ . Claims of a small spike alignment for a ZnO/CZTS-junction [124] with a VBM of 2.12 eV for sputtered ZnO do not match our findings and especially the resulting solar cell performance.

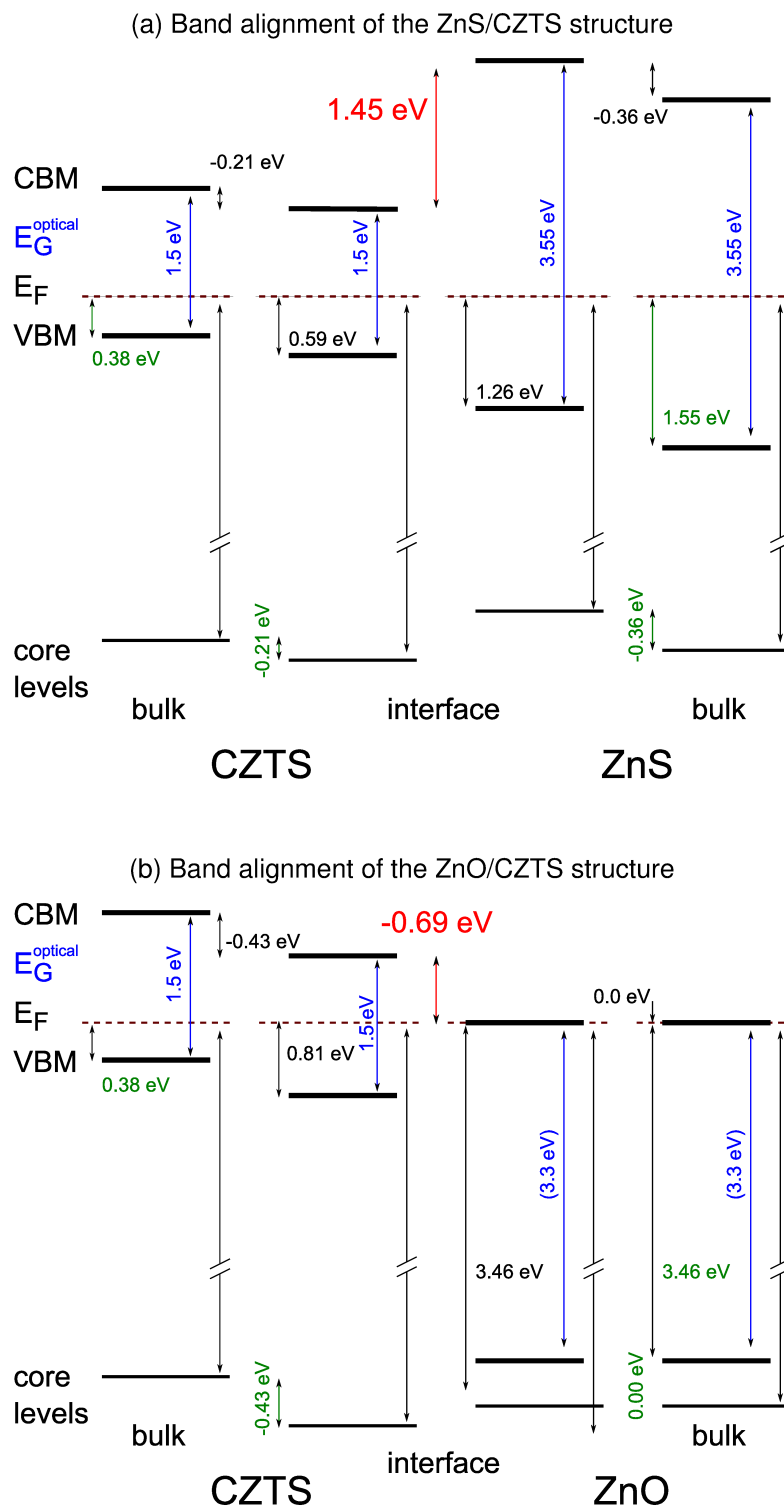


FIGURE 4.60: Calculated band alignment of the ZnS/CZTS and ZnO/CZTS structure using XPS and HAXPES derived band bending and HAXPES derived VBM values. The conduction band values were obtained by assuming the optical bandgap to be valid and adding it to the measured VBM position. The bulk VBM values are measured far away from the interface. The two sides of the interface in the center of the graphs illustrate the band bending at the contact area and the actual band alignment.

The ZnOS absorber in figure 4.61 shows a more complicated structure with a ZnS-like interlayer. The scheme obtained with the ZnOS-bandgap of 2.6 eV [79] shows a cliff of 0.21 eV, smaller than what we found for ZnO. However, the finding of a ZnS-like interlayer means, that the assumption of an unchanged bandgap at the junction is not valid. A compositional change in any direction means a band gap increase as shown in [79]. The ZnS-rich interface therefore implies a reduction of the cliff. The probable CBO is in the range of a flat conduction band alignment.

The junction yielded 3.13% efficiency in a solar cell which is 54% of the efficiency of the kesterite cell with CdS buffer, suggesting a band gap that is pretty well suited for charge carrier extraction. So the optimization of the band alignment could actually be done by altering the initial growth of the ZnOS compound on the CZTS.

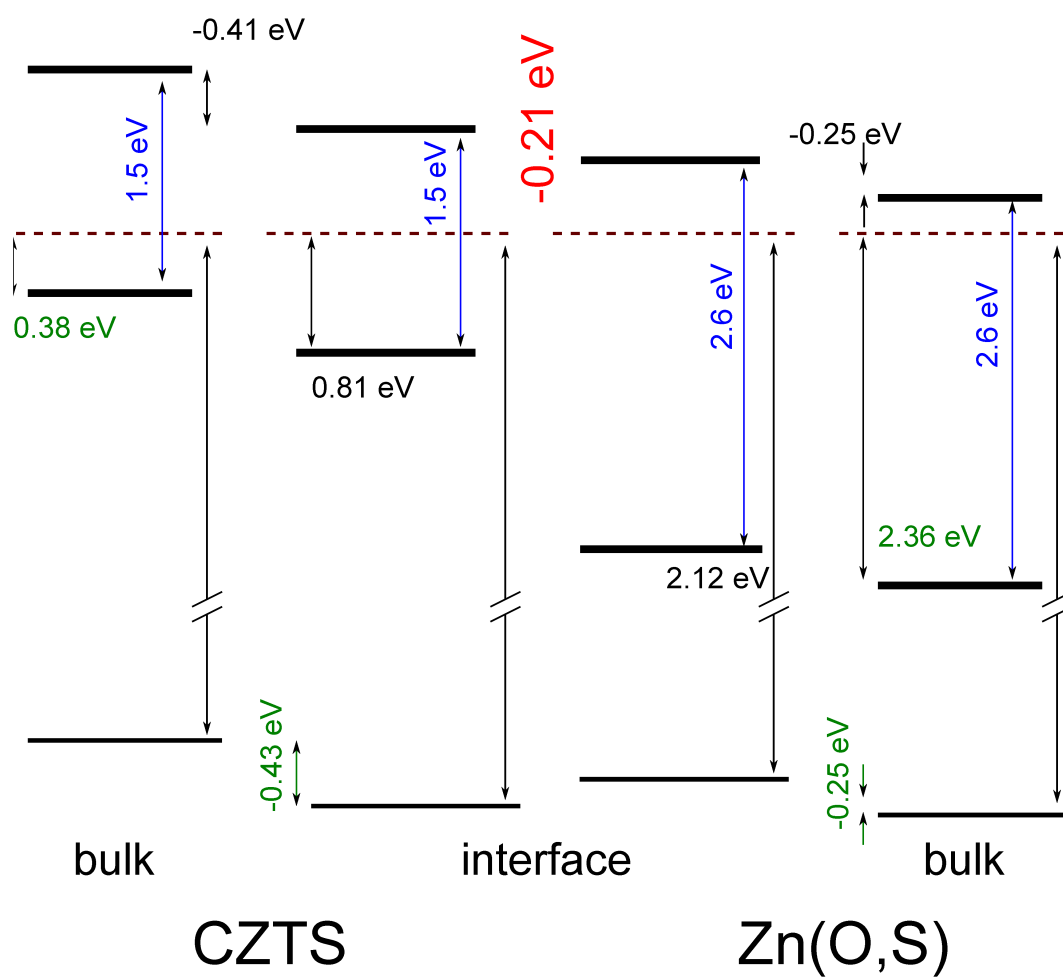


FIGURE 4.61: Band alignment of the ZnOS/CZTS structure. The bulk VBM values are measured far away from the interface. The two sides of the interface in the center of the graph illustrate the band bending at the ZnOS/CZTS contact area and the actual band alignment.

**Conclusion:** The measured electronic structures of the junction between CZTS and ZnS or ZnO are in accordance with the respective cell performance.

## 4.5 Summary

**Chemical structure:** In the two binary buffer series all evidence points towards pure ZnS or ZnO with a significant surface contribution of  $\text{Zn(OH)}_2$  growing directly on the pure CZTS. There is no indication for secondary phase formation on the CZTS or diffusion. For ZnOS buffer the CZTS surface stays unchanged as well but the buffer composition is heavily influenced by CZTS. We find evidence in for S-rich and very O-poor material growing directly on the CZTS. The supplied ZnO precursor material is not incorporated in the initial growth stage. The composition then gradually changes towards the incoming O-rich  $\text{ZnO}_x\text{S}_{1-x}$ . On the one hand this effect makes it harder to adapt a  $\text{ZnO}_x\text{S}_{1-x}$  buffer to the needs of a kesterite-based solar cell. Even theoretically ideal  $\text{ZnO}_x\text{S}_{1-x}$  buffers cannot be grown directly on CZTS because this will massively alter the buffer composition.

On the other hand the compositional gradient can have a beneficial effect on the band alignment if the growth can be controlled.

**Electronic structure:** For ZnS we find a big positive CB offset (spike) of  $1.45(\pm 0.15)$  eV as expected. The ZnO buffer shows a cliff of  $-0.47(\pm 0.15)$  eV that enhances recombination, contradicting claims of a small spike in ZnO/CZTS and VBM measurements of 2.12 eV for sputtered ZnO buffers [124].

The ZnOS absorber shows a small cliff if a constant buffer composition is assumed. The findings of a S-rich interlayer places the measured CBO in a range of a flat CB alignment. This explains the pretty well-performing cell with this buffer material.

Careful investigation of a series focusing on the initial growth of the first 5 nm of ZnOS compounds in CZTS, using a small step thickness series and also direct measurement of the conduction band alignment can provide further insight into this promising junction.





## Chapter 5

# $\text{Cu}_2\text{ZnSnS}_4$ - back side reactions with molybdenum

### 5.1 Molybdenum as back contact

Molybdenum is a common back contact material used for most CIGSSe and CZTSSe thin film solar cells as shown e.g. in figure 5.1. The formation of  $\text{MoS}_2$ - or  $\text{MoSe}_2$ -interlayers at this back contact [57, 125] and a possible decomposition or incomplete formation of kesterite are concerns for the cell performance [125–127].  $\text{MoS}_2$  is actually more stable than kesterite [128] so once formed  $\text{MoS}_2$  cannot be reconverted.

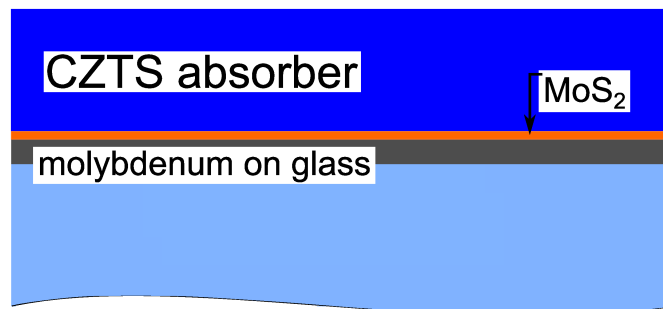


FIGURE 5.1: CZTS/ $\text{MoS}_2$ /Mo-stack of a typical CZTS thin film solar cell. The interlayer (orange) might contain further secondary phases.

The electronic structure of  $\text{MoS}_2$  bulk material is well understood [129] but thin layers show differing electronic properties [130, 131]. Strong electronic changes including shifts of XPS core levels have been observed at surfaces and defects in  $\text{MoS}_2$  [132, 133]. Interface recombination caused at the back contact seems to be a problem for the solar cell performance [126].

High sulfur partial pressure might compensate for S-loss at the back surface but on the cost of the formation of a very thick and potentially even more detrimental  $\text{MoS}_2$ -layer

compared to the secondary phases of CZTS. A passivation layer that is not detrimental would be ideal. Passivation by TiN [126, 134],  $\text{TiB}_2$  [135]  $\text{Al}_2\text{O}_3$  [136], or ZnO [137] has been reported.

### 5.1.1 Sample preparation

The back side (BS) of CZTS samples with thicknesses around  $1\ \mu\text{m}$  (see figure 5.1) cannot be reached easily with surface sensitive spectroscopic techniques like PES. We partly rely on model systems (Mo/CZTS) to reveal interactions at the CZTS/Mo interface in the device.

CZTS precursors have been deposited with magnetron sputtering [84] and annealed in a tube furnace [47, 85] at  $470^\circ\text{C}$ ,  $490^\circ\text{C}$ ,  $530^\circ\text{C}$ , and  $570^\circ\text{C}$ .

The CZTS precursor was only analyzed on the front side (FS). The annealed samples could be measured on the FS and BS. This was reached after a liftoff procedure as shown in figure 5.2 using ultrasonic and shock cooling to break the layer stack between the Mo/glass and the absorber with its potential back side phases.

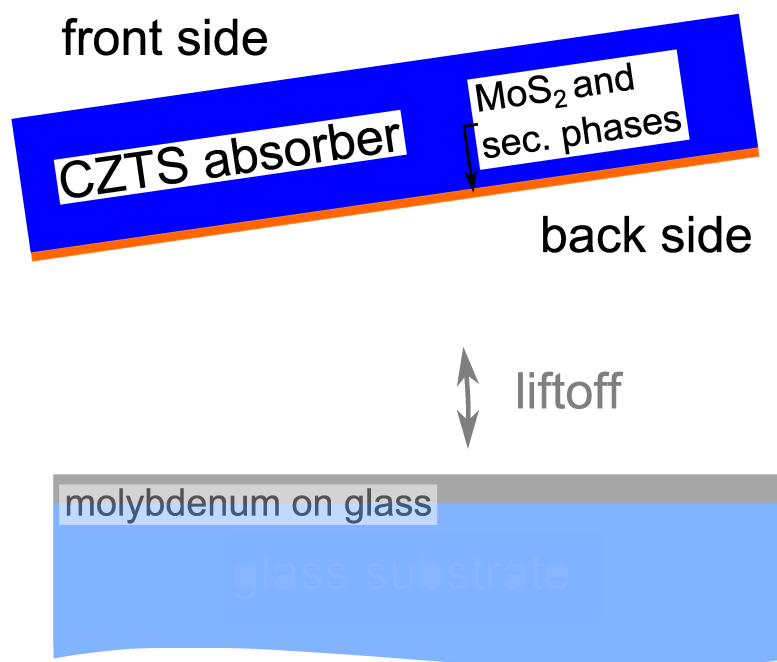


FIGURE 5.2: The liftoff process allows to directly investigate not only the front side (FS) but also the back side (BS) of the kesterite layer. The remaining Mo/glass doesn't show any traces of CZTS-related signals (not shown). Secondary phases and  $\text{MoS}_2$  ideally stay on the BS of the CZTS.

To measure the CZTS material in contact with the Mo-interface, model systems were produced by direct current (DC) sputter deposition of molybdenum (10 nm and 20 nm) onto the CZTS precursor. The samples were produced with and without a TiN diffusion

barrier as shown in figure 5.3. This model system could be annealed ex-situ and in situ to investigate the formation of  $\text{MoS}_2$  and possible binary phases.

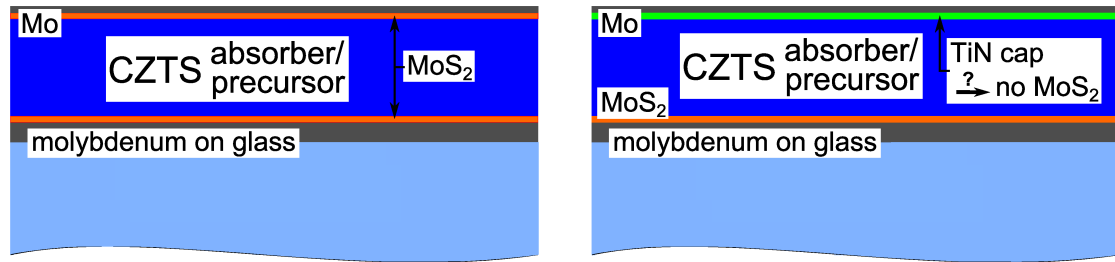


FIGURE 5.3: Potential  $\text{Mo}/\text{MoS}_2/\text{CZTS}/\text{MoS}_2/\text{Mo}/\text{glass}$  with 10 nm and 20 nm toplayer of Mo as model system. The structures were grown with and without a thin TiN interlayer (green) as diffusion barrier. The Mo and TiN was deposited onto the CZTS precursor material to monitor the kesterite formation at the critical interface.

## 5.2 CZTS/Mo interface interaction

The survey spectra measured with 2 keV HAXPES as shown in figure 5.4 contain all the well-known CZTS lines as well as O, C, and partly Na signals. In all the back side spectra we see small Mo-signals.

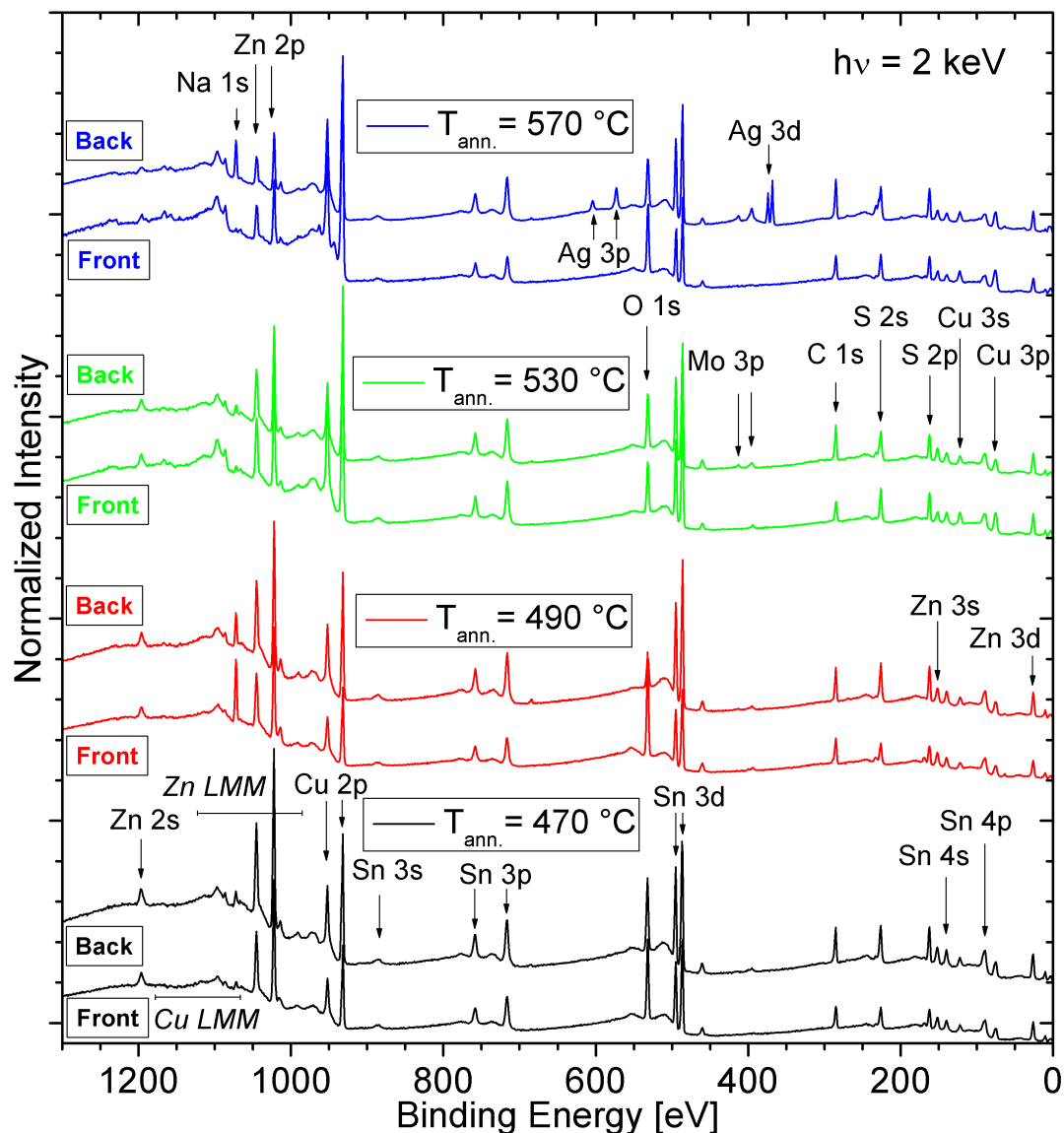


FIGURE 5.4: HAXPES survey spectra of the back contact series. Front and back side of all samples have been measured. Vertical offsets have been added for clarity.

In one back side spectrum (570°C, blue line) we find Ag lines that originate from the silver glue that we used in the liftoff process (see page 92).

In figure 5.5 the valence band region of all front and back sides is shown. The lines can be recognized from figure 4.54 where, due to the different scattering cross sections at 2 and 8 keV, the shape of the VB region is a little different.

The front side spectra show the most prominent change visible in the Sn 4d. A significant low- $E_B$ -side shoulder appears for annealed backsides and the shape of the doublet shows multiple species in changing composition. More detailed analysis of these chemical modifications is shown for the sharpest core levels (see page 96 and following).

The back side spectrum of the 570°C-sample shows a prominent change around 5 eV that we attribute to the silver glue that we found at this back surface.

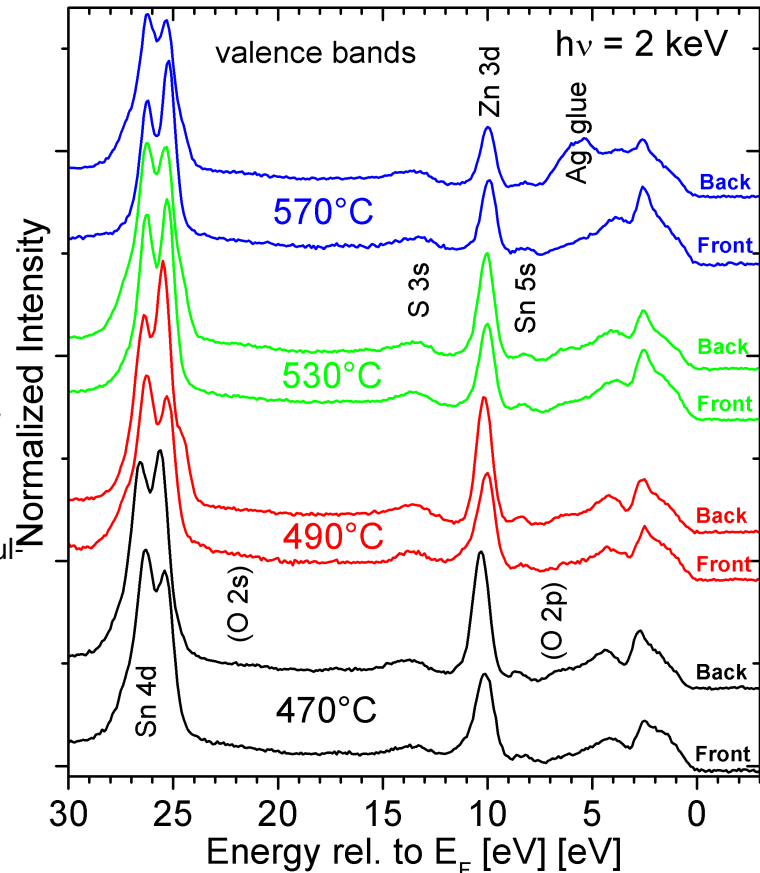


FIGURE 5.5: HAXPES valence bands of the back contact series. Vertical offsets have been added for clarity. We see only small changes in this region.

The **core levels** give more detailed information about chemical changes. Fits have been done as described in section 3.5.

### 5.2.1 Liftoff samples

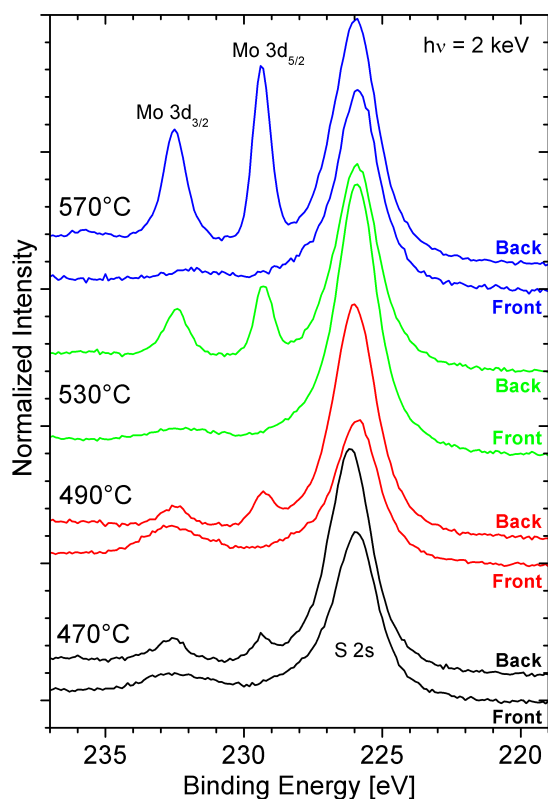


FIGURE 5.6: Mo 3d spectra measured with 2 keV excitation. The sharp single line is S 2s. Vertical offsets have been added for clarity.

tra (figure 5.4) at around 1070 eV. Since we barely observe sulfate indications in the Zn, Cu, and Sn detail spectra, we attribute this to  $\text{Na}_2\text{SO}_4$ . Na actually accelerates the sulfate formation under x-ray illumination<sup>1</sup>.

[66]

The area ratio of the S 2s and Mo  $3d_{5/2}$  peak, taking into account  $\sigma$  of 22.56 and 41.78, respectively, give a Mo/(Mo+S) ratio of up to 10% for the 570°C-sample. The overall signal of (assumed) stoichiometric  $\text{MoS}_2$  consequently contributes 2/9 of the S-signal while 7/9 come from the buried CZTS backside. Considering that more than 60% of the PES signal originate from a depth of less than the IMFP, this indicates, that the thickness of the  $\text{MoS}_2$ -layer, in a bilayer model, is well below the IMFP of 3.14 nm. In case of a doping gradient the depth distribution cannot be given.

<sup>1</sup>Source: Communication with M.Bär

In the region shown in figure 5.6 we see a clear single species Mo 3d doublepeak that appears only in the back side spectra and increases for higher annealing temperatures ( $T_{\text{ann}}$ ).

The S 2s line appears increased in the back side spectra compared to the front sides which is attributed to the higher S-content in  $\text{MoS}_2$  compared to CZTS.

The only exception is the 530°C sample. Here we find an surprisingly high S peak on the front side where we don't expect any big compositional changes for different  $T_{\text{ann}}$ . The back side spectrum shows a shape right in between the 490°C and the 570°C back side spectrum.

This region already suggests a  $\text{MoS}_2$  formation that increases with higher  $T_{\text{ann}}$ . We also observe a typical sulfate ( $-\text{SO}_4$ ) signal that is clear to see in the range of 232.5 eV for the front side spectra, most pronounced at 409°C (red line). This scales with the Na 1s peak observed in the survey spectra

In figure 5.7a and b the Cu  $2p_{3/2}$  fits show that in addition to the dominant CZTS phase (red line) on front and back side, a secondary phase (green line) appears. While being rather constant on the front side, this secondary phase shows a growing signal on the back side with higher annealing temperatures, suggesting back side decomposition. This has also been observed in [138] with the formation of a  $\text{Cu}_x\text{SnS}_y$ -phase where typically  $x=2$  and  $y=3$  and Cu-diffusion into the  $\text{MoS}_2$  layer, suggesting some Cu-Mo-S-phase. We do not observe additional Mo-species so a  $\text{Cu}_x\text{Sn}_y\text{S}_z$ ,  $\text{CuS}_2$ , or  $\text{CuO}_x$  is the best explanation for the secondary phase. Ranges for different compounds have been attributed according to [89], CZTS ranges come from this work. The  $570^\circ\text{C}$  front side shows two additional species at higher  $E_B$  (blue and cyan line) that fall in the range of oxides ( $\text{CuO}$ ,  $\text{CuO}_2$ ) and sulfates. The origin could be oxygen contamination during the production or transfer of the sample.

The Auger lines shown in figure 5.7d and c do not reveal any change in shape for the FS.

The BS spectra show a broadening of the main peak at 935 eV for higher  $T_{\text{ann}}$  as expected from the growing secondary phase signal in the core level.

The sharp overlapping line in the  $490^\circ\text{C}$  FS and the  $470^\circ\text{C}$  BS spectrum is Na 1s.

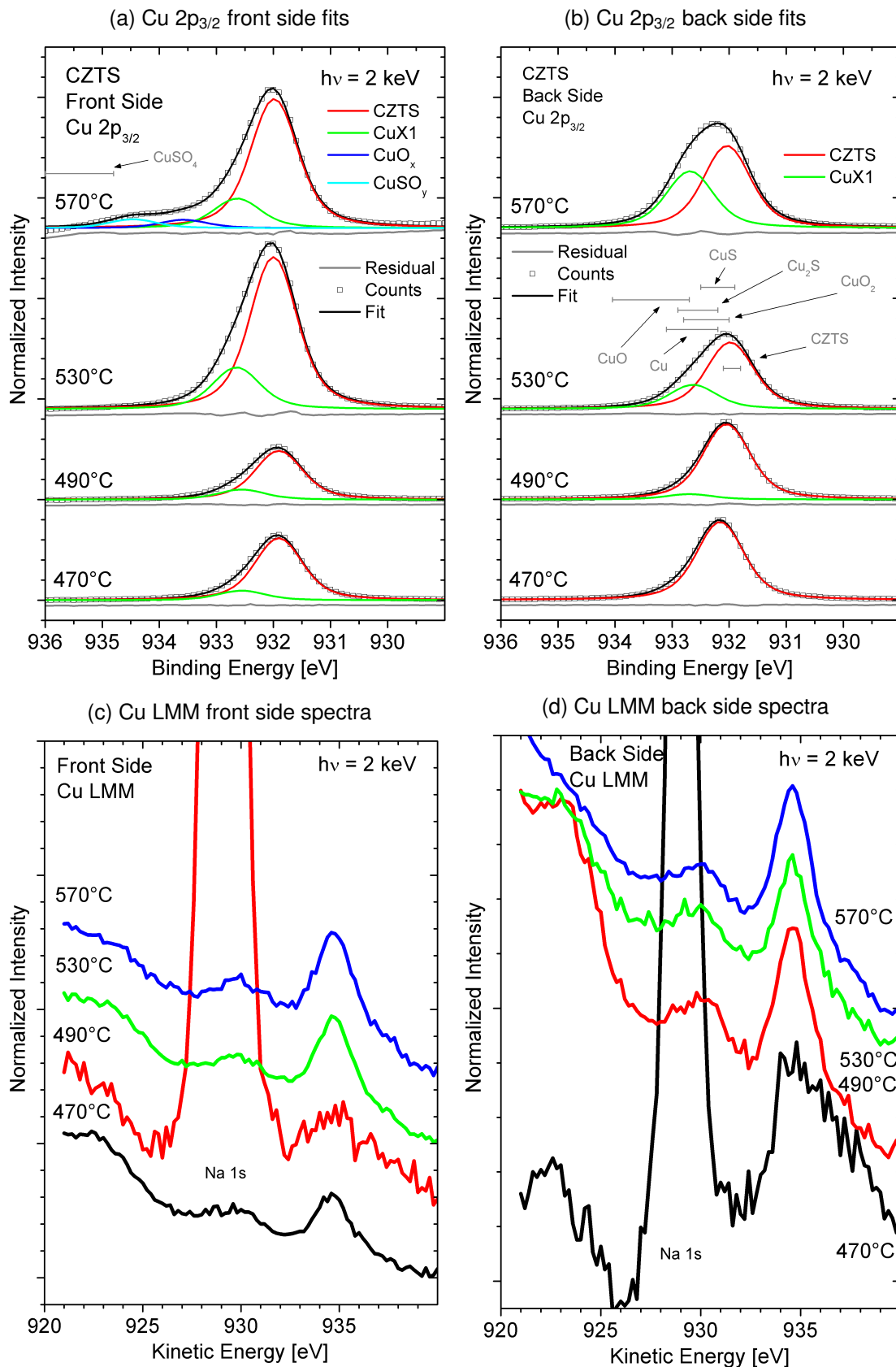


FIGURE 5.7:  $\text{Cu } 2p_{3/2}$  fits and  $\text{Cu LMM}$  HAXPES spectra measured with 2 keV excitation at FS and BS. Vertical offsets have been added for clarity.



For Zn  $2p_{3/2}$  fits in figure 5.8a and b the secondary phase ZnX1 (green line) on the FS slightly decreases in intensity with respect to the CZTS phase (red line) at higher  $T_{\text{ann}}$ . A small signal of this phase on the back side is visible for most temperatures. The phase follows the line intensity of the O 1s in figure 5.4 and is attributed to ZnO. The Auger lines shown in figure 5.8d show a clear sharpening of the main peak and the peak on the right shoulder for higher  $T_{\text{ann}}$  in the FS spectra. The BS Auger spectra in figure 5.8c do not reveal any significant change in shape. The ZnO evolution agrees with the driving forces in the annealing procedure; the S-rich atmosphere during annealing leads to a decreased ZnO amount on the front side, while the backside stays mostly unaffected.

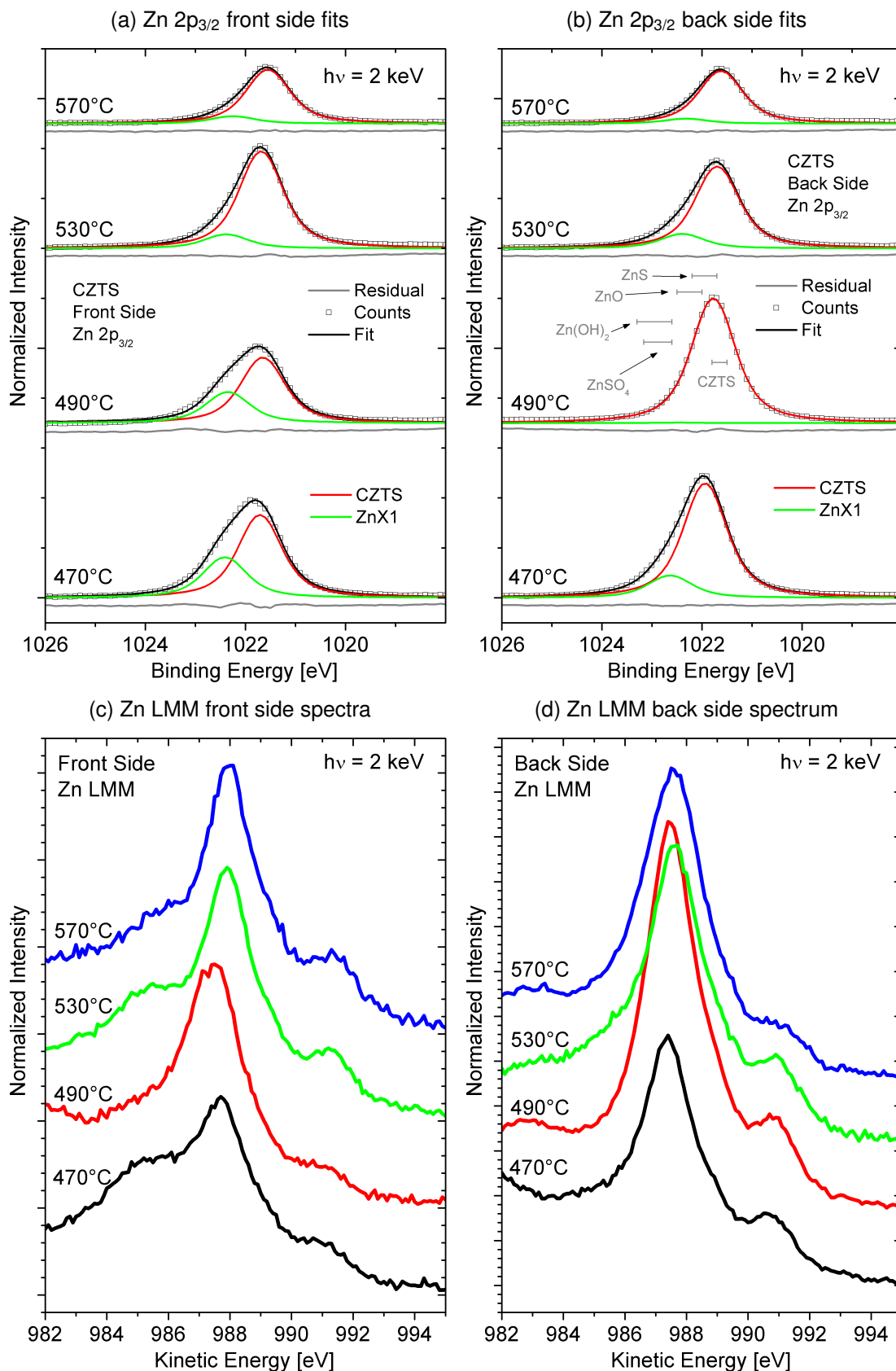


FIGURE 5.8: Zn  $2p_{3/2}$  fits and Zn LMM HAXPES spectra measured with 2 keV excitation at FS and BS. Vertical offsets have been added for clarity.

Sn shows the most chemical changes as we see from the up to 4 species in 5.9a and b. The attribution of species is done with respect to figure 6.4 from a pure Sn-S-O-Zn-material system. The multiphase FS at 470°C shows a development towards nearly single phase kesterite at 570°C.

The BS spectra show no transformation to CZTS. They also show an additional phase (cyan line) that we attribute to SnS. This easily evaporates from the surface so we find it only at the backside. The annealing cannot dissolve any of those phases. The non systematic modifications could be due to the liftoff process.

The species SnX2 at highest  $E_B$  (red line) is oxidized tin ( $\text{SnO}_2$ ) (compare e.g. figure 6.4). We see the identical intensity trends as for the ZnO species (figure 5.8a and b) and O 1s (figure 5.4).

None of the secondary species in Cu or Zn follow the intensity that we find for the SnX1. We can therefore rule out the potential  $\text{Cu}_x\text{SnS}_y$ -species that we found in the Cu-fits and assume an oxide in figure 5.7a and b). As Cu-free Sn-species we therefore attribute SnX1 to SnO. A possible  $\text{SnS}_2$  would be expected to decompose and evaporate from the front side, leaving the SnO only possibility.

The Auger lines in figure 5.9c and d support the fits of the core levels. The FS shows the same evolution from a broad multi-peak signal to a sharper line. The BS spectra show no clear trend and the 490°C spectrum is less broadened by secondary phases.

**Conclusion:** We can summarize that the FS of the samples contains a secondary Cu species (oxide or  $\text{Cu}_2\text{S}$ ) and ZnO as well as  $\text{SnO}_2$  and SnO for low  $T_{\text{ann}}$ . For high  $T_{\text{ann}}$  the Cu species is unaffected but the other phases dissolve and form a kesterite. Small amounts of oxidized Sn and Zn species remain on the surface. These have been shown to be more easily oxidized than Cu [139].

The back side shows the formation of  $\text{MoS}_2$  at all  $T_{\text{ann}}$ . For the other phases we find a reduction in the ZnO intensity, formation of  $\text{Cu}_2\text{S}$  or oxides, and mostly unchanged Sn-species.

The CZTS/Mo contact leads to  $\text{MoS}_2$  formation and this  $\text{MoS}_2/\text{CZTS}$  contact prevents the CZTS precursor from forming a kesterite. Detrimental secondary phases are not dissolved in the current layer stack and annealing step. If altered annealing approaches cannot overcome this problem, the back contact has to be modified to reach a fully crystallized CZTS-layer.

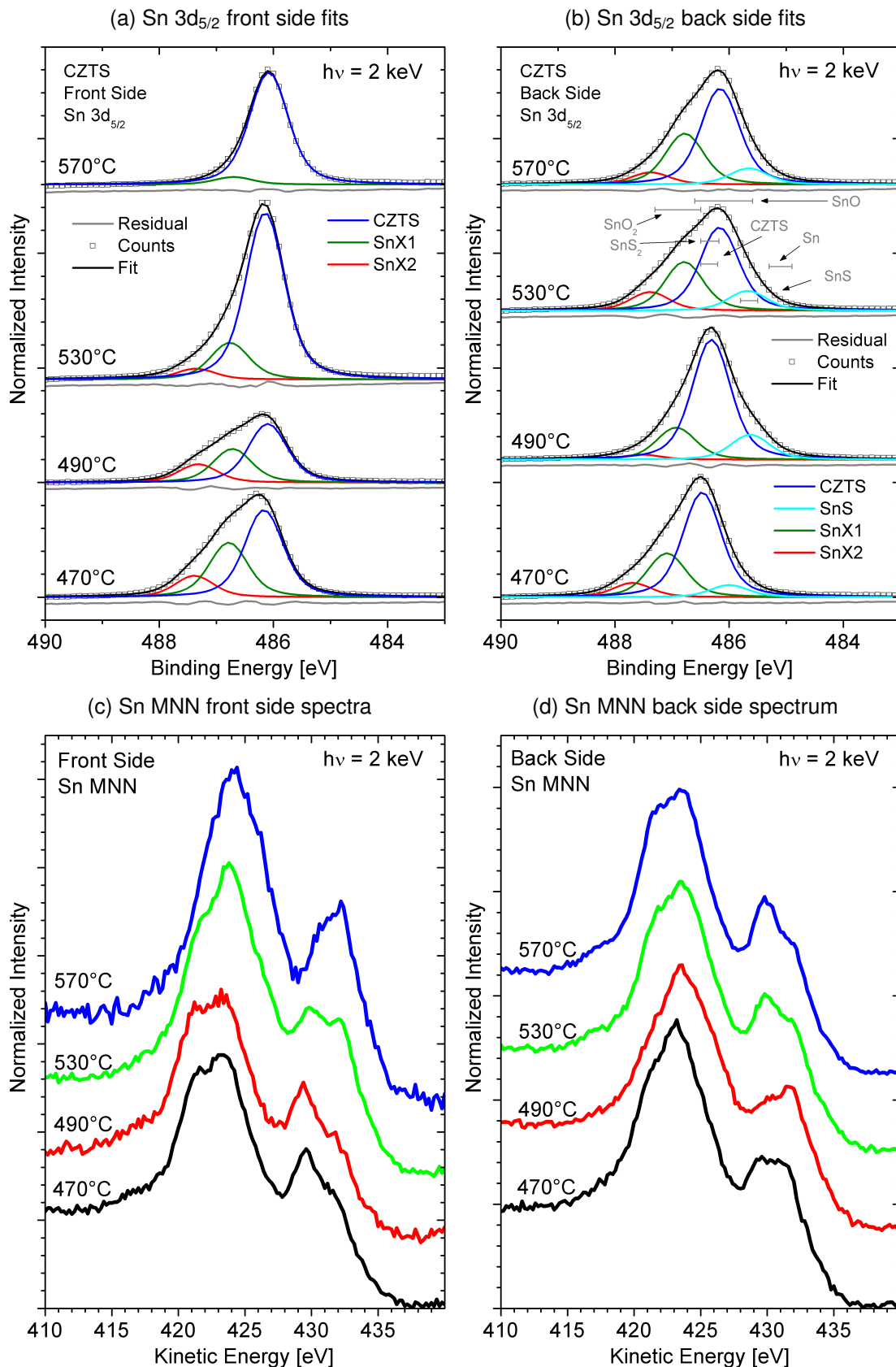


FIGURE 5.9: Sn  $3d_{5/2}$  fits and Sn MNN HAXPES spectra measured with 2 keV excitation at FS and BS. Vertical offsets have been added for clarity.

### 5.2.2 Model system samples

The ex-situ annealed model system samples with 10 nm molybdenum on top of CZTS were investigated with 8 keV HAXPES.

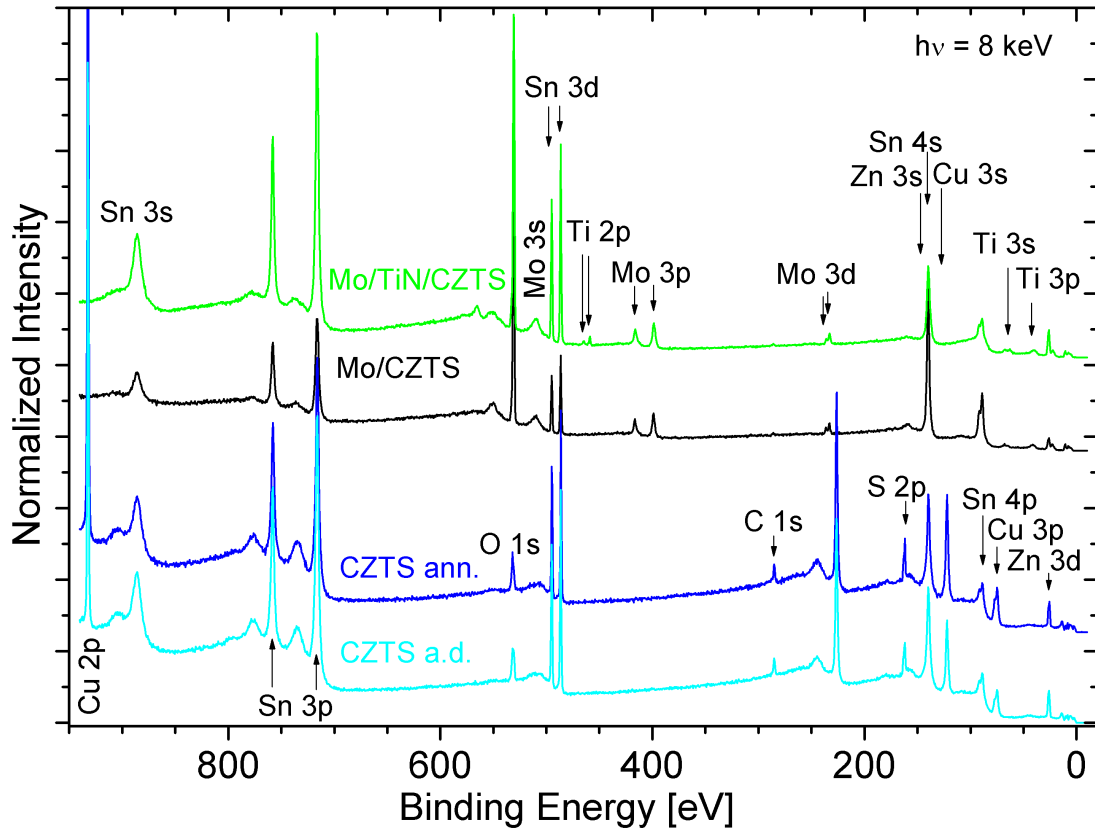


FIGURE 5.10: HAXPES survey spectra of the model system samples. Vertical offsets have been added for clarity.

In figure 5.10 we see a CZTS precursor (cyan line) and as-deposited CZTS (blue line) for comparison. As deposited CZTS refers to CZTS annealed in a tube furnace with added S to prevent S-loss. The two model system samples are shown as Mo/CZTS (black and red line) with a thin Mo layer sputtered directly onto the CZTS precursor. Additionally, one sample with TiN-layer between CZTS and Mo to prevent any chemical contact has been measured (green line).

All samples show the CZTS- lines of Cu, Zn, Sn, and S as well as O and C lines. The Mo signal is visible in all capped layers. The sample with TiN interlayer shows additional Ti lines.

The Sn fits in figure 5.11a show two main differences to the previously shown FS and liftoff-BS Sn fits in figure 5.9a and b. Firstly the species with highest  $E_B$  that we attribute to a  $\text{SnO}_2$  surface species is not resolved in the 8 keV fits due to a smaller interface contribution in the spectrum.

Secondly the Mo/CZTS sample shows a clear metallic Sn signal (magenta line). A very weak metallic signal can also be found for the other capped layer, the Mo/TiN/CZTS. We see that the sputter deposition of Mo (and TiN) on a CZTS precursor leads to the formation of metallic Sn (or Sn alloys).

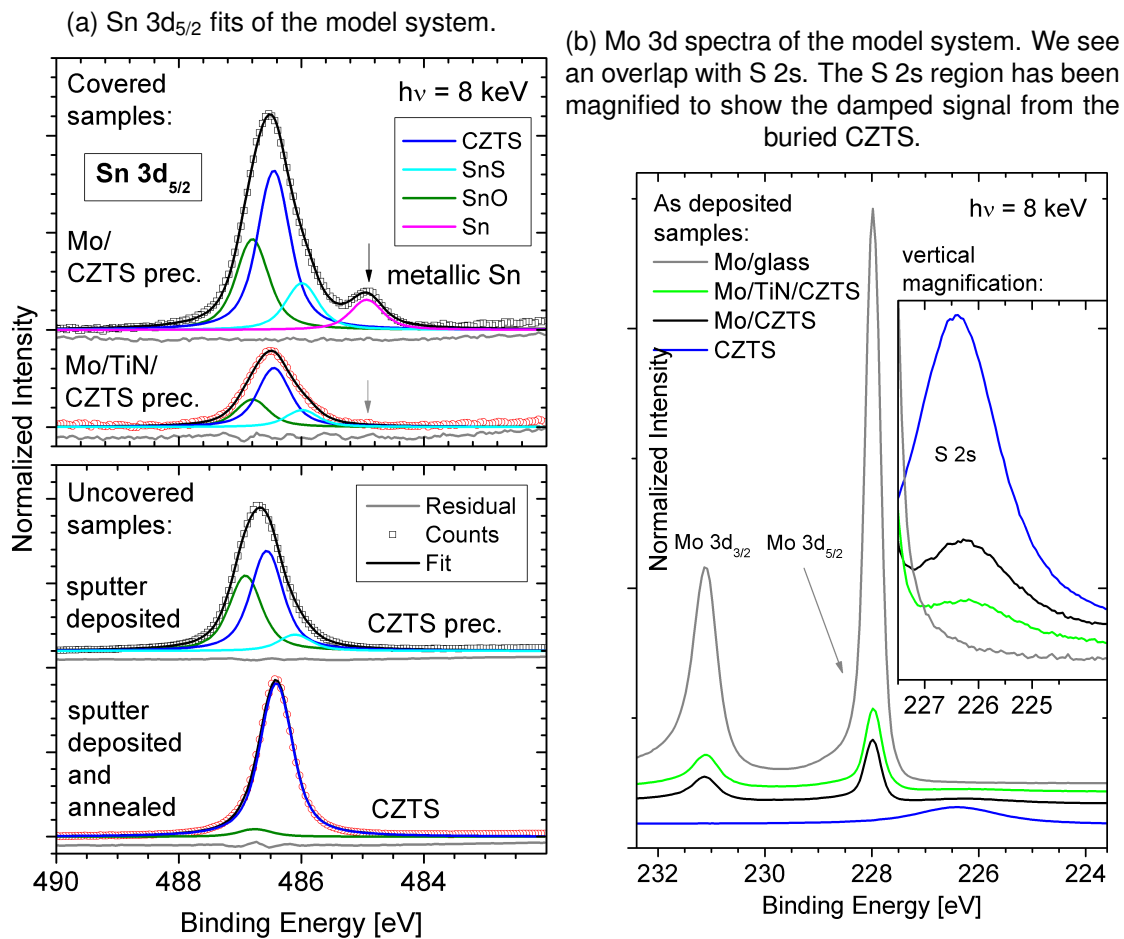


FIGURE 5.11: Sn  $3d_{5/2}$  fits and Mo 3d region measured with 8 keV excitation. Vertical offsets have been added for clarity in all graphs.

The Mo 3d region in figure 5.11b is shown with a magnified inset due to the extreme differences in intensity. The CZTS (blue line) shows a S 2s peak that is heavily reduced for the capped layers. The sharp Mo 3d peak is most prominent for the Mo-reference (gray line) and of similar intensity for the thin Mo layer deposited directly on CZTS (black line) and on TiN on CZTS (green line).

The valence band spectra of the Mo/CZTS structure are shown in figure 5.12a. We see a characteristic three-peak structure in the spectrum of pure Mo (gray line) that is similarly found in  $\text{MoS}_2$  [132] and  $\text{MoO}_3$  [140]. The bare CZTS (blue line) shows the well known CZTS valence band structure (compare page 81) and the bare precursor spectrum is slightly broadened in all its features.

The Mo/CZTS spectrum shows all features of the CZTS and Mo spectra.

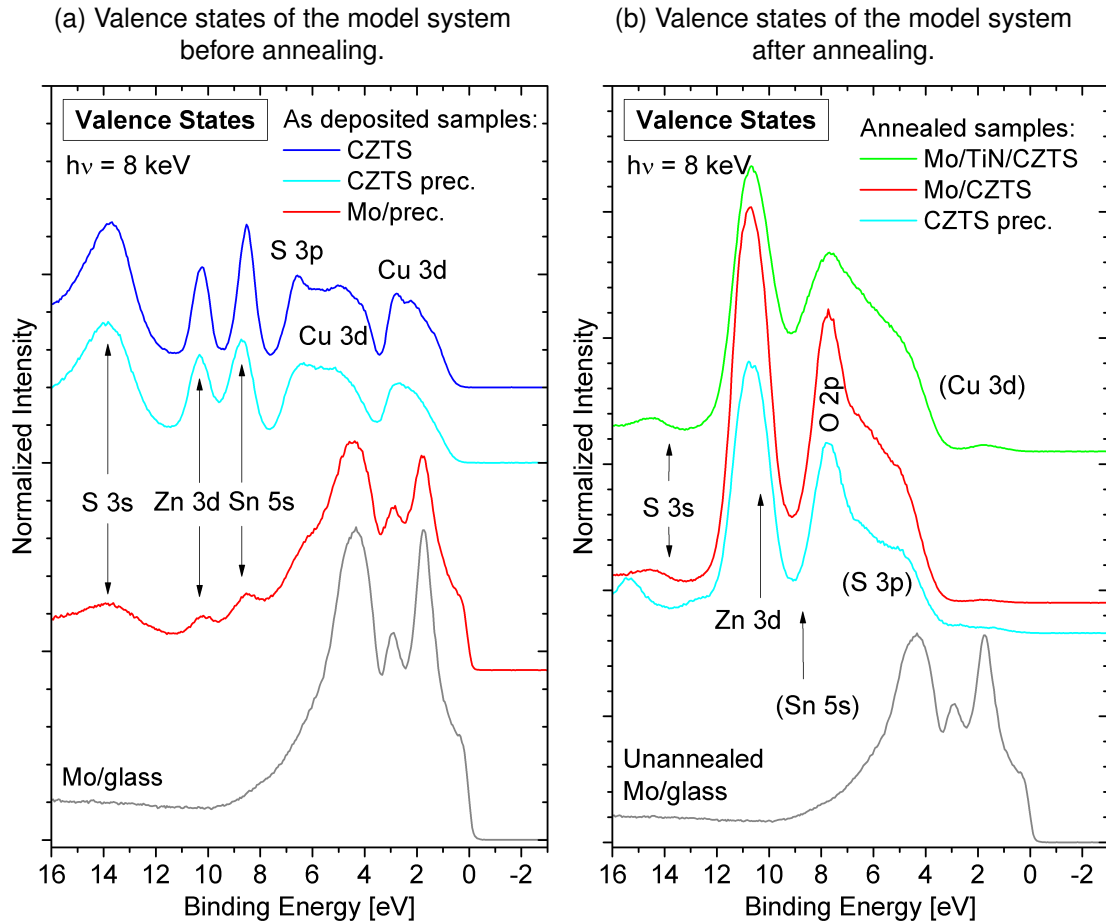


FIGURE 5.12: Valence states of the model system before and after annealing measured with 8 keV excitation. Vertical offsets have been added for clarity in both graphs.

After annealing the VB structures in figure 5.12b have vastly changed. For all three CZTS materials the spectrum looks like ZnO or O-rich  $\text{ZnO}_x\text{S}_{1-x}$  as known from figure 4.54 (page 80). For TiN we find a much more pronounced right hand shoulder of the O 2p peak that is caused by Ti-states.

The Cu and Sn lines have nearly vanished and the S 3s and 3d are heavily reduced, too. The completely missing molybdenum-signatures in Mo/CZTS and Mo/TiN/CZTS indicate that the thin top layers have fallen off during the annealing step. A complete oxidation could hide the Mo signal but the nearly perfectly matching spectra of the precursor and Mo/CZTS sample after annealing in vacuum makes any presence of Mo improbable. Additionally, we find lightly increased signals in the S-region in the Mo/CZTS sample. This could be explained with an initial protection of the surface by

the Mo layer. The thermal stress during the heating or cooling could have broken the contact between CZTS and Mo and the unprotected layer decomposed for a shorter time than the CZTS precursor, leading to less S-loss.



### 5.2.3 In situ annealing

Samples have been annealed in situ and S  $L_{2,3}$  XES spectra have been measured. For in situ annealing a sample was heated to the respective peak temperature, held there for approximately 6 minutes, and allowed to cool until the measurement chamber pressure had improved before measuring. The investigated structures are 20 nm Mo/CZTS precursor and 20 nm Mo/TiN/CZTS precursor as well as bare CZTS and CZTS precursor.

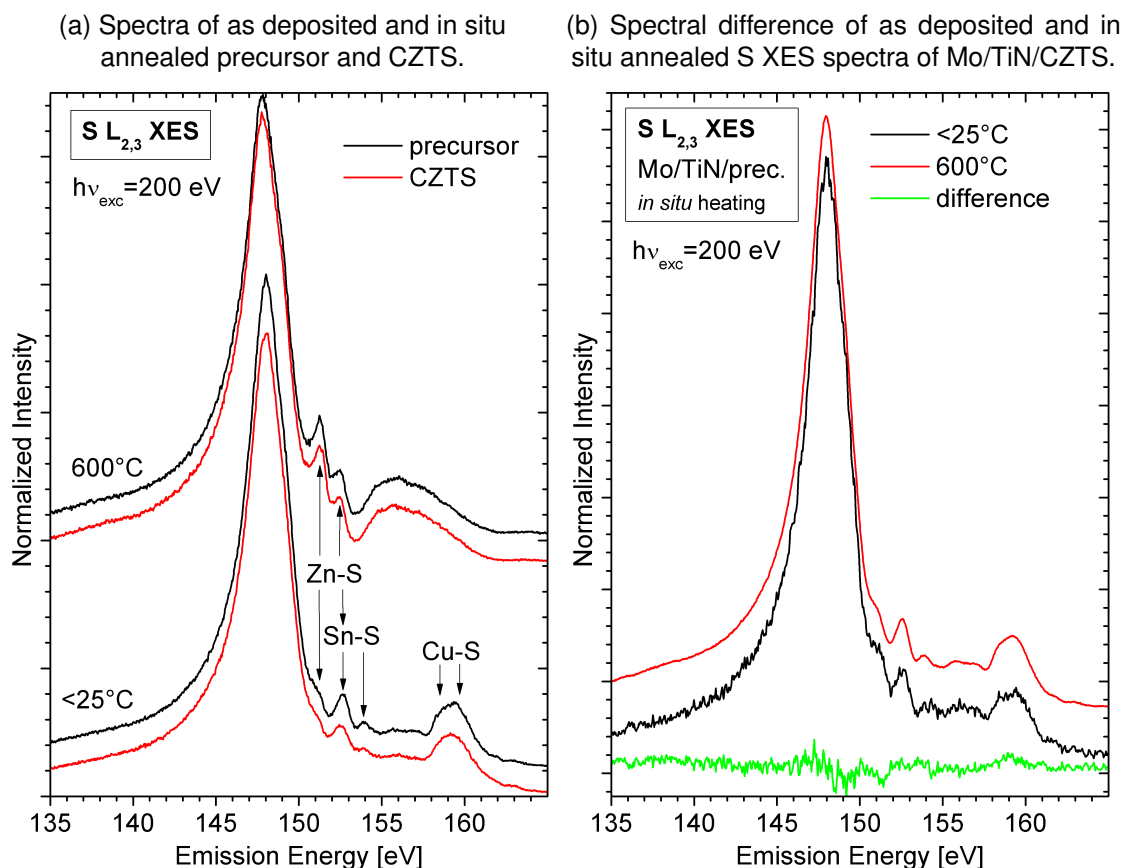


FIGURE 5.13: In situ annealed precursor, CZTS, and Mo/TiN/CZTS S XES spectra. Vertical offsets have been added for clarity. We see a transition to ZnS-like spectra without capping and a nearly unchanged spectrum for the Mo/TiN/CZTS structure.

In figure 5.13a the effect of annealing in vacuum on the uncapped CZTS samples is shown. Differences in the S  $L_{2,3}$  XES spectra before heating may be due to disorder, binary phases, or off-stoichiometry. After annealing, both samples show ZnS-like spectra (compare page 43) and all features attributed to Sn or Cu have disappeared. In-vacuum annealing clearly leads to heavy Cu- and Sn depletion of unprotected CZTS surfaces.

The TiN-capped layer shows a different behavior in figure 5.13b. No spectral differences can be seen after annealing as proven by the nearly flat difference spectrum (green line). The increased intensity (improved signal-to-noise) may be from cracking of Mo/TiN capping layer during heating and/or cooling.

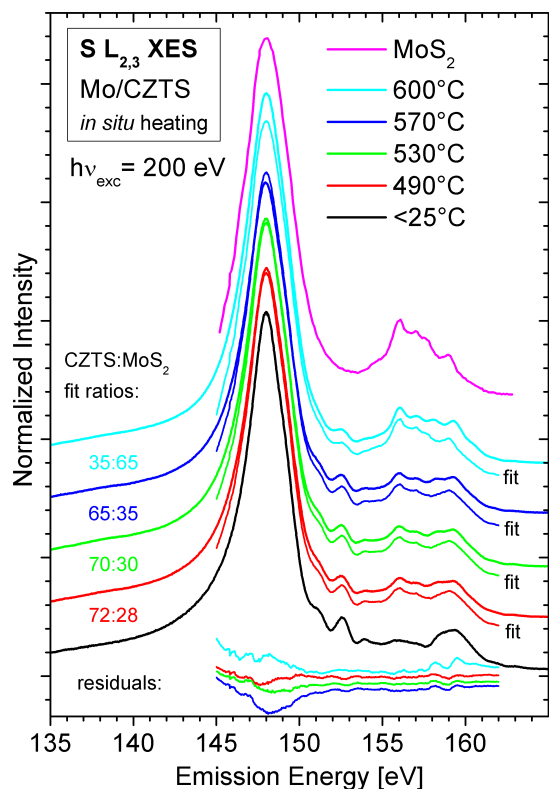


FIGURE 5.14: S XES spectra of in situ heating of Mo/CZTS. Fits by adding the  $\text{MoS}_2$  and room temperature spectrum and the respective residuals are shown. Vertical offsets have been added for clarity.

differences, this does not contradict the observation of interface species in the liftoff samples.

The Mo/CZTS structure has been annealed subsequently at different temperatures. In figure 5.14 we see the resulting spectra and a  $\text{MoS}_2$  reference spectrum for comparison. We see a clear evolution with more and more  $\text{MoS}_2$  signal for higher  $T_{\text{ann}}$ . This is better illustrated by the fits that model the spectra of the annealed samples as a superposition of the pure  $\text{MoS}_2$  spectrum and the pure CZTS spectrum before annealing (black line). The intensity ratios are indicated in the graph and range from 28%  $\text{MoS}_2$ -signal after annealing at 490°C to 65% for the 600°C-sample. Residuals show differences in the main peak and in the high energy region. Both can be attributed to differences in alignment and analyzer settings between the CZTS-series and the  $\text{MoS}_2$  reference.

Details of the CZTS spectra are discussed in chapter 4. We cannot resolve any secondary interface species in these XES spectra. Since the spectra of precursor and CZTS in figure 5.13a did not show any

**Conclusion:**  $\text{MoS}_2$  is formed at the CZTS/Mo (or Mo/CZTS) interface even at low annealing temperatures. Cu and Sn concentrations at unprotected surfaces are heavily reduced when annealing is performed either in UHV or ambient environment. A kinetic model of this decomposition has been presented in [86]. The remaining surface resembles ZnS or ZnO depending on the availability of oxygen.

Sn spectra of liftoff CZTS back sides resemble the precursor at all temperatures and show SnS and Sn-oxides while Sn spectra of CZTS front sides are almost single phase after standard annealing. Cu also shows an increasing contribution of a secondary phase.

A metallic Sn (Sn metal or Mo-Sn alloy) phase occurs when Mo is sputter deposited on the CZTS precursor. A TiN interlayer can effectively prevent reactions at the CZTS/Mo interface.

In summary, we observed a stabilization of secondary phases, especially of Sn, at the  $\text{MoS}_2$ -back contact. To overcome potential harmful effects of this multiphase backside, the back contact needs to be modified.



## Chapter 6

# SnS solar cell absorber with ZnO contact layers

### 6.1 SnS solar cells

SnS as inexpensive, earth-abundant absorber material [141] with a direct band gap of (1.1-1.4) eV [142–144] and an absorption coefficient of  $10^4 \text{ cm}^{-1}$  that crystallizes in an orthorhombic structure. The SnS phase is stable over a wide range of temperatures and a range of Sn-S-ratio that can easily be reached experimentally [145]. It shows intrinsic p-type doping at desirable concentrations due to  $V_{\text{Sn}}$  defects and no detrimental deep centers when grown under suitable condition according to defect formation enthalpies calculated in [146].

With these properties SnS is a very good starting point to find solar cell absorber materials. Sn-S compounds combined with additional elements yield a variety of interesting light absorbing compounds [147, 148], among them the CZTS system.

Phase stability and formation enthalpies for pure SnS have also been theoretically investigated and promise a practical material in production [149].

Efficiencies of pure SnS solar cells are, however, still below 5% [150–152].

**ZnO contact layers** are used as buffer material to investigate the chemical and electronic interaction at the interface.

For this SnS material,  $\text{ZnO}_x\text{S}_{1-x}$  contact layers have been studied e.g. to successfully make solar cells with over 4% efficiency [152] using a  $\text{SnO}_2$  interlayer and N-doping to reduce the free electron concentration in the buffer.

The same mechanism can apply in ZnO, where we have intrinsic n-doping primarily by oxygen vacancies ( $V_{\text{O}}$ ) and Zn interstitials ( $I_{\text{Zn}}$ ) as main defects [153, 154]. The resistivity can be increased with N incorporation [155] since N on O sites acts as an acceptor in ZnO that can compensate the intrinsic n-doping [156].

### 6.1.1 Sample preparation

Our SnS was grown by ALD [152, 157, 158]. The surface was intentionally oxidized by air exposure for one day at room temperature before contact layers of ZnO (or N-doped ZnO) were ALD-deposited. Figure 6.1a shows the easiest possible sample structure without any interface interaction or surface oxidation of SnS. The expected structure after surface oxidation and deposition of doped or undoped ZnO contact layers is shown in Figure 6.1b.

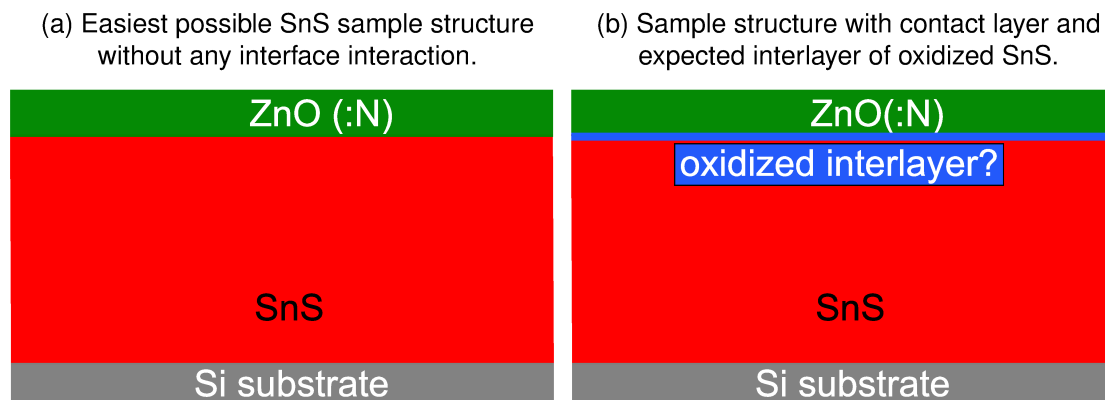


FIGURE 6.1: The ZnO/SnS sample structure grown on Si substrates with (doped and undoped) ZnO contact layers.

## 6.2 Chemical structure of the SnS-ZnO interface

The impact of the contact layer deposition on the oxidized surface was investigated with HAXPES measurements using excitation energies of 2 keV and 6 keV.

Survey spectra are shown in figure 6.2 and reveal all chemical signatures that we expect. We see Sn and S core levels and Sn Auger lines from the absorber and Zn and O core levels and Auger lines from the contact layers. Additional Cl and C (and O) signals will be treated separately and are expected to have no influence on our findings for the main elements.

Measurements with higher photon flux (see figure A.19 and A.20), performed at beamline 15XU at SPring-8 synchrotron, are shown for completeness.

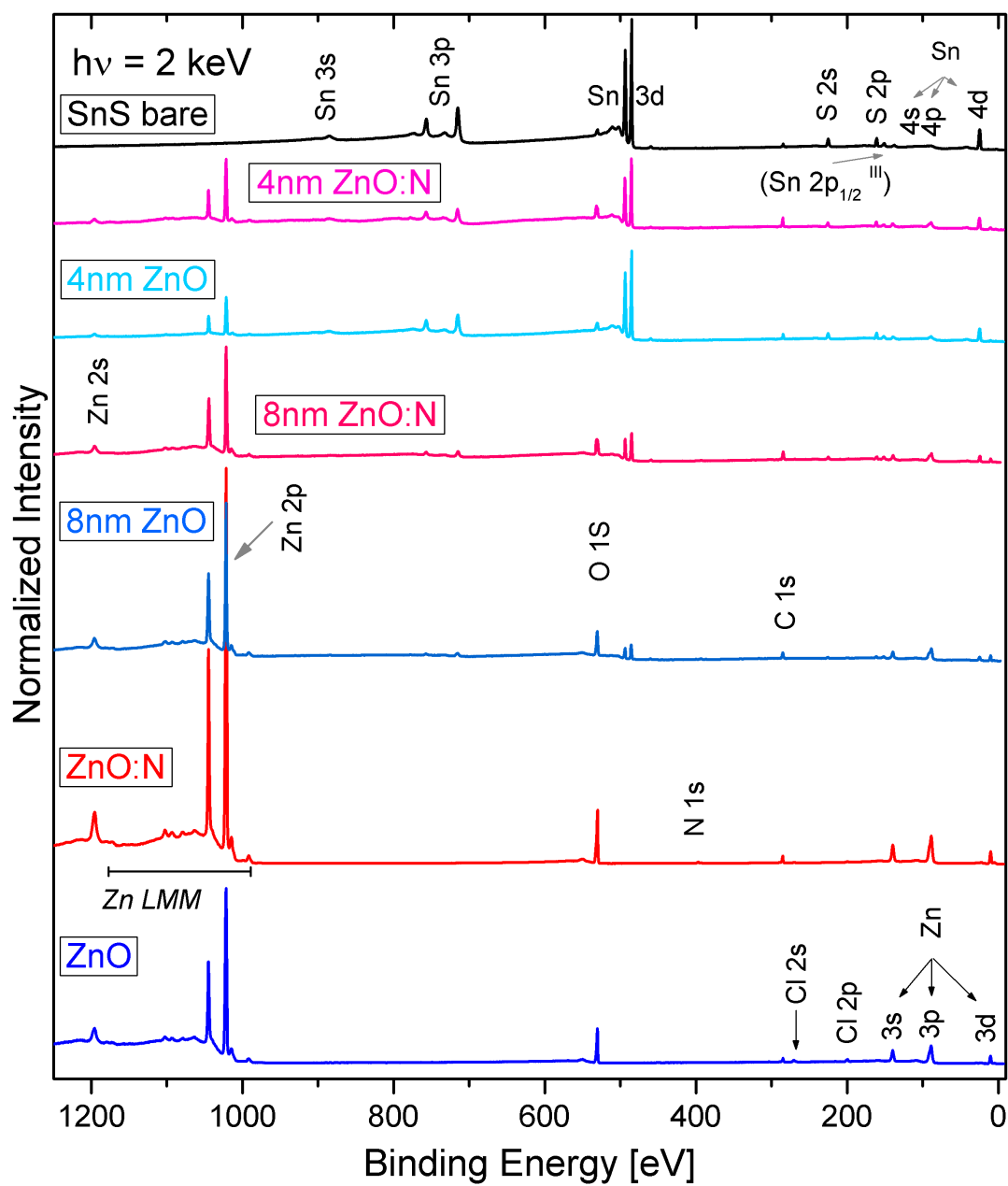


FIGURE 6.2: HAXPES survey spectra of the SnS series. Vertical offsets have been added for clarity.

## 6.2.1 SnS-side of the interface

Core levels are used to determine the chemical changes in the samples.

The Sn  $3d_{5/2}$  signal was measured with excitation energies of 2 and 6 keV as shown in figure 6.3.

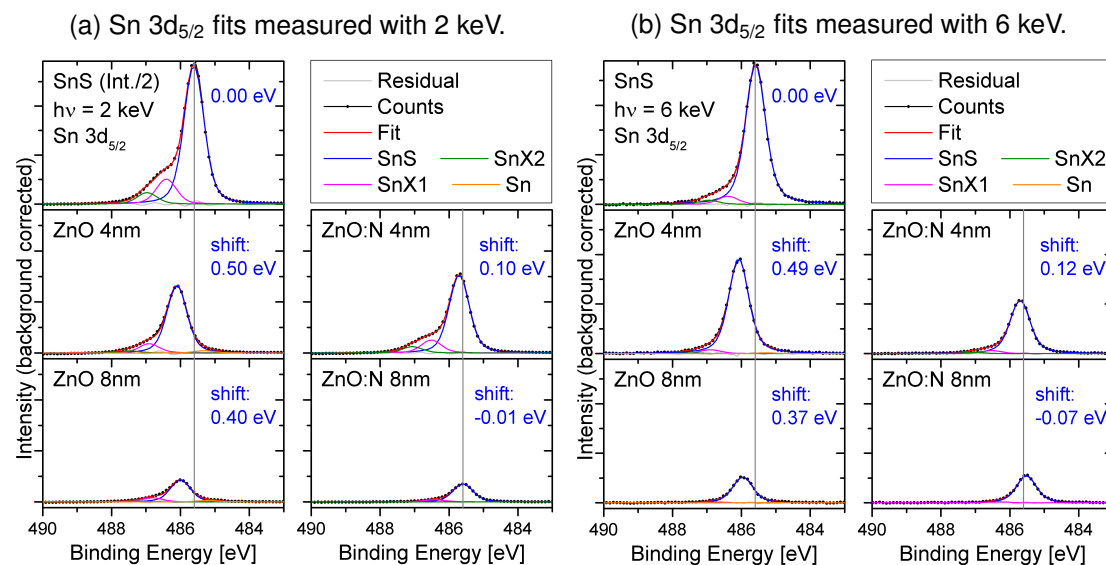


FIGURE 6.3: Sn  $3d_{5/2}$  spectra and fits measured with 2 and 6 keV for both contact layer materials.

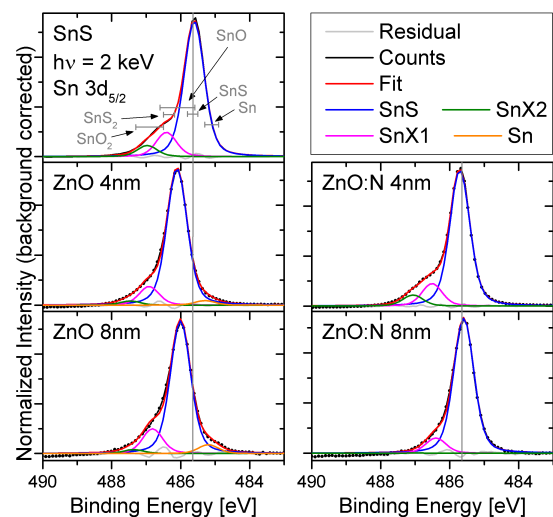


FIGURE 6.4: The Sn  $3d$  2 keV HAXPES fits have been normalized to the main peak height.

The fits of Sn species measured at 2 keV have been normalized to the main peak height in figure 6.4. The evolution of secondary species is more directly visible and typical energy ranges for relevant species are shown.

The attribution of species firstly follows the differences between the binding states  $\text{Sn}^0$ ,  $\text{Sn}^{2+}$ , and  $\text{Sn}^{4+}$  as e.g. found for Sn-oxides [125, 159, 160]. Direct attributions of  $\text{Sn}_x\text{S}_y$  species are found in comparison to [161, 162]. The dominant signal (blue line) comes from SnS. The orange species at lowest

$E_B$  that only appears at the interface between SnS and undoped ZnO layers is metallic Sn. The green species SnX2 at highest  $E_B$  must be  $\text{SnO}_2$  or another highly oxidized species like  $\text{SnSO}_x$ . The remaining SnX1 (magenta line) appears in the range of several possible compounds ( $\text{SnO}$ ,  $\text{SnS}_2$  but also  $\text{Sn}_2\text{S}_3$  or partly oxidized SnS).  $\text{SnS}_2$  was found to irreversibly decompose to SnS [163, 164], only to form under strict stoichiometry at high temperatures [165], and high partial pressure of S [86]. Also considering larger (absolute) formation enthalpies of oxides compared to sulfides (see table 4.3)



and of SnS compared to SnS<sub>2</sub> (and Sn<sub>2</sub>S<sub>3</sub>) [149] we therefore attribute the species ranging above 486 eV (magenta) to substoichiometrically oxidized SnO<sub>2-x</sub>, mostly containing SnO-like bonds. This phase has also been observed previously in the transition from SnS to SnO<sub>2</sub> [125, 166].

The bare SnS (top row) shows a strong SnS peak and a shoulder composed of oxidized species (compare [167–169]). The formation of SnO<sub>x</sub> with x approaching 2 but staying smaller in particular in the initial phase of oxide formation has been studied for air-exposed SnS before [166]. At higher excitation energy which means higher IMFP (see page 150), these species lose in relative intensity. This confirms our expectation of an oxidized surface mainly composed of SnO<sub>2</sub> and SnO (or SnO<sub>2-x</sub>) with pure SnS underneath.

The 6 keV measurements also support the statements derived from the 2 keV measurements which show the secondary species more pronounced due to the higher surface sensitivity.

We clearly see metallic Sn for the undoped material. In contrast, the 4nm ZnO:N sample looks very similar to the bare SnS and even though for the 8nm ZnO:N the SnX2 species is nearly gone, there is still no metallic Sn.

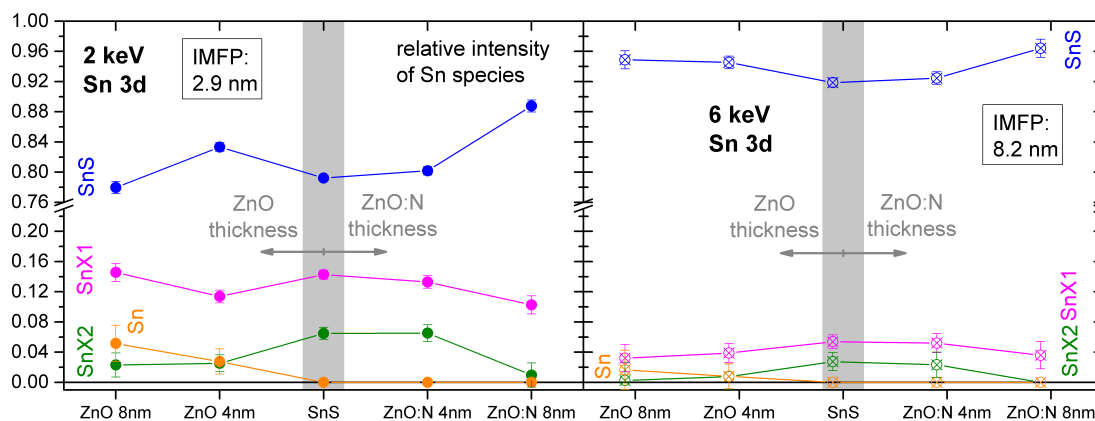


FIGURE 6.5: Relative intensities of Sn species measured with different  $E_{exc}$ .

The relative intensities of the Sn species for all HAXPES measurements are shown in figure 6.5. The SnS is shown in the center and samples with doped and undoped contact layers are on the left and right side, respectively. A break has been included in the Y-axis for better visibility of the smaller contributions. We see that the contribution of oxidized species generally shows a decrease for thicker layers while the SnS contribution increases. This reduction of the oxidized SnS layer is in accordance with the expected affinity to oxygen according to reaction enthalpies (see table 4.3 on page 76). The Sn covered by undoped ZnO shows a metallic species that cannot be found with doped ZnO. This shows that the two contact layer materials have a different chemical impact on the SnS surface.

Well above 90% of the Sn signal comes from SnS for all 6 keV measurements. The 2 keV measurements are much more surface sensitive (compare page 150). Here, SnS

contributes with around 80%. The contribution of the surface and interface species consequently is approximately twice as big.

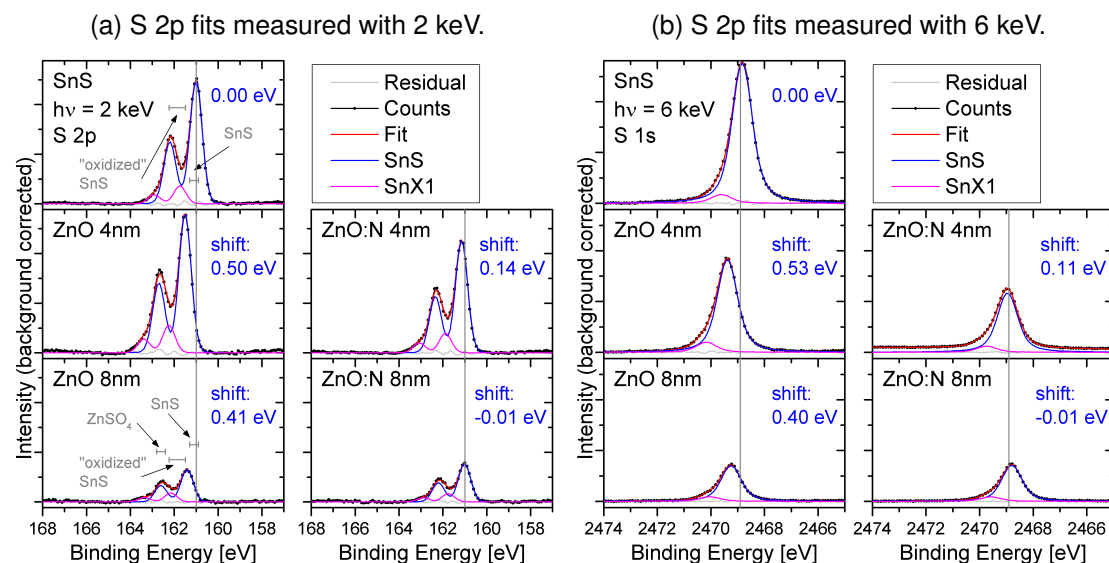


FIGURE 6.6: S 2p spectra and fits measured with 2 and 6 keV for both contact layer materials. The S  $2p_{1/2}$  and  $2p_{3/2}$  contributions have been added for clarity.

The sulfur lines in figure 6.6 show a surface oxidation, too. Here we find the dominant SnS species (blue line) and one oxidized SX1 surface species that shows a weaker relative signal at higher excitation energy. It is impossible to distinguish S lines from SnS and SnS<sub>2</sub> [161]. An additional S-species like SX1 at oxidized surfaces has been reported ([161, 162]) without identifying the specific species or composition. Any oxidized SO<sub>x</sub>-compound is usually found in a higher E<sub>B</sub>-range around 163-168 eV [89], however, ZnSO<sub>4</sub> has been reported below 163 eV and no SnSO<sub>4</sub> or SnSO<sub>3</sub> reports could be found. SO<sub>x</sub>-compounds need to be bound to a metal, so the best explanation for SX1 is a SnSO<sub>x</sub> or ZnSO<sub>x</sub>. This would be in agreement with the observed oxidized Sn-species SnX2. The composition of this compound cannot be calculated due to unclear species distribution and O-speciation.

The relative intensity of the oxidized SX1 species for sulfur is shown in figure 6.7 along with the respective results from Sn 3d fits for the SnX1 and SnX2 compound. With the different IMFP for the shown core levels, the contribution of the oxidized surface (or interface) species cannot be compared directly. To compensate for the IMFP differences, the relative amount of surface oxide was multiplied with the respective IMFP value (IMFP  $\propto$  probed volume). The good agreement between the resulting values at the two different E<sub>exc</sub> for each individual element show that the requirement of a very thin surface oxide is valid for our samples.

The remaining differences in the relative intensity of the oxidized contribution of S and Sn as shown in figure 6.7 are due to different amounts of oxidized Sn and S and therefore show off-stoichiometry from a possible Sn<sub>x</sub>O<sub>y</sub>S<sub>z</sub> compound. We find a reduction of both Sn-species and an increase in the SnX1. This means, they cannot be the same

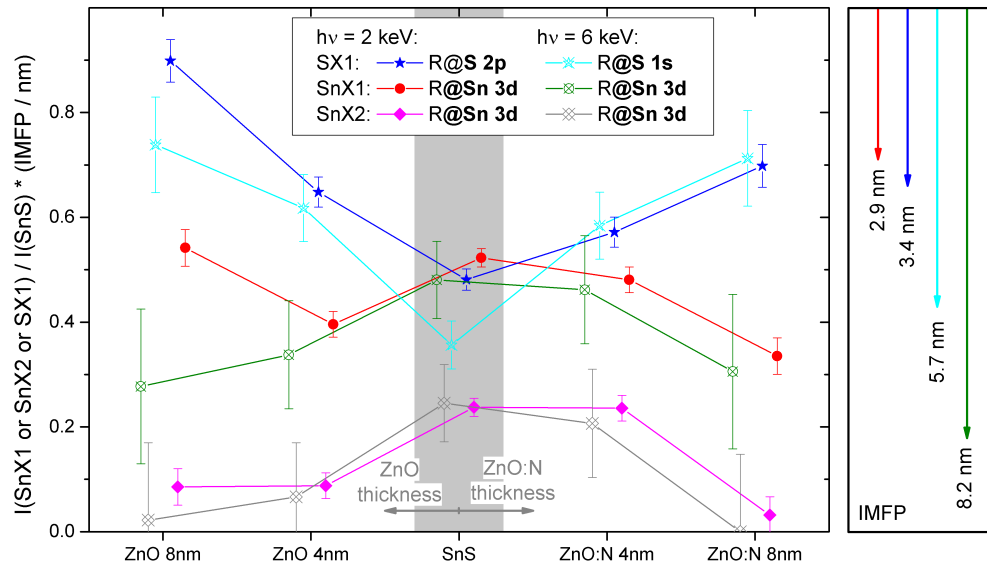


FIGURE 6.7: Relative intensities of SnX and SX species in Sn (dots) and S (stars) fits measured at different core levels and different  $E_{\text{exc}}$  compared to SnS. Full symbols are measured with  $E_{\text{exc}}$  of 2 keV and crossed symbols were measured using 6 keV. The values have been multiplied with the respective IMFP shown on the right side to account for the varying surface sensitivity of the photoelectrons as explained in equation 2.2. Values are shifted horizontally for better visibility.

species throughout the series.

A part of the SnX1 and SnX2 is reduced and transforms into SnS (or metallic Sn). At the same time the incoming ZnO precursor reacts with some of the S and O at the interface causing an increase in the amount of SX1 in the spectra. The undoped ZnO reduces the Sn so effectively that metallic Sn is formed.

The best possible attribution is therefore SnX1 as SnO and SnX2 as SnO<sub>2</sub> including a possible SnSO<sub>x</sub> signal that cannot be distinguished. This species also contributes to the SX1 signal. During the buffer deposition, all oxidized species are partly reduced, resulting in the SO<sub>x</sub> component bound to Zn that can still contribute the strong SX1 signal while the SnX1 and SnX2 intensities decrease. The additional formation of new ZnSO<sub>x</sub> with S from the absorber is also possible.

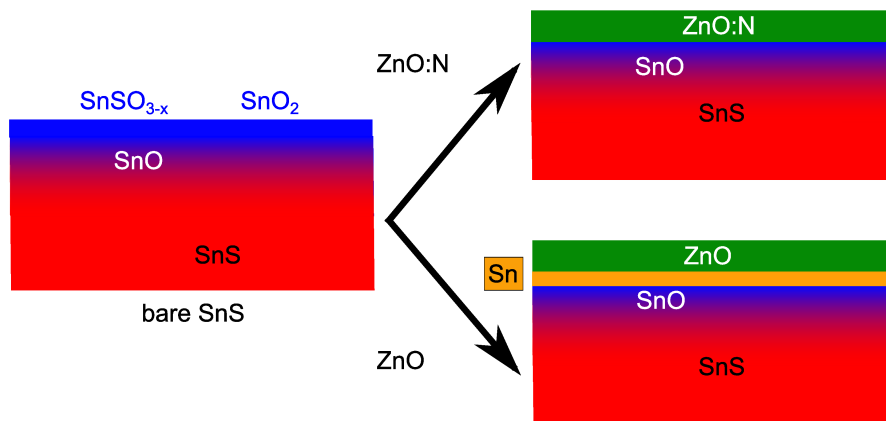


FIGURE 6.8: Chemical structure of the ZnO:N/SnS and ZnO/SnS interface drawn according to HAXPES results. The layer thicknesses are not to scale and inhomogeneous distributions or clusters cannot be resolved.

We can draw the chemical structure of the oxidized SnS at the interface now as shown in figure 6.8, based on HAXPES fits of Sn and S lines at different excitation energies. As main difference we see the formation of metallic Sn for undoped contact layers, represented by orange material at the interface. The  $\text{SnX}_2$  species is mostly removed by the ZnO deposition. We expect a decomposition to Sn metal or SnO and a bonding of the sulfite group to Zn. We cannot comment on the in-plane distribution of species so the most probable scenario with strongest chemical impact on the surface and remaining SnO below the surface is drawn in 6.8.

## 6.2.2 ZnO-side of the interface

The cover layers are analyzed by fitting HAXPES spectra of the Zn  $2p_{3/2}$  line measured at 2 and 6 keV.

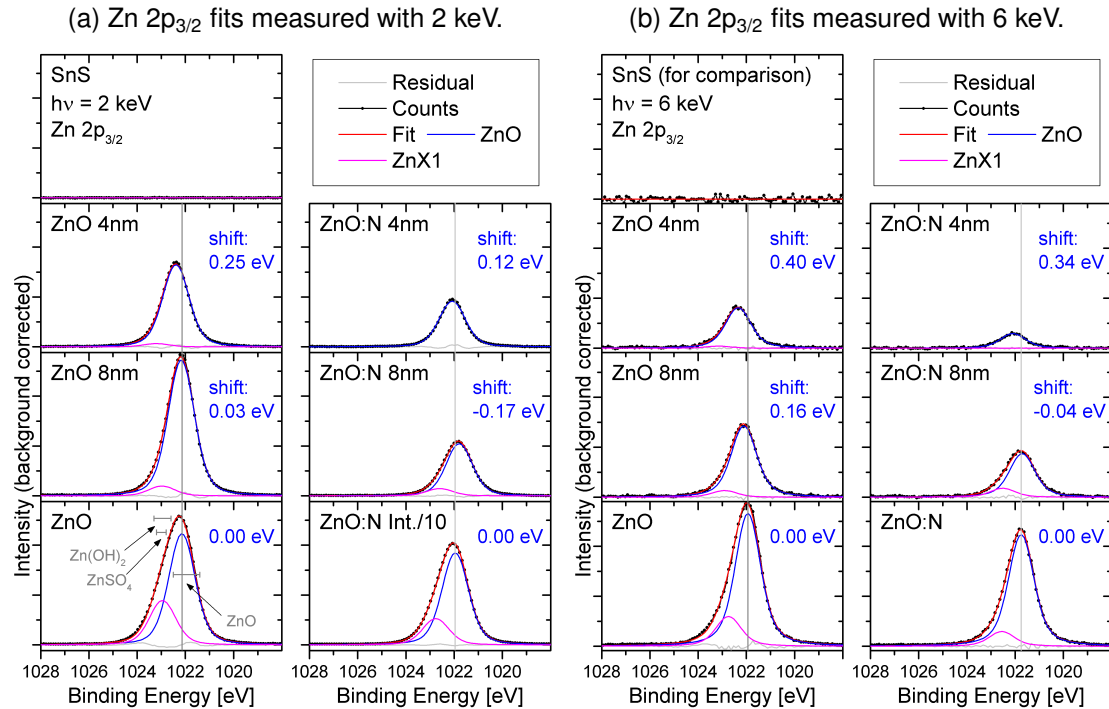


FIGURE 6.9: Zn  $2p_{3/2}$  spectra and fits measured with 2 and 6 keV for both contact layer materials.

We find a dominant ZnO species here, accompanied by a secondary species that we attribute to a mixture of  $ZnSO_x$  as discussed in the S-species attribution and predominantly  $Zn(OH)_2$  for thicker layers (compare e.g. [90, 170]).

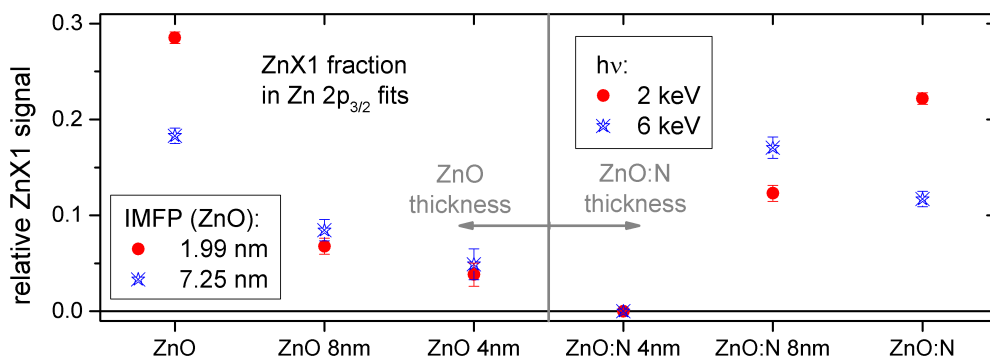


FIGURE 6.10: Relative intensity of Zn species. Full symbols are measured with  $E_{exc}$  of 2 keV and crossed symbols were measured using 6 keV.

In figure 6.10 the relative ZnX1-intensity with respect to the overall Zn signal is shown. The stronger relative ZnX1-signal at 2 keV excitation compared to 6 keV for both thick reference layers shows that ZnX1 is a surface species since the amount of signal from

deeper in the material is significantly increased with higher excitation energy. In the thin layers on SnS we can measure through the full ZnO-thickness with both excitation energies so we get very similar values for both energies. For the thin doped sample no ZnX1 is detected. The 8nm ZnO sample shows nearly identical values at both excitation energies as well.

The stronger ZnX1 signal for 6 keV measurements on sample ZnO:N 8nm is surprising. If it was caused by interface species we would have seen in for thin layers, too. We also have to consider a surface contamination that affected the surface in the UHV-chamber in between the measurements.

The O 1s does not allow to distinguish between the different O species. We have already identified at least 2 different Sn-O compounds and two Zn-O compounds and expect additional surface species e.g. bound to C (see figure A.18). The peaks shown in 6.11a do not allow to identify all these species. We expect the ZnO and SnO to contribute to the sharp feature at lower  $E_B$  and hydroxides and sulfites to contribute to the broader signal at higher  $E_B$ .

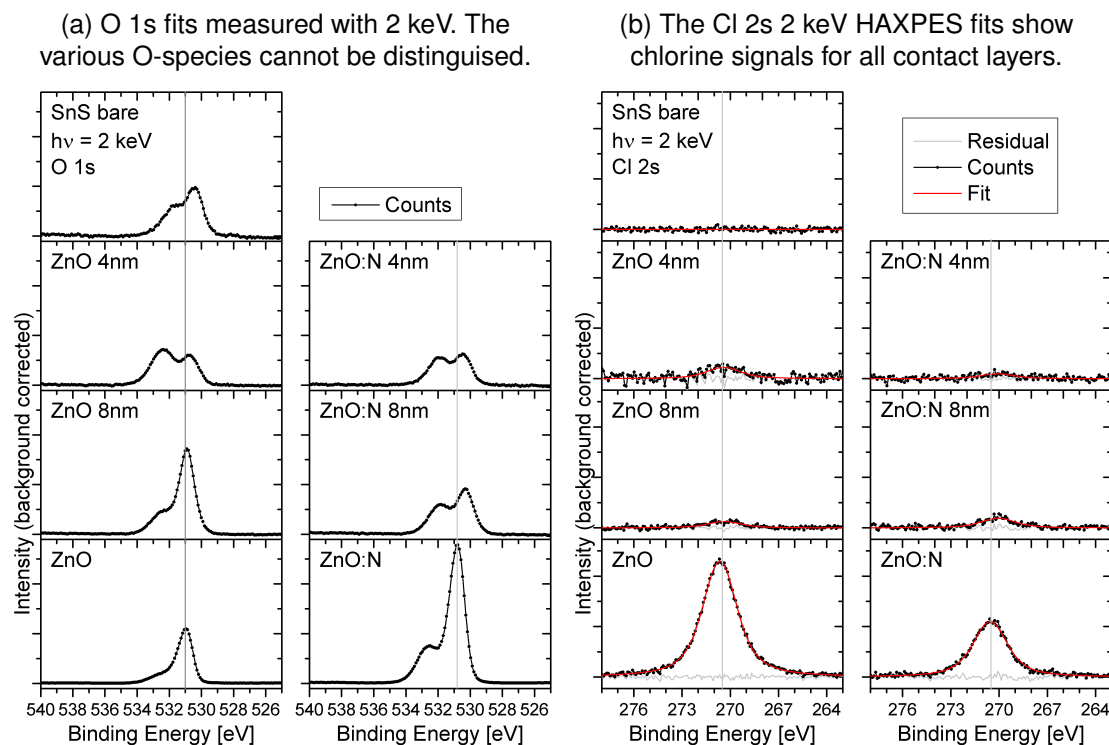


FIGURE 6.11: O 1s and Cl 2s peaks spectra measured with 2 keV for both contact layer materials.

We find small Cl peaks in all the doped and undoped ZnO contact layers (see figure 6.11b). The origin of the Cl is not definitely known. We assume a Cl source in the ZnO-ALD process since we also find Cl-signals in fresh samples (both 8 nm layers) that have been measured in the chamber after other samples were measured without detectable Cl signal.

The HAXPES system has been used to measure a SnCl-samples right before the thick references were measured. Additional Cl-contamination from that sample cannot be

ruled out but no other Cl-free samples have shown any indication for Cl cross contamination in the measurement system.

**Conclusion:** To summarize the findings, the essential points are shown in figure 6.12.

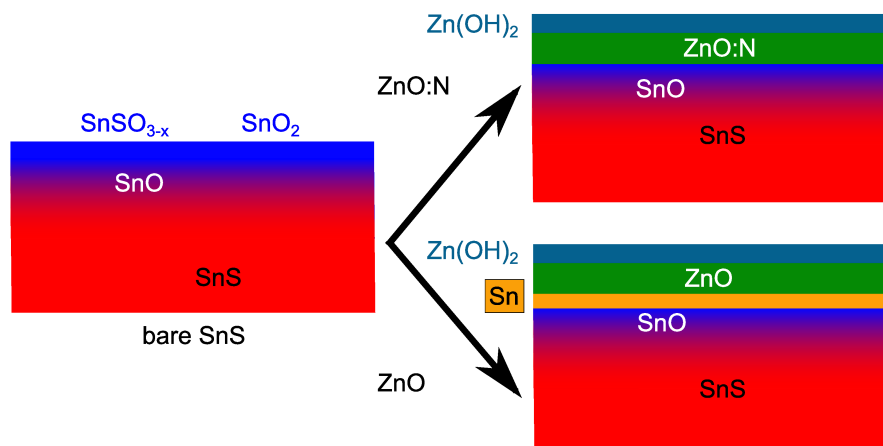


FIGURE 6.12: Chemical structure of the ZnO:N/SnS and ZnO/SnS interface drawn according to HAXPES results. The layer thicknesses are not to scale and inhomogeneous distributions or clusters cannot be resolved.

We see a mild reduction of the oxidized SnS surface in case of a ZnO:N deposition and a Zn(OH)<sub>2</sub> as surface species on top of the contact layer.

The undoped ZnO, in contrast, reduces the oxidized SnS much more aggressively resulting in the additional formation of metallic Sn at the interface. The Zn(OH)<sub>2</sub> surface layer is found on these samples, too.

SnO<sub>2</sub> or SnSO<sub>x</sub> species are heavily reduced by the ZnO-precursor for both buffer materials. Possible surface SnSO<sub>x</sub> on the bare sample and interface ZnSSO<sub>4</sub> is not shown in the graph. Small remaining quantities of SnO<sub>2</sub> are also not specifically depicted.

### 6.3 Electronic structure of the SnS-ZnO interface

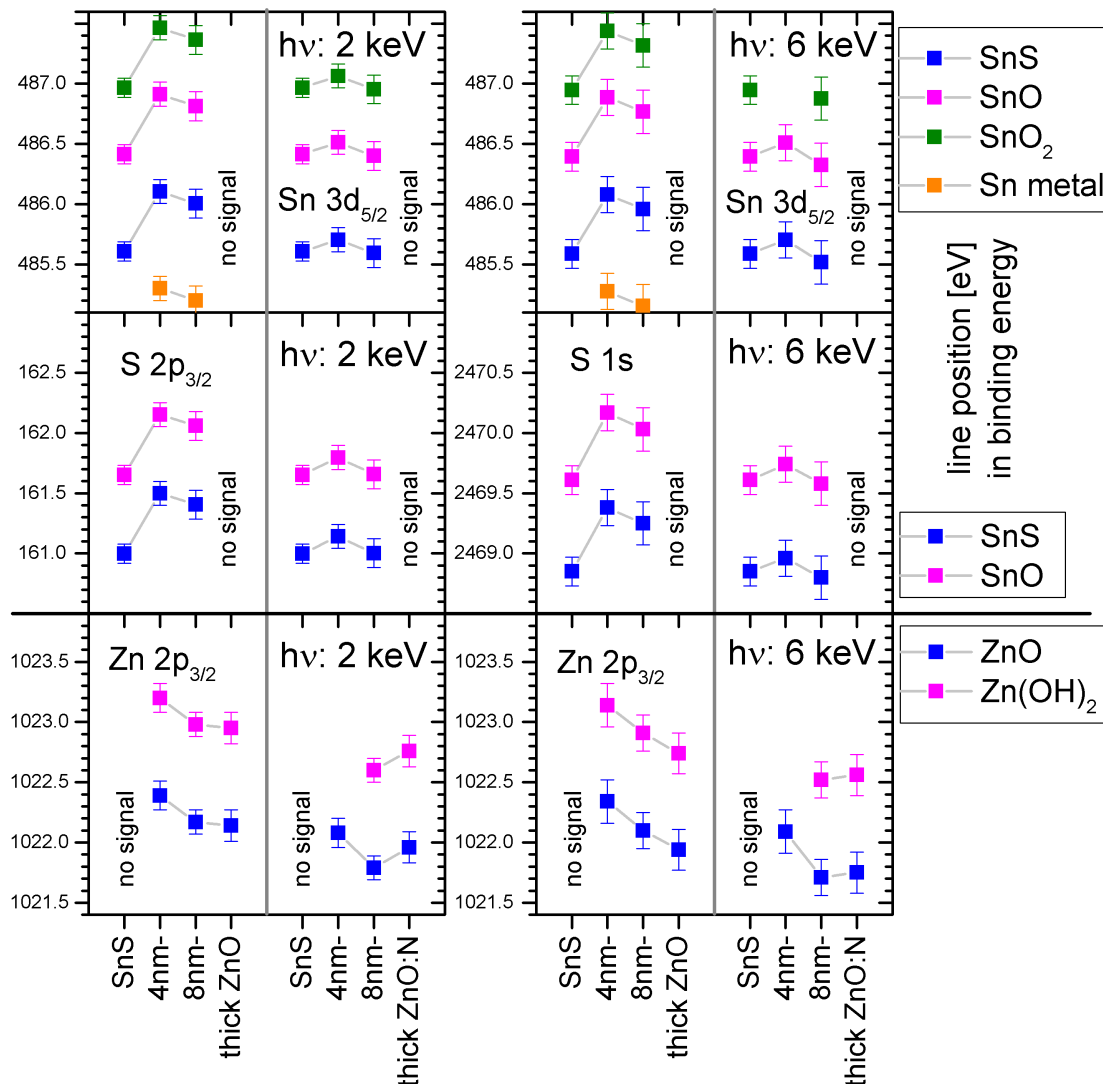


FIGURE 6.13: HAXPES line positions of the fitted core levels in direct comparison. Except for C and O on top, we find the 2 keV measurements on the left and the 6 keV measurements on the right side.

To investigate the electronic structure of the interface, the development of the core level position as shown in figure 6.13 is used. The Sn and S lines originate exclusively from the absorber layer. For these, the line shifts of the samples against each other match for both elements and both excitation energies. The shifts observed in the Zn lines from the contact layers match for both excitation energies within the error bars. Average values of the peak shifts for each side are calculated from these positions.

VB spectra have been measured for all samples as shown in figure 6.14. For the SnS sample we can recognize a typical SnS valence band structure as measured and calculated in [161]. The expected sharp and dominant SnS peak at 1.5 eV is broadened and surrounded by intensity at lower  $E_B$ . This can be attributed to SnO<sub>2</sub> with a strong



feature at 1.5 eV as shown in [161, 171].

ZnO spectra (lab-based) have been discussed in figure 4.53 (page 79). Differences in line intensity arise mainly from the different  $E_{exc}$ .

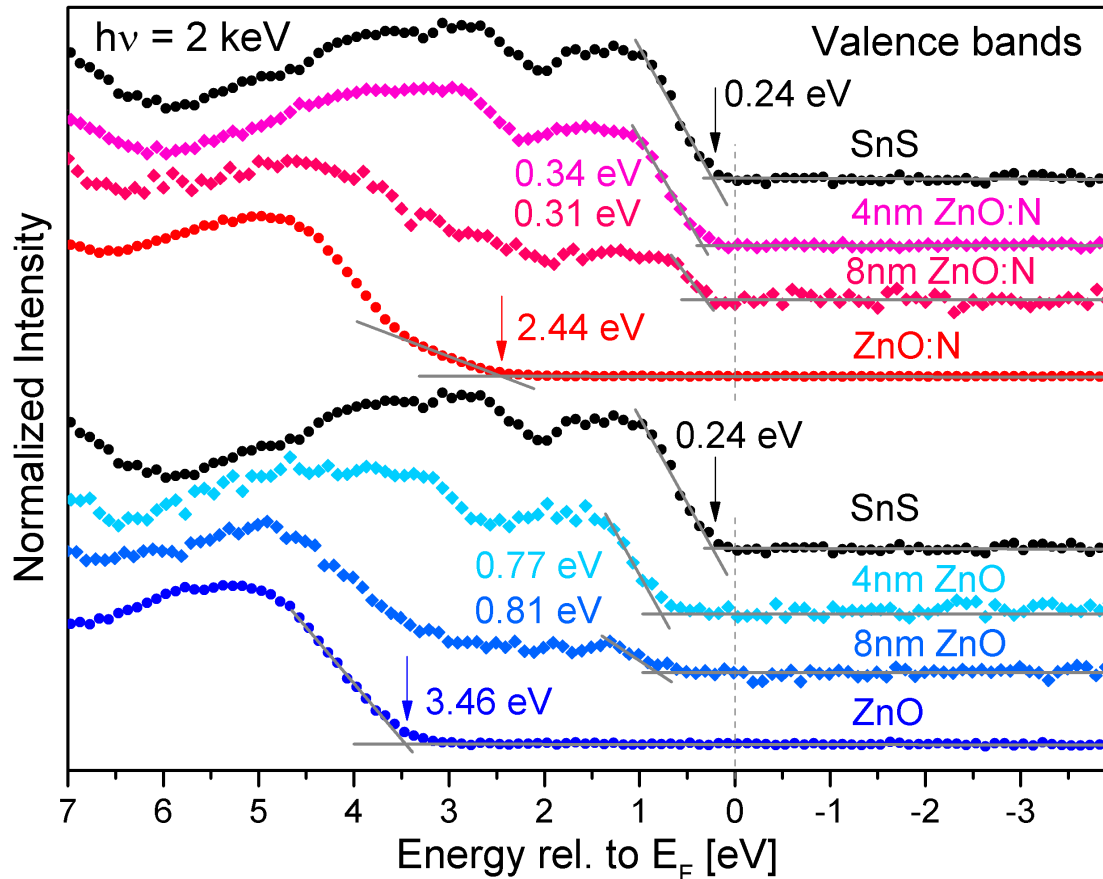


FIGURE 6.14: VB spectra of the SnS series measured with  $E_{exc}$  of 2 keV and normalized to the highest intensity in the shown region. The VBM values have been determined with linear approximations of the leading edge as drawn. Vertical offsets have been added for clarity.

The valence band structure of the buried SnS can easily be recognized in the thin layer samples. The VBM values have been determined by linear approximations of the leading edge. In the doped material (red line) the shift is much smaller than in the undoped thin layers (blue line). The error margin is  $\pm 0.1$  eV. The weak SnS-signal in the two 8nm samples increases the error margin to  $\pm 0.2$  eV.

In the valence band spectra of the thin ZnO layers on SnS, the structures at lowest binding energy come from SnS. VBM values obtained by linear approximation of the leading edge provide information exclusively from the SnS material. We get the interface induced shift in binding energy when we subtract the VBM value of the bare SnS material. This shift should follow the shift of the Sn and S lines seen in figure 6.13.

The band bending towards the interface can best be calculated from the positions of the sharp core level peaks. We assume bending towards the interface between Zn-material and Sn-material. The used lines are therefore Sn- and S-lines for the absorber side and Zn-lines for the contact layer side. The calculated shift is  $\Delta E = E_{\text{interface}} - E_{\text{thick}}$  where  $E_{\text{interface}}$  is the line position measured in a thin layer sample (4 nm, 8 nm) and  $E_{\text{thick}}$  is the line position found in the bare SnS or the thick ZnO or ZnO:N reference. Calculated values for different excitation energies (and lines for the absorber) are used to compute an average value shown in figure 6.15 along with the measured shifts directly seen for the valence band maxima.

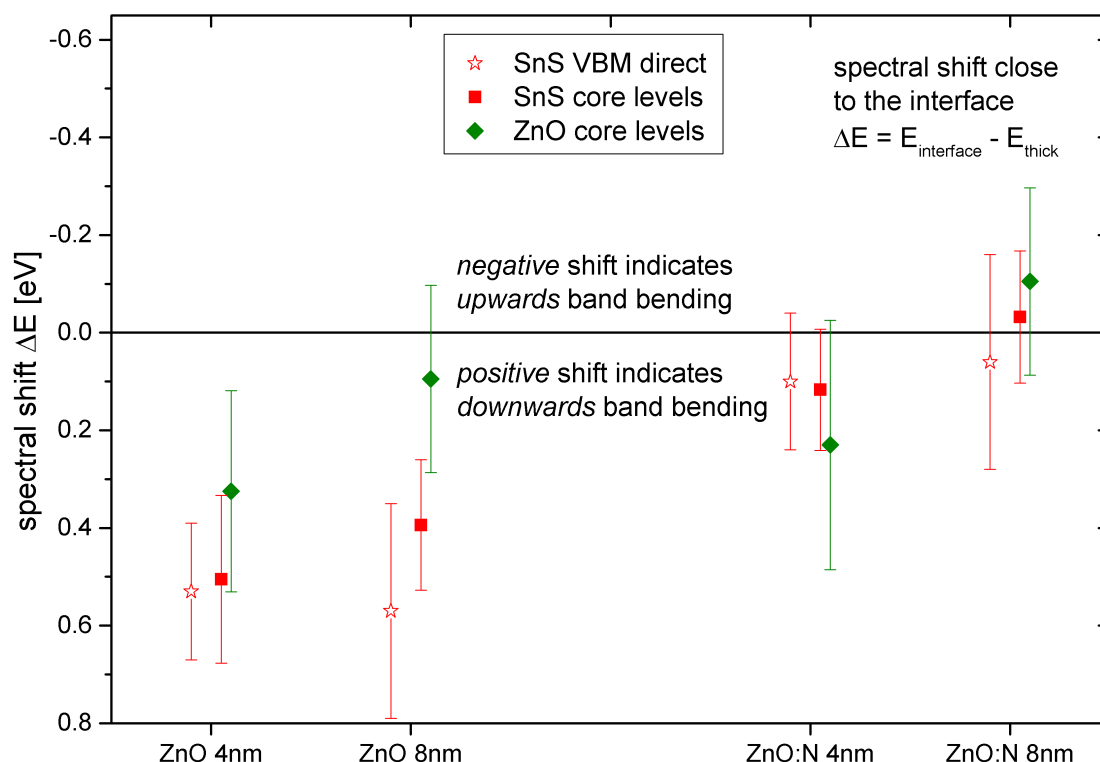


FIGURE 6.15: Spectral shifts obtained from averaged core level shifts on both sides of the junction and valence band analysis. The direct shift of the VBM that can only be seen for the SnS with lower VBM value compared to ZnO(:N) is shown for comparison. Horizontal offsets have been added for clarity.

Average values from the core levels give the most precise values and are drawn as red squares for the SnS side and green diamonds for the ZnO side. The direct linear approximation of the SnS VBM is shown as red stars and matches the SnS shifts within the error margin.

The Y-axis has a negative sign to show the negative  $\Delta E$ , that means upwards band bending, physically higher and vice versa.

We see a pronounced downwards bending towards the interface for both sides of the ZnO/SnS unction. The maximal shift is reached for *ZnO 4nm* with  $0.51(\pm 0.17)$  eV for the SnS and  $0.33(\pm 0.2)$  eV for the ZnO side.

The doped material (with lower charge carrier density) shows little to no band bending.

The value for  $ZnO:N$  4nm is  $0.23(\pm 0.26)$  eV for the absorber. For  $ZnO:N$  8nm we count the small values as 0.

We have to consider a generally increased error margin for the buffer-side, because the ZnO and ZnO:N was not grown on SnS but directly on a Si substrate. This difference causes additional uncertainty for the buffer references.

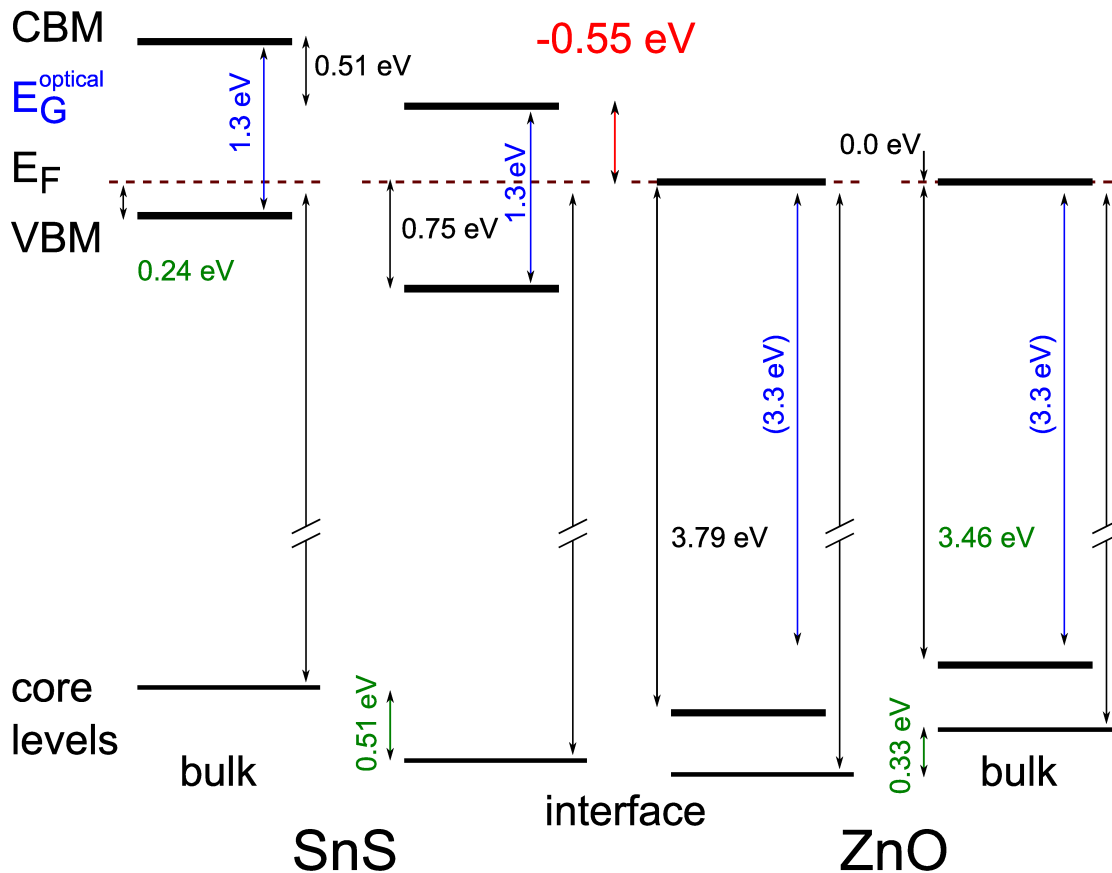


FIGURE 6.16: Band alignment of the ZnO/SnS structure. The bulk values are as measured far away from the interface. The two sides of the interface in the center of the graph illustrate the band bending at the ZnOS/CZTS contact area and the actual band alignment.

The band alignment of the two buffer materials on SnS looks very different according to the measured core level shifts and VBM values. The optical band gap of ALD ZnO with a value of 3.3 eV [79] has been used to align the conduction bands according to the measured VBM values and core level shifts. The cliff of 0.55 eV found for the ZnO/SnS junction combined with the metallic Sn species makes this a poor choice for a solar cell device because recombination will limit the solar cell performance. The strong downwards band bending on both sides of the junction combined with the large measured VBM for ZnO makes a larger band gap than the reported 3.3 eV for ZnO necessary.

The doped ZnO:N material without any significant band bending on either side of the junction shows a much smaller cliff of 0.2 eV when the assumption of a band gap of 3.3 eV is valid. This is a much better solar cell junction but an adjustment to a flat

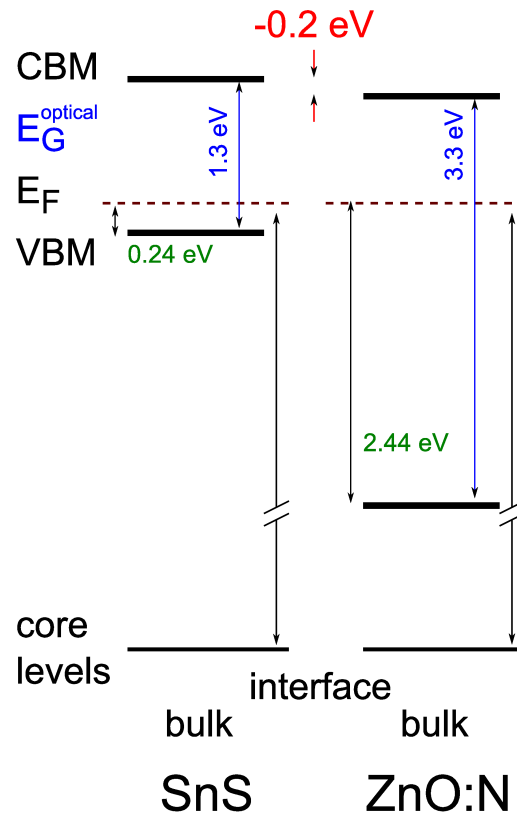


FIGURE 6.17: Band alignment of the ZnO:N/SnS structure. No band bending effect at the interface was measured.

conduction band or a small spike would make this interface more suited for solar cell applications.

**Conclusion:** The chemical and electronic structure of ZnO/SnS and ZnO:N/SnS using oxidized SnS absorber has been investigated with Synchrotron based HAXPES measurements.

The SnS material is heavily affected by ZnO deposition, resulting in metallic Sn formation. The doped ZnO:N reduces the SnS much less aggressively, affecting mainly the SnO<sub>2</sub> species. The contact layers show the formation of Zn(OH)<sub>2</sub> that is mainly at the layer surface.

The band bending is also changed by the modified interface structure.

The strong downwards bending for both ZnO and SnS that we find for undoped ZnO contact layers is drastically reduced if metallic ZnO:N contact layers are used. The effect can also be affected by metallic Sn at the interface.

The band alignment of both junctions shows a cliff in the conduction band. The smaller cliff of 0.2 eV for ZnO:N/SnS makes this junction much more interesting for solar cell applications than the ZnO/SnS with a large cliff of 0.55 eV.



## Chapter 7

# The (Cd,Zn)S:Ga / CuSbS<sub>2</sub> interface

### 7.1 CuSbS<sub>2</sub> as thin film solar cell absorber

In the field of abundant solar cell absorber materials (see chapter 1) CuSbS<sub>2</sub> is another alternative replacing the rare element In in the CuInS<sub>2</sub> with more abundant Sb [6]. It shows promising properties of good solar cell absorber materials like a direct band gap of 1.5 eV, intrinsic p-doping, and a high absorption coefficient [172–177].

After the material has proven to yield working devices [175, 178], the absorber material itself needs to be improved and the thin-film stack has to be adjusted to the new absorber to reach higher efficiencies. At this point the device heterostructure is adapted from similar materials like CIGSSe and CZTS (compare figure 4.1) including, in the ideal case, a specifically tailored buffer material between absorber and window layer. We evaluate the (Cd,Zn)S:Ga/CuSbS<sub>2</sub> as a potential buffer layer by examining the interface. In this partial device without the top layers (from the window upwards, see page 26 for an example of a full device structure) we call the (Cd,Zn)S-layers buffer layers, referring to the intended use in the full device. With Cd and Ga this buffer material contains two expensive elements and is toxic. The material used in the very thin buffer layer is, however, small compared to the absorber material.

#### 7.1.1 Sample preparation

CuSbS<sub>2</sub> absorbers were prepared by radio frequency magnetron sputtering on Mo-coated glass substrates as described in [176, 177].

The (Cd,Zn)S buffers were deposited by ALD after a mild KOH etch to remove Sb-oxides. Identical surface conditions can be reached by mild Ar<sup>+</sup> treatment (500 eV for

20 min) followed by low temperature annealing in vacuum (200°C for 60 min). This second procedure has been used to prepare the bare CuSbS<sub>2</sub> sample for PES in situ.

## 7.2 Chemical structure of the (Cd,Zn)S:Ga/CuSbS<sub>2</sub> interface

The impact of the buffer deposition on the CuSbS<sub>2</sub>-surface was investigated with HAX-PES measurements at  $E_{\text{exc}}$  of 2 keV and 6 keV.

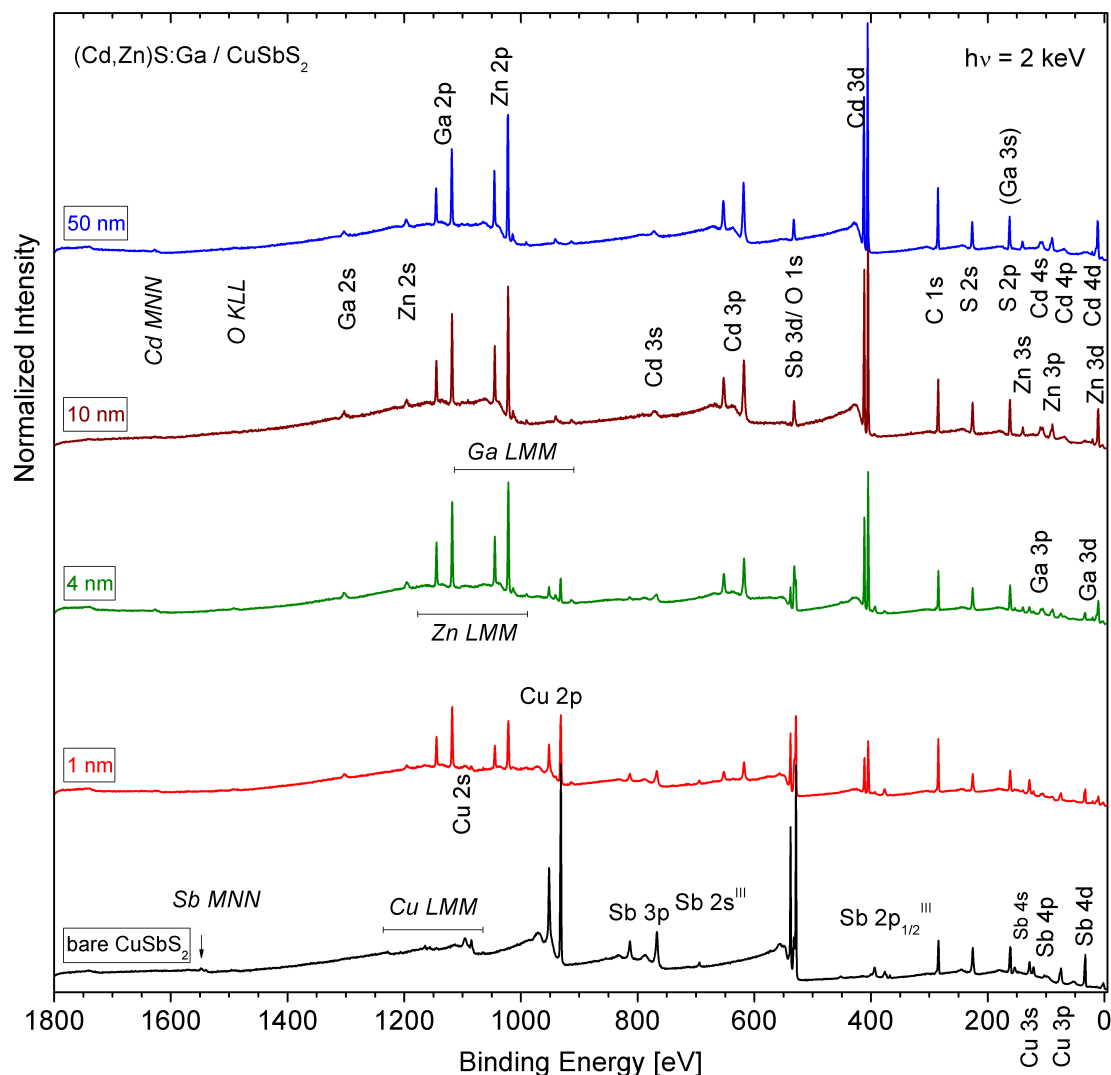


FIGURE 7.1: 2 keV HAXPES survey spectra of the CuSbS<sub>2</sub>-series. We find decaying Cu- and Sb-signals, increasing Cd-, Zn-, and Ga- signals and a rather constant S signature. Additional O and C peaks from surface species can be found. Vertical offsets have been added for clarity.

In figure 7.1 the gradual change of the signal from pure CuSbS<sub>2</sub> (black line) to pure (Cd,Zn)S (blue line) is visible. Most prominent peaks are Cu 2p and Sb 3d for the absorber and Zn 2p and Cd 3d for the buffer layer as well as Ga 2p that was used as dopant.



S 2p signals are found in both absorber and buffer material. We find additional surface C and O signals, presumably from transport and transfer of the samples. C in the buffer material can also originate from the ALD produre.

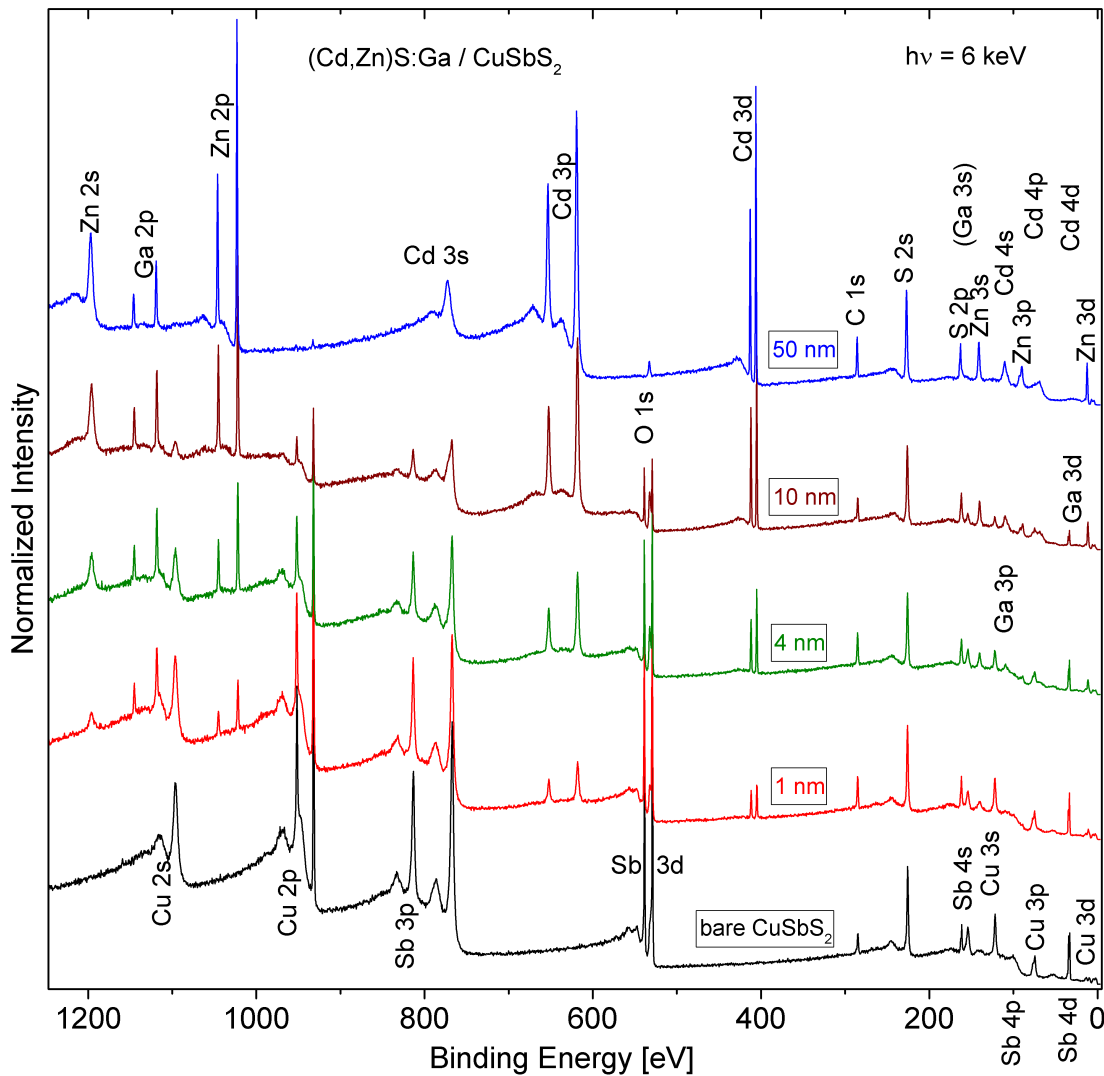


FIGURE 7.2: 6 keV HAXPES survey spectra of the CuSbS<sub>2</sub>-series with increased IMFP compared to 2 keV HAXPES. Vertical offsets have been added for clarity.

The 6 keV HAXPES spectra in figure 7.2 with higher probing depth show relatively stronger Cu and Sb signal from the buried absorber material compared to the Cd and Zn from the covering contact layer. Furthermore, the spectra are less affected by the very surface with potential modifications and contaminations. We can see decreased C and O signals.

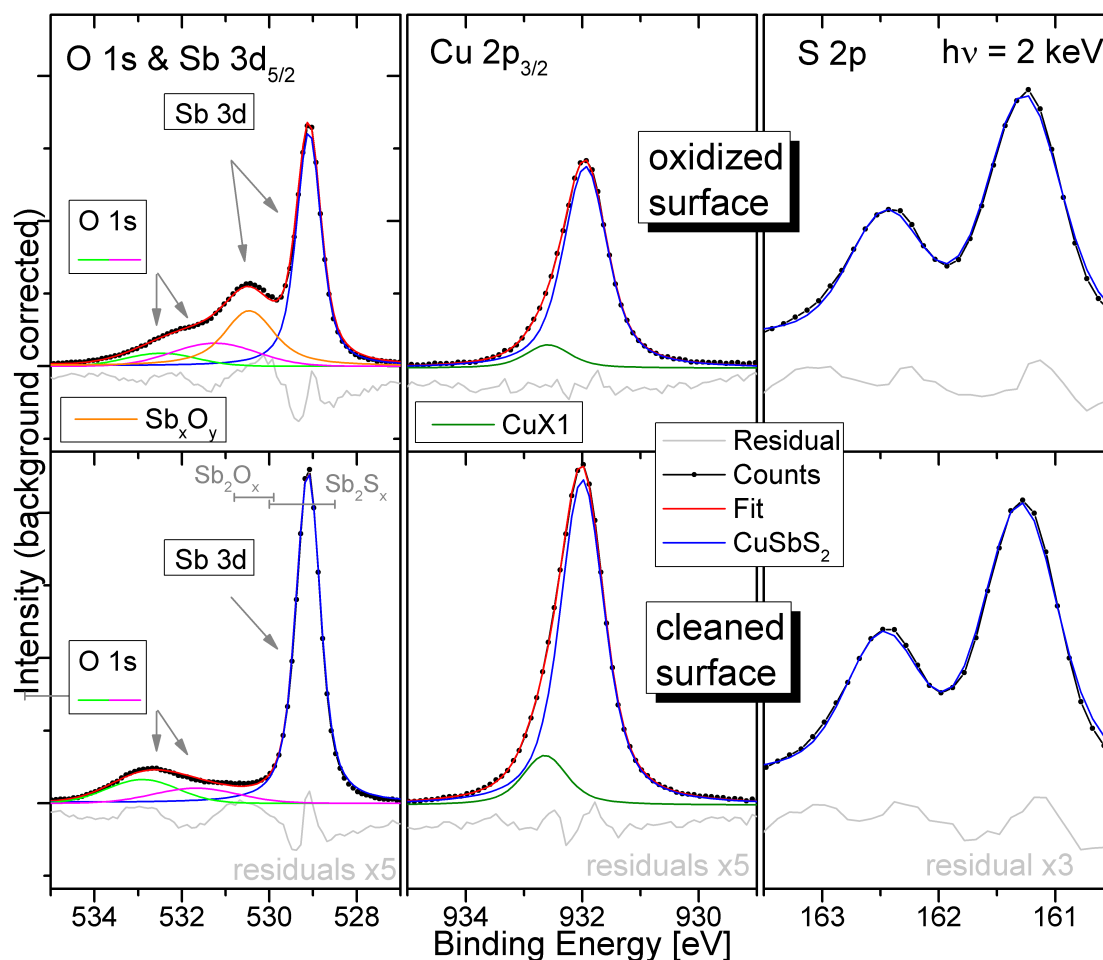


FIGURE 7.3: Core levels of Sb, Cu, and S from lightly oxidized CuSbS<sub>2</sub> and the cleaned surface. The only difference to the previously treated clean surface is visible in the Sb line.

The bare CuSbS<sub>2</sub> was briefly air exposed during the packing procedure after growth. It has been measured before and after in-situ cleaning. For further investigation (and in the shown survey spectra) the cleaned absorber is used. The surface was restored with a mild Ar<sup>+</sup> treatment and low temperature reannealing as described in section 7.1.1. The main differences after cleaning are in the Sb line. The lightly oxidized absorber surface shows an oxidized species for Sb as presented in figure 7.3 that is removed in the cleaning process. The remaining O species are therefore not bound to Sb. The Sb-oxide contributes to the oxide peak (magenta line) that is less pronounced for the Sb-oxide-free sample (figure 7.8). The O-species cannot be attributed to specific compounds. We also see an increase in the line intensity of the shown Sb 3d and Cu 2p that we explain with the removal of surface species that contain less Cu and Sb than the cleaner surface that is exposed after the cleaning procedure. For Cu 2p and S 2p we see no change in speciation. S also shows a small line intensity increase. The differences in the intensity increase, being bigger for Cu 2p than for Sb 3d and smallest for S 2p correspond well with the increasing IMFP at lower E<sub>B</sub>.

The extended VB regions measured at different  $E_{\text{exc}}$  are shown in figure 7.4. The spectral differences are caused by changes in information depth and the differing photoionization cross sections of the shallow core levels for varying photon energy  $h\nu$ . The biggest differences can be seen for the thin layers (1-10 nm thickness) where IMFP variations (see page 150) can significantly alter the ratio of signal from the buried absorber and the thin contact layer. With increasing (Cd,Zn)S thickness we see increasing Cd and Zn signals and decreasing Cu and Sb line intensities as seen in the survey spectra. Ga signals are present in similar intensity for all samples except for bare CuSbS<sub>2</sub>.

Valence band maxima measured with 2 keV and 6 keV HAXPES have been determined with linear approximations of the leading edge as shown in 7.5. We find a VBM value of 3.45 eV for the thick (Cd,Zn)S. The bare absorber shows a VBM of 0 eV for  $E_B=2$  keV and 0.15 eV for  $E_B=6$  keV. For 1 nm (Cd,Zn)S (0.15 eV and 0.35 eV) and 4 nm (Cd,Zn)S (0.15 eV and 0.35 eV) the difference in VBM is still present. Due to the different IMFP at the different  $E_{\text{exc}}$  this indicates surface band bending. It will be considered for the discussion of the band alignment. CuSbS<sub>2</sub>. The differences between the 2 keV and measurements and the less surface sensitive 6 keV results are best explained with surface band bending. The extremely small VBM value for the bare absorber shows the very p-type character of the absorber that can negatively affect the potential solar cell performance. This is caused by the potentially less extended space charge region and the shorter minority carrier lifetime at increased doping densities. The 10 nm (Cd,Zn)S spectrum measured with 2 keV shows a very high VBM value. The weak signal from the buried absorber (better seen in the 6 keV measurement) is not very well resolved here. This is the weakest signal that is still visible of the buried absorber material. We have to consider a larger error margin here due to the very small signal that disappears in the measurement noise close to the VBM. At higher  $E_{\text{exc}}$ , the VBM for this sample can be determined at 0.4 eV.

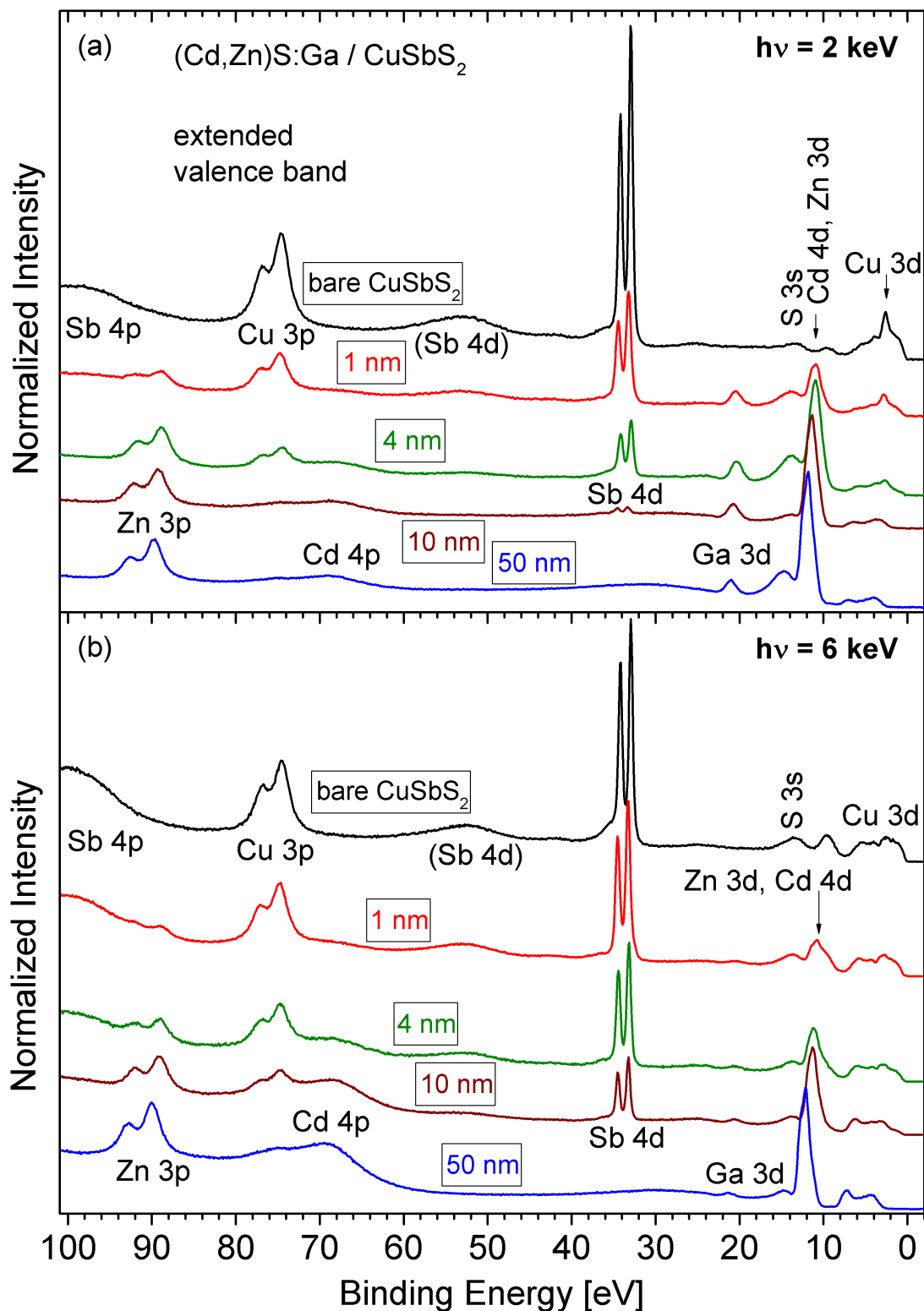


FIGURE 7.4: HAXPES VB spectra of the CuSbS<sub>2</sub>-series measured with 2 keV (a) and 6 keV (b). Vertical offsets have been added for clarity. We find decaying Cu and Sb signals and increasing Zn, Cd, and Ga-signals.

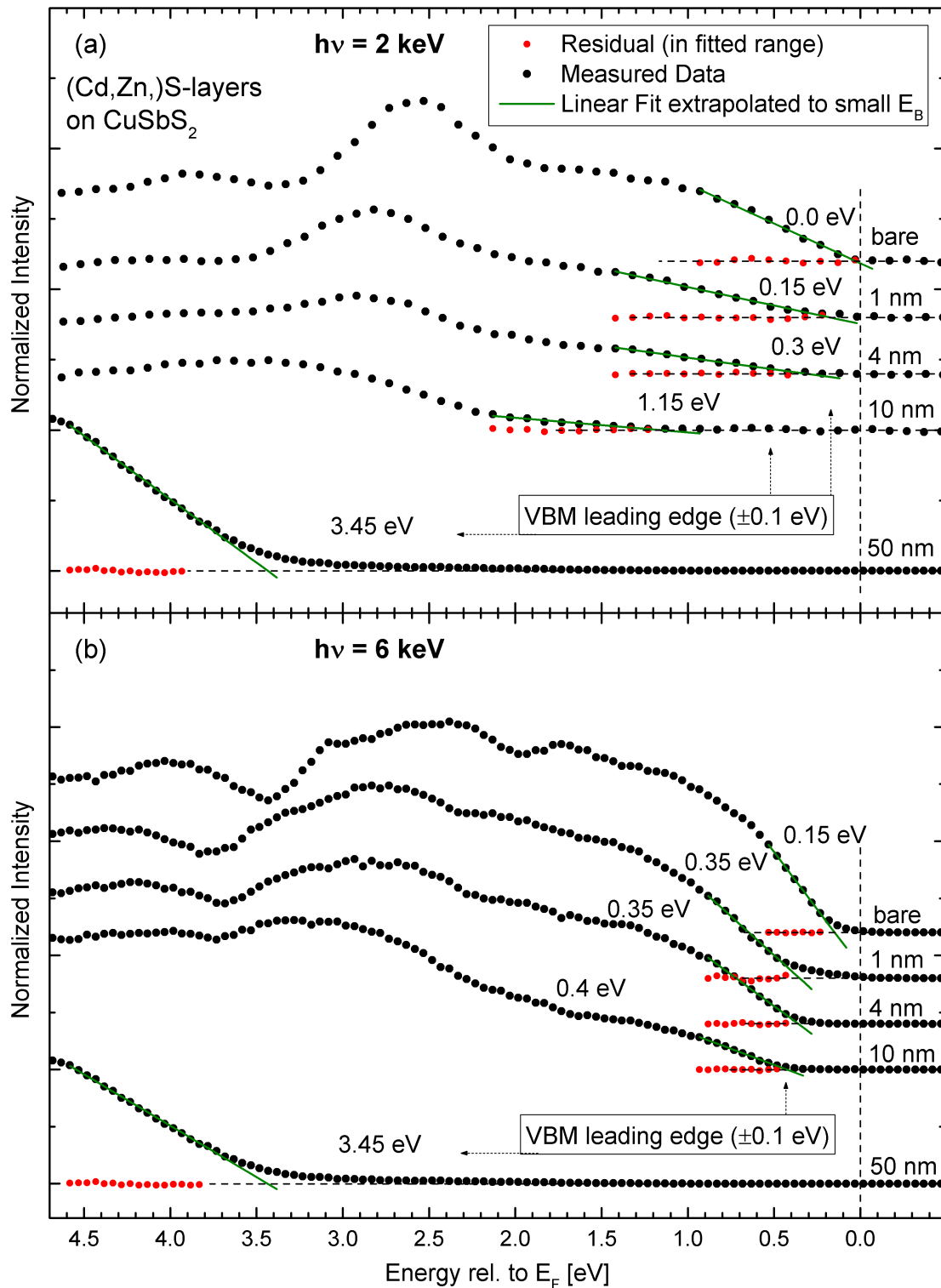


FIGURE 7.5: HAXPES VBM fits of the CuSbS<sub>2</sub>-series measured with  $E_{\text{exc}}$  of 2 and 6 keV normalized to the highest intensity in the region. We used linear approximations to determine the leading edge. Vertical offsets have been added for clarity.

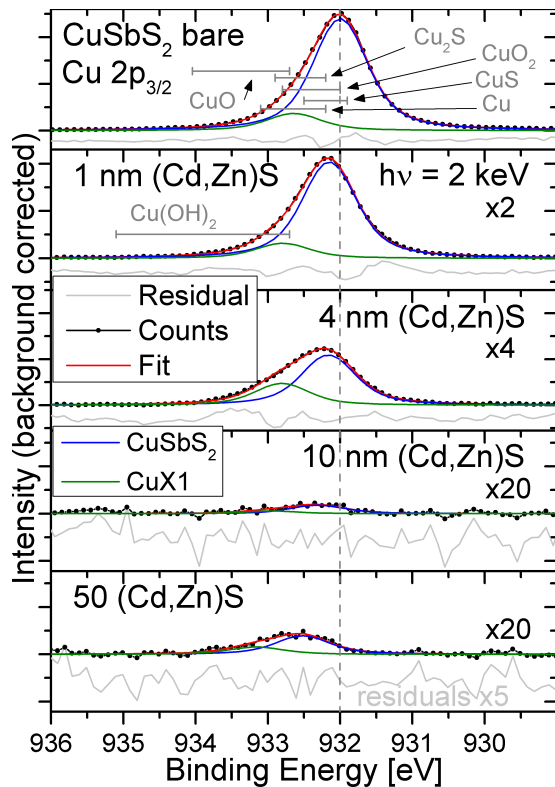


FIGURE 7.6: Cu  $2p_{3/2}$  fits of spectra measured with 2 keV HAXPES.

reference and the thickest (Cd,Zn)S layer on CuSbS<sub>2</sub>.

A clear Cu-signature is found. The line intensity in counts per second, normalized by the photon flux of the enstation, appears smaller for the 10 nm sample which has been measured with lower photon flux. A possible explanation for a Cu signal is always bad alignment of the sample that exposes the Cu-sample plate to the beam. This scenario is always carefully avoided in the alignment process and no unexpected Cu signals could be found on any other sample. We observe the Cu signal in measurements at two different synchrotron facilities. The probability that misalignment caused similar amounts of Cu signal exclusively for the identical 50 nm sample twice at different synchrotron facilities is negligible. The Cu therefore must come from the absorber material or an external contamination.

The Cu  $2p_{3/2}$  fits are shown in figure 7.6. We see a dominant CuSbS<sub>2</sub> species (blue line) that shifts to higher  $E_B$  after buffer deposition and a second species that we attribute to Cu that is not bound in the absorber crystal but mobile in an unclear chemical state, most probably bond to S, O, or  $-(OH)_2$ . The signal from the 50nm sample can only be explained with such mobile Cu diffusing through the buffer. We can rule out a thinned or scratched buffer layer since no Sb could be detected on this sample that would appear if the (Cd,Zn)S layer was damaged. To prove the presence of Cu and rule out a Ga LMM line from the buffer layer as origin for this signal, we use the Cu 3p signal as seen in the extended valence band 7.4 which has a smaller photoionization cross section of 22.6 at 2 keV, compared to 74.5 for Cu  $2p_{3/2}$ . In figure 7.7 we see the contrast between the respective region measured on a CdS

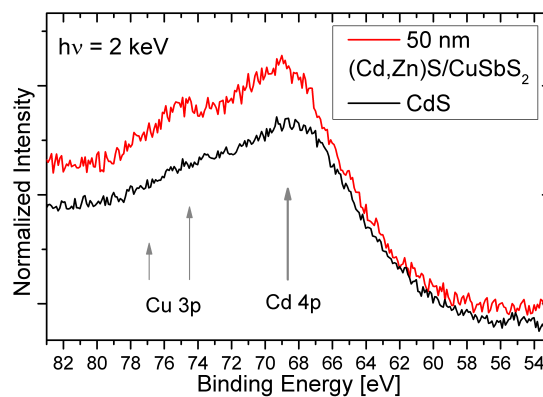


FIGURE 7.7: Cu 3p spectra of 50 nm CuSbS<sub>2</sub> (red line) and a CdS reference spectrum (black line), measured at 2 keV.

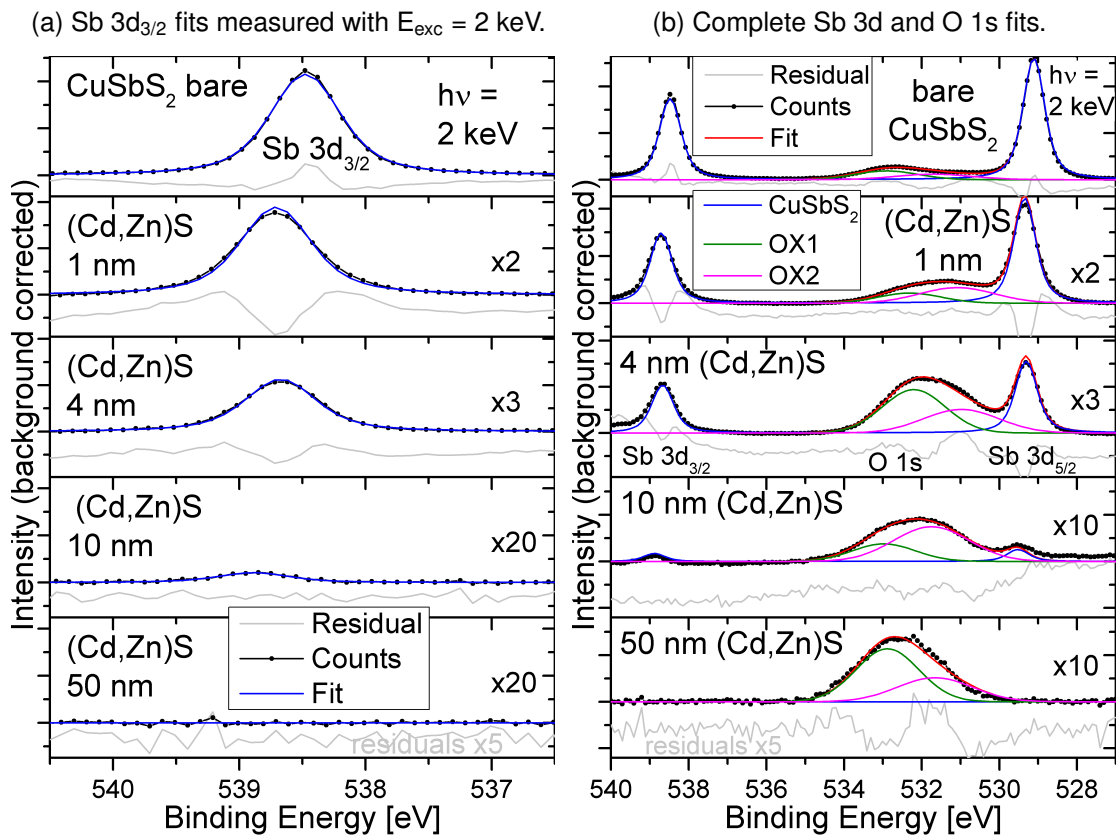


FIGURE 7.8: Sb 3d and O 1s fits. The separate fit of Sb 3d<sub>3/2</sub> was used to minimize effects of the long linear background for the fit.

The Sb 3d<sub>3/2</sub> peak in figure 7.8a shows a single species and a shift to lower  $E_B$  as was seen for Cu lines. The 3d<sub>5/2</sub> overlaps with O 1s as shown in figure 7.8b. The oxygen line shows at least two species. Possible species are e.g. Cu-oxides, carbonates and hydroxides. The stronger O-signal measured on the (Cd,Zn)S layers indicates that O has come in contact with the buffer layers, most probably by unintended air exposure.

The absorber composition changes as shown in figure 7.9. The results calculated with core level intensities at different  $E_{exc}$  show an offset of nearly 0.1. The higher Cu-content measured with lower  $E_{exc}$  suggests a Cu-rich surface. Cu-rich Cu-Sb-S compounds that could be present here are Cu<sub>3</sub>SbS<sub>3</sub> [179] or Cu<sub>12</sub>Sb<sub>4</sub>S<sub>13</sub> [176].

The trends for each individual  $E_{exc}$  within the series match each other nearly perfectly. This suggests varying Cu/Sb-ratios for the individual samples but very similar surface enrichment with Cu. The downwards trend of the Cu amount for thicker buffer layers suggests a Cu loss in the ALD system during buffer growth or Cu diffusion away from the measured surface and near-surface. Cu-depleted surfaces during annealing have been observed before [175]. A high mobility of Cu in the material was shown in the production of CuSbS<sub>2</sub> with a diffusion process of Cu into Sb<sub>2</sub>S<sub>3</sub> that proves to be effective at temperatures as low as 300°C.

The Cu 2p signal found on top of the 50nm sample measured with 2 keV HAXPES (figure 7.6) already suggested the mobility of Cu out of the absorber and into the buffer,

but contradicts the loss of Cu from the measured surface-regions.

The Cu-signal on the 50 nm sample could be explained with Cu-particles moved onto the sample surface during sample breaking or mounting. From what we see for the other samples, a Cu-rich CuSbS<sub>2</sub> surface and Cu-loss during the buffer-ALD is a plausible explanation.

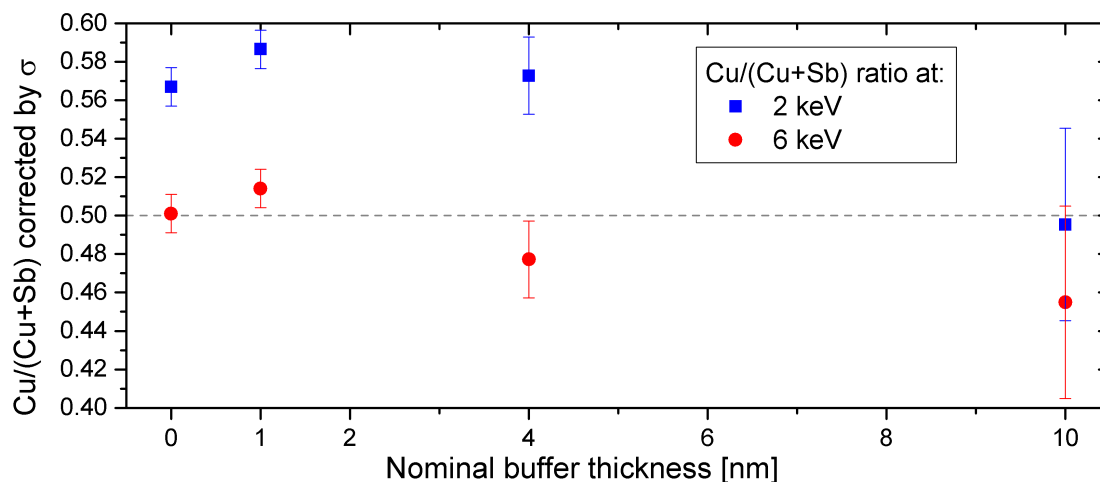


FIGURE 7.9: Ratio of Cu and Sb calculated from Cu 3p and Sb 4d line intensities in the extended VB spectra measured with 2 keV and 6 keV HAXPES.

The fits are shown in figure A.21 and A.22. The fitted areas are divided by photoionization cross sections. Minimal differences in the transmission function of the analyzer and in the IMFP of the photoelectrons are neglected since these shallow core levels are only separated by 40 eV.

The buffer thickness can be calculated from the signal decay of absorber lines as described in equation 2.1 using IMFP values shown in table A.2. Results from different Cu and Sn lines are shown in figure 7.10. The weighted average values indicate a growth speed that exceeds the expected buffer growth as indicated with gray lines.

The the intensity development of the secondary Cu species (gray stars) results in buffer thickness values consistently below the average. The effect is, however, too small to support the assumption of diffusion of Cu into the buffer. The origin of the Cu-signal on the thickest buffer layers stays unclear.



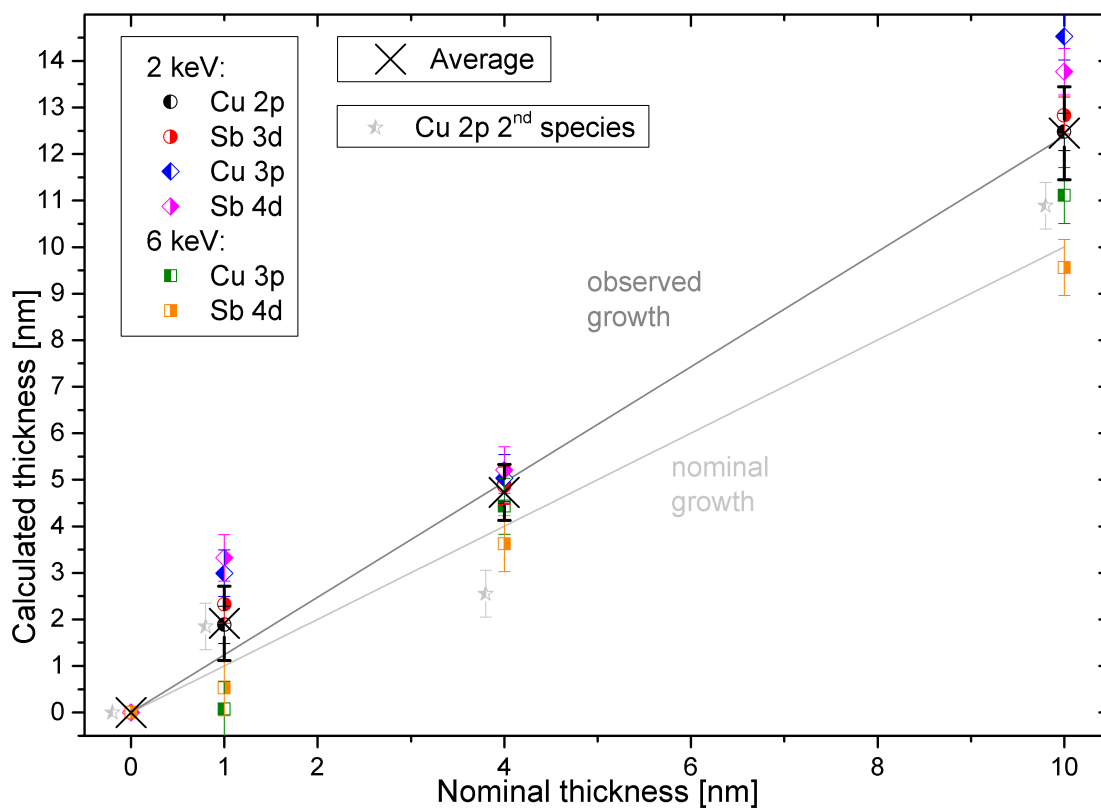


FIGURE 7.10: Buffer thickness calculated from Cu and Sb signals measured with 2 keV and 6 keV HAXPES. The additional fits of shallow core levels are shown in figure A.21 and A.22. Our measured sample thicknesses exceed the nominal values as indicated with gray lines. Values for the additional Cu species are shown with a small X-shift for clarity.

Sulfur is present in both the absorber and buffer material. As shown in figure 7.11 the S 2p doublet and S 1s peak from the different materials can clearly be distinguished in HAXPES spectra using 2 keV (figure 7.11a) and 6 keV (figure 7.11b).

We see a decreasing absorber signal (blue line) and an increasing buffer signal (green line). The signal from buried CuSbS<sub>2</sub> (blue line) shows a shift to lower  $E_B$ . This is in agreement with the shift observed for Cu and Sb signals. The S signal from (Cd,Zn)S also shows a shift to higher  $E_B$ . We expect the shifted features to belong to the identical species since no decreasing signal at the original position is observed. we do not see indication for sulfates (not in the shown range).

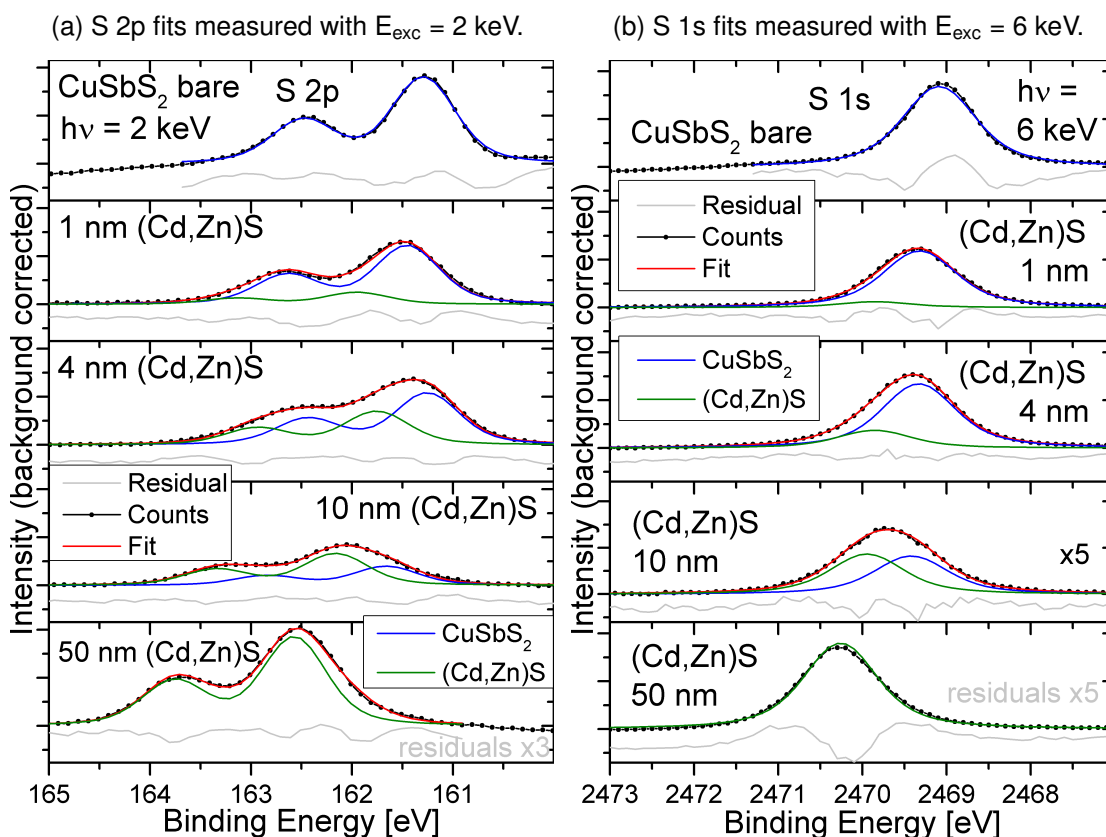


FIGURE 7.11: Sulfur line fits measured with 2 and 6 keV HAXPES. The more surface sensitive 2 keV spectra show weaker signals from the buried CuSbS<sub>2</sub> absorber.

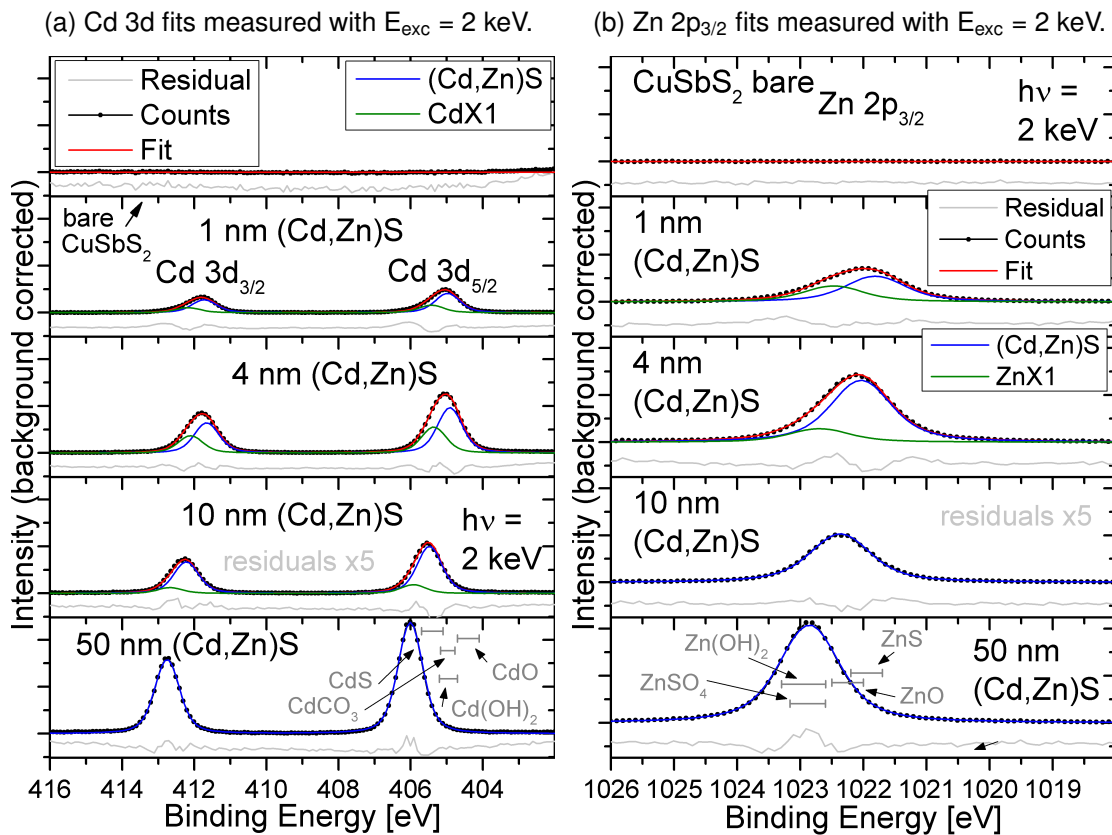


FIGURE 7.12: Cd 3d and Zn 2p<sub>3/2</sub> fits with increasing intensity of the buffer signal (blue line) for thicker layers. Both elements show a broadening represented by the small secondary species (green line) close to the interface.

An additional interface species for Cd 3d and Zn 2p<sub>3/2</sub> can be seen in figure 7.12a and b, respectively. This increased binding energy can be caused by stress due to the lattice mismatch between the absorber and buffer or by chemical changes. The increased O-signal seen in figure 7.8 for samples with buffer layer makes oxides and hydroxides probable. The relative energy position of ZnS and ZnO speaks in favor of ZnO formation at the interface. The CdO is expected on the low-binding-energy side of CdS-like compounds. Inhomogeneous doping and band bending over the measured spot could also cause a broadening of the measured peak. With thicker layers, Cd, Zn and S peaks shift to higher  $E_B$ . We can rule out surface charging caused by bad conductivity in the layer because this would cause different shifts for different photon flux during HAXPES. The consistent results measured at BESSY II and SPring-8 indicate, that the shift is caused by the sample itself.

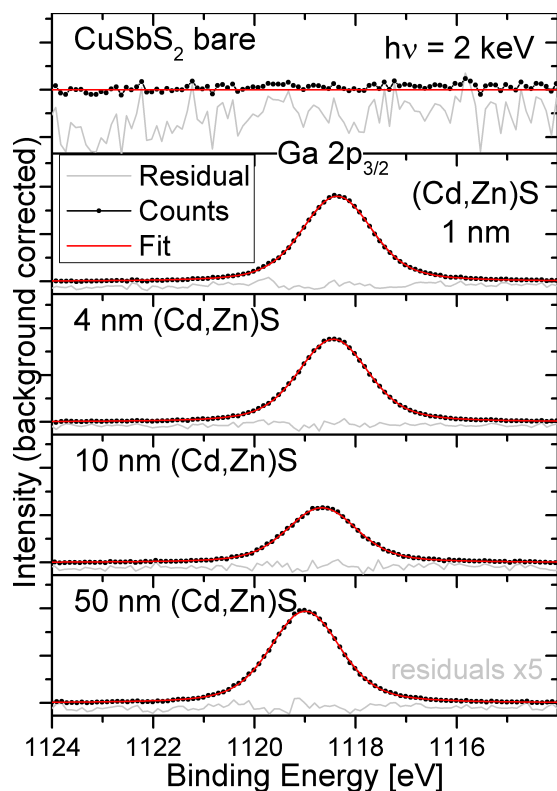


FIGURE 7.13: Ga  $2p_{3/2}$  fits show a single species from Ga that was doped into the layer.

Ga 2p spectra as seen in figure 7.13 also show a shift to higher  $E_B$  with increasing layer thickness. If we consider the expected peak development when changing from 2 keV to 6 keV compared to Zn 2p (and S 2s) in the survey spectra (see table A.3), we see that Ga and Zn show a very similar intensity development. Only the 50 nm sample shows lower Ga 2p intensity for 6 keV which means Ga accumulation at the surface.

The comparison of Ga 3d in the extended valence band regions in figure 7.4 with Ga 3d alone doesn't allow any statements. The line is much more pronounced for 2 keV but there is no sharp S-line in the measurement window for intensity comparison, and compared to S 2s and all other lines shown in table A.3, we expect a decrease to less than 20% in 6 keV HAXPES.

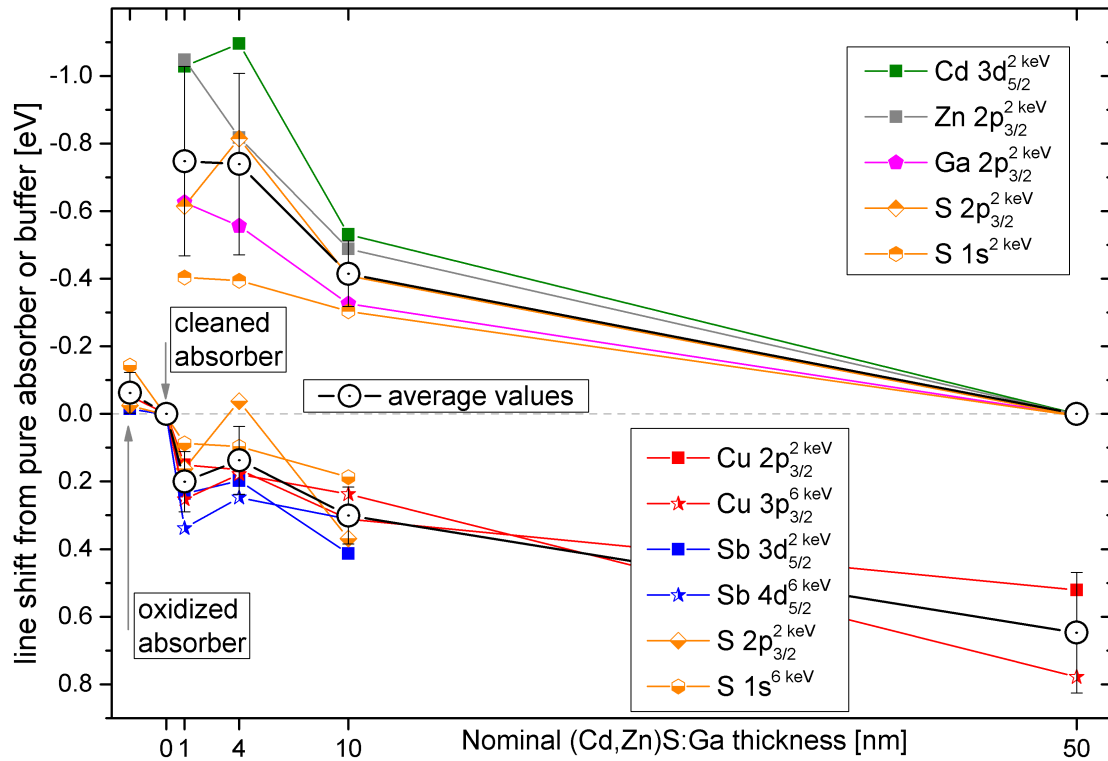


FIGURE 7.14: Core level shifts of the (Cd,Zn)S:Ga layers on CuSbS<sub>2</sub>. To obtain shifts for each core level, the  $E_B$ -position of the 50 nm sample  $E_B(50 \text{ nm (Cd,Zn)S})$  or of the bare cleaned substrate ( $E_B(\text{CuSbS}_2)$ ) was subtracted from the  $E_B$ -position of the respective sample. The inverse Y-axis gives downwards band bending as downshift in the graph and vice versa.

The core level shifts shown in 7.14 indicate a strong band bending in opposite directions on the two sides of the junction. Secondary species follow the shift of the respective dominant line and are not shown. The Cu species on the thickest sample is shown for completeness although it cannot represent the absorber shift.

The Cu and Sb lines measured at 6 keV have been measured with significantly higher photon flux at SPring-8 synchrotron. Spectral shifts caused by charging due to the photoelectron loss would be much more pronounced here so that charging can be ruled out. The buffer band bending reaches a maximum upwards bending of about  $-0.75(\pm 0.28) \text{ eV}$  for the two thinnest layers, while the absorber shows the strongest downwards bending for the 10 nm sample with  $0.30(\pm 0.09) \text{ eV}$ .

We can now calculate the conduction band offsets using optical bandgaps of 2.7 eV for (Cd,Zn)S and 1.1 eV CuSbS<sub>2</sub><sup>1</sup>. The used VBM for the buffer is 0 eV from the 2 keV measurement of the absorber. The resulting band alignment shows a cliff of  $-1.3(\pm 0.25) \text{ eV}$ . This cliff alignment makes recombination at the interface very easy and will therefore decrease the open circuit voltage.

The buffer composition is shown in figure 7.16 as calculated from core level intensities, photoionization cross sections and IMFPs in CdS (for ZnS the values are very similar

<sup>1</sup>Communication with A. Zakutayev, unpublished

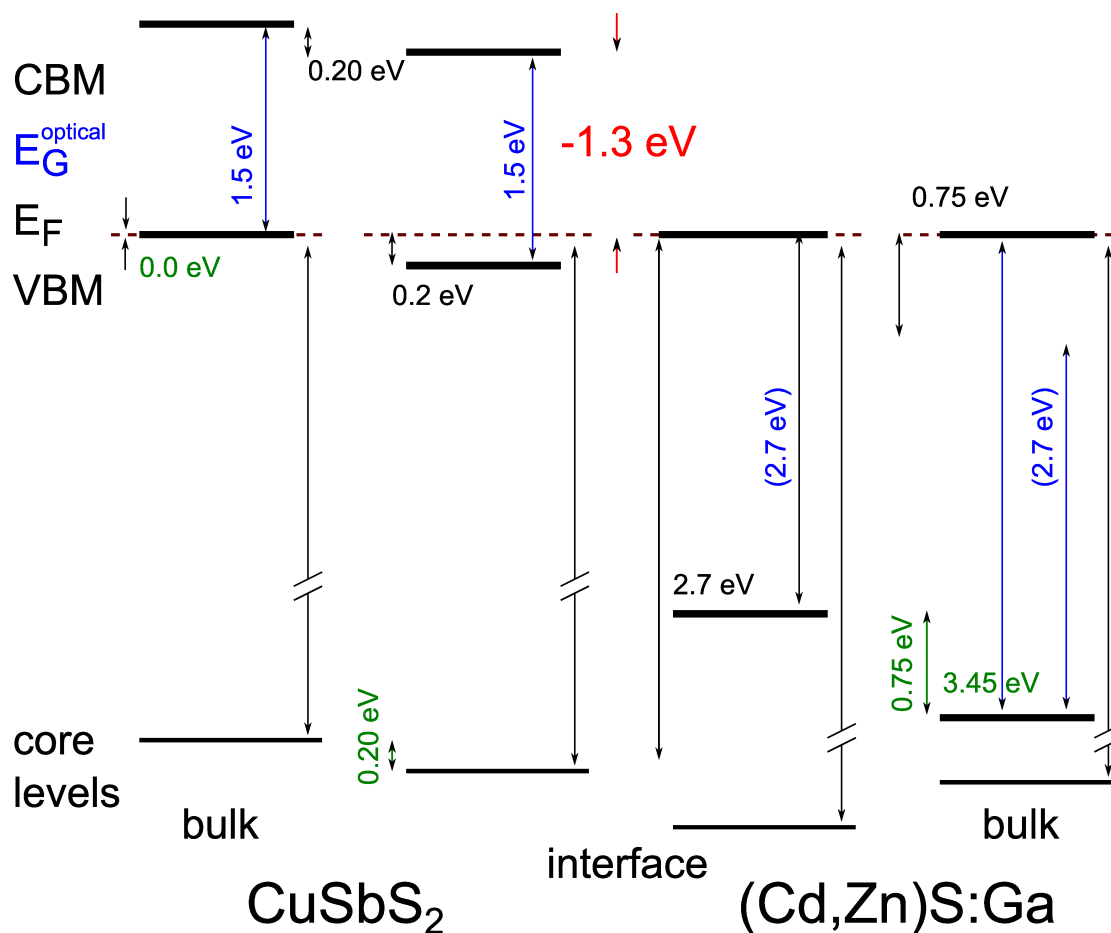


FIGURE 7.15: Band alignment of the CuSbS<sub>2</sub>/(Zn,Cd)S:Ga structure as obtained from the values for the thinnest layer. The two sides of the interface in the center of the graph illustrate the band bending at the contact area and the actual band alignment.

and follow the same trends). We find a very low S content in the buffer material that is exceeded by even the Ga amount. We find more Zn than Cd and increased Ga content for thinner layers. The S content of only 20% for the thick buffer decreases to below 10% for the thinnest layers.

The measured amount of C is also included for comparison and exceeds the quantity of all the buffer elements. We have to consider that surface species will be overestimated due to the undamped signal, however, we have a very C-rich material.

The S L<sub>2,3</sub> XES spectra shown in figure 7.17 show the influence of the covering layers on the spectra increasing with layer thickness.

The main peak is composed of S 3s for all spectra. The CdS spectrum shows two features a and b that are caused by transitions from the hybridized Cd 4d states as shown in [25] or [102]. The prominent peaks in the ZnS spectrum are due to hybridized Zn 3d electrons (compare fig 4.16).

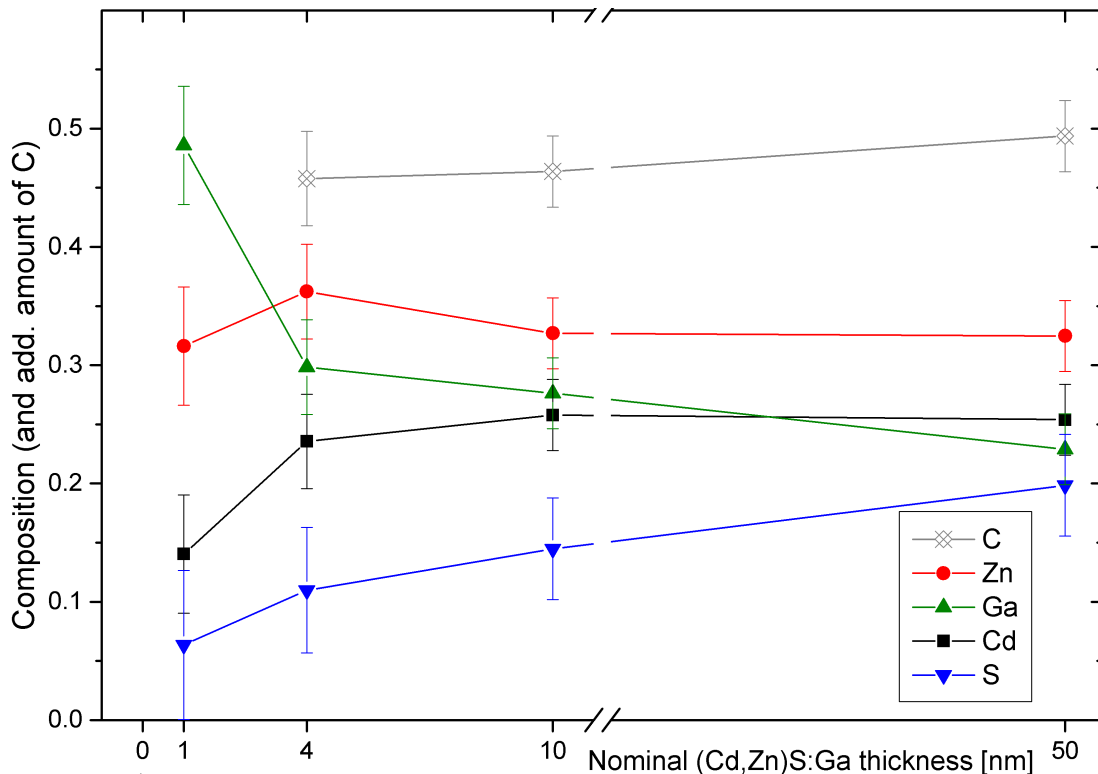


FIGURE 7.16: Composition of the (Cd,Zn)S:Ga buffer layers as calculated from line intensities of Zn 2p<sub>3/2</sub>, Ga 2p<sub>3/2</sub>, Cd 3d<sub>5/2</sub> and S 2p<sub>3/2</sub>. The C 1s signal was also included as additional element. The fitted areas have been divided by photoionization cross sections and IMFP of the respective photoelectrons in CdS-like compounds.

The buffer signal cannot be adequately reproduced by adding reference spectra of CdS and ZnS. The sharpness of the overlapping features a, b, c, and d decreases for the real (Cd,Zn)S compound and we still see a small influence of the buried absorber material, best visible in the region around feature f.

The absorber shows clear spectral changes compared to the best superposition of the binary references. Feature e in the SbS spectrum is caused by Sb 5s electrons. We find very similar intensities of this feature in SbS and CuSbS<sub>2</sub>, indicating a similar density of Sb 5s electrons that hybridize with S states.

The high energy range of the CuS and CuSbS<sub>2</sub> spectra is dominated by feature f that we attribute to hybridized antibonding Cu 3d - S 3p states. This feature changes shape and doesn't lose intensity in CuSbS<sub>2</sub> compared to CuS so that it resembles the respective hybridized antibonding Cu 3d - S 3p feature found for CZTS samples (compare figure 4.16, page 43). The bonding Cu 3d - S 3p hybrid causes the weaker signal seen in the CuS spectrum around 155.5 eV. The changes can be explained with changed bonding angles and lengths in the alloy compared to the pure binary materials.

The spectrum of the bare absorber has been subtracted from the other spectra to extract pure (Cd,Zn)S:Ga spectra. Feature f was used as a measure to adequately weight the subtracted spectrum and reach a flat line in this region. The resulting pure buffer contributions resemble each other in the range of the Cd- and Zn-features. For the 1 nm

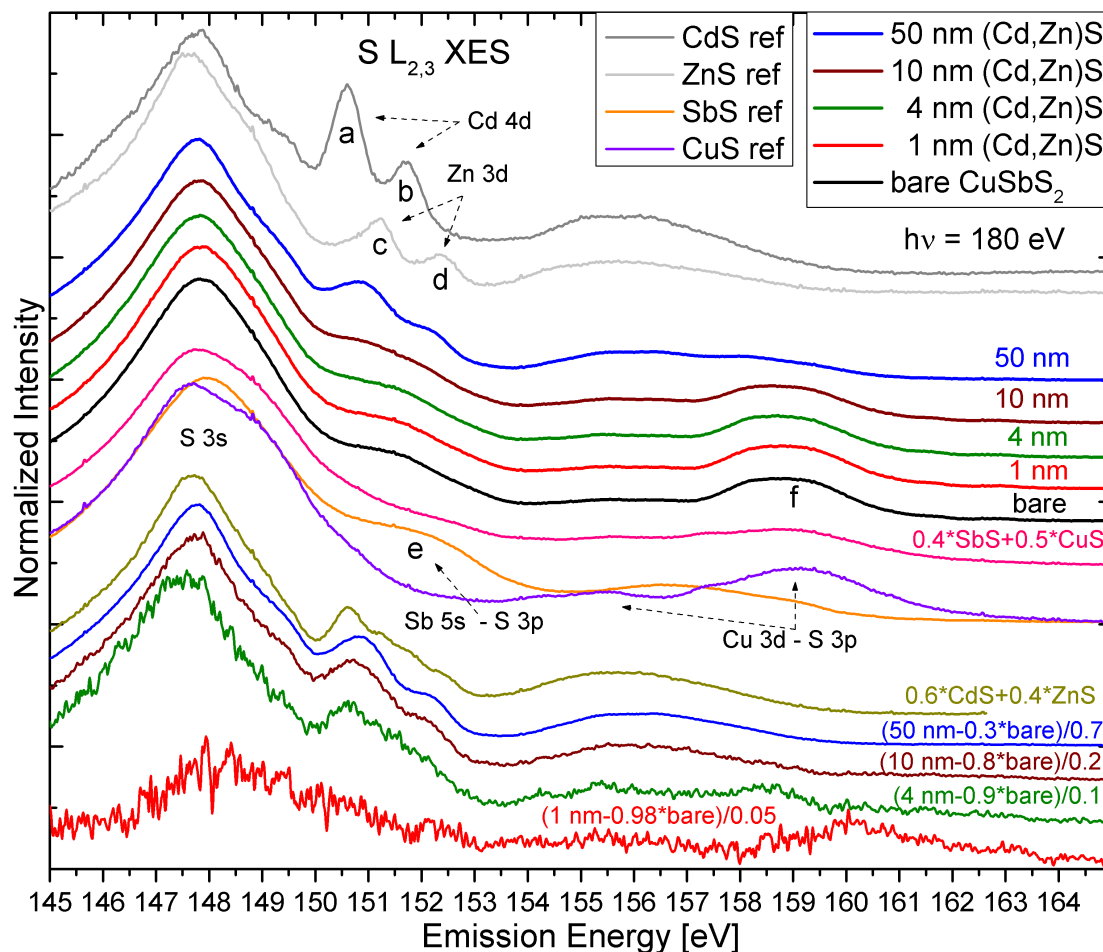


FIGURE 7.17: S  $L_{2,3}$  XES spectra of the CuSbS<sub>2</sub>-series normalized to the main peak. Vertical offsets have been added for clarity. We find the buffer signal to be similar to added signals of ZnS and CdS. The absorber material shows strong changes in the feature intensities compared to added up spectra of CuS and SbS references.

sample the Cd-Zn-S features cannot clearly be seen. The small contribution resembles more the Zn features. This agrees with the low Cd amount in this layer. Additional intensity in the region of 158-160 eV for the most magnified spectra of the thinnest layers is best explained with the interface species that have also been observed in HAXPES for Zn and Cd.

The extracted buffer signal cannot be perfectly fitted with a superposition of CdS and ZnS which is plausible considering the low S- and high Ga-content. As for the absorber, changed bonding angles and lengths in this alloy, compared to the pure binary materials, can modify the peak sharpnesses and positions. The main difference is found in the Cd-features that don't appear as sharp in our measured buffer spectra. The best superposition supports the finding of more Zn than Cd.



**Conclusion:** The chemical analysis reveals chemical interaction at the junction. The single-species Sb as well as S with one species in each material appear unaffected. In contrast, we find an additional species on the high energy side of the Cu peak for all samples. Since we can also exclude a Cu-oxide, the second chemical environment of Cu is most likely a more Cu-rich Cu<sub>3</sub>SbS<sub>3</sub> or Cu<sub>12</sub>Sb<sub>4</sub>S<sub>13</sub> at the surface or interface. The second finding that is contrary to expectation for Cu is the weak but clear Cu signal on the thickest buffer layer where we don't find any Sb and don't expect any absorber signal. The Cu must be more mobile than Sb and diffuse into the buffer material forming a Cu species with  $E_B$  similar to the Cu-rich species. The effect has to be observed on another sample to exclude contamination.

In the buffer we find modified species in the thin layers that are Cd- and S-depleted and contain more Ga. The interface species can be explained with the changed buffer composition at the interface, particularly low S and Cd content, and could also be affected by the presence of O and hydroxides.

We find an upwards surface band bending of -0.15 eV for the absorber. At the junction, we see downwards band bending of up to  $0.3(\pm 0.09)$  eV in the absorber ( $0.2(\pm 0.09)$  eV for the thinnest layer) and strong upwards band bending of  $-0.75(\pm 0.28)$  eV in the buffer. The junction is definitely not an abrupt transition from one homogenous material to another. The buffer growth is strongly affected by the absorber. Also the electronic structure on both sides is significantly affected. We find a good conduction band alignment with a small spike of  $-0.1(\pm 0.3)$  eV.



## **Appendix A**

# **Additional graphs and tables**



## A.2 ZnOS/CZTS

### A.2.1 Auger lines

The Auger lines shown in figure A.1, A.2 and A.3 have been used to calculate modified Auger parameter. The sharp features that determine the binding energy value are tagged with red arrows.

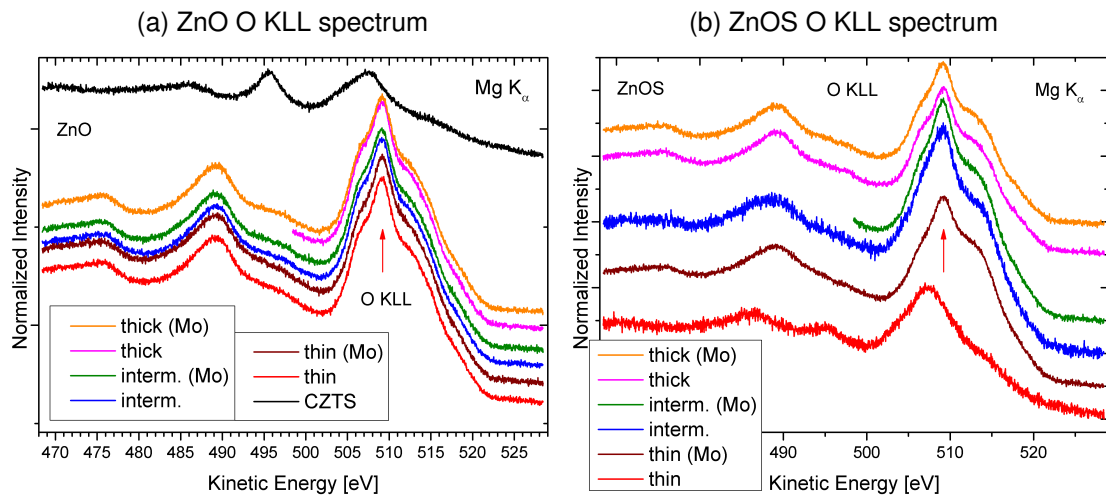


FIGURE A.1: O KLL Auger spectra measured with Mg K $\alpha$  excitation on the ZnO and ZnOS series and normalized to the background. The red arrows indicate the feature used to calculate  $\alpha'$ -values. Vertical offsets have been added for clarity.

The O KLL spectra in figure A.1 show an identical shape for all ZnO layers and ZnOS layers except for ZnOS thin. This resembles the clearly different shape of the CZTS spectrum measured in the ZnO series (figure A.1a).

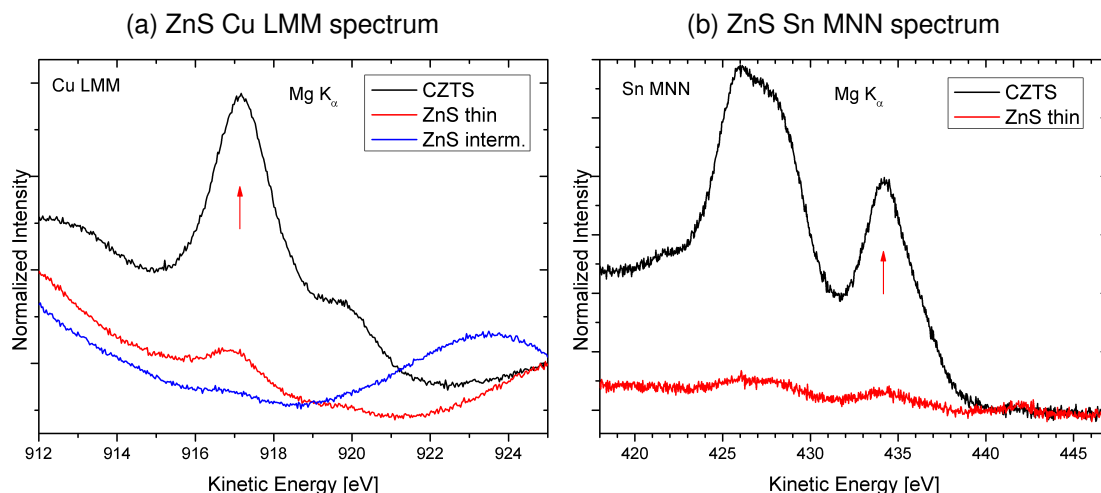


FIGURE A.2: ZnS Cu and Sn Auger spectra measured with Mg K<sub>α</sub> excitation and normalized to the background. The red arrows indicate the feature used to calculate  $\alpha'$ -values.

The Cu and Sn Auger lines shown in figure A.2 and A.3 come from either bare CZTS or deeper and deeper buried CZTS. In both series they show:

1. a decrease in line intensity with growing buffer thickness,
2. a shift to lower kinetic energy in accordance with the shifts we see in the core levels on the reverse binding energy scale,
3. no changes in shape and no new spectral features, indicating unchanged chemical environments for Cu and Sn.

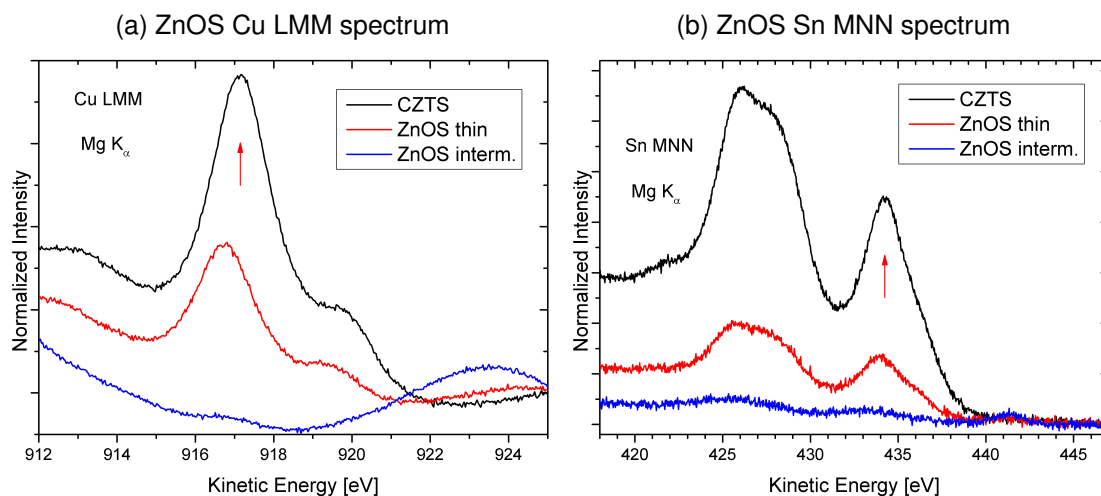


FIGURE A.3: ZnOS Cu and Sn Auger spectra measured with Mg K<sub>α</sub> excitation and normalized to the background. The red arrows indicate the feature used to calculate  $\alpha'$ -values.

## A.2.2 Additional elements

The oxygen species have been evaluated with respect to literature (e.g. [180]). Closer examination of the O 1s line shows that the buffers have more oxygen in the surface than the CZTS and Mo. The oxygen on CZTS can come from the KCN etching that is followed by a water rinse and from transfers through air from the deposition machines and ovens. The Mo has not been protected from air so we are not surprised to find oxidized Mo. On ZnS the adventitious oxygen is found at 532 eV, for CZTS the position is 0.5 eV higher. The prominent  $\text{MoO}_3$  peak can still be seen through the thin ZnS/Mo layer.

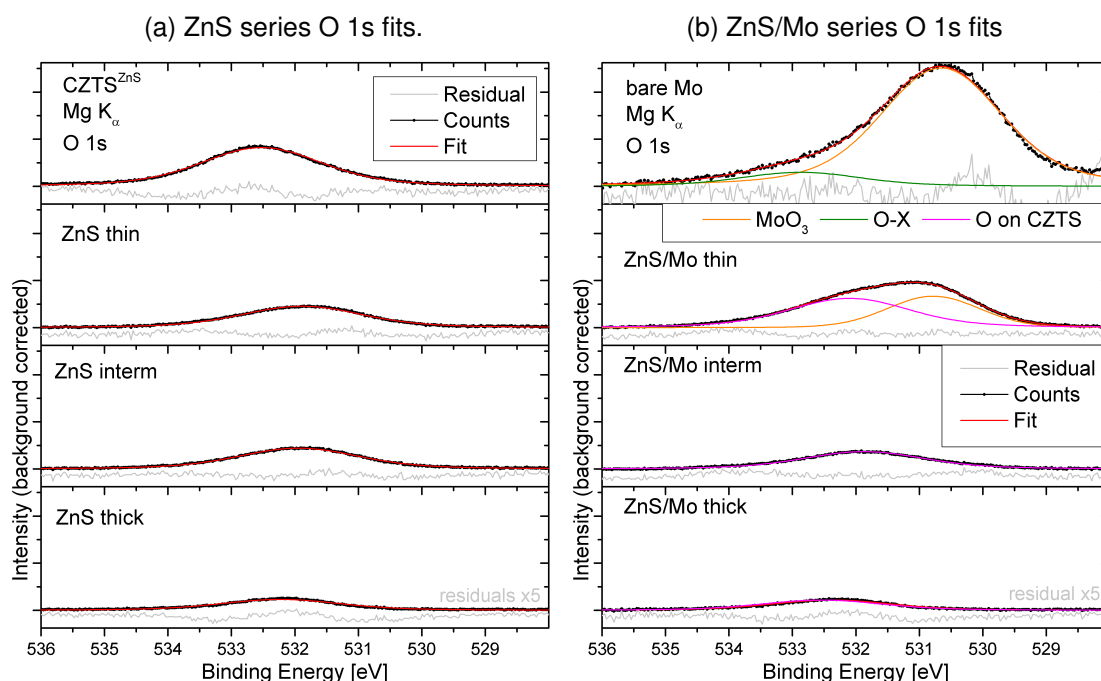


FIGURE A.4: O 1s spectra of ZnS/Mo measured with Mg  $K_\alpha$  excitation and fits. The residuals have been magnified for better visibility.

### A.2.3 Additional information

All samples have been investigated for Mo related signals to find out about scratches or uncovered spots. Mo  $3p_{3/2}$  signals could, as shown in figure A.5, only be found for the reference samples grown directly on untreated Mo. As expected from the strong O 1s signal in the survey spectra of bare Mo (see page 32: figure 4.3) it has an oxidized surface. We see a MoO<sub>3</sub> signal (green line) next to the main metallic Mo peak (blue line) in the Mo  $3p_{3/2}$  peak. The Mo  $3p_{3/2}$  was measured with Al K<sub>α</sub> excitation instead of the sharper Mg K<sub>α</sub> excitation line to avoid overlaps with the broad multi-feature Zn (and Cu) LMM Auger lines (see page 19).

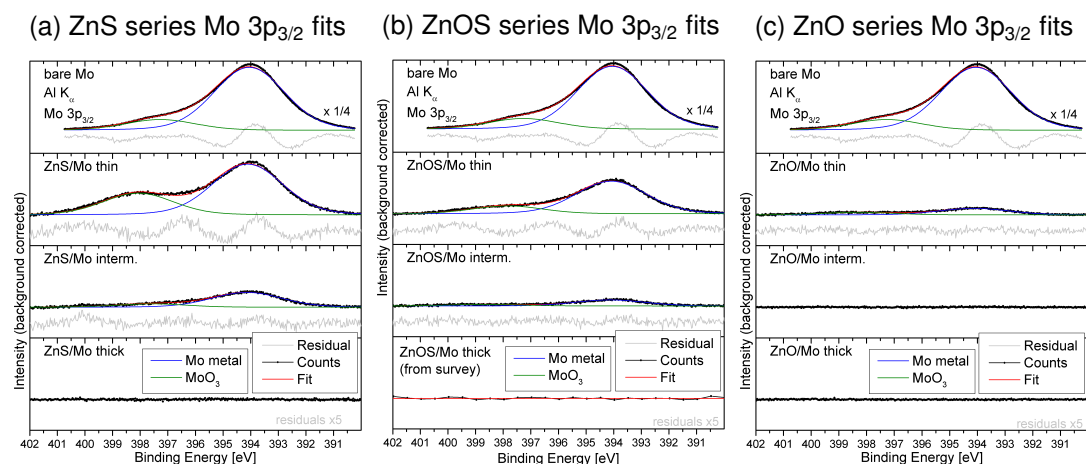


FIGURE A.5: Mo 3p spectra of all reference buffers measured with Al K<sub>α</sub> excitation and fits. The residuals have been magnified for better visibility.

The bare Mo sample was measured after significant changes of the electron analyzer settings compared to the settings used for the other samples. The transmission function therefore changed by a factor of about 4.2. We decrease the intensity measured on the bare Mo by this factor to be able to compare the remaining Mo-intensity measured through thin buffer layers.

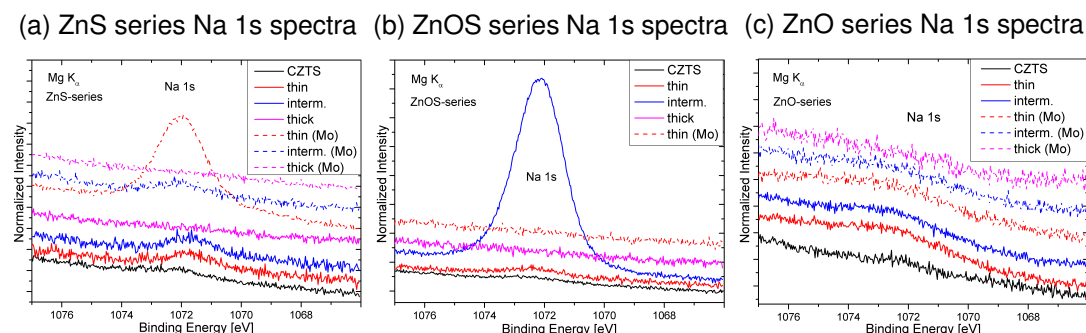


FIGURE A.6: Na 1s spectra of all samples measured with Mg K<sub>α</sub> excitation. Vertical offsets have been added for clarity. Traces of Na are visible in most samples. *ZnS/Mo thin* and *ZnOS interm.* show significant Na peaks.



We see a very small Na 1s signal for most samples as shown in figure A.6. Not all samples have been measured as a detail scan but the survey spectra of the omitted samples show no significant Na signal. The samples *ZnS/Mo thin* and *ZnOS intermediate* show a strong Na peak as discussed in the Zn-chapter (page 40 and 66).

The origin of the sodium signature is the glass substrate [54, 181]. The strong surface accumulation for just two samples can best be explained with humidity, that can act as an attractor to Na atoms [182, 183]. The fast diffusion of Na through Mo and CZTS will permit surface accumulation of Na if small quantities of water come in contact with the sample during transport. Even though all samples were packed in pure nitrogen gas and vacuum sealed for transport, incorporation of small amounts of moisture can occasionally occur for single samples.

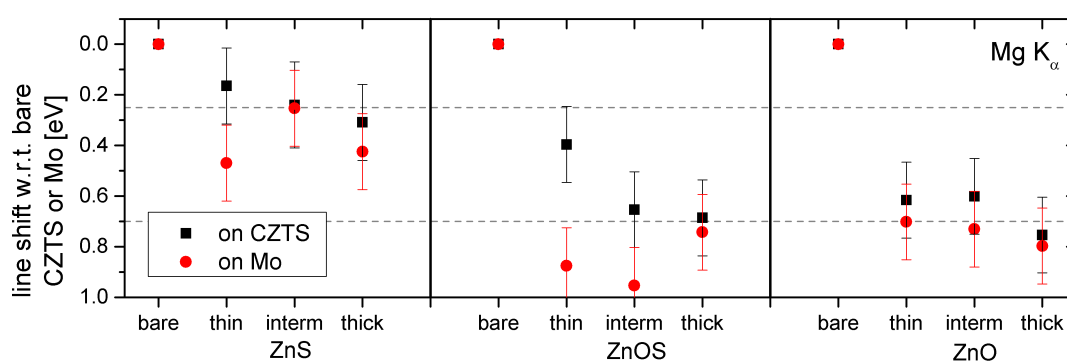


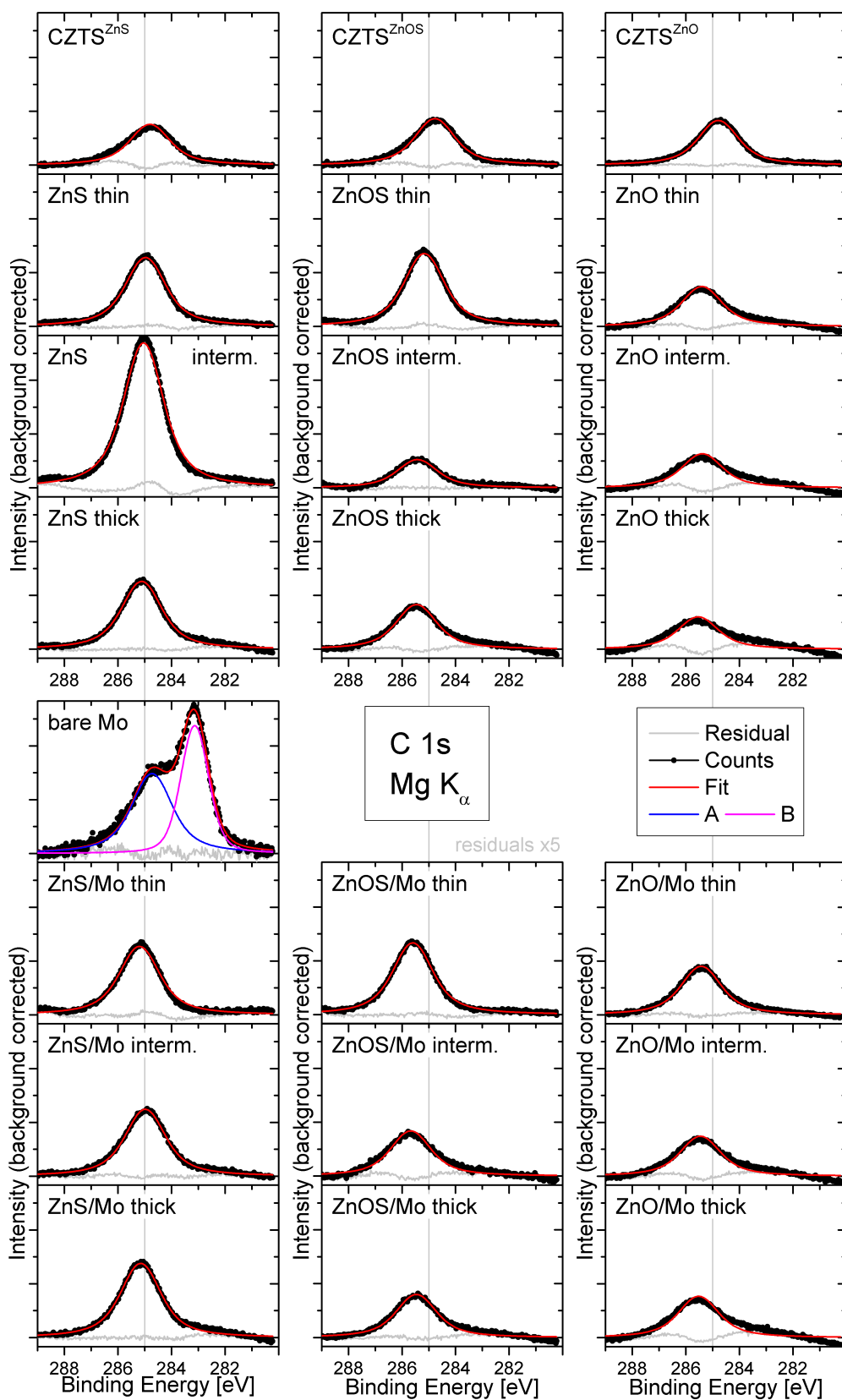
FIGURE A.7: Spectral shifts of C 1s peaks measured with Mg  $K_{\alpha}$ . The dashed lines are a guide to the eye.

We see a C 1s signal for all samples as shown in figure A.8. No changes in speciation can be found. The bare Mo shows a second peak at lower binding energy where C-O-compounds on Mo are expected according to literature [184, 185].

The main Carbon peak is located at 284.8 eV for the bare kesterite samples and at 284.7 eV for the bare Mo sample. On bare Mo we find another strong species at lower binding energy.

The shifts are shown in figure A.7. All ZnS layers on CZTS and Mo show a small positive shift of the C 1s position to around 285 eV. *ZnS/Mo thin* falls out of the pattern. This sample shows a higher C 1s peak and a larger shift.

The buffers with oxygen show the C 1s position at at even higher  $E_B$ . Only *ZnOS thin* shows the C 1s at a similar position as found on ZnS layers. The C 1s position for all other ZnO and ZnOS layers is around 285.4-285.5 eV with a shift of around 0.7 eV compared to the bare CZTS and Mo. *ZnOS thin* and *ZnOS intermediate* exceed even this shift but are, within the error margin, still very close to the 0.7 eV shift.

FIGURE A.8: C 1s fits measured with Mg  $K_{\alpha}$ 

The  $\text{Zn}(\text{OH})_2$  contribution in the ZnO and ZnOS buffer material has been calculated

from the Zn  $2p_{3/2}$  and O 1s fit contributions. We see  $\text{Zn}(\text{OH})_2$  contributions in the range of 25% and slightly more for ZnO. The thin ZnOS layers on CZTS show very small ZnO-contributions and do not seem to contain ZnO, so the values are not included here. Deviations of especially O come from the inclusion of additional species in the simple O 1s fit on a sample that has been grown with an O-rich precursor. Further O species seem to be present on the buffer layers.

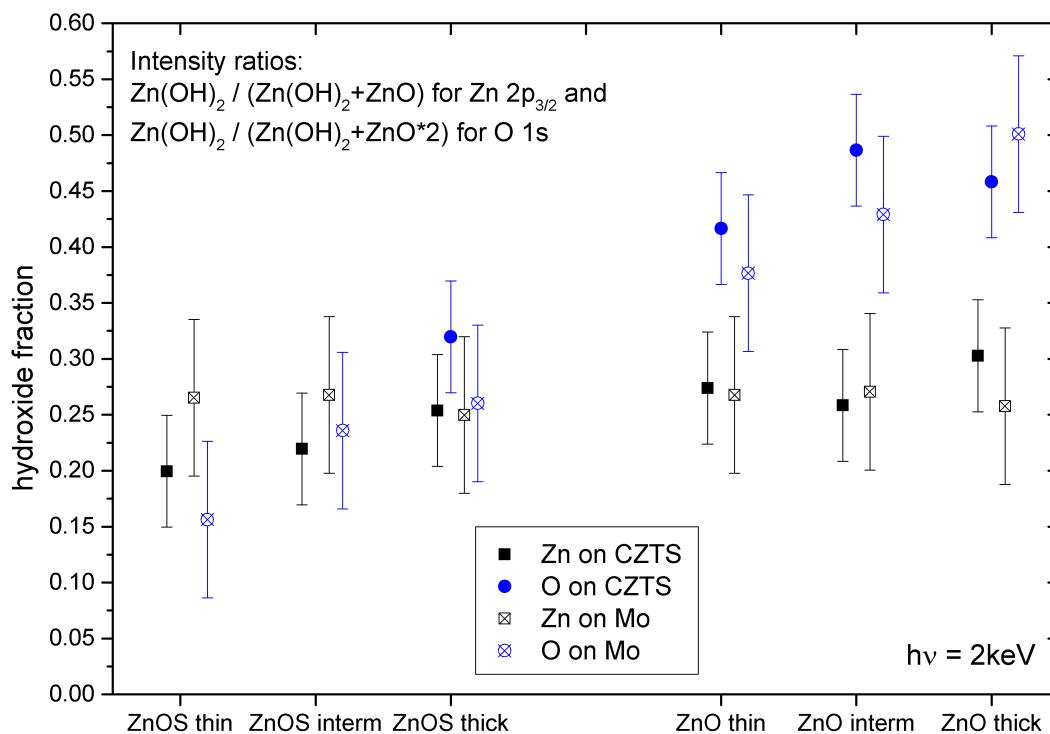


FIGURE A.9: Relative amount of  $\text{Zn}(\text{OH})_2$  contribution in the fits of Zn  $2p_{3/2}$  and O 1s measured with Mg  $K_{\alpha}$ . The ZnO contribution has been doubled in the O 1s intensity ratios to account for the different stoichiometry of ZnO and  $\text{Zn}(\text{OH})_2$ .

### A.2.4 Additional XAS spectra

**ZnS series XAS spectra** have been measured in PFY and TEY for less and more surface sensitive results (for details see experimental section). For completeness, the TFY has been measured, too, despite the usually worse noise level. All XAS spectra have been normalized to the edge jump, partly after linear backgrounds, fitted to the plateau below the edge jump, were subtracted. Vertical offsets between the spectra have been added for clarity.

The S  $L_{2,3}$  edge shows transitions of S 2p electrons into hybridized S 3p states. We find the characteristic CZTS feature at about 164 eV caused by hybridization of antibonding S 3p with Sn 5s states. The main jump shows hybridized Zn 4s states for the pure buffer and additionally hybridized Cu 4s and Sn 5p states for the CZTS (compare XES measurements in [186] and DFT calculations in [187]).

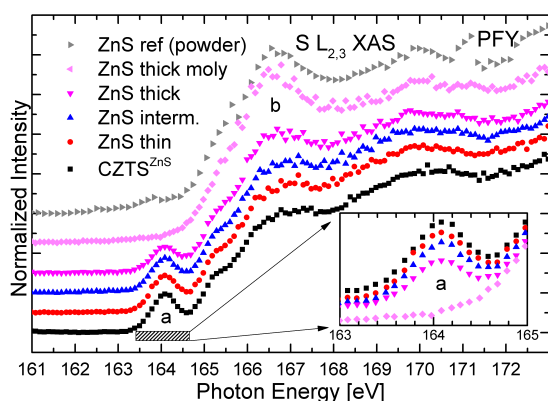


FIGURE A.10: S  $L_{2,3}$  XAS spectra of the ZnS series.

for the CZTS (compare [186]).

The CZTS signal (best represented by feature (a)) has still more than 50% of its intensity for *ZnS thick*, which illustrates the increased information depth of XAS compared to HAXPES<sup>1</sup>. There are no indications for additional chemical phases.

Cu  $L_3$  absorption probes transitions from Cu  $2p_{3/2}$  into unoccupied conduction band states of primarily Cu 4s and 4d. The Cu  $L_3$  absorption spectra in figure A.11 match each other perfectly within this series. This is in agreement with the single species XPS and HAXPES spectra (see page 34). The TEY spectrum, measuring the sample current, depends on photoelectrons with limited IMFP so we expect to get less Cu signal for thicker buffer layers. The thick ZnS layer is thinner than expected in the thickness calculations (page 45) and here the unchanged signal-to-noise ratio suggests that the

The S  $L_{2,3}$  absorption spectra of the ZnS series, measured in partial fluorescence mode, are shown in figure A.10. We see the reduction of the characteristic CZTS-feature (a) that is shown in the inset, composed of hybridized antibonding S 3p with Sn 5s states (compare e.g. [121, 186, 187]) at 164 eV towards the pure ZnS spectrum that we see as light magenta line for *ZnS/Mo thick*. The main jump shows hybridized Zn 4s states (most pronounced feature (b)) for the pure buffer and additionally hybridized Cu 4s and Sn 5p states

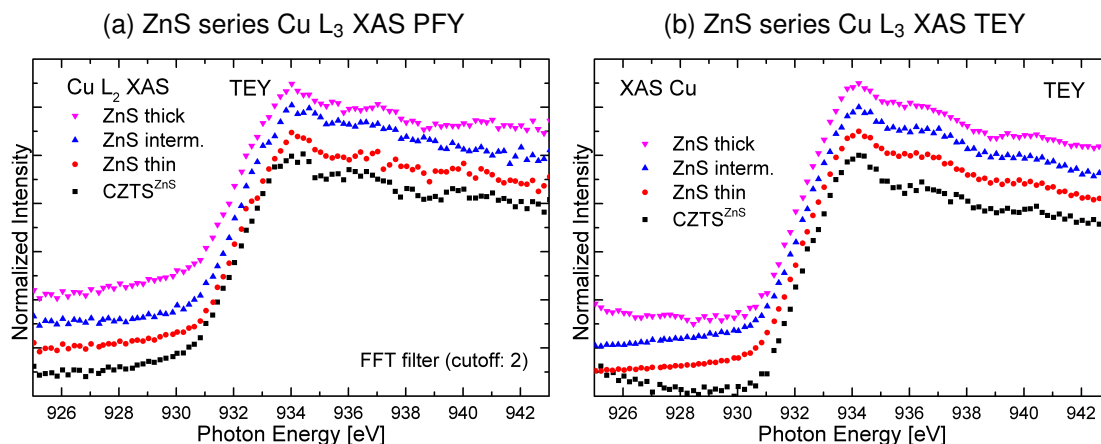


FIGURE A.11: Cu  $L_3$  XAS spectra of the ZnS series. A linear background has been subtracted.

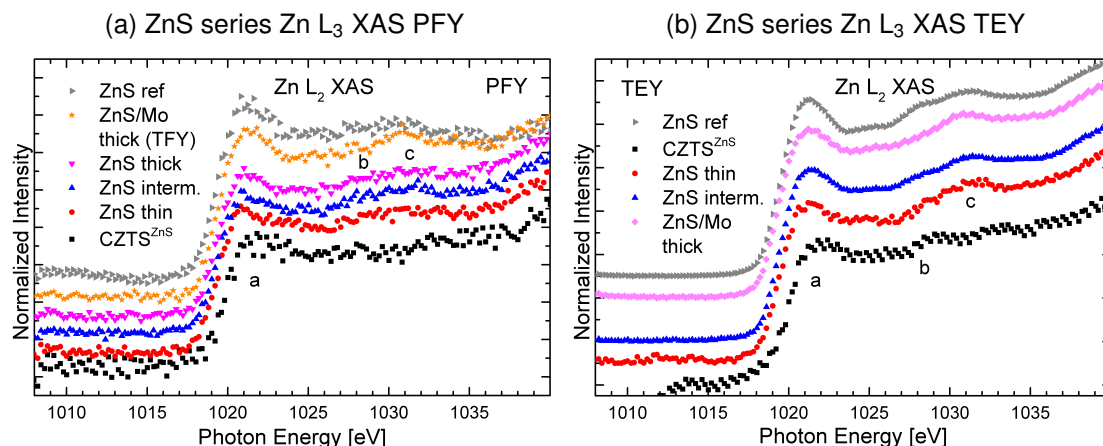
photoelectrons can easily penetrate the thick ZnS layer, too. The TEY spectra showed a modulation as measurement artifact that was removed with a FFT filter.

Zn  $L_3$  absorption probes transitions from Zn  $2p_{3/2}$  electrons into Zn 4s and 4d states. The Zn absorption spectra in figure A.12 show the differences between ZnS and CZTS. ZnS powder (gray line) that was used as a reference gives a structured signal as well as the ZnS layers. The CZTS (black line) with comparatively low Zn content shows mainly a jump and two weak features (a) and (b).

*ZnS/Mo thick* could not be measured in PFY, so we added in the total fluorescence yield spectrum (orange line). This includes the whole spectral range of photons instead of just a small window around the respective edge energy. Spectra therefore have a worse signal-to-background.

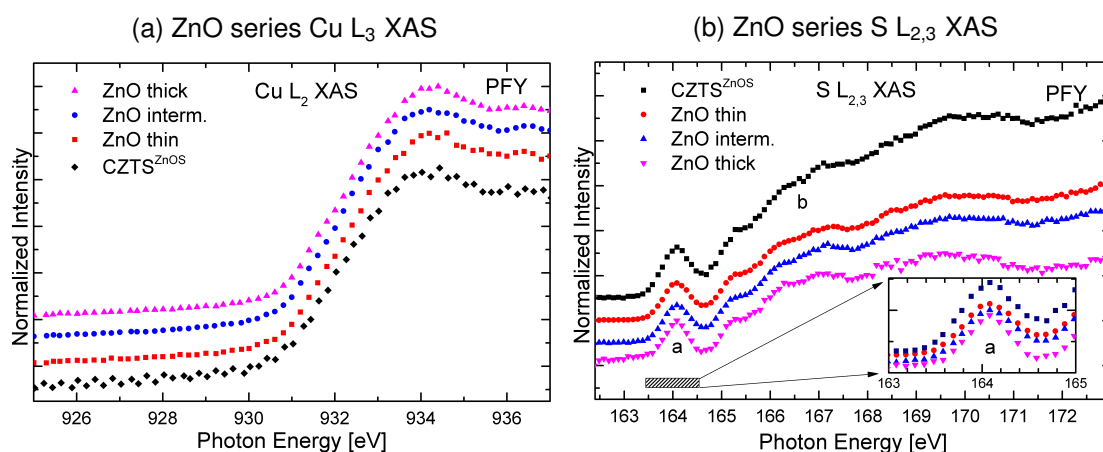
Here we see a good agreement with the HAXPES trends of the ZnS layers grown on CZTS. The edge jump is more pronounced for the ZnS and forms a pronounced peak (a) at 121.5 eV and two other features (b) at 128.5 eV and (c) at 1031.0 eV. Especially feature (c) appears for all ZnS layers and is missing in the CZTS spectra.

<sup>1</sup>With HAXPES at 8 keV we still see 37% of the CZTS signal close to the VBM (see page 163).

FIGURE A.12: Zn  $L_3$  XAS spectra of the ZnS series.

**ZnO series XAS spectra** have been measured as described on page 158. All XAS spectra have been normalized to the edge jump, partly after linear backgrounds fitted to the plateau below the edge jump were subtracted. Vertical offsets between the spectra have been added for clarity.

The S  $L_{2,3}$  absorption spectra in figure A.13b show a pure CZTS-like signal including feature (a) that is shown in the inset, with increasing noise level for thicker ZnO layers. No ZnS-feature (b) is seen. For the Cu  $L_3$  XAS (figure A.13a) we don't even see a change in the noise level. This supports the assumption of no difference in the absorber surface chemistry between the samples of the series and bare CZTS. Both spectra selectively probe the absorber material for this buffer series.

FIGURE A.13: Cu  $L_3$  and S  $L_{2,3}$  XAS PFY spectra of the ZnO series. A linear background has been subtracted.

The Zn  $L_3$  edge spectrum of CZTS measured in PFY (figure A.14a) shows much less structure than the *ZnO/Mo thick* spectrum, which resembles the ZnO reference. This is very similar to what we observed for the ZnS-series except for the stronger buffer influence on the spectrum of the thick ZnO on CZTS that is simply caused by the thicker buffer layer. We see a clear thickness effect, represented by the change towards a

ZnO-signal for the ZnO-series, that we could not observe with PES.

The TEY spectra of all samples in figure A.14b look very similar since they are probing only buffer material. This illustrates the difference in probing depth between PFY measuring photons (table 3.1 for attenuation lengths) and TEY that uses photoelectrons (table A.1 for IMFPs).

The ZnS-feature (c) is not observed. The ZnO spectra are dominated by feature (b) that was seen in ZnS samples, too, and (e) that we only find in ZnO. The leading edge of CZTS (a) is replaced by a foot (d) in the ZnO buffer signal. The features found for *ZnO ref* and *ZnO/Mo thick* (e) at 1023 eV and the low energy shoulder around 1019 eV match the shape of reported ZnO  $L_3$  XAS spectra and are attributed to transitions into Zn 4s and 4p states (e.g. [188]).

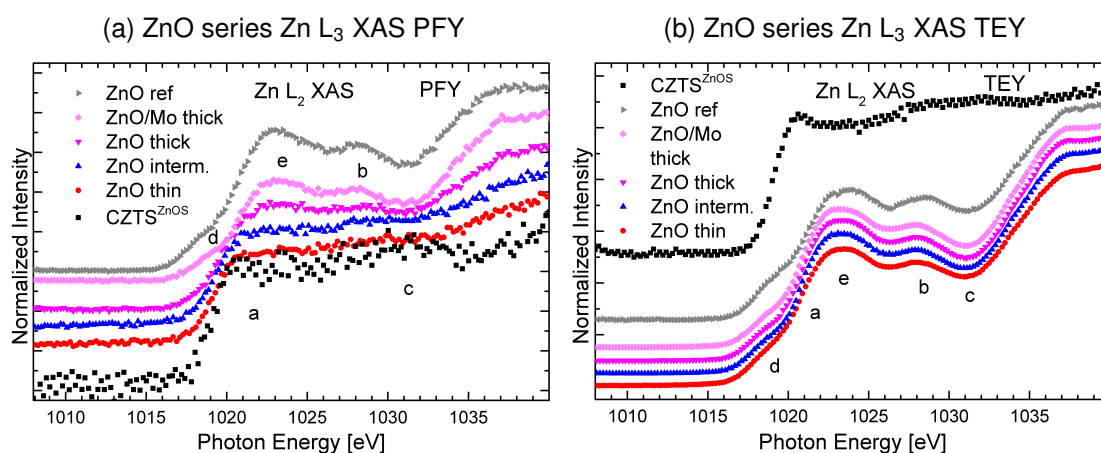


FIGURE A.14: Zn  $L_3$  XAS spectra of the ZnO series. A linear background has been subtracted.

The O K absorption probes O 1s transitions to O 2p states. The O K edge in figure A.15 shows that the weak and noisy O-signal on CZTS (black line) has no features that can be attributed to any specific crystallized oxide. The spectra of the series show only small differences. Feature (b) is much more dominant for thin layers compared to (a), (c), and (d). The decreased intensity and sharpness of the features between 541 eV and 456 eV for thin ZnO layers compared to the ZnO reference indicates structural disorder [189]. The evolution of the region for thinner layers shows that the buffer material gets more disordered towards the interface. This is in agreement with shown strong differences in the crystal structure of thin ZnO layers [190].

The spectral details can be explained by Zn levels that partly hybridize with O 2p states. The region around features a and b is dominated by hybridized Zn 4s states. Around features c and d the Zn 4p hybrids are dominant and we find Zn 3d as broad feature higher than 550 eV [191–197].

The changes in shape in the series as visible for thin layers in PFY (figure A.15a) is most probably a thickness effect.

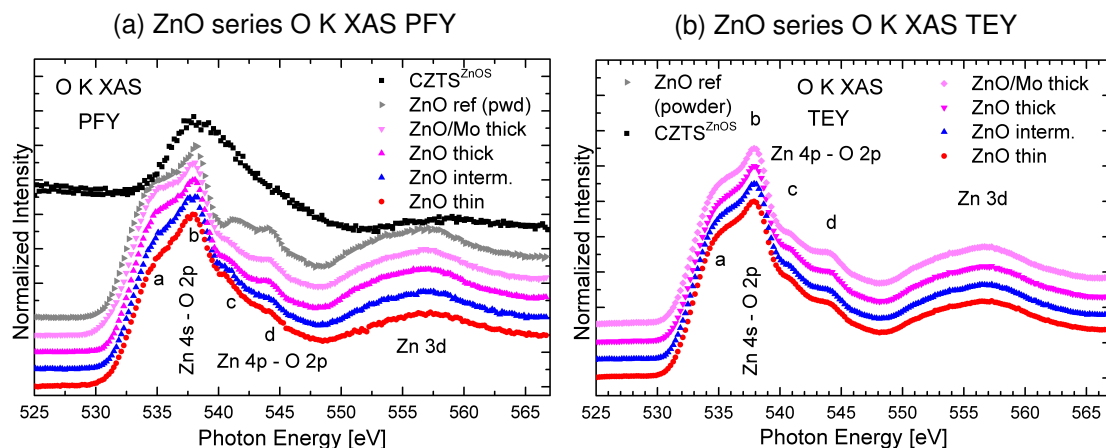


FIGURE A.15: O K XAS spectra of the ZnO series. A linear background has been subtracted.

**ZnOS series XAS spectra** have been measured as described on page 158. All XAS spectra have been normalized to the edge jump, partly after linear backgrounds fitted to the plateau below the edge jump were subtracted. Vertical offsets between the spectra have been added for clarity.

The spectra show again that the Cu stays unchanged in the CZTS. We see higher noise levels with PFY in figure A.16a compared to TEY in figure A.16b. In TEY the less damped spectra of thin layers and especially bare CZTS have the lowest noise level, as expected.

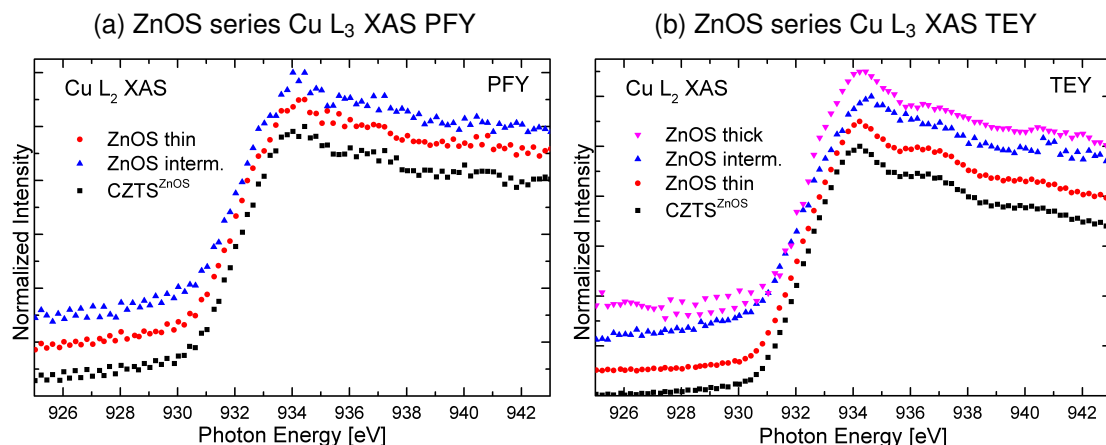


FIGURE A.16: Cu L<sub>3</sub> XAS spectra of the ZnOS series. A linear background has been subtracted.



### A.2.5 ZnS correction

We scale the CZTS spectrum according to the most prominent absorber peak in the extended valence band which is Sn 4d. In figure A.17a we see that the Sn 4d peak is shifted by 0.1 eV in between the CZTS and *ZnS thick* spectra. This is in accordance with the calculated band bending in the absorber of ZnS/CZTS as shown in figure 4.56a. The CZTS spectra is shifted accordingly for the subtraction.

The resulting region around the valence band maximum as seen in figure A.17b neither shows any Sn or Cu signals nor negative intensity or other artifacts from the subtraction.

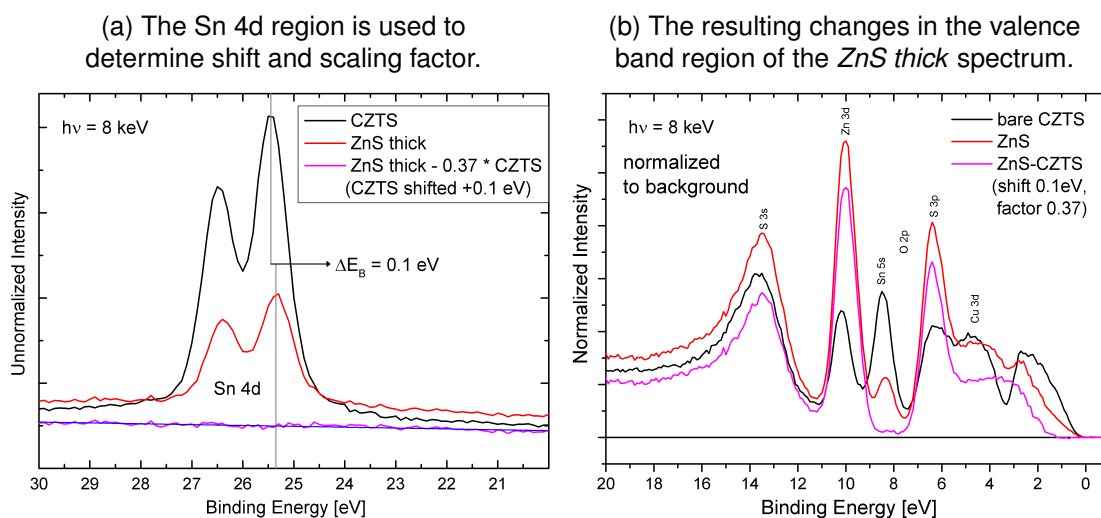
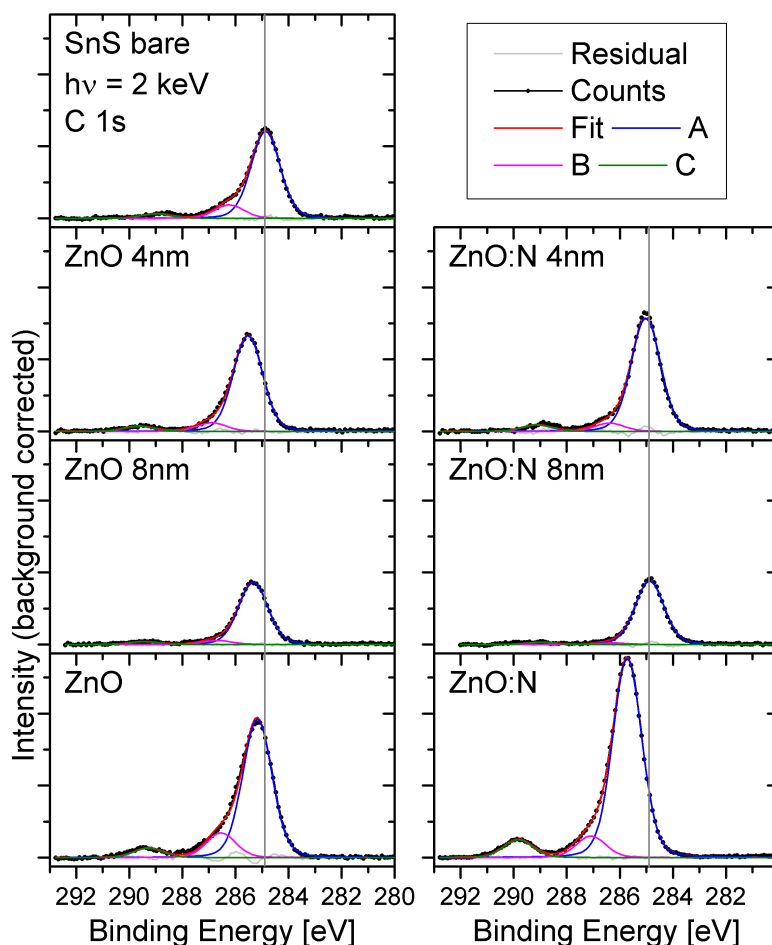


FIGURE A.17: The subtraction of the CZTS signal from the spectrum of *ZnS thick* is based on the Sn 4d region as sharpest absorber related peak in the valence band region that doesn't overlap with buffer related lines. The resulting pure ZnS signal is used for the determination of the valence band maximum.

### A.3 ZnO/SnS

FIGURE A.18: C 1s fits measured with 2 keV.



The carbon appears with a peak structure composed of a dominant carbon peak (blue line) and two carbonates at higher binding energies. C is expected to be found at the surface as well as in the both Sn and ZnO as residue from the ALD process.

Survey spectra measured at higher  $E_{exc}$  are shown in figure A.19. The IMFP goes up to 8.5 (9.2) nm for ZnO (SnS) for this excitation. With this increased probing depth we can better resolve structures that are buried several nm deep. Surface species affect the spectra much less. Compared to the 2 keV surveys in figure 6.2 we see increased Sn and S signals and weaker O and C lines. The weak Cl signal is not detected here.

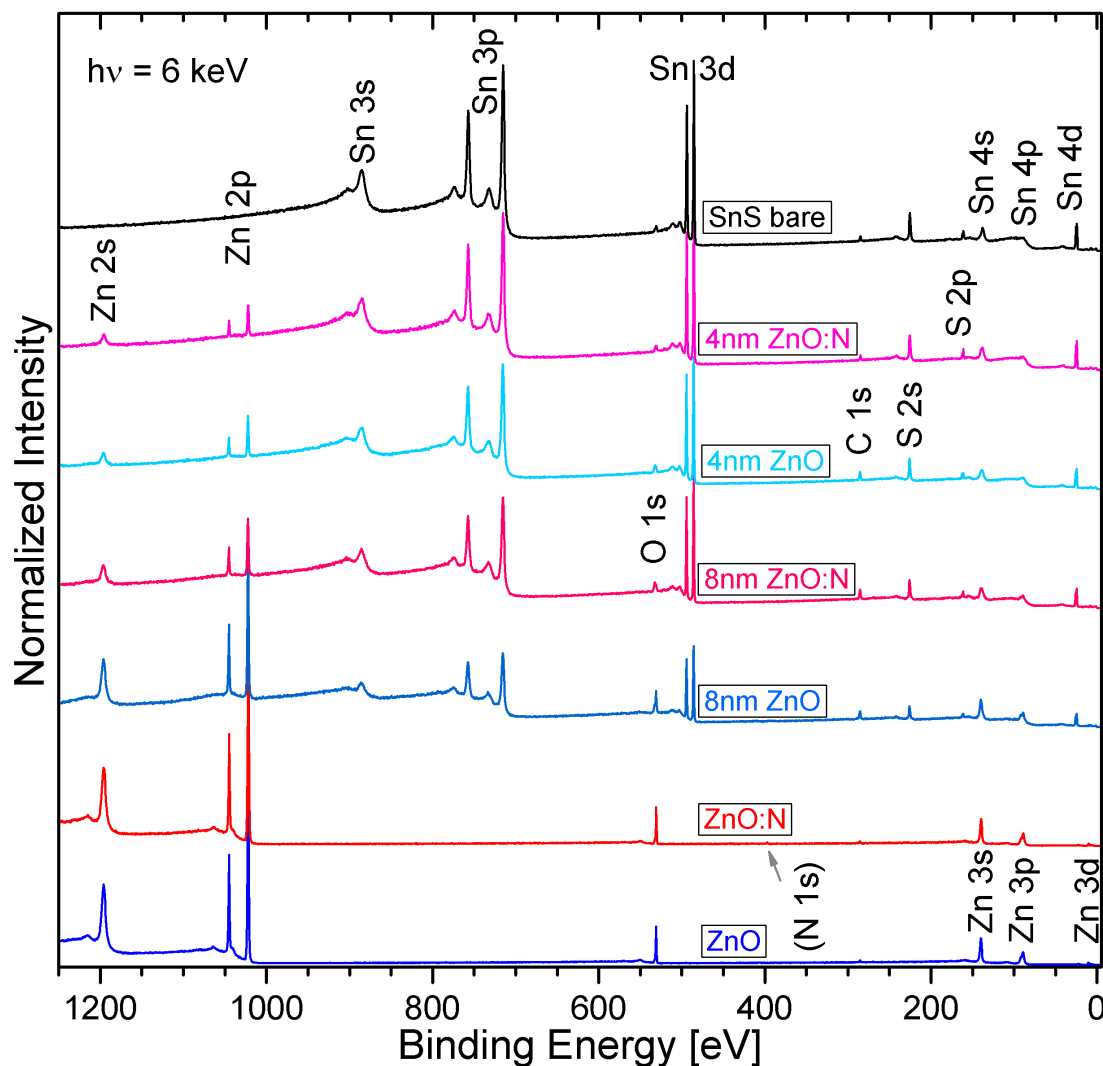


FIGURE A.19: SnS survey spectra measured at  $E_{\text{exc}} = 6$  keV and normalized to the intensity at  $\approx 1250$  eV. Vertical offsets have been added for clarity.

Valence band structure measured at 6 keV are shown in figure A.20. We find a much more dominant buried SnS signal due to the increased IMFP (see page 150).

Previous findings are supported except for the 8nm ZnO:N sample. The shift to higher binding energy can only be explained with charging of this sample due to insufficient contacting during the SPring-8 experiments.

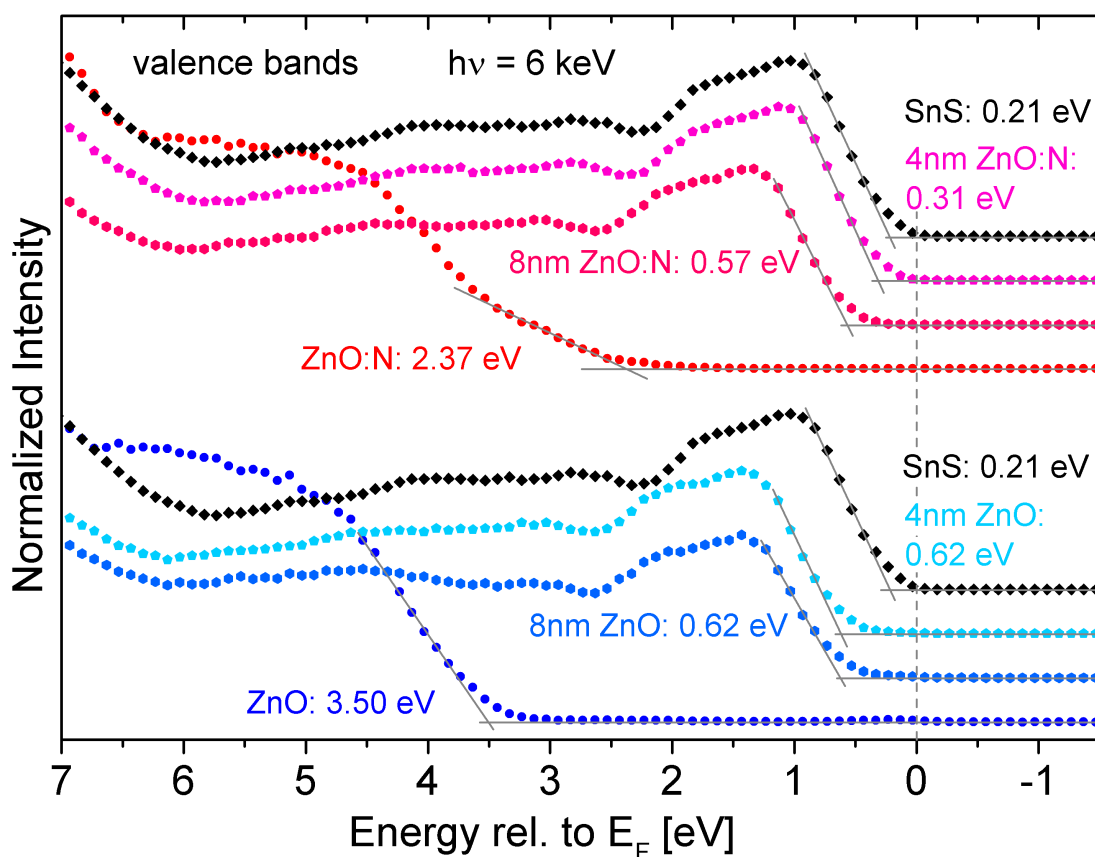


FIGURE A.20: VB spectra and VBM determination for 6 keV HAXPES spectra normalized to the highest intensity in the shown region. Vertical offsets have been added for clarity.

## A.4 (Cd,Zn)S/CuSbS<sub>2</sub>

TABLE A.2: IMFP values for core levels from CuSbS<sub>2</sub> for transport through ZnS and CdS calculated with the TPP2M code [12]. The averaged value IMFP with the statistical error margin is used for thickness calculations of the (Cd,Zn)S buffer.

Core level	IMFP [nm] at 2 keV in:				IMFP [nm] at 6 keV in:			
	ZnS	CdS	$\overline{\text{IMFP}}$	$\Delta\overline{\text{IMFP}}$	ZnS	CdS	$\overline{\text{IMFP}}$	$\Delta\overline{\text{IMFP}}$
S 1s					5.81	5.44	5.63	0.19
Cu 2p <sub>3/2</sub>	2.24	2.24	2.24	0.01	7.84	7.34	7.59	0.25
Sb 3d <sub>3/2</sub>	2.86	2.68	2.77	0.09	8.35	7.81	8.08	0.27
S 2p <sub>3/2</sub>	3.42	3.21	3.32	0.11	8.83	8.26	8.55	0.29
Cu 3p <sub>3/2</sub>	3.55	3.33	3.44	0.11	8.94	8.36	8.65	0.29
Sb 4d <sub>5/2</sub>	3.61	3.39	3.50	0.11	8.99	8.41	8.70	0.29

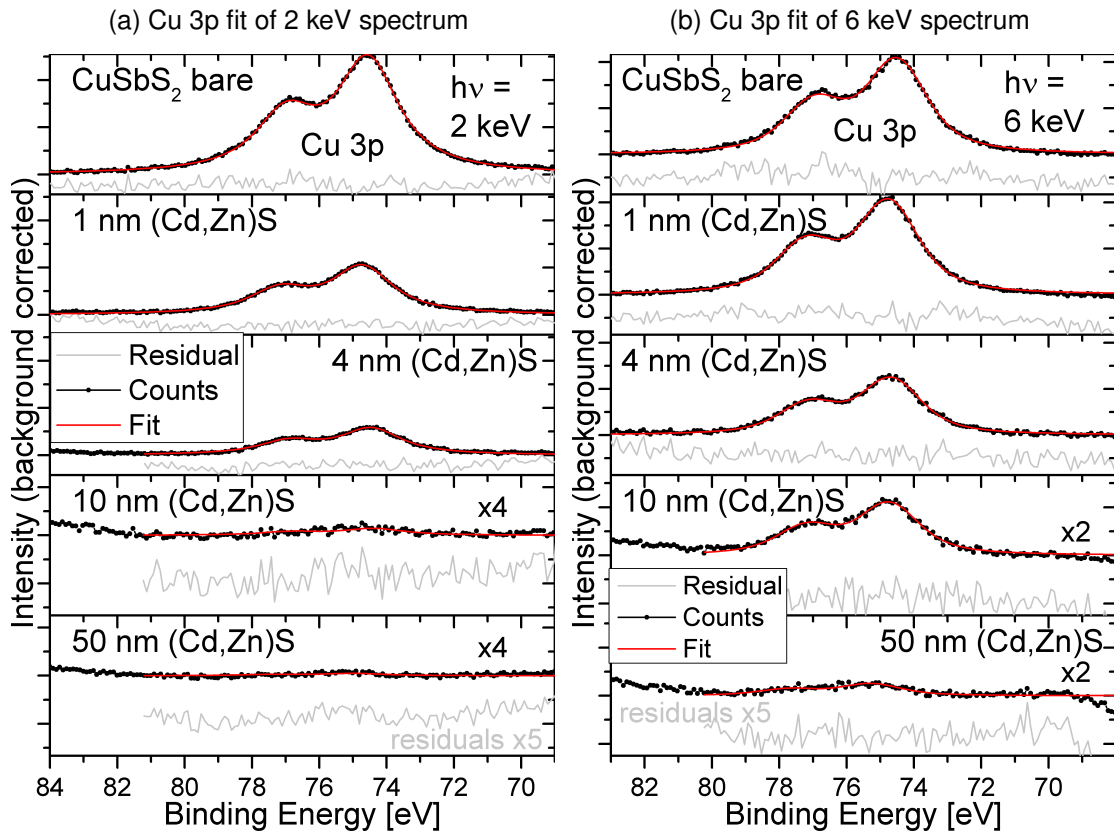


FIGURE A.21: Cu 3p fits of HAXPES spectra have been used to calculate the absorber composition. The shown fits are calibrated using C 1s.

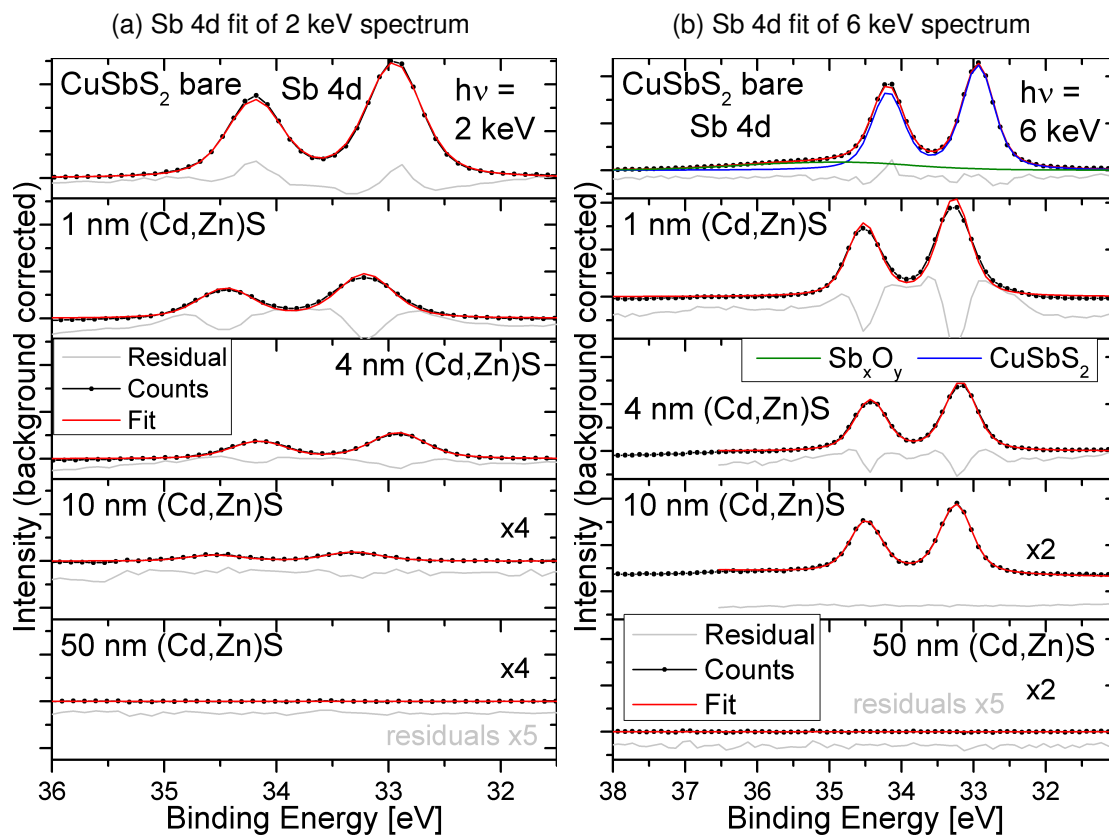


FIGURE A.22: Sb 4d fits of HAXPES spectra have been used to calculate the absorber composition. The shown fits are calibrated using C 1s.

core level	$\sigma(2 \text{ keV})$	$\sigma(6 \text{ keV})$	$\sigma(6 \text{ keV}) / \sigma(2 \text{ keV})$	normalized to S 2s
S 2s	22.56	1.74	0.077	1.00
O 1s	24.11	1.48	0.061	0.79
C 1s	10.44	0.49	0.047	0.61
Ga 2p <sub>1/2</sub>	43.40	3.19	0.074	0.96
Ga 3d <sub>5/2</sub>	5.51	0.075	0.014	0.18
Zn 2p <sub>1/2</sub>	41.05	2.77	0.067	0.87

TABLE A.3: Photoionization cross sections  $\sigma$  of C 1s and O 1s compared to S 2s in CuSbS<sub>2</sub> and direct and S 2s-normalized ratios of  $\sigma$  at different  $E_{\text{exc}}$ .

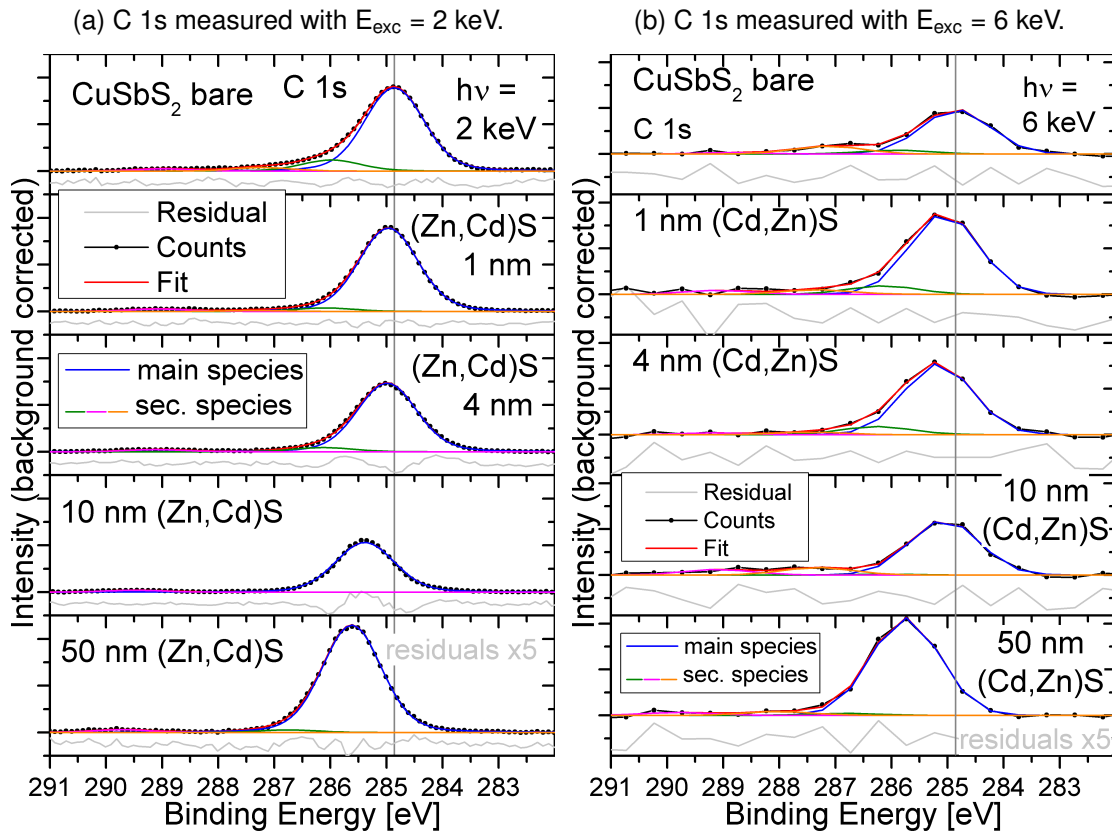


FIGURE A.23: C 1s fits for all samples measured with different  $E_{\text{exc}}$ . The 6 keV spectra have been extracted from survey spectra.

The main C 1s peak in 2 keV fits (figure A.23a) shows a clear shift to higher  $E_B$  with increasing contact layer thickness.

For fits of the 6 keV spectra (figure A.23b) the position differences of the species are fixed according to results from 2 keV fits which is more precise due to the much smaller step width. Within the error margin, the 6 keV positions confirm the findings with the more precise 2 keV measurements except for the 10 nm sample.

TABLE A.4: Shifts of the main C 1s peak to move to the literature value of 284.8 eV.

$E_{\text{exc}}$	error margin	$284.8 \text{ eV} - E_B^{\text{C}1\text{s}}$ [eV]				
		bare	1nm	4nm	10nm	50nm
2 keV	0.02	-0.061	-0.165	-0.190	-0.584	-0.818
6 keV	0.20	-0.053	-0.261	-0.364	-0.255	-0.951





# Bibliography

- [1] W. Pauli. 1931 in a letter from New York to R. Peierls, in: Pauli, Briefwechsel II, 1985, Nr. 287, p 94. Condensed Matter News, 2(15):15–16, 1993.
- [2] Richard Phillips Feynman. Feynman Lectures on Computation. Addison-Wesley Longman Publishing Co., Inc., 1998. ISBN 978-0-201-38628-8.
- [3] Martin A. Green. Thin-film solar cells: review of materials, technologies and commercial status. Journal of Materials Science: Materials in Electronics, 18(1):15–19, 2007. ISSN 0957-4522, 1573-482X. doi: 10.1007/s10854-007-9177-9. URL <http://link.springer.com/article/10.1007/s10854-007-9177-9>.
- [4] O. Vigil-Galán, Maykel Courel, J. A. Andrade-Arvizu, Y. Sánchez, M. Espíndola-Rodríguez, E. Saucedo, D. Seuret-Jiménez, and Matthew Titsworth. Route towards low cost-high efficiency second generation solar cells: current status and perspectives. Journal of Materials Science: Materials in Electronics, 26(8):5562–5573, 2014. ISSN 0957-4522, 1573-482X. doi: 10.1007/s10854-014-2196-4. URL <http://link.springer.com/article/10.1007/s10854-014-2196-4>.
- [5] National Center for Photovoltaics. NREL efficiency chart, 2016. URL [http://www.nrel.gov/ncpv/images/efficiency\\_chart.jpg](http://www.nrel.gov/ncpv/images/efficiency_chart.jpg).
- [6] U.S. Geological survey. Mineral Commodity Summaries, 2016. URL <http://minerals.usgs.gov/minerals/pubs/mcs/2016/mcs2016.pdf>.
- [7] William Shockley and Hans J. Queisser. Detailed balance limit of efficiency of p-n junction solar cells. Journal of Applied Physics, 32(3):510–519, 1961. ISSN 0021-8979, 1089-7550. doi: 10.1063/1.1736034. URL <http://scitation.aip.org/content/aip/journal/jap/32/3/10.1063/1.1736034>.
- [8] W. Schottky. Vereinfachte und erweiterte Theorie der Randschicht-gleichrichter. Zeitschrift für Physik, 118(9):539–592, 1942. ISSN 0044-3328. doi: 10.1007/BF01329843. URL <http://link.springer.com/article/10.1007/BF01329843>.
- [9] A. Einstein. Über einen die Erzeugung und Verwandlung des Lichtes betreffenden heuristischen Gesichtspunkt. Annalen der Physik, 322(6):132–148, 1905. ISSN 1521-3889. doi: 10.1002/andp.19053220607. URL <http://onlinelibrary.wiley.com/doi/10.1002/andp.19053220607/abstract>.
- [10] Susanne Siebentritt. What limits the efficiency of chalcopyrite solar cells? Solar Energy Materials and Solar Cells, 95(6):1471–1476, 2011. ISSN 0927-0248. doi: 10.1016/j.solmat.2010.12.014. URL <http://www.sciencedirect.com/science/article/pii/S0927024810006914>.
- [11] M. P. Seah and W. A. Dench. Quantitative electron spectroscopy of surfaces: A standard data base for electron inelastic mean free paths in solids. Surface and Interface Analysis, 1(1):2–11, February 1979. ISSN 1096-9918. doi: 10.1002/sia.740010103. URL <http://onlinelibrary.wiley.com/doi/10.1002/sia.740010103/abstract>.
- [12] Sven Tougaard. QUASES-IMFP-TPP2m code for the calculation of the inelastic electron mean free path, Version 2.2, 2014. URL <http://www.quases.com/>.
- [13] David Attwood. Soft X-ray and Extreme Ultraviolet Radiation - Principles and Applications. Cambridge University Press, 1999.

- [14] D. Briggs and M. P. Seah. *Practical Surface Analysis, Auger and X-ray Photoelectron Spectroscopy*. Wiley, November 1990. ISBN 978-0-471-92081-6.
- [15] M. Gorgoi, S. Svensson, F. Schäfers, G. Öhrwall, M. Mertin, P. Bressler, O. Karis, H. Siegbahn, A. Sandell, H. Rensmo, W. Doherty, C. Jung, W. Braun, and W. Eberhardt. The high kinetic energy photoelectron spectroscopy facility at BESSY; progress and first results. *Nuclear Instruments and Methods in Physics Research Section A*, 601(1):48–53, 2009. ISSN 01689002. doi: 10.1016/j.nima.2008.12.244. URL <http://linkinghub.elsevier.com/retrieve/pii/S0168900208020111>.
- [16] F. Schaefers, M. Mertin, and M. Gorgoi. KMC-1: A high resolution and high flux soft x-ray beamline at BESSY. *Review of Scientific Instruments*, 78(12):123102, 2007. ISSN 0034-6748, 1089-7623. doi: 10.1063/1.2808334. URL <http://scitation.aip.org/content/aip/journal/rsi/78/12/10.1063/1.2808334>.
- [17] Shigenori Ueda, Yoshio Katsuya, Masahiko Tanaka, Hideki Yoshikawa, Yoshiyuki Yamashita, Satoshi Ishimaru, Yoshitaka Matsushita, Keisuke Kobayashi, R. Garrett, I. Gentle, K. Nugent, and S. Wilkins. Present status of the NIMS contract beamline BL15XU at SPring-8. In *AIP Conference Proceedings*, pages 403–406. AIP Publishing, 2010. doi: 10.1063/1.3463225. URL <http://scitation.aip.org/content/aip/proceeding/aipcp/10.1063/1.3463225>.
- [18] S. Ueda. Application of hard x-ray photoelectron spectroscopy to electronic structure measurements for various functional materials. *Journal of Electron Spectroscopy and Related Phenomena*, 190, Part B:235–241, 2013. ISSN 0368-2048. doi: 10.1016/j.elspec.2013.01.009. URL <http://www.sciencedirect.com/science/article/pii/S036820481300011X>.
- [19] Eiji Ikenaga, Masaaki Kobata, Hiroyuki Matsuda, Takeharu Sugiyama, Hiroshi Daimon, and Keisuke Kobayashi. Development of high lateral and wide angle resolved hard X-ray photoemission spectroscopy at BL47XU in SPring-8. *Journal of Electron Spectroscopy and Related Phenomena*, 190, Part B:180–187, October 2013. ISSN 0368-2048. doi: 10.1016/j.elspec.2013.04.004. URL <http://www.sciencedirect.com/science/article/pii/S0368204813000571>.
- [20] Eric Gullikson. X-ray attenuation length, 2016. URL [http://henke.lbl.gov/optical\\_constants/atten2.html](http://henke.lbl.gov/optical_constants/atten2.html).
- [21] B. L. Henke, E. M. Gullikson, and J. C. Davis. X-Ray Interactions: Photoabsorption, Scattering, Transmission, and Reflection at  $E = 50\text{--}30,000$  eV,  $Z = 1\text{--}92$ . *Atomic Data and Nuclear Data Tables*, 54(2):181–342, July 1993. ISSN 0092-640X. doi: 10.1006/adnd.1993.1013. URL <http://www.sciencedirect.com/science/article/pii/S0092640X83710132>.
- [22] M. Bar, L. Weinhardt, O. Fuchs, J. Klaer, J. Peiser, H. w Schock, and C. Heske. Chemical bath deposition of CdS thin films on  $\text{CuInS}_2$  and Si substrates - A comparative x-ray emission study. In *2006 IEEE 4th World Conference on Photovoltaic Energy Conference*, volume 1, pages 416–419, 2006. doi: 10.1109/WCPEC.2006.279478.
- [23] J. J. Jia, T. A. Callcott, J. Yurkas, A. W. Ellis, F. J. Himpsel, M. G. Samant, J. Stöhr, D. L. Edler, J. A. Carlisle, E. A. Hudson, L. J. Terminello, D. K. Shuh, and R. C. C. Perera. First experimental results from IBM/TENN/TULANE/LLNL/LBL undulator beamline at the advanced light source. *Review of Scientific Instruments*, 66(2):1394–1397, 1995. ISSN 0034-6748, 1089-7623. doi: 10.1063/1.1145985. URL <http://scitation.aip.org/content/aip/journal/rsi/66/2/10.1063/1.1145985>.
- [24] M. Blum, L. Weinhardt, O. Fuchs, M. Bär, Y. Zhang, M. Weigand, S. Krause, S. Pookpanratana, T. Hofmann, W. Yang, J. D. Denlinger, E. Umbach, and C. Heske. Solid and liquid spectroscopic analysis (SALSA)—a soft x-ray spectroscopy endstation with a novel flow-through liquid cell. *Review of Scientific Instruments*, 80(12):123102, 2009. ISSN 0034-6748, 1089-7623. doi: 10.1063/1.3257926. URL <http://scitation.aip.org/content/aip/journal/rsi/80/12/10.1063/1.3257926>.
- [25] L. Weinhardt, O. Fuchs, E. Umbach, C. Heske, A. Fleszar, W. Hanke, and J. D. Denlinger. Resonant inelastic soft x-ray scattering, x-ray absorption spectroscopy, and density functional theory calculations of the electronic bulk band structure of CdS. *Physical Review B*, 75(16):165207, 2007. doi: 10.1103/PhysRevB.75.165207. URL <http://link.aps.org/doi/10.1103/PhysRevB.75.165207>.

- [26] <http://xdb.lbl.gov/>. *X-ray Data Booklet*. Lawrence Berkeley National Laboratory, University of California, Berkeley, CA 94720, 3rd edition, 2009.
- [27] Siew Wei Goh, Alan N. Buckley, William M. Skinner, and Liang-Jen Fan. An X-ray photoelectron and absorption spectroscopic investigation of the electronic structure of cubanite,  $\text{CuFe}_2\text{S}_3$ . *Physics and Chemistry of Minerals*, 37(6):389–405, 2009. ISSN 0342-1791, 1432-2021. doi: 10.1007/s00269-009-0341-z. URL <http://link.springer.com/article/10.1007/s00269-009-0341-z>.
- [28] S. Tanuma, C. J. Powell, and D. R. Penn. Calculations of electron inelastic mean free paths. V. Data for 14 organic compounds over the 50–2000 eV range. *Surface and Interface Analysis*, 21(3):165–176, 1994. ISSN 1096-9918. doi: 10.1002/sia.740210302. URL <http://onlinelibrary.wiley.com/doi/10.1002/sia.740210302/abstract>.
- [29] Kentaro Ito and Tatsuo Nakazawa. Electrical and Optical Properties of Stannite-Type Quaternary Semiconductor Thin Films. *Japanese Journal of Applied Physics*, 27(Part 1, No. 11):2094–2097, November 1988. ISSN 0021-4922, 1347-4065. doi: 10.1143/JJAP.27.2094. URL <http://adsabs.harvard.edu/abs/1988JaJAP..27.2094I>.
- [30] Hironori Katagiri, Nobuyuki Sasaguchi, Shima Hando, Suguro Hoshino, Jiro Ohashi, and Takaharu Yokota. Preparation and evaluation of  $\text{Cu}_2\text{ZnSnS}_4$  thin films by sulfurization of E-B evaporated precursors. *Solar Energy Materials and Solar Cells*, 49(1):407–414, 1997. ISSN 0927-0248. doi: 10.1016/S0927-0248(97)00119-0. URL <http://www.sciencedirect.com/science/article/pii/S0927024897001190>.
- [31] Ingrid Repins, Nirav Vora, Carolyn Beall, Su-Huai Wei, Yanfa Yan, Manuel Romero, Glenn Teeter, Hui Du, Bobby To, Matt Young, and Rommel Noufi. Kesterites and Chalcopyrites: A Comparison of Close Cousins. *MRS Online Proceedings Library*, 1324:null–null, 2011. doi: 10.1557/opl.2011.844.
- [32] A. Redinger, D.M. Berg, P.J. Dale, R. Djemour, L. Gütay, T. Eisenbarth, N. Valle, and S. Siebentritt. Route Toward High-Efficiency Single-Phase  $\text{Cu}_2\text{ZnSn}(\text{S},\text{Se})_4$  Thin-Film Solar Cells: Model Experiments and Literature Review. *IEEE Journal of Photovoltaics*, 1(2):200–206, 2011. ISSN 2156-3381. doi: 10.1109/JPHOTOV.2011.2168811.
- [33] Hongxia Wang. Progress in Thin Film Solar Cells Based on  $\text{Cu}_2\text{ZnSnS}_4$ . *International Journal of Photoenergy*, 2011, September 2011. ISSN 1110-662X. doi: 10.1155/2011/801292. URL <http://www.hindawi.com/journals/ijp/2011/801292/abs/>.
- [34] Susanne Siebentritt and Susan Schorr. Kesterites - a challenging material for solar cells. *Progress in Photovoltaics: Research and Applications*, 20(5):512–519, 2012. ISSN 1099-159X. doi: 10.1002/pip.2156. URL <http://onlinelibrary.wiley.com/doi/10.1002/pip.2156/abstract>.
- [35] S. Delbos. Kesterite thin films for photovoltaics : A review. *EPJ Photovoltaics*, 3:35004, August 2012. ISSN 2105-0716. doi: 10.1051/epjpv/2012008. URL [http://www.epj-pv.org/articles/epjpv/full\\_html/2012/01/pv110023/pv110023.html](http://www.epj-pv.org/articles/epjpv/full_html/2012/01/pv110023/pv110023.html).
- [36] M. P. Suryawanshi, G. L. Agawane, S. M. Bhosale, S. W. Shin, P. S. Patil, J. H. Kim, and A. V. Moholkar. CZTS based thin film solar cells: A status review. *Materials Technology*, 28(1-2):98–109, March 2013. ISSN 1066-7857. doi: 10.1179/1753555712Y.0000000038. URL <http://dx.doi.org/10.1179/1753555712Y.0000000038>.
- [37] I.D. Olekseyuk, I.V. Dudchak, and L.V. Piskach. Phase equilibria in the  $\text{Cu}_2\text{S-ZnS-SnS}_2$  system. *Journal of Alloys and Compounds*, 368(1–2):135–143, April 2004. ISSN 0925-8388. doi: 10.1016/j.jallcom.2003.08.084. URL <http://www.sciencedirect.com/science/article/pii/S0925838803008843>.
- [38] X. Fontané, L. Calvo-Barrio, V. Izquierdo-Roca, E. Saucedo, A. Pérez-Rodríguez, J. R. Morante, D. M. Berg, P. J. Dale, and S. Siebentritt. In-depth resolved Raman scattering analysis for the identification of secondary phases: Characterization of  $\text{Cu}_2\text{ZnSnS}_4$  layers for solar cell applications. *Applied Physics Letters*, 98(18):181905, May 2011. ISSN 00036951. doi:10.1063/1.3587614. URL [http://apl.aip.org/resource/1/applab/v98/i18/p181905\\_s1](http://apl.aip.org/resource/1/applab/v98/i18/p181905_s1).
- [39] Susan Schorr, Hans-Joachim Hoebler, and Michael Tovar. A neutron diffraction study of the stannite-kesterite solid solution series. *European Journal of Mineralogy*, 19(1):65–73, 2007. ISSN 0935-1221, 1617-4011. doi: 10.1127/0935-1221/2007/0019-0065. URL <http://eurjmin.geoscienceworld.org/content/19/1/65>.

- [40] Susan Schorr. The crystal structure of kesterite type compounds: A neutron and X-ray diffraction study. *Solar Energy Materials and Solar Cells*, 95(6):1482–1488, June 2011. ISSN 0927-0248. doi: 10.1016/j.solmat.2011.01.002. URL <http://www.sciencedirect.com/science/article/pii/S0927024811000031>.
- [41] Alain Lafond, Léo Choubrac, Catherine Guillot-Deudon, Philippe Deniard, and Stephane Jobic. Crystal structures of photovoltaic chalcogenides, an intricate puzzle to solve: the cases of CIGSe and CZTS materials. *Zeitschrift für anorganische und allgemeine Chemie*, 638(15):2571–2577, 2012. ISSN 1521-3749. doi: 10.1002/zaac.201200279. URL <http://onlinelibrary.wiley.com/doi/10.1002/zaac.201200279/abstract>.
- [42] Alain Lafond, Léo Choubrac, Catherine Guillot-Deudon, Pierre Fertey, Michel Evain, and Stéphane Jobic. X-ray resonant single-crystal diffraction technique, a powerful tool to investigate the kesterite structure of the photovoltaic  $\text{Cu}_2\text{ZnSnS}_4$  compound. *Acta Crystallographica Section B, Structural Science, Crystal Engineering and Materials*, 70:390–394, 2014. ISSN 2052-5206. doi: 10.1107/S2052520614003138.
- [43] Adam J. Jackson and Aron Walsh. Ab initio thermodynamic model of  $\text{Cu}_2\text{ZnSnS}_4$ . *Journal of Materials Chemistry A*, 2(21):7829–7836, 2014. ISSN 2050-7496. doi: 10.1039/C4TA00892H. URL <http://pubs.rsc.org/en/content/articlelanding/2014/ta/c4ta00892h>.
- [44] Aron Walsh, Shiyu Chen, X. G. Gong, and Su-Huai Wei. Crystal structure and defect reactions in the kesterite solar cell absorber  $\text{Cu}_2\text{ZnSnS}_4$  (CZTS): Theoretical insights. In *AIP Conference Proceedings*, volume 1399, pages 63–64. AIP Publishing, December 2011. doi: 10.1063/1.3666258. URL <http://scitation.aip.org/content/aip/proceeding/aipcp/10.1063/1.3666258>.
- [45] Shiyu Chen, Aron Walsh, Xin-Gao Gong, and Su-Huai Wei. Classification of Lattice Defects in the Kesterite  $\text{Cu}_2\text{ZnSnS}_4$  and  $\text{Cu}_2\text{ZnSnSe}_4$  Earth-Abundant Solar Cell Absorbers. *Advanced Materials*, 25(11):1522–1539, March 2013. ISSN 1521-4095. doi: 10.1002/adma.201203146. URL <http://onlinelibrary.wiley.com/doi/10.1002/adma.201203146/abstract>.
- [46] V. Kosyak, N. B. Mortazavi Amiri, A. V. Postnikov, and M. A. Scarpulla. Model of native point defect equilibrium in  $\text{Cu}_2\text{ZnSnS}_4$  and application to one-zone annealing. *Journal of Applied Physics*, 114(12):124501, 2013. ISSN 0021-8979, 1089-7550. doi: 10.1063/1.4819206. URL <http://scitation.aip.org/content/aip/journal/jap/114/12/10.1063/1.4819206>.
- [47] Jonathan J. Scragg, Tove Ericson, Xavier Fontané, Victor Izquierdo-Roca, Alejandro Pérez-Rodríguez, Tomas Kubart, Marika Edoff, and Charlotte Platzer-Björkman. Rapid annealing of reactively sputtered precursors for  $\text{Cu}_2\text{ZnSnS}_4$  solar cells. *Progress in Photovoltaics: Research and Applications*, 22(1):10–17, 2014. ISSN 1099-159X. doi: 10.1002/ppp.2265. URL <http://onlinelibrary.wiley.com/doi/10.1002/ppp.2265/abstract>.
- [48] Jonathan J. S. Scragg, Léo Choubrac, Alain Lafond, Tove Ericson, and Charlotte Platzer-Björkman. A low-temperature order-disorder transition in  $\text{Cu}_2\text{ZnSnS}_4$  thin films. *Applied Physics Letters*, 104(4):041911, 2014. ISSN 0003-6951, 1077-3118. doi: 10.1063/1.4863685. URL <http://scitation.aip.org/content/aip/journal/apl/104/4/10.1063/1.4863685>.
- [49] Hironori Katagiri, Kazuo Jimbo, Satoru Yamada, Tsuyoshi Kamimura, Win Shwe Maw, Tatsuo Fukano, Tadashi Ito, and Tomoyoshi Motohiro. Enhanced Conversion Efficiencies of  $\text{Cu}_2\text{ZnSnS}_4$ -Based Thin Film Solar Cells by Using Preferential Etching Technique. *Applied Physics Express*, 1(4):041201, 2008. doi: 10.7567/APEX.1.041201. URL <http://apex.jsap.jp/link?APEX/1/041201/>.
- [50] K. Timmo, M. Altosaar, J. Raudoja, M. Grossberg, M. Danilson, O. Volobujeva, and E. Melnikov. Chemical etching of  $\text{Cu}_2\text{ZnSn(S,Se)}_4$  monograin powder. In *2010 35th IEEE Photovoltaic Specialists Conference (PVSC)*, pages 001982–001985, 2010. doi: 10.1109/PVSC.2010.5616411.
- [51] Andrew Fairbrother, Eric García-Hemme, Victor Izquierdo-Roca, Xavier Fontané, Fabián A. Pulgarín-Agudelo, Osvaldo Vigil-Galán, Alejandro Pérez-Rodríguez, and Edgardo Saucedo. Development of a Selective Chemical Etch To Improve the Conversion Efficiency of Zn-Rich  $\text{Cu}_2\text{ZnSnS}_4$  Solar Cells. *Journal of the American Chemical Society*, 134(19):8018–8021, May 2012. ISSN 0002-7863. doi: 10.1021/ja301373e. URL <http://dx.doi.org/10.1021/ja301373e>.
- [52] Marina Mousel, Alex Redinger, Rabie Djemour, Monika Arasimowicz, Nathalie Valle, Phillip Dale, and Susanne Siebentritt. HCl and  $\text{Br}_2$ -MeOH etching of  $\text{Cu}_2\text{ZnSnSe}_4$  polycrystalline absorbers. *Thin Solid Films*, 535:83–87, May 2013. ISSN 0040-6090. doi: 10.1016/j.tsf.2012.12.095. URL <http://www.sciencedirect.com/science/article/pii/S0040609013000217>.

- [53] K. Granath, L. Stolt, M. Bodegard, A. Rockett, and D. Schroeder. Sodium in sputtered Mo back contacts for Cu(In,Ga)Se<sub>2</sub> devices: incorporation, diffusion, and relationship to oxygen. In *Proceedings of the 14th European Photovoltaic Solar Energy Conference*, pages 1278–1282, 1997.
- [54] Robert V. Forest, Erten Eser, Brian E. McCandless, Robert W. Birkmire, and Jingguang G. Chen. Understanding the role of oxygen in the segregation of sodium at the surface of molybdenum coated soda-lime glass. *AIChE Journal*, 60(6):2365–2372, 2014. ISSN 1547-5905. doi: 10.1002/aic.14425. URL <http://onlinelibrary.wiley.com/doi/10.1002/aic.14425/abstract>.
- [55] Leeor Kronik, David Cahen, and Hans Werner Schock. Effects of sodium on polycrystalline Cu(In,Ga)Se<sub>2</sub> and its solar cell performance. *Advanced Materials*, 10(1):31–36, 1998. ISSN 1521-4095. doi: 10.1002/(SICI)1521-4095(199801)10:1<31::AID-ADMA31>3.0.CO;2-3. URL [http://onlinelibrary.wiley.com/doi/10.1002/\(SICI\)1521-4095\(199801\)10:1<31::AID-ADMA31>3.0.CO;2-3/abstract](http://onlinelibrary.wiley.com/doi/10.1002/(SICI)1521-4095(199801)10:1<31::AID-ADMA31>3.0.CO;2-3/abstract).
- [56] Leeor Kronik, Uwe Rau, Jean-François Guillemoles, Dieter Braunger, Hans-Werner Schock, and David Cahen. Interface redox engineering of Cu(In,Ga)Se<sub>2</sub> – based solar cells: oxygen, sodium, and chemical bath effects. *Thin Solid Films*, 361–362:353–359, 2000. ISSN 0040-6090. doi: 10.1016/S0040-6090(99)00768-3. URL <http://www.sciencedirect.com/science/article/pii/S0040609099007683>.
- [57] Kee-Jeong Yang, Jun-Hyoung Sim, Boram Jeon, Dae-Ho Son, Dae-Hwan Kim, Shi-Joon Sung, Dae-Kue Hwang, Soomin Song, Dhruva B. Khadka, JunHo Kim, and Jin-Kyu Kang. Effects of Na and MoS<sub>2</sub> on Cu<sub>2</sub>ZnSnS<sub>4</sub> thin-film solar cell. *Progress in Photovoltaics: Research and Applications*, 23(7):862–873, 2015. ISSN 1099-159X. doi: 10.1002/pip.2500. URL <http://onlinelibrary.wiley.com/doi/10.1002/pip.2500/abstract>.
- [58] W. Shan, W. Walukiewicz, J. W. Ager III, K. M. Yu, J. Wu, E. E. Haller, Y. Nabetani, T. Mukawa, Y. Ito, and T. Matsumoto. Effect of oxygen on the electronic band structure in ZnO<sub>x</sub>Se<sub>1-x</sub> alloys. *Applied Physics Letters*, 83(2):299–301, July 2003. ISSN 0003-6951, 1077-3118. doi: 10.1063/1.1592885. URL <http://scitation.aip.org/content/aip/journal/apl/83/2/10.1063/1.1592885>.
- [59] Huibin Liu, Xinhua Pan, Ping Ding, Zhizhen Ye, Haiping He, and Jingyun Huang. Effects of diffusion temperature and diffusion time on fabrication of Na-diffused p-type ZnO thin films. *Materials Letters*, 80:175–177, August 2012. ISSN 0167-577X. doi: 10.1016/j.matlet.2012.04.092. URL <http://www.sciencedirect.com/science/article/pii/S0167577X12005824>.
- [60] Saliha Ilican. Effect of Na doping on the microstructures and optical properties of ZnO nanorods. *Journal of Alloys and Compounds*, 553:225–232, March 2013. ISSN 0925-8388. doi: 10.1016/j.jallcom.2012.11.081. WOS:000314640600041.
- [61] Teodor K. Todorov, Kathleen B. Reuter, and David B. Mitzi. High-Efficiency Solar Cell with Earth-Abundant Liquid-Processed Absorber. *Advanced Materials*, 22(20):E156–E159, 2010. ISSN 1521-4095. doi: 10.1002/adma.200904155. URL <http://onlinelibrary.wiley.com/doi/10.1002/adma.200904155/abstract>.
- [62] Wei Wang, Mark T. Winkler, Oki Gunawan, Tayfun Gokmen, Teodor K. Todorov, Yu Zhu, and David B. Mitzi. Device Characteristics of CZTSSe Thin-Film Solar Cells with 12.6% Efficiency. *Advanced Energy Materials*, 4(7):n/a–n/a, May 2014. ISSN 1614-6840. doi: 10.1002/aenm.201301465. URL <http://onlinelibrary.wiley.com/doi/10.1002/aenm.201301465/abstract>.
- [63] Ingrid Repins, Carolyn Beall, Nirav Vora, Clay DeHart, Darius Kuciauskas, Pat Dippo, Bobby To, Jonathan Mann, Wan-Ching Hsu, Alan Goodrich, and Rommel Noufi. Co-evaporated Cu<sub>2</sub>ZnSnSe<sub>4</sub> films and devices. *Solar Energy Materials and Solar Cells*, 101:154–159, June 2012. ISSN 0927-0248. doi: 10.1016/j.solmat.2012.01.008. URL <http://www.sciencedirect.com/science/article/pii/S0927024812000098>.
- [64] Huanping Zhou, Wan-Ching Hsu, Hsin-Sheng Duan, Brion Bob, Wenbing Yang, Tze-Bin Song, Chia-Jung Hsu, and Yang Yang. CZTS nanocrystals: A promising approach for next generation thin film photovoltaics. *Energy & Environmental Science*, August 2013. ISSN 1754-5706. doi: 10.1039/C3EE41627E. URL <http://pubs.rsc.org/en/content/articlelanding/2013/ee/c3ee41627e>.
- [65] Grayson M. Ford, Qijie Guo, Rakesh Agrawal, and Hugh W. Hillhouse. Earth Abundant Element Cu<sub>2</sub>Zn(Sn<sub>1-x</sub>Ge<sub>x</sub>)S<sub>4</sub> Nanocrystals for Tunable Band Gap Solar Cells: 6.8% Efficient Device Fabrication. *Chemistry of Materials*, 23(10):2626–2629, May 2011. ISSN 0897-4756. doi: 10.1021/cm2002836. URL <http://dx.doi.org/10.1021/cm2002836>.

- [66] Yi Ren, Jonathan J. S. Scragg, Marika Edoff, Jes K. Larsen, and Charlotte Platzer-Björkman. Evolution of Na-S(-) compounds on the  $\text{Cu}_2\text{ZnSnS}_4$  absorber surface and their effects on CdS thin film growth. *ACS Applied Materials & Interfaces*, 8(28):18600–18607, 2016. ISSN 1944-8244. doi: 10.1021/acsami.6b04978. URL <http://dx.doi.org/10.1021/acsami.6b04978>.
- [67] M. Bär, B. Schubert, B. Marsen, T. Unold, R. G. Wilks, H. W. Schock, S. Pookpanratana, M. Blum, S. Krause, Y. Zhang, C. Heske, W. Yang, and L. Weinhardt.  $\text{Cu}_2\text{ZnSnS}_4$  thin-film solar cell absorber composition revealed by energy-dispersive and soft x-ray emission spectroscopy. In *2010 35th IEEE Photovoltaic Specialists Conference (PVSC)*, pages 000646–000649, 2010. doi: 10.1109/PVSC.2010.5616878.
- [68] M. Bär, B.-A. Schubert, B. Marsen, R.g. Wilks, M. Blum, S. Krause, S. Pookpanratana, Y. Zhang, T. Unold, W. Yang, L. Weinhardt, C. Heske, and H.-W. Schock.  $\text{Cu}_2\text{ZnSnS}_4$  thin-film solar cell absorbers illuminated by soft x-rays. *Journal of Materials Research*, 27(08):1097–1104, 2012. doi: 10.1557/jmr.2012.59.
- [69] M. Bär, S. Pookpanratana, L. Weinhardt, R.G. Wilks, B.A. Schubert, B. Marsen, T. Unold, M. Blum, S. Krause, Y. Zhang, A. Ranasinghe, K. Ramanathan, I. Repins, M.A. Contreras, S. Nishiwaki, X. Liu, N.R. Paudel, O. Fuchs, T.P. Niesen, W. Yang, F. Karg, A.D. Compaan, W.N. Shafarman, R. Noufi, H.-W. Schock, and C. Heske. Soft X-rays shedding light on thin-film solar cell surfaces and interfaces. *Journal of Electron Spectroscopy and Related Phenomena*, October 2013. ISSN 0368-2048. doi: 10.1016/j.elspec.2012.10.004. URL <http://www.sciencedirect.com/science/article/pii/S0368204812001296>.
- [70] Susan Schorr, Roland Mainz, Harry Mönig, Iver Laueremann, and Marcus Bär. The complex material properties of chalcopyrite and kesterite thin-film solar cell absorbers tackled by synchrotron-based analytics. *Progress in Photovoltaics: Research and Applications*, 20(5):557–567, 2012. ISSN 1099-159X. doi: 10.1002/pip.1256. URL <http://onlinelibrary.wiley.com/doi/10.1002/pip.1256/abstract>.
- [71] Kaiwen Sun, Chang Yan, Fangyang Liu, Jialiang Huang, Fangzhou Zhou, John A. Stride, Martin Green, and Xiaojing Hao. Over 9% efficient kesterite  $\text{Cu}_2\text{ZnSnS}_4$  solar cell fabricated by using  $\text{Zn}_{1-x}\text{Cd}_x\text{S}$  buffer layer. *Advanced Energy Materials*, 6(12):n/a–n/a, 2016. ISSN 1614-6840. doi: 10.1002/aenm.201600046. URL <http://onlinelibrary.wiley.com/doi/10.1002/aenm.201600046/abstract>.
- [72] M. Bär, B.-A. Schubert, B. Marsen, R. G. Wilks, S. Pookpanratana, M. Blum, S. Krause, T. Unold, W. Yang, L. Weinhardt, C. Heske, and H.-W. Schock. Cliff-like conduction band offset and KCN-induced recombination barrier enhancement at the CdS/ $\text{Cu}_2\text{ZnSnS}_4$  thin-film solar cell heterojunction. *Applied Physics Letters*, 99(22):222105–222105–3, November 2011. ISSN 00036951. doi: doi:10.1063/1.3663327. URL [http://apl.aip.org/resource/1/applab/v99/i22/p222105\\_s1](http://apl.aip.org/resource/1/applab/v99/i22/p222105_s1).
- [73] Alex Niemegeers, Marc Burgelman, and Alexis De Vos. On the CdS/CuInSe<sub>2</sub> conduction band discontinuity. *Applied Physics Letters*, 67:843–845, 1995. ISSN 0003-6951. doi: 10.1063/1.115523. URL <http://adsabs.harvard.edu/abs/1995ApPhL..67..843N>.
- [74] Reiner Klenk. Characterisation and modelling of chalcopyrite solar cells. *Thin Solid Films*, 387(1):135–140, 2001. ISSN 0040-6090. doi: 10.1016/S0040-6090(00)01736-3. URL <http://www.sciencedirect.com/science/article/pii/S0040609000017363>.
- [75] Takashi Minemoto, Yasuhiro Hashimoto, Takuya Satoh, Takayuki Negami, Hideyuki Takakura, and Yoshihiro Hamakawa. Cu(In,Ga)Se<sub>2</sub> solar cells with controlled conduction band offset of window/Cu(In,Ga)Se<sub>2</sub> layers. *Journal of Applied Physics*, 89(12):8327–8330, 2001. ISSN 0021-8979, 1089-7550. doi: 10.1063/1.1366655. URL <http://scitation.aip.org/content/aip/journal/jap/89/12/10.1063/1.1366655>.
- [76] B. K. Meyer, A. Polity, B. Farangis, Y. He, D. Hasselkamp, Th Krämer, and C. Wang. Structural properties and bandgap bowing of  $\text{ZnO}_{1-x}\text{S}_x$  thin films deposited by reactive sputtering. *Applied Physics Letters*, 85(21):4929–4931, November 2004. ISSN 0003-6951, 1077-3118. doi: 10.1063/1.1825053. URL <http://scitation.aip.org/content/aip/journal/apl/85/21/10.1063/1.1825053>.
- [77] Y.-Z. Yoo, Zheng-Wu Jin, T. Chikyow, T. Fukumura, M. Kawasaki, and H. Koinuma. S doping in ZnO film by supplying ZnS species with pulsed-laser-deposition method. *Applied Physics Letters*, 81(20):3798–3800, November 2002. ISSN 0003-6951, 1077-3118. doi: 10.1063/1.1521577. URL <http://scitation.aip.org/content/aip/journal/apl/81/20/10.1063/1.1521577>.

- [78] K. Iwata, P. Fons, A. Yamada, H. Shibata, K. Matsubara, K. Nakahara, H. Takasu, and S. Niki. Bandgap Engineering of ZnO Using Se. *physica status solidi (b)*, 229(2):887–890, January 2002. ISSN 1521-3951. doi: 10.1002/1521-3951(200201)229:2<887::AID-PSSB887>3.0.CO;2-G. URL [http://onlinelibrary.wiley.com/doi/10.1002/1521-3951\(200201\)229:2<887::AID-PSSB887>3.0.CO;2-G/abstract](http://onlinelibrary.wiley.com/doi/10.1002/1521-3951(200201)229:2<887::AID-PSSB887>3.0.CO;2-G/abstract).
- [79] C. Platzer-Björkman, T. Törndahl, D. Abou-Ras, J. Malmström, J. Kessler, and L. Stolt. Zn(o,s) buffer layers by atomic layer deposition in Cu(In,Ga)Se<sub>2</sub> based thin film solar cells: Band alignment and sulfur gradient. *Journal of Applied Physics*, 100(4):044506, 2006. ISSN 0021-8979, 1089-7550. doi: 10.1063/1.2222067. URL <http://scitation.aip.org/content/aip/journal/jap/100/4/10.1063/1.2222067>.
- [80] Charlotte Platzer-Björkman, Adam Hultqvist, Jonas Pettersson, and Tobias Törndahl. Band gap engineering of ZnO for high efficiency CIGS based solar cells. In *Oxide-based Materials and Devices*, volume 7603, pages 76030F–76030F–9, 2010. doi: 10.1117/12.846017. URL <http://dx.doi.org/10.1117/12.846017>.
- [81] M. Bär, A. Ennaoui, J. Klaer, T. Kropp, R. Sáez-Araoz, N. Allsop, I. Lauermann, H.-W. Schock, and M. C. Lux-Steiner. Formation of a ZnS/Zn(S,O) bilayer buffer on CuInS<sub>2</sub> thin film solar cell absorbers by chemical bath deposition. *Journal of Applied Physics*, 99(12):123503, June 2006. ISSN 0021-8979, 1089-7550. doi: 10.1063/1.2202694. URL <http://scitation.aip.org/content/aip/journal/jap/99/12/10.1063/1.2202694>.
- [82] K. Xerxes Steirer, Rebekah L. Garris, Jian V. Li, Michael J. Dzara, Paul F. Ndione, Kannan Ramanathan, Ingrid Repins, Glenn Teeter, and Craig L. Perkins. Co-solvent Enhanced Zinc Oxysulfide Buffer Layers in Kesterite Copper Zinc Tin Selenide Solar Cells. *Physical Chemistry Chemical Physics*, 17(23), May 2015. ISSN 1463-9084. doi: 10.1039/C5CP01607J. URL [https://www.researchgate.net/publication/276363808\\_Co-solvent\\_Enhanced\\_Zinc\\_Oxysulfide\\_Buffer\\_Layers\\_in\\_Kesterite\\_Copper\\_Zinc\\_Tin\\_Selenide\\_Solar\\_Cells](https://www.researchgate.net/publication/276363808_Co-solvent_Enhanced_Zinc_Oxysulfide_Buffer_Layers_in_Kesterite_Copper_Zinc_Tin_Selenide_Solar_Cells).
- [83] D. Aaron R. Barkhouse, Richard Haight, Noriyuki Sakai, Homare Hiroi, Hiroki Sugimoto, and David B. Mitzi. Cd-free buffer layer materials on Cu<sub>2</sub>ZnSn(S<sub>x</sub>Se<sub>1-x</sub>)<sub>4</sub>: Band alignments with ZnO, ZnS, and In<sub>2</sub>S<sub>3</sub>. *Applied Physics Letters*, 100(19):193904, May 2012. ISSN 0003-6951, 1077-3118. doi: 10.1063/1.4714737. URL <http://scitation.aip.org/content/aip/journal/apl/100/19/10.1063/1.4714737>.
- [84] Tove Ericson, Tomas Kubart, Jonathan J. Scragg, and Charlotte Platzer-Björkman. Reactive sputtering of precursors for Cu<sub>2</sub>ZnSnS<sub>4</sub> thin film solar cells. *Thin Solid Films*, 520(24):7093–7099, October 2012. ISSN 0040-6090. doi: 10.1016/j.tsf.2012.08.002. URL <http://www.sciencedirect.com/science/article/pii/S0040609012010152>.
- [85] Tove Ericson, Jonathan J. Scragg, Tomas Kubart, Tobias Törndahl, and Charlotte Platzer-Björkman. Annealing behavior of reactively sputtered precursor films for Cu<sub>2</sub>ZnSnS<sub>4</sub> solar cells. *Thin Solid Films*, 535:22–26, May 2013. ISSN 0040-6090. doi: 10.1016/j.tsf.2012.10.081. URL <http://www.sciencedirect.com/science/article/pii/S004060901201351X>.
- [86] Jonathan J. Scragg, Tove Ericson, Tomas Kubart, Marika Edoff, and Charlotte Platzer-Björkman. Chemical insights into the instability of Cu<sub>2</sub>ZnSnS<sub>4</sub> films during annealing. *Chemistry of Materials*, 23(20):4625–4633, 2011. ISSN 0897-4756, 1520-5002. doi: 10.1021/cm202379s. URL <http://pubs.acs.org/doi/abs/10.1021/cm202379s>.
- [87] Uwe Zimmermann, Marta Ruth, and Marika Edoff. Cadmium-free CIGS mini-modules with ALD-grown Zn(O,S)-based buffer layers. presented at: 21st EPSEC, 4-8 September 2006, Dresden, Germany, pages 1831–1834, 2006. URL <http://www.diva-portal.org/smash/record.jsf?pid=diva2%3A52367&dswid=-1051>.
- [88] T. Ericson, J.J. Scragg, A. Hultqvist, J.T. Watjen, P. Szaniawski, T. Torndahl, and C. Platzer-Bjorkman. Zn(O, S) Buffer Layers and Thickness Variations of CdS Buffer for Cu<sub>2</sub>ZnSnS<sub>4</sub> Solar Cells. *IEEE Journal of Photovoltaics*, 4(1):465–469, January 2014. ISSN 2156-3381. doi: 10.1109/JPHOTOV.2013.2283058.
- [89] NIST x-ray photoelectron spectroscopy (XPS) database, version 3.5, accessed 2013, 2014, 2015, 2016. URL <http://srdata.nist.gov/xps/>.

- [90] G. Deroubaix and P. Marcus. X-ray photoelectron spectroscopy analysis of copper and zinc oxides and sulphides. *Surface and Interface Analysis*, 18(1):39–46, January 1992. ISSN 1096-9918. doi: 10.1002/sia.740180107. URL <http://onlinelibrary.wiley.com/doi/10.1002/sia.740180107/abstract>.
- [91] C. D. Wagner. Chemical shifts of auger lines, and the auger parameter. *Faraday Discussions of the Chemical Society*, 60(0):291–300, 1975. ISSN 0301-7249. doi: 10.1039/DC9756000291. URL <http://pubs.rsc.org/en/content/articlelanding/1975/dc/dc9756000291>.
- [92] S. K. Chawla, N. Sankarraman, and J. H. Payer. Diagnostic spectra for XPS analysis of Cu-O-S-H compounds. *Journal of electron spectroscopy and related phenomena*, 61(1):1–18, 1992. ISSN 0368-2048. URL <http://cat.inist.fr/?aModele=afficheN&cpsidt=4611198>.
- [93] Mark C. Biesinger, Leo W. M. Lau, Andrea R. Gerson, and Roger St. C. Smart. Resolving surface chemical states in XPS analysis of first row transition metals, oxides and hydroxides: Sc, Ti, V, Cu and Zn. *Applied Surface Science*, 257(3):887–898, November 2010. ISSN 0169-4332. doi: 10.1016/j.apsusc.2010.07.086. URL <http://www.sciencedirect.com/science/article/pii/S0169433210010287>.
- [94] Andrea R. Gerson and Thomas Bredow. Interpretation of sulphur 2p XPS spectra in sulfide minerals by means of ab initio calculations. *Surface and Interface Analysis*, 29(2):145–150, February 2000. ISSN 1096-9918. doi: 10.1002/(SICI)1096-9918(200002)29:2<145::AID-SIA727>3.0.CO;2-N. URL [http://onlinelibrary.wiley.com/doi/10.1002/\(SICI\)1096-9918\(200002\)29:2<145::AID-SIA727>3.0.CO;2-N/abstract](http://onlinelibrary.wiley.com/doi/10.1002/(SICI)1096-9918(200002)29:2<145::AID-SIA727>3.0.CO;2-N/abstract).
- [95] B. R. Strohmeier, W. T. Evans, and D. M. Schroll. Preparation and surface characterization of zincated aluminium memory-disc substrates. *Journal of Materials Science*, 28(6):1563–1572, 1993. ISSN 0022-2461, 1573-4803. doi: 10.1007/BF00363350. URL <http://link.springer.com/10.1007/BF00363350>.
- [96] A. N. Buckley, H. J. Wouterlood, and R. Woods. The surface composition of natural sphalerites under oxidative leaching conditions. *Hydrometallurgy*, 22(1):39–56, June 1989. ISSN 0304-386X. doi: 10.1016/0304-386X(89)90040-6. URL <http://www.sciencedirect.com/science/article/pii/0304386X89900406>.
- [97] L. S. Dake, D. R. Baer, and J. M. Zachara. Auger parameter measurements of zinc compounds relevant to zinc transport in the environment. *Surface and Interface Analysis*, 14(1-2):71–75, January 1989. ISSN 1096-9918. doi: 10.1002/sia.740140115. URL <http://onlinelibrary.wiley.com/doi/10.1002/sia.740140115/abstract>.
- [98] Michelle Mezher, Rebekah Garris, Lorelle M. Mansfield, Kimberly Horsley, Lothar Weinhardt, Douglas A. Duncan, Monika Blum, Samantha G. Rosenberg, Marcus Bär, Kannan Ramanathan, and Clemens Heske. Electronic structure of the Zn(O,S)/Cu(In,Ga)Se<sub>2</sub> thin-film solar cell interface. *Progress in Photovoltaics: Research and Applications*, 24(8):1142–1148, August 2016. ISSN 1099-159X. doi: 10.1002/pip.2764. URL <http://onlinelibrary.wiley.com/doi/10.1002/pip.2764/abstract>.
- [99] J. R. Waldrop, R. W. Grant, S. P. Kowalczyk, and E. A. Kraut. Measurement of semiconductor heterojunction band discontinuities by x-ray photoemission spectroscopy. *Journal of Vacuum Science & Technology A*, 3(3):835–841, May 1985. ISSN 0734-2101, 1520-8559. doi: 10.1116/1.573326. URL <http://scitation.aip.org/content/avs/journal/jvsta/3/3/10.1116/1.573326>.
- [100] T. V. Kuznetsova, V. I. Grebennikov, H. Zhao, C. Derks, C. Taubitz, M. Neumann, C. Persson, M. V. Kuznetsov, I. V. Bodnar, R. W. Martin, and M. V. Yakushev. A photoelectron spectroscopy study of the electronic structure evolution in CuInSe<sub>2</sub>-related compounds at changing copper content. *Applied Physics Letters*, 101(11):111607, 2012. ISSN 0003-6951, 1077-3118. doi: 10.1063/1.4752723. URL <http://scitation.aip.org/content/aip/journal/apl/101/11/10.1063/1.4752723>.
- [101] C. Heske, U. Groh, O. Fuchs, E. Umbach, N. Franco, C. Bostedt, L.j. Terminello, R.c.c. Perera, K.h. Hallmeier, A. Preobrajenski, R. Szargan, S. Zweigart, W. Riedl, and F. Karg. X-Ray Emission Spectroscopy of Cu(In,Ga)(S,Se)<sub>2</sub>-Based Thin Film Solar Cells: Electronic Structure, Surface Oxidation, and Buried Interfaces. *physica status solidi (a)*, 187(1):13–24, 2001. ISSN 1521-396X. doi: 10.1002/1521-396X(200109)187:1(13::AID-PSSA13)3.0.CO;2-D. URL [http://onlinelibrary.wiley.com/doi/10.1002/1521-396X\(200109\)187:1\(13::AID-PSSA13\)3.0.CO;2-D/abstract](http://onlinelibrary.wiley.com/doi/10.1002/1521-396X(200109)187:1(13::AID-PSSA13)3.0.CO;2-D/abstract).



- [102] L. Zhou, T. A. Callcott, J. J. Jia, D. L. Ederer, and Rupert Perera. Sulfur  $L_{2,3}$  and zinc  $M_{2,3}$  soft-x-ray fluorescence spectra in CdS and ZnS. *Physical Review B*, 55(8):5051–5061, February 1997. doi: 10.1103/PhysRevB.55.5051. URL <http://link.aps.org/doi/10.1103/PhysRevB.55.5051>.
- [103] T. Ericson, J.J. Scragg, A. Hultqvist, J.T. Watjen, P. Szaniawski, T. Torndahl, and C. Platzer-Bjorkman. Zn(O, S) Buffer Layers and Thickness Variations of CdS Buffer for  $\text{Cu}_2\text{ZnSnS}_4$  Solar Cells. *IEEE Journal of Photovoltaics*, Early Access Online, 2013. ISSN 2156-3381. doi: 10.1109/JPHOTOV.2013.2283058.
- [104] P. A. Zhdan, A. P. Shepelin, Z. G. Osipova, and V. D. Sokolovskii. The extent of charge localization on oxygen ions and catalytic activity on solid state oxides in allylic oxidation of propylene. *Journal of Catalysis*, 58(1):8–14, 1997. ISSN 0021-9517. doi: 10.1016/0021-9517(79)90237-9. URL <http://www.sciencedirect.com/science/article/pii/0021951779902379>.
- [105] C. D. Wagner, D. A. Zatko, and R. H. Raymond. Use of the oxygen KLL auger lines in identification of surface chemical states by electron spectroscopy for chemical analysis. *Analytical Chemistry*, 52(9):1445–1451, 1980. ISSN 0003-2700, 1520-6882. doi: 10.1021/ac50059a017. URL <http://pubs.acs.org/doi/abs/10.1021/ac50059a017>.
- [106] C. L. Dong, C. Persson, L. Vayssieres, A. Augustsson, T. Schmitt, M. Mattesini, R. Ahuja, C. L. Chang, and J.-H. Guo. Electronic structure of nanostructured ZnO from x-ray absorption and emission spectroscopy and the local density approximation. *Physical Review B*, 70(19):195325, 2004. doi: 10.1103/PhysRevB.70.195325. URL <http://link.aps.org/doi/10.1103/PhysRevB.70.195325>.
- [107] T Strunskus, O Fuchs, L Weinhardt, C Heske, M Guraya, M Muhler, V Staemmler, and Ch Wöll. The valence electronic structure of zinc oxide powders as determined by x-ray emission spectroscopy: Variation of electronic structure with particle size. *Journal of Electron Spectroscopy and Related Phenomena*, 134(2):183–189, 2004. ISSN 0368-2048. doi: 10.1016/j.elspec.2003.10.003. URL <http://www.sciencedirect.com/science/article/pii/S0368204803001798>.
- [108] M. Bär, K.-S. Ahn, S. Shet, Y. Yan, L. Weinhardt, O. Fuchs, M. Blum, S. Pookpanratana, K. George, W. Yang, J. D. Denlinger, M. Al-Jassim, and C. Heske. Impact of air exposure on the chemical and electronic structure of  $\text{ZnO}:\text{Zn}_3\text{N}_2$  thin films. *Applied Physics Letters*, 94(1):012110, 2009. ISSN 0003-6951, 1077-3118. doi: 10.1063/1.3056638. URL <http://scitation.aip.org/content/aip/journal/apl/94/1/10.1063/1.3056638>.
- [109] M. B. TRZHASKOVSKAYA, V. I. NEFEDOV, and V. G. YARZHEMSKY. PHOTOELECTRON ANGULAR DISTRIBUTION PARAMETERS FOR ELEMENTS  $z=1$  TO  $z=54$  IN THE PHOTOELECTRON ENERGY RANGE 100-5000 eV. *Atomic Data and Nuclear Data Tables*, 77(1):97–159, 2001. ISSN 0092-640X. doi: 10.1006/adnd.2000.0849. URL <http://www.sciencedirect.com/science/article/pii/S0092640X00908490>.
- [110] M. B. TRZHASKOVSKAYA, V. I. NEFEDOV, and V. G. YARZHEMSKY. PHOTOELECTRON ANGULAR DISTRIBUTION PARAMETERS FOR ELEMENTS  $z=55$  to  $z=100$  IN THE PHOTOELECTRON ENERGY RANGE 100-5000 eV. *Atomic Data and Nuclear Data Tables*, 82(2):257–311, 2002. ISSN 0092-640X. doi: 10.1006/adnd.2002.0886. URL <http://www.sciencedirect.com/science/article/pii/S0092640X02908867>.
- [111] M. B. Trzhaskovskaya, V. K. Nikulin, V. I. Nefedov, and V. G. Yarzhemsky. Non-dipole second order parameters of the photoelectron angular distribution for elements  $z = 1-100$  in the photoelectron energy range 1-10 keV. *Atomic Data and Nuclear Data Tables*, 92(2):245–304, 2006. ISSN 0092-640X. doi: 10.1016/j.adt.2005.12.002. URL <http://www.sciencedirect.com/science/article/pii/S0092640X05000859>.
- [112] Sergey V. Baryshev and Elijah Thimsen. Enthalpy of formation for Cu-Zn-Sn-S (CZTS). *arXiv:1403.4922 [cond-mat]*, 2014. URL <http://arxiv.org/abs/1403.4922>.
- [113] Tsuyoshi Maeda, Satoshi Nakamura, and Takahiro Wada. First principles calculations of defect formation in in-free photovoltaic semiconductors  $\text{Cu}_2\text{ZnSnS}_4$  and  $\text{Cu}_2\text{ZnSnSe}_4$ . *Japanese Journal of Applied Physics*, 50(4):04DP07, 2011. ISSN 0021-4922, 1347-4065. doi: 10.1143/JJAP.50.04DP07. URL <http://stacks.iop.org/1347-4065/50/04DP07>.

- [114] Aron Walsh, Shiyu Chen, Su-Huai Wei, and Xin-Gao Gong. Kesterite Thin-Film Solar Cells: Advances in Materials Modelling of  $\text{Cu}_2\text{ZnSnS}_4$ . *Advanced Energy Materials*, 2(4):400–409, 2012. ISSN 1614-6840. doi: 10.1002/aenm.201100630. URL <http://onlinelibrary.wiley.com/doi/10.1002/aenm.201100630/abstract>.
- [115] Dd Wagman, Wh Evans, Vb Parker, Rh Schumm, I. Halow, Sm Bailey, Kl Churney, and RI Nuttall. The Nbs Tables of Chemical Thermodynamic Properties - Selected Values for Inorganic and C-1 and C-2 Organic-Substances in Si Units. *Journal of Physical and Chemical Reference Data*, 11: 1–8, 1982. ISSN 0047-2689. WOS:A1982QZ27200001.
- [116] Vladan Stevanović, Stephan Lany, Xiuwen Zhang, and Alex Zunger. Correcting density functional theory for accurate predictions of compound enthalpies of formation: Fitted elemental-phase reference energies. *Physical Review B*, 85(11):115104, 2012. doi: 10.1103/PhysRevB.85.115104. URL <http://link.aps.org/doi/10.1103/PhysRevB.85.115104>.
- [117] Steven S. Zumdahl. *Chemical Principles*. Houghton Mifflin Company, 6th edition, 2009. ISBN 0-618-94690-X.
- [118] I. Lefebvre, M. Lannoo, J. Olivier-Fourcade, and J. C. Jumas. Tin oxidation number and the electronic structure of  $\text{SnS-In}_2\text{S}_3\text{-SnS}_2$  systems. *Physical Review B*, 44(3):1004–1012, July 1991. doi: 10.1103/PhysRevB.44.1004. URL <http://link.aps.org/doi/10.1103/PhysRevB.44.1004>.
- [119] N. S. Pavlov, V. A. Galkin, I. A. Nekrasov, and E. Z. Kurmaev. Electronic structure and X-ray spectra of transition metal sulfides NiS, CuS, and ZnS. *Physics of the Solid State*, 51(11):2207–2210, November 2009. ISSN 1063-7834, 1090-6460. doi: 10.1134/S1063783409110018. URL <http://link.springer.com/article/10.1134/S1063783409110018>.
- [120] Joachim Paier, Ryoji Asahi, Akihiro Nagoya, and Georg Kresse.  $\text{Cu}_2\text{ZnSnS}_4$  as a potential photovoltaic material: A hybrid Hartree-Fock density functional theory study. *Physical Review B*, 79(11):115126, March 2009. doi: 10.1103/PhysRevB.79.115126. URL <http://link.aps.org/doi/10.1103/PhysRevB.79.115126>.
- [121] Shiyu Chen, X. G. Gong, Aron Walsh, and Su-Huai Wei. Crystal and electronic band structure of  $\text{Cu}_2\text{ZnSnX}_4$  (X=S and Se) photovoltaic absorbers: First-principles insights. *Applied Physics Letters*, 94(4):041903, January 2009. ISSN 0003-6951, 1077-3118. doi: 10.1063/1.3074499. URL <http://scitation.aip.org/content/aip/journal/apl/94/4/10.1063/1.3074499>.
- [122] Tsuyoshi Maeda, Satoshi Nakamura, and Takahiro Wada. Electronic structure and phase stability of In-free photovoltaic semiconductors,  $\text{Cu}_2\text{ZnSnSe}_4$  and  $\text{Cu}_2\text{ZnSnS}_4$  by first-principles calculation. *MRS Proceedings*, 1165, January 2009. ISSN 1946-4274. doi: 10.1557/PROC-1165-M04-03. URL [http://journals.cambridge.org/abstract\\_S1946427400008836](http://journals.cambridge.org/abstract_S1946427400008836).
- [123] M. Bär, B.-A. Schubert, B. Marsen, S. Krause, S. Pookpanratana, T. Unold, L. Weinhardt, C. Heske, and H.-W. Schock. Impact of KCN etching on the chemical and electronic surface structure of  $\text{Cu}_2\text{ZnSnS}_4$  thin-film solar cell absorbers. *Applied Physics Letters*, 99(15):152111–152111–3, October 2011. ISSN 00036951. doi: 10.1063/1.3650717. URL [http://apl.aip.org/resource/1/applab/v99/i15/p152111\\_s1](http://apl.aip.org/resource/1/applab/v99/i15/p152111_s1).
- [124] Gang Yang, Yong-Feng Li, Bin Yao, Zhan-Hui Ding, Rui Deng, Jie-Ming Qin, Fang Fang, Xuan Fang, Zhi-Peng Wei, and Lei Liu. Band alignments at interface of  $\text{Cu}_2\text{ZnSnS}_4/\text{ZnO}$  heterojunction: An x-ray photoelectron spectroscopy and first-principles study. *Journal of Alloys and Compounds*, 628: 293–297, 2015. ISSN 09258388. doi: 10.1016/j.jallcom.2014.12.174. URL <http://linkinghub.elsevier.com/retrieve/pii/S0925838814031028>.
- [125] Jörn Timo Wätjen, Jonathan J. Scragg, Tove Ericson, Marika Edoff, and Charlotte Platzer-Björkman. Secondary compound formation revealed by transmission electron microscopy at the  $\text{Cu}_2\text{ZnSnS}_4/\text{Mo}$  interface. *Thin Solid Films*, 535:31–34, 2013. ISSN 0040-6090. doi: 10.1016/j.tsf.2012.11.079. URL <http://www.sciencedirect.com/science/article/pii/S0040609012015763>.
- [126] Jonathan J. Scragg, J. Timo Wätjen, Marika Edoff, Tove Ericson, Tomas Kubart, and Charlotte Platzer-Björkman. A detrimental reaction at the molybdenum back contact in  $\text{Cu}_2\text{ZnSn(S,Se)}_4$  thin-film solar cells. *Journal of the American Chemical Society*, 134(47):19330–19333, 2012. ISSN 1520-5126. doi: 10.1021/ja308862n.

- [127] Santanu Bag, Oki Gunawan, Tayfun Gokmen, Yu Zhu, Teodor K. Todorov, and David B. Mitzi. Low band gap liquid-processed CZTSe solar cell with 10.1% efficiency. *Energy & Environmental Science*, 5(5):7060–7065, 2012. ISSN 1754-5706. doi: 10.1039/C2EE00056C. URL <http://pubs.rsc.org/en/content/articlelanding/2012/ee/c2ee00056c>.
- [128] Jonathan J. Scragg, Phillip J. Dale, Diego Colombara, and Laurence M. Peter. Thermodynamic aspects of the synthesis of thin-film materials for solar cells. *ChemPhysChem*, 13(12):3035–3046, 2012. ISSN 1439-7641. doi: 10.1002/cphc.201200067. URL <http://onlinelibrary.wiley.com/doi/10.1002/cphc.201200067/abstract>.
- [129] R. Coehoorn, C. Haas, J. Dijkstra, C. J. F. Flipse, R. A. de Groot, and A. Wold. Electronic structure of  $\text{MoSe}_2$ ,  $\text{MoS}_2$ , and  $\text{WSe}_2$ . i. Band-structure calculations and photoelectron spectroscopy. *Physical Review B*, 35(12):6195–6202, 1987. doi: 10.1103/PhysRevB.35.6195. URL <http://link.aps.org/doi/10.1103/PhysRevB.35.6195>.
- [130] Wencan Jin, Po-Chun Yeh, Nader Zaki, Datong Zhang, Jerzy T. Sadowski, Abdullah Al-Mahboob, Arend M. van der Zande, Daniel A. Chenet, Jerry I. Dadap, Irving P. Herman, Peter Sutter, James Hone, and Richard M. Osgood. Direct measurement of the thickness-dependent electronic band structure of  $\text{MoS}_2$  using angle-resolved photoemission spectroscopy. *Physical Review Letters*, 111(10):106801, 2013. doi: 10.1103/PhysRevLett.111.106801. URL <http://link.aps.org/doi/10.1103/PhysRevLett.111.106801>.
- [131] Yu Li Huang, Yifeng Chen, Wenjing Zhang, Su Ying Quek, Chang-Hsiao Chen, Lain-Jong Li, Wei-Ting Hsu, Wen-Hao Chang, Yu Jie Zheng, Wei Chen, and Andrew T. S. Wee. Bandgap tunability at single-layer molybdenum disulphide grain boundaries. *Nature Communications*, 6:6298, 2015. doi: 10.1038/ncomms7298. URL <http://www.nature.com/ncomms/2015/150217/ncomms7298/full/ncomms7298.html>.
- [132] Sang Wook Han, Gi-Beom Cha, Emmanouil Frantzeskakis, Ivy Razado-Colambo, José Avila, Young S. Park, Daehyun Kim, Jihoon Hwang, Jeong Soo Kang, Sunmin Ryu, Won Seok Yun, Soon Cheol Hong, and Maria C. Asensio. Band-gap expansion in the surface-localized electronic structure of  $\text{MoS}_2(0002)$ . *Physical Review B*, 86(11):115105, 2012. doi: 10.1103/PhysRevB.86.115105. URL <http://link.aps.org/doi/10.1103/PhysRevB.86.115105>.
- [133] S. K. Mahatha and Krishnakumar S. R. Menon. Inhomogeneous band bending on  $\text{MoS}_2(0001)$  arising from surface steps and dislocations. *Journal of Physics: Condensed Matter*, 24(30):305502, 2012. ISSN 0953-8984. doi: 10.1088/0953-8984/24/30/305502. URL <http://stacks.iop.org/0953-8984/24/i=30/a=305502>.
- [134] Byungha Shin, Oki Gunawan, Yu Zhu, Nestor A. Bojarczuk, S. Jay Chey, and Supratik Guha. Thin film solar cell with 8.4% power conversion efficiency using an earth-abundant  $\text{Cu}_2\text{ZnSnS}_4$  absorber. *Progress in Photovoltaics: Research and Applications*, 21(1):72–76, 2013. ISSN 1099-159X. doi: 10.1002/pip.1174. URL <http://onlinelibrary.wiley.com/doi/10.1002/pip.1174/abstract>.
- [135] Fangyang Liu, Kaiwen Sun, Wei Li, Chang Yan, Hongtao Cui, Liangxing Jiang, Xiaojing Hao, and Martin A. Green. Enhancing the  $\text{Cu}_2\text{ZnSnS}_4$  solar cell efficiency by back contact modification: Inserting a thin  $\text{TiB}_2$  intermediate layer at  $\text{Cu}_2\text{ZnSnS}_4/\text{Mo}$  interface. *Applied Physics Letters*, 104(5):051105, 2014. ISSN 0003-6951, 1077-3118. doi: 10.1063/1.4863736. URL <http://scitation.aip.org/content/aip/journal/apl/104/5/10.1063/1.4863736>.
- [136] B. Vermang, Y. Ren, O. Donzel-Gargand, C. Frisk, J. Joel, P. Salomé, J. Borme, S. Sadewasser, C. Platzer-Björkman, and M. Edoff. Rear surface optimization of CZTS solar cells by use of a passivation layer with nanosized point openings. *IEEE Journal of Photovoltaics*, 6(1):332–336, 2016. ISSN 2156-3381. doi: 10.1109/JPHOTOV.2015.2496864.
- [137] Haibing Xie, Simon López-Marino, Tetiana Olar, Yudania Sánchez, Markus Neuschitzer, Florian Oliva, Sergio Giraldo, Victor Izquierdo-Roca, Iver Laueremann, Alejandro Pérez-Rodríguez, and Edgardo Saucedo. Impact of Na Dynamics at the  $\text{Cu}_2\text{ZnSn}(\text{S},\text{Se})_4/\text{CdS}$  Interface During Post Low Temperature Treatment of Absorbers. *ACS Applied Materials & Interfaces*, 8(7):5017–5024, 2016. ISSN 1944-8244, 1944-8252. doi: 10.1021/acsami.5b12243. URL <http://pubs.acs.org/doi/abs/10.1021/acsami.5b12243>.

- [138] Kejia Wang, Byungha Shin, Kathleen B. Reuter, Teodor Todorov, David B. Mitzi, and Supratik Guha. Structural and elemental characterization of high efficiency  $\text{Cu}_2\text{ZnSnS}_4$  solar cells. *Applied Physics Letters*, 98(5):051912, 2011. ISSN 0003-6951, 1077-3118. doi: 10.1063/1.3543621. URL <http://scitation.aip.org/content/aip/journal/apl/98/5/10.1063/1.3543621>.
- [139] M. Bär, B.-A. Schubert, B. Marsen, S. Krause, S. Pookpanratana, T. Unold, L. Weinhardt, C. Heske, and H.-W. Schock. Native oxidation and Cu-poor surface structure of thin film  $\text{Cu}_2\text{ZnSnS}_4$  solar cell absorbers. *Applied Physics Letters*, 99(11):112103–112103–3, September 2011. ISSN 00036951. doi: doi:10.1063/1.3637574. URL [http://apl.aip.org/resource/1/applab/v99/i11/p112103\\_s1](http://apl.aip.org/resource/1/applab/v99/i11/p112103_s1).
- [140] L. E. Firment and A. Ferretti. Stoichiometric and oxygen deficient  $\text{MoO}_3(010)$  surfaces. *Surface Science*, 129(1):155–176, 1983. ISSN 0039-6028. doi: 10.1016/0039-6028(83)90100-0. URL <http://www.sciencedirect.com/science/article/pii/0039602883901000>.
- [141] Jacob A. Andrade-Arvizu, Maykel Courel-Piedrahita, and Osvaldo Vigil-Galán. SnS-based thin film solar cells: perspectives over the last 25 years. *Journal of Materials Science: Materials in Electronics*, 26(7):4541–4556, 2015. ISSN 0957-4522, 1573-482X. doi: 10.1007/s10854-015-3050-z. URL <http://link.springer.com/article/10.1007/s10854-015-3050-z>.
- [142] A. P. Lambros, D. Geraleas, and N. A. Economou. Optical absorption edge in SnS. *Journal of Physics and Chemistry of Solids*, 35(4):537–541, 1974. ISSN 0022-3697. doi: 10.1016/S0022-3697(74)80008-9. URL <http://www.sciencedirect.com/science/article/pii/S0022369774800089>.
- [143] A. R. H. F. Ettema, R. A. de Groot, C. Haas, and T. S. Turner. Electronic structure of SnS deduced from photoelectron spectra and band-structure calculations. *Physical Review B*, 46(12):7363–7373, 1992. doi: 10.1103/PhysRevB.46.7363. URL <http://link.aps.org/doi/10.1103/PhysRevB.46.7363>.
- [144] Georgios A. Tritsarlis, Brad D. Malone, and Efthimios Kaxiras. Optoelectronic properties of single-layer, double-layer, and bulk tin sulfide: A theoretical study. *Journal of Applied Physics*, 113(23):233507, 2013. ISSN 0021-8979, 1089-7550. doi: 10.1063/1.4811455. URL <http://scitation.aip.org/content/aip/journal/jap/113/23/10.1063/1.4811455>.
- [145] W. Albers, C. Haas, H. J. Vink, and J. D. Wasscher. Investigations on SnS. *Journal of Applied Physics*, 32(10):2220–2225, 1961. ISSN 0021-8979, 1089-7550. doi: 10.1063/1.1777047. URL <http://scitation.aip.org/content/aip/journal/jap/32/10/10.1063/1.1777047>.
- [146] Julien Vidal, Stephan Lany, Mayeul d’Avezac, Alex Zunger, Andriy Zakutayev, Jason Francis, and Janet Tate. Band-structure, optical properties, and defect physics of the photovoltaic semiconductor SnS. *Applied Physics Letters*, 100(3):032104, January 2012. ISSN 0003-6951, 1077-3118. doi: 10.1063/1.3675880. URL <http://scitation.aip.org/content/aip/journal/apl/100/3/10.1063/1.3675880>.
- [147] S. A. Kissin and D. R. Owens. New data on stannite and related tin sulfide minerals. *The Canadian Mineralogist*, 17(1):125–135, 1979. ISSN 0008-4476, 1499-1276. URL <http://canmin.geoscienceworld.org/content/17/1/125>.
- [148] Tong Jiang and Geoffrey A. Ozin. New directions in tin sulfide materials chemistry. *Journal of Materials Chemistry*, 8(5):1099–1108, 1998. ISSN 09599428, 13645501. doi: 10.1039/a709054d. URL <http://xlink.rsc.org/?DOI=a709054d>.
- [149] Lee A. Burton and Aron Walsh. Phase stability of the earth-abundant tin sulfides  $\text{SnS}$ ,  $\text{SnS}_2$ , and  $\text{Sn}_2\text{S}_3$ . *The Journal of Physical Chemistry C*, 116(45):24262–24267, 2012. ISSN 1932-7447, 1932-7455. doi: 10.1021/jp309154s. URL <http://pubs.acs.org/doi/abs/10.1021/jp309154s>.
- [150] Takashi Ikuno, Ryo Suzuki, Kosuke Kitazumi, Naoko Takahashi, Naohiko Kato, and Kazuo Higuchi. SnS thin film solar cells with  $\text{Zn}_{1-x}\text{Mg}_x\text{O}$  buffer layers. *Applied Physics Letters*, 102(19):193901, 2013. ISSN 0003-6951, 1077-3118. doi: 10.1063/1.4804603. URL <http://scitation.aip.org/content/aip/journal/apl/102/19/10.1063/1.4804603>.
- [151] Vasudeva Reddy Minnam Reddy, Sreedevi Gedi, Chinho Park, Miles R.W., and Ramakrishna Reddy K.T. Development of sulphurized SnS thin film solar cells. *Current Applied Physics*, 15(5):588–598, 2015. ISSN 1567-1739. doi: 10.1016/j.cap.2015.01.022. URL <http://www.sciencedirect.com/science/article/pii/S1567173915000310>.

- [152] Prasert Sinsersuksakul, Leizhi Sun, Sang Woon Lee, Helen Hejin Park, Sang Bok Kim, Chuanxi Yang, and Roy G. Gordon. Overcoming Efficiency Limitations of SnS-Based Solar Cells. *Advanced Energy Materials*, 4(15):n/a–n/a, October 2014. ISSN 1614-6840. doi: 10.1002/aenm.201400496. URL <http://onlinelibrary.wiley.com/doi/10.1002/aenm.201400496/abstract>.
- [153] S. J. Clark, J. Robertson, S. Lany, and A. Zunger. Intrinsic defects in ZnO calculated by screened exchange and hybrid density functionals. *Physical Review B*, 81(11):115311, March 2010. doi: 10.1103/PhysRevB.81.115311. URL <http://link.aps.org/doi/10.1103/PhysRevB.81.115311>.
- [154] Stephan Lany and Alex Zunger. Many-body GW calculation of the oxygen vacancy in ZnO. *Physical Review B*, 81(11):113201, March 2010. doi: 10.1103/PhysRevB.81.113201. URL <http://link.aps.org/doi/10.1103/PhysRevB.81.113201>.
- [155] Xin-Li Guo, Jae-Hyoung Choi, Hitoshi Tabata, and Tomoji Kawai. Fabrication and Optoelectronic Properties of a Transparent ZnO Homostructural Light-Emitting Diode. *Japanese Journal of Applied Physics*, 40:L177–L180, 2001. ISSN 00214922. doi: 10.1143/JJAP.40.L177. URL <http://stacks.iop.org/1347-4065/40/L177>.
- [156] Eun-Cheol Lee, Y.-S. Kim, Y.-G. Jin, and K. J. Chang. Compensation mechanism for N acceptors in ZnO. *Physical Review B*, 64(8):085120, 2001. doi: 10.1103/PhysRevB.64.085120. URL <http://link.aps.org/doi/10.1103/PhysRevB.64.085120>.
- [157] Vera Steinmann, R. Jaramillo, Katy Hartman, Rupak Chakraborty, Riley E. Brandt, Jeremy R. Poindexter, Yun Seog Lee, Leizhi Sun, Alexander Polizzotti, Helen Hejin Park, Roy G. Gordon, and Tonio Buonassisi. 3.88% Efficient Tin Sulfide Solar Cells using Congruent Thermal Evaporation. *Advanced Materials*, 26(44):7488–7492, November 2014. ISSN 1521-4095. doi: 10.1002/adma.201402219. URL <http://onlinelibrary.wiley.com/doi/10.1002/adma.201402219/abstract>.
- [158] Helen Hejin Park, Rachel Heasley, Leizhi Sun, Vera Steinmann, Rafael Jaramillo, Katy Hartman, Rupak Chakraborty, Prasert Sinsersuksakul, Danny Chua, Tonio Buonassisi, and Roy G. Gordon. Co-optimization of SnS absorber and Zn(O,S) buffer materials for improved solar cells. *Progress in Photovoltaics: Research and Applications*, 23(7):901–908, July 2015. ISSN 1099-159X. doi: 10.1002/pip.2504. URL <http://onlinelibrary.wiley.com/doi/10.1002/pip.2504/abstract>.
- [159] L. Kövér, G. Moretti, Zs Kovács, R. Sanjinés, I. Cserny, G. Margaritondo, J. Pálincás, and H. Adachi. High resolution photoemission and auger parameter studies of electronic structure of tin oxides. *Journal of Vacuum Science & Technology A*, 13(3):1382–1388, 1995. ISSN 0734-2101, 1520-8559. doi: 10.1116/1.579568. URL <http://scitation.aip.org/content/avs/journal/jvsta/13/3/10.1116/1.579568>.
- [160] Jia Ding, Zhi Li, Huanlei Wang, Kai Cui, Alireza Kohandehghan, Xuehai Tan, Dimitre Karpuzov, and David Mitlin. Sodiation vs. lithiation phase transformations in a high rate – high stability SnO<sub>2</sub> in carbon nanocomposite. *J. Mater. Chem. A*, 3(13):7100–7111, 2015. ISSN 2050-7496. doi: 10.1039/C5TA00399G. URL <http://pubs.rsc.org/en/content/articlelanding/2015/ta/c5ta00399g>.
- [161] Thomas J. Whittles, Lee A. Burton, Jonathan M. Skelton, Aron Walsh, Tim D. Veal, and Vin R. Dhanak. Band Alignments, Valence Bands, and Core Levels in the Tin Sulfides SnS, SnS<sub>2</sub>, and Sn<sub>2</sub>S<sub>3</sub>: Experiment and Theory. *Chemistry of Materials*, 28(11):3718–3726, 2016. ISSN 0897-4756, 1520-5002. doi: 10.1021/acs.chemmater.6b00397. URL <http://pubs.acs.org/doi/abs/10.1021/acs.chemmater.6b00397>.
- [162] M. Fondell, M. Gorgoi, M. Boman, and A. Lindblad. An HAXPES study of sn, SnS, SnO and SnO<sub>2</sub>. *Journal of Electron Spectroscopy and Related Phenomena*, 195:195–199, 2014. ISSN 0368-2048. doi: 10.1016/j.elspec.2014.07.012. URL <http://www.sciencedirect.com/science/article/pii/S0368204814001601>.
- [163] Tengfei Zhou, Wei Kong Pang, Chaofeng Zhang, Jianping Yang, Zhixin Chen, Hua Kun Liu, and Zaiping Guo. Enhanced sodium-ion battery performance by structural phase transition from two-dimensional hexagonal-SnS<sub>2</sub> to orthorhombic-SnS. *ACS Nano*, 8(8):8323–8333, 2014. ISSN 1936-0851. doi: 10.1021/nn503582c. URL <http://dx.doi.org/10.1021/nn503582c>.
- [164] Zhi Li, Jia Ding, and David Mitlin. Tin and tin compounds for sodium ion battery anodes: Phase transformations and performance. *Accounts of Chemical Research*, 48(6):1657–1665, 2015. ISSN 0001-4842. doi: 10.1021/acs.accounts.5b00114. WOS:000356754600012.

- [165] M. Cruz, J. Morales, J. P. Espinos, and J. Sanz. XRD, XPS and sn-119 NMR study of tin sulfides obtained by using chemical vapor transport methods. *Journal of Solid State Chemistry*, 175(2): 359–365, 2003. ISSN 0022-4596. doi: 10.1016/S0022-4596(03)00329-3. WOS:000186126600031.
- [166] P. K. Nair, M. T. S. Nair, Ralph A. Zingaro, and Edward A. Meyers. XRD, XPS, optical and electrical studies on the conversion of SnS thin films to SnO<sub>2</sub>. *Thin Solid Films*, 239(1):85–92, 1994. ISSN 0040-6090. doi: 10.1016/0040-6090(94)90112-0. URL <http://www.sciencedirect.com/science/article/pii/0040609094901120>.
- [167] Jean-Marc Themlin, Mohammed Chtaïb, Luc Henrard, Philippe Lambin, Jacques Darville, and Jean-Marie Gilles. Characterization of tin oxides by x-ray-photoemission spectroscopy. *Physical Review B*, 46(4):2460–2466, July 1992. doi: 10.1103/PhysRevB.46.2460. URL <http://link.aps.org/doi/10.1103/PhysRevB.46.2460>.
- [168] W. Jaegermann, F. S. Ohuchi, and B. A. Parkinson. Interaction of cu, ag and au with van der waals faces of WS<sub>2</sub>, and SnS<sub>2</sub>. *Surface Science*, 201(1):211–227, 1988. ISSN 0039-6028. doi: 10.1016/0039-6028(88)90607-3. URL <http://www.sciencedirect.com/science/article/pii/0039602888906073>.
- [169] Anja Schneikart. *Herstellung und Charakterisierung von SnS-Dünnschichtsolarzellen*. Ph.D. Thesis, TU Darmstadt, 2014. URL <http://tuprints.ulb.tu-darmstadt.de/3916/>.
- [170] B. J. Coppa, C. C. Fulton, P. J. Hartlieb, R. F. Davis, B. J. Rodriguez, B. J. Shields, and R. J. Nemanich. In situ cleaning and characterization of oxygen- and zinc-terminated, n-type, ZnO{0001} surfaces. *Journal of Applied Physics*, 95(10):5856–5864, May 2004. ISSN 0021-8979, 1089-7550. doi: 10.1063/1.1695596. URL <http://scitation.aip.org/content/aip/journal/jap/95/10/10.1063/1.1695596>.
- [171] M. Sugiyama, K. T. R. Reddy, N. Revathi, Y. Shimamoto, and Y. Murata. Band offset of SnS solar cell structure measured by X-ray photoelectron spectroscopy. *Thin Solid Films*, 519(21):7429–7431, August 2011. ISSN 0040-6090. doi: 10.1016/j.tsf.2010.12.133. URL <http://www.sciencedirect.com/science/article/pii/S0040609010017827>.
- [172] C. Garza, S. Shaji, A. Arato, E. Perez Tijerina, G. Alan Castillo, T. K. Das Roy, and B. Krishnan. p-type CuSbS<sub>2</sub> thin films by thermal diffusion of copper into Sb<sub>2</sub>S<sub>3</sub>. *Solar Energy Materials and Solar Cells*, 95(8):2001–2005, 2011. ISSN 0927-0248. doi: 10.1016/j.solmat.2010.06.011. URL <http://www.sciencedirect.com/science/article/pii/S0927024810003648>.
- [173] D. Colombara, L. M. Peter, K. D. Rogers, J. D. Painter, and S. Roncallo. Formation of CuSbS<sub>2</sub> and CuSbSe<sub>2</sub> thin films via chalcogenisation of Sb–Cu metal precursors. *Thin Solid Films*, 519(21):7438–7443, 2011. ISSN 0040-6090. doi: 10.1016/j.tsf.2011.01.140. URL <http://www.sciencedirect.com/science/article/pii/S0040609011001830>.
- [174] Liping Yu, Robert S. Kokenyesi, Douglas A. Keszler, and Alex Zunger. Inverse design of high absorption thin-film photovoltaic materials. *Advanced Energy Materials*, 3(1):43–48, 2013. ISSN 1614-6840. doi: 10.1002/aenm.201200538. URL <http://onlinelibrary.wiley.com/doi/10.1002/aenm.201200538/abstract>.
- [175] Bo Yang, Liang Wang, Jun Han, Ying Zhou, Huaibing Song, Shiyu Chen, Jie Zhong, Lu Lv, Dongmei Niu, and Jiang Tang. CuSbS<sub>2</sub> as a promising earth-abundant photovoltaic absorber material: A combined theoretical and experimental study. *Chemistry of Materials*, 26(10):3135–3143, 2014. ISSN 0897-4756. doi: 10.1021/cm500516v. URL <http://dx.doi.org/10.1021/cm500516v>.
- [176] Adam W. Welch, Pawel P. Zawadzki, Stephan Lany, Colin A. Wolden, and Andriy Zakutayev. Self-regulated growth and tunable properties of CuSbS<sub>2</sub> solar absorbers. *Solar Energy Materials and Solar Cells*, 132:499–506, 2015. ISSN 0927-0248. doi: 10.1016/j.solmat.2014.09.041. URL <http://www.sciencedirect.com/science/article/pii/S0927024814005297>.
- [177] Adam W. Welch, Lauryn L. Baranowski, Pawel Zawadzki, Clay DeHart, Steve Johnston, Stephan Lany, Colin A. Wolden, and Andriy Zakutayev. Accelerated development of CuSbS<sub>2</sub> thin film photovoltaic device prototypes. *Progress in Photovoltaics: Research and Applications*, 24(7):929–939, 2016. ISSN 1099-159X. doi: 10.1002/pip.2735. URL <http://onlinelibrary.wiley.com/doi/10.1002/pip.2735/abstract>.

- [178] Adam W. Welch, Lauryn L. Baranowski, Pawel Zawadzki, Stephan Lany, Colin A. Wolden, and Andriy Zakutayev. CuSbSe<sub>2</sub> photovoltaic devices with 3% efficiency. *Applied Physics Express*, 8(8): 082301, 2015. ISSN 1882-0778, 1882-0786. doi: 10.7567/APEX.8.082301. URL <http://stacks.iop.org/1882-0786/8/i=8/a=082301?key=crossref.e704bce239cfe699ff75e88f3c6358f9>.
- [179] Asahiko Sugaki, Hirorni Shima, and Arashi Kitakaze. Phase Relations of the Cu<sub>2</sub>S-Sb<sub>2</sub>S<sub>3</sub> System. *Yamaguchi University Technology reports*, 1973. URL <http://ci.nii.ac.jp/naid/110004779903/en>.
- [180] Jean-Charles Dupin, Danielle Gonbeau, Philippe Vinatier, and Alain Levasseur. Systematic XPS studies of metal oxides, hydroxides and peroxides. *Physical Chemistry Chemical Physics*, 2(6): 1319–1324, January 2000. ISSN 1463-9084. doi: 10.1039/A908800H. URL <http://pubs.rsc.org/en/content/articlelanding/2000/cp/a908800h>.
- [181] Robert V. Forest, Kunhee Han, Erten Eser, Jingguang G. Chen, and Robert W. Birkmire. Understanding the Effect of Na in Improving the Performance of Cu(In,Ga)S<sub>2</sub>-Based Photovoltaics. In *2013 IEEE 39th Photovoltaic Specialists Conference (PVSC)*, pages 371–375. IEEE, 2013. ISBN 978-1-4799-3299-3. WOS:000340054100085.
- [182] M. B. Zellner, R. W. Birkmire, E. Eser, W. N. Shafarman, and J. G. Chen. Determination of activation barriers for the diffusion of sodium through CIGS thin-film solar cells. *Progress in Photovoltaics: Research and Applications*, 11(8):543–548, 2003. ISSN 1099-159X. doi: 10.1002/pip.515. URL <http://onlinelibrary.wiley.com/doi/10.1002/pip.515/abstract>.
- [183] J. Lee, L. Chen, U. Obahiagbon, C. Thompson, W. N. Shafarman, and R. W. Birkmire. In-situ resistance measurement during the growth of Cu(In,Ga)Se<sub>2</sub> films by multi-source evaporation. In *2013 IEEE 39th Photovoltaic Specialists Conference (PVSC)*, pages 0398–0401. IEEE, 2013. doi: 10.1109/PVSC.2013.6744176.
- [184] Z. Bastl and S. Černý. X-ray photoelectron spectroscopy study of the interaction of carbon monoxide and propylene with dysprosium and yttrium surfaces. *Journal of Alloys and Compounds*, 176(1): 159–165, October 1991. ISSN 0925-8388. doi: 10.1016/0925-8388(91)90021-M. URL <http://www.sciencedirect.com/science/article/pii/092583889190021M>.
- [185] M. K. Weldon, P. Uvdal, C. M. Friend, and J. G. Serafin. Decoupling of vibrational modes as a structural tool: Coverage-induced reorientation of methoxide on Mo<sub>(110)</sub>. *The Journal of Chemical Physics*, 103(12):5075–5084, September 1995. ISSN 0021-9606, 1089-7690. doi: 10.1063/1.470594. URL <http://scitation.aip.org/content/aip/journal/jcp/103/12/10.1063/1.470594>.
- [186] M. Bär, B.-A. Schubert, B. Marsen, S. Schorr, R. G. Wilks, L. Weinhardt, S. Pookpanratana, M. Blum, S. Krause, Y. Zhang, W. Yang, T. Unold, C. Heske, and H.-W. Schock. Electronic structure of Cu<sub>2</sub>ZnSnS<sub>4</sub> probed by soft x-ray emission and absorption spectroscopy. *Physical Review B*, 84(3), July 2011. ISSN 1098-0121, 1550-235X. doi: 10.1103/PhysRevB.84.035308. URL <http://adsabs.harvard.edu/abs/2011PhRvB..84c5308B>.
- [187] Aron Walsh and Graeme W. Watson. Influence of the anion on lone pair formation in Sn(II) monochalcogenides: A DFT study. *The Journal of Physical Chemistry B*, 109(40):18868–18875, October 2005. ISSN 1520-6106. doi: 10.1021/jp051822r. URL <http://dx.doi.org/10.1021/jp051822r>.
- [188] Adolfo A. Mosquera, David Horwat, Alexandr Rashkovskiy, Anatoly Kovalev, Patrice Miska, Dmitry Wainstein, Jose M. Albella, and Jose L. Endrino. Exciton and core-level electron confinement effects in transparent ZnO thin films. *Scientific Reports*, 3, April 2013. ISSN 2045-2322. doi: 10.1038/srep01714. URL <http://www.nature.com/articles/srep01714>.
- [189] C. Guglieri and J. Chaboy. O K-Edge X-ray Absorption Spectroscopy in Al-Doped ZnO Materials: Structural vs Electronic Effects. *The Journal of Physical Chemistry C*, 118(44):25779–25785, November 2014. ISSN 1932-7447. doi: 10.1021/jp508461d. URL <http://dx.doi.org/10.1021/jp508461d>.
- [190] Frederik Claeysens, Colin L. Freeman, Neil L. Allan, Ye Sun, Michael N. R. Ashfold, and John H. Harding. Growth of ZnO thin films - experiment and theory. *J. Mater. Chem.*, 15(1):139–148, 2005. ISSN 0959-9428, 1364-5501. doi: 10.1039/B414111C. URL <http://xlink.rsc.org/?DOI=B414111C>.

- [191] W. H. Huang, S. J. Sun, J. W. Chiou, H. Chou, T. S. Chan, H.-J. Lin, Krishna Kumar, and J.-H. Guo. Electronic structure of Al-doped ZnO transparent conductive thin films studied by x-ray absorption and emission spectroscopies. *Journal of Applied Physics*, 110(10):103705, November 2011. ISSN 0021-8979, 1089-7550. doi: 10.1063/1.3662202. URL <http://scitation.aip.org/content/aip/journal/jap/110/10/10.1063/1.3662202>.
- [192] J. W. Chiou, K. P. Krishna Kumar, J. C. Jan, H. M. Tsai, C. W. Bao, W. F. Pong, F. Z. Chien, M.-H. Tsai, I.-H. Hong, R. Klauser, J. F. Lee, J. J. Wu, and S. C. Liu. Diameter dependence of the electronic structure of ZnO nanorods determined by x-ray absorption spectroscopy and scanning photoelectron microscopy. *Applied Physics Letters*, 85(15):3220–3222, 2004. ISSN 0003-6951, 1077-3118. doi: 10.1063/1.1802373. URL <http://scitation.aip.org/content/aip/journal/apl/85/15/10.1063/1.1802373>.
- [193] J. W. Chiou, J. C. Jan, H. M. Tsai, C. W. Bao, W. F. Pong, M.-H. Tsai, I.-H. Hong, R. Klauser, J. F. Lee, J. J. Wu, and S. C. Liu. Electronic structure of ZnO nanorods studied by angle-dependent x-ray absorption spectroscopy and scanning photoelectron microscopy. *Applied Physics Letters*, 84(18):3462–3464, May 2004. ISSN 0003-6951, 1077-3118. doi: 10.1063/1.1737075. URL <http://scitation.aip.org/content/aip/journal/apl/84/18/10.1063/1.1737075>.
- [194] J. G. Chen, B. Frühberger, and M. L. Colaianni. Near-edge x-ray absorption fine structure characterization of compositions and reactivities of transition metal oxides. *Journal of Vacuum Science & Technology A*, 14(3):1668–1673, 1996. ISSN 0734-2101, 1520-8559. doi: 10.1116/1.580316. URL <http://scitation.aip.org/content/avs/journal/jvsta/14/3/10.1116/1.580316>.
- [195] J.-H. Guo, L. Vayssieres, C. Persson, R. Ahuja, B. Johansson, and J. Nordgren. Polarization-dependent soft-x-ray absorption of highly oriented ZnO microrod arrays. *Journal of Physics: Condensed Matter*, 14(28):6969, 2002. ISSN 0953-8984. doi: 10.1088/0953-8984/14/28/308. URL <http://stacks.iop.org/0953-8984/14/i=28/a=308>.
- [196] E. P. Mikheeva, S. V. Koscheev, S. P. Ruzankin, G. M. Zhidomirov, S. A. Leontiev, V. G. Devjatov, and A. E. Cherkashin. An effect of the Zn 3d-states on UV and x-ray spectra in ZnO. *Journal of Electron Spectroscopy and Related Phenomena*, 94(1):59–71, 1998. ISSN 0368-2048. doi: 10.1016/S0368-2048(98)00147-9. WOS:000074806800008.
- [197] P. J. Møller, S. A. Komolov, and E. F. Lazneva. A total current spectroscopy study of metal oxide surfaces: I. Unoccupied electronic states of ZnO and MgO. *Journal of Physics: Condensed Matter*, 11(48):9581, 1999. ISSN 0953-8984. doi: 10.1088/0953-8984/11/48/315. URL <http://stacks.iop.org/0953-8984/11/i=48/a=315>.